REALISTIC CADAVER MECHANICAL TESTING & QUANTITATIVE MAGNETIC RESONANCE IMAGING FOR EVALUATING KNEES THROUGHOUT WALKING

A Thesis Submitted to the College of

Graduate and Postdoctoral Studies

In Partial Fulfillment of the Requirements

For the Degree of Master of Science

In the Department of Mechanical Engineering

University of Saskatchewan

Saskatoon

By

Álvaro Andrés Espinosa Maldonado

Permission to use

In presenting this thesis/dissertation in partial fulfillment of the requirements for a Postgraduate degree from the University of Saskatchewan, I agree that the Libraries of this University may make it freely available for inspection. I further agree that permission for copying of this thesis/dissertation in any manner, in whole or in part, for scholarly purposes may be granted by the professor or professors who supervised my thesis/dissertation work or, in their absence, by the Head of the Department or the Dean of the College in which my thesis work was done. It is understood that any copying or publication or use of this thesis/dissertation or parts thereof for financial gain shall not be allowed without my written permission. It is also understood that due recognition shall be given to me and to the University of Saskatchewan in any scholarly use which may be made of any material in my thesis/dissertation.

Disclaimer

Reference in this thesis/dissertation to any specific commercial products, process, or service by trade name, trademark, manufacturer, or otherwise, does not constitute or imply its endorsement, recommendation, or favoring by the University of Saskatchewan. The views and opinions of the author expressed herein do not state or reflect those of the University of Saskatchewan, and shall not be used for advertising or product endorsement purposes.

Requests for permission to copy or to make other uses of materials in this thesis/dissertation in whole or part should be addressed to:

Head of the Department of Mechanical Engineering
57 Campus Drive
University of Saskatchewan
Saskatoon, Saskatchewan S7N 5A9 Canada

OR

Dean
College of Graduate and Postdoctoral Studies
University of Saskatchewan
116 Thorvaldson Building, 110 Science Place
Saskatoon, Saskatchewan S7N 5C9 Canada

Abstract

Introduction: Knees are subjected to daily physical activities, injuries and diseases, such as osteoarthritis (OA). Such complications represent significant costs (billions and thousands of USD/year for countries and individuals, respectively). Moreover, there is no OA cure and its risk factors (obesity, malalignment and injury) affect joints' mechanical loading. Thus, knees must be studied under realistic loading conditions. Unfortunately, due to joints' complexity (geometry, mechanical properties and loading), current experimental methods seldom achieve this. Quantitative magnetic resonance imaging (qMRI) potentially offers a non-invasive evaluation of tissue structure, biochemistry and mechanics, thereby facilitating injury or disease tracking if links between these properties and imaging outcomes were well established. However, the connections between tissue health and mechanical properties remain unclear, as is the relation between tissue- and joint-level biomechanics.

Objective: Determine if tissue structure and joint function are related in whole cadaver knees under physiologically realistic loading conditions applied via a novel MRI-safe loading device.

Methods: A novel MRI-safe knee loading device was designed, built and its repeatability assessed. Physiologic loading conditions (simulating walking) suitable for mechanical tests were determined via musculoskeletal (MSK) modelling, verified and validated against published data, and applied to a cadaver knee. To measure tibio- and patello-femoral (T-F and P-F) contact responses, a pressure sensing system was used in conjunction with the instrumented loading device. Then, to search for T_2 relaxation-deformation associations, tibial and patellar cartilage deformations and T_2 relaxation responses of other six ex-vivo knees subjected to axial compression (simulating standing) were measured and correlation analyses performed.

Results & Discussion: The MRI-safe loading system developed was able to simulate healthy or pathologic gait with adequate repeatability (e.g., 1.23 to 2.91 CV% for compression, comparable to existing simulators), leading to generally consistent contact responses in agreement with published experimental and finite element studies. Cartilage thickness and T_2 relaxation time magnitudes measured fell within expected values, while their loading-induced changes agreed with previous studies but exhibited larger variability. Moreover, a moderate negative correlation ($r = -0.402$, $p = 0.019$) was found between unloaded tibial cartilage thickness and T_2 relaxation time, which may be linked to cartilage composition (relating collagen fibers and water content).

Preface

The roles of the people directly involved in this project are:

- Alvaro Espinosa - Primary researcher responsible for all aspects of this project, including literature review, experimental design, tools (hardware and software) and methods (SOPs) development, data collection and processing; specific contributions for each study listed below

MRI-safe loading simulator R&D:

- Alvaro Espinosa – MRI-safe load-control system, MSK biomechanics codes I & II
- Emily McWalter – MSc. supervisor, consulting, funding and research equipment
- James Johnston – Consulting, research equipment
- Allan Dolovich – Consulting
- Robert Peace – Consulting, manufacturing, research equipment
- Shawn Reinink – Consulting, research equipment
- *Engineering Shops* – Consulting, manufacturing

Study I:

- Alvaro Espinosa – Specimen misalignment calculator, knee contacts processing code, novel pressure sensing system setup, potting equipment, specimen preparation, mechanical testing
- Robert Peace – Novel pressure sensing system setup and technical assistance during data collection
- Clara Machtaler – Igloo icepacks

Study II:

- Alvaro Espinosa – Specimen preparation, qMRI-mechanics algorithm, image processing
- Maddie Martel - MRI-safe displacement-control rig
- Chelsey Thorson - MRI-safe displacement-control rig, specimen preparation, mechanical testing
- Brennan Berryman - Specimen preparation
- Kirstin Olsen - Specimen preparation
- Lumeng Cui - Imaging
- Natasha Bzowey – Image segmentation

Acknowledgements & disclosures

No words can accurately describe how grateful I am for all the support I have received from "a few" singular creatures (human) that have become an essential part of my life; thanks so much, endeavours like this, which should help the world someday, are possible because of you. That being said, I will try to "sketch" this out, which most of you know is something I enjoy:

First, I would like to thank my blood family, especially my mom and dad for their unconditional love, support and sacrifice, my little "twin" brother for teaching me how to become a better brother, and my grandparents, uncles, aunts and a few *select* cousins for all your valuable teachings and inspiration. Totally kidding, every single family member has a very special place in my heart; thanks for bringing me joy and keeping my inner child alive.

Next, I would like to thank my academic family, Drs. McWalter, Dolovich, Johnston and Kontulainen, for all your continuous support, mentorship, lessons and friendship, especially my supervisor, Emily, for opening the doors to the biomechanics world and this amazing research group when I was just a naïve student (ok fine, more naïve). On that same boat, I would like to thank my current (and past) colleagues for the technical advice and laughter we shared (I may or not have been joking only about half of the time). I would also like to thank my Advisory Committee (Drs. Lanovaz, Johnston and Feldman) for their input, the University of Saskatchewan's Department of Mechanical Engineering, in particular Robert Peace and Shawn Reinink for technical advice, equipment and time, as well as Blair Cole and Dan Vessey from Engineering Shops for helping me bring my creations to life.

Now, to the family I have chosen, which overlaps with the previous and includes remarkable high school teachers and the rest of my dear friends, thanks for all the lessons, encouragement and fun.

Lastly, I would like to thank *G_d* for all the gifts and obstacles, as well as for looking after and helping me through the darkest nights. If you exist, I cannot wait to meet you the day I finally part from this world.

This research received support from NSERC Discovery Grant, Siemens Healthineers and the University of Saskatchewan's Department of Mechanical Engineering.

Dedication

For those about to fail…

Don't

Give up!

Sorry, don't give up!

Table of contents

Permission to use i
Disclaimer i
Abstract ii
Preface iii
Acknowledgements & disclosures iv
Dedication v
Table of contents vi
List of tables xiii
List of figures xv
List of terms, symbols & acronyms xxiii
1. Introduction 1
1.1. Motivation (Problem) 1
1.2. Current practices & limitations 1
1.3. Research objectives 2
1.4. Thesis “mechanics” & scope 4
2. Background & literature review 5
2.1. Anatomy, physiology & epidemiology background 5
2.1.1. Lower-body locomotor system 5
2.1.2. Joint of interest: The knee 6
2.1.2.1. Bones 6
2.1.2.2. Articular soft tissues (cartilage & menisci) 7
2.1.2.3. Other soft tissues (ligaments, tendons, muscles & capsules) 7
2.1.2.4. Material behaviour of knee tissues 8
2.1.3. Knee function 9
2.1.3.1. Coordinate systems 9
2.1.3.2. Healthy behaviour 11
2.1.3.3. Pathologic behaviour 13
2.2. Review of experimental tests & techniques in biomechanics 14
2.2.1. Ex-vivo (ex-situ & in-situ) studies 15
2.3. Review of computational techniques in biomechanics 19

2.3.1. MSK modelling 20
2.4. Review of medical imaging 22
2.4.1. MRI and qMRI 23
2.5. Summary of gaps & connection to project 27
3. Development of a novel MRI-safe physiologic loading device for ex-vivo joints 28
3.1. System development 28
3.1.1. Software (MSK biomechanics) 29
3.1.1.1. MSK modelling 29
3.1.1.2. MSK processing 30
3.1.2. Hardware (pneumatic device) – a.k.a. “MR creep rig” 32
3.2. Discussion 36
3.3. Conclusion 37
4. Study I: Human knee mechanical loading & response repeatability – What may be going on inside knees at different gait phases? (Preliminary findings from a static approach) 38
4.1. Introduction 38
4.2. Methods 38
4.2.1. Study overview 38
4.2.2. Study scope 40
4.2.2.1. Anatomy & loads of interest 40
4.2.2.2. Gait time point discretization 40
4.2.3. Specimens 41
4.2.3.1. Specimen preparation 41
Intact-capsule general preparation 41
Open-capsule preparation adaptations 42
4.2.4. Mechanical testing 44
4.2.5. Statistical analysis 47
4.2.5.1. Repeatability of gait experimental simulation (loading & response parameters) 47
4.3. Results 48
4.4. Discussion 52
4.5. Conclusion 53
5. Study II: Are loading-induced changes in knee cartilage morphology related to T_2 relaxation times? 54

5.1. Introduction 54
5.2. Methods 55
5.2.1. Study overview 55
5.2.2. Study scope 56
5.2.2.1. Tissues, regions & sites of interest 56
5.2.3. Specimens & preparation 56
5.2.4. Mechanical testing 57
5.2.4.1. Experimental loading protocols 58
5.2.5. Imaging & processing 58
5.2.5.1. Imaging sequences (data acquisition) 58
5.2.5.2. Pre-processing 59
Segmentation 59
Image Resampling 59
Registration 59
5.2.5.3. qMRI-mechanics algorithm (data processing) 60
5.2.5.4. Post-processing 61
Thresholding 61
Analogous T_2 relaxation & deformation metrics 61
5.2.6. Statistical analysis: qMRI-mechanics correlations (exploratory) 62
5.3. Results 64
5.3.1. Estimated knee deformation & T_2 relaxation response during prolonged standing 64
5.3.2. T_2-deformation correlations (exploratory) 65
5.4. Discussion 68
5.4.1. Knee deformation and T_2 relaxation response to loading 68
5.4.2. T_2-deformation correlations 70
5.4.2.1. Physical interpretation possibilities 72
5.5. Conclusion 73
6. Integrated discussion 74
6.1. Research direction reminder 74
6.2. Key findings overview 74
6.3. Linking pilot studies 75
6.4. Suggested future studies & directions 76

6.4.1. Study I improvements 76
6.4.2. Study II improvements 78
6.5. Contributions & research significance 79
7. Concluding remarks 80
References 81
Appendices 102
A1. Ethics certificate 102
A2. Additional background 104
A2.1. Deformable body mechanics (from machines to biological systems under load) 104
A2.1.1. Loading 104
A2.1.2. Material constitution 107
A2.1.2.1. General material behaviour 107
A2.1.2.2. Biological materials (including bi-phasic, anisotropic, natural composites) 110
Bone 112
Articular cartilage 113
Menisci 116
Longitudinal soft tissues 117
A2.1.3. Deformation 118
A2.1.4. FE modelling 121
A2.2. Current in-vivo (in-situ) experimental biomechanics techniques 124
A2.2.1. Gait analysis (non-invasive) 124
A2.2.2. Instrumented TKRs (invasive) 125
A2.2.3. Simplified loading (non-invasive) 126
A2.3. Comparison of ex-vivo load devices used to existing technologies 128
A2.4. Medical imaging & image processing 133
A2.4.1. Current medical imaging modalities 133
A2.4.2. Image processing 134
A3. Additional resources for MR creep rig system 136
A3.1. MSK biomechanics modelling protocols 136
A3.2. SOP for MSK biomechanics modelling/processing for experimental simulation 141
A3.2.1. MSK biomechanics processing details 141

A3.2.2. MSK biomechanics code I: Continuous gait simulation 141
A3.2.3. MSK biomechanics code II: Discrete gait variability simulation..... 141
A3.2.4. Specimen misalignment calculator code 141
A3.2.5. MR creep rig configuration calculations (including muscle guide positions)141
A3.3. SOP for MRI-compatible physiologic loading simulator for cadaveric joints 142
A3.3.1. Instructional video (tutorial/demo for MR creep rig)..... 142
A3.3.2. MRI-safe loading system (aka. “MR creep rig”) 3D CAD models and G-codes 142
A3.3.3. MRI-safe loading system (aka. “MR creep rig”) blueprints for main structural components 143
A3.3.3.1. Top assembly..... 143
A3.3.3.2. Middle (specimen case) assembly 152
A3.3.3.3. Potted specimen assembly..... 157
A3.3.3.4. Bottom assembly 159
A3.4. Raw data..... 168
A3.4.1. Flex & rigid coil images..... 168
A3.4.2. MSK anonymous gait data (OpenSim subject) 168
A3.4.2.1. Anthropometrics (BW, dimensions)..... 168
A3.4.2.2. Kinematics (marker position, velocity, acceleration)..... 168
A3.4.2.3. Kinetics (GRFs)..... 168
A3.4.3. Friction measurements for compressive indenter / tibia pot interface..... 168
A3.4.4. MR creep rig calibration..... 168
A3.4.4.1. Load cell force data (tensile & compressive actuators)..... 168
A3.4.4.2. Pressure gauges data..... 168
A3.4.5. Loading variability for left/right knees (non-dimensionalized) 168
A3.5. Processed data..... 169
A3.5.1. Flex & rigid coils’ SNR..... 169
A3.5.2. MSK anonymous gait data (1kN, 1.8m subject) 169
A3.5.2.1. Statically optimized muscle tension 169
A3.5.2.2. External knee joint reactions 169
A3.5.3. Loading regime & rig configuration (1kN, 1.8m subject)..... 169
A3.5.4. Friction coefficients for compressive indenter / tibia pot interface..... 169

A3.5.5. Rig calibration 170
A3.5.6. Agreement between processed MSK estimates & instrumented TKR measurements 173
A4. Additional resources for study I 175
A4.1. Study design 175
A4.2. SOP for ex-vivo contacts measurements using MR creep rig & novel system 176
A4.2.1. Preliminary pressure sensors testing 177
A4.2.2. Knee contacts processing code: Steady response 178
A4.3. Testing protocols 179
A4.3.1. Mechanical testing protocols 179
A4.3.2. Loading rig configuration 180
A4.3.3. Specimen log (K07) 182
A4.4. Raw data 185
A4.5. Processed data 186
A4.5.1. Muscle force repeatability 187
A4.6. Loading assessment via gait variability 189
A4.6.1. Determining loading conditions for gait variability simulation (methods) 189
A4.6.2. Experimental repeatability comparison to gait variability (loading parameters) 193
A4.6.3. Agreement between experimental loading repeatability & gait loading variability (results) 193
A4.6.4. Applied loading physiologic realism assessment against gait variability data (discussion) 197
A4.7. Preliminary findings on valgum-like human knee mechanical response during walking (exploratory) 199
A4.7.1.1. Preliminary associations between load input and contact response parameters 201
A4.7.1.2. Human knee mechanical response discussion 204
A5. Additional resources for study II 209
A5.1. Study design 209
A5.2. SOP for the qMRI-mechanics Correlations Assessment 210
A5.2.1. qMRI-mechanics sampling code: T_2 time vs deformation 211
A5.3. Testing protocols 212

A5.3.1. Imaging protocols 213
A5.4. Raw data 214
A5.5. Processed data 215
A5.5.1. Thickness and T_2 changes further examination 218
A5.5.2. T_2-deformation correlations assessment 222
A5.5.3. Outlier or influence point removal 227
A5.5.4. T_2 relaxation time-thickness models for the unloaded tibial cartilage (exploratory) 232
A6. Additional resources for future studies 234
A6.1. Mechanical testing & imaging protocols 234
A6.2. Further improvements/extensions 236
A6.3. Main future research direction for this project 238
A6.4. Additional future projects 240

List of tables

Table 4-1: Rig kinematic and kinetic parameters for valgum-like walking experimental simulation (subject = K07, limb = left, sex = male, age = 68 years, height = 1.78m, BW = 743N) 44
Table 4-2: Input and steady-state output measures considered for repeatability assessment 48
Table 4-3: Summary of (input) kinematic & kinetic testing parameters & repeatability [intra-subject AVG ± SD (CV%)] of knee specimen (limb = left, sex = male, age = 68 years, height = 1.78m, BW = 743N); x-y-z coordinates relative to rig origin 49
Table 4-4: Summary of (output) load response parameters & repeatability [intra-subject AVG ± SD (CV%)] of a knee specimen (limb = left, sex = male, age = 68 years, height = 1.78m, BW = 743N); x-y local coordinates relative to individual pressure sensors' origin 50
Table 5-1: Specimen bank for study II 57
Table 5-2: T_2 relaxation and deformation variable definitions 61
Table 5-3: Adopted correlations strength ranges (positive/negative sign of correlation coefficient denotes correlation direction)[203] 62
Table 5-4: Thickness and T_2 relaxation values for unloaded & loaded cartilage sites of all 6 knees [inter-subject AVG ± SD (100%·SD/AVG)]; only uncorrupted measurements shown 64
Table 5-5: Changes in thickness and T_2 relaxation time due to loading for different cartilage sites [inter-subject AVG ± SD (100%·SD/AVG)]; only including data after thresholding 65
Table 0-1: Representative TIPE material properties (inter-subject weighted averages) for patellar, femoral and tibial cartilages [in curvilinear (t-n-b) coordinates] 115
Table 0-2: Representative TIE material properties (inter-subject weighted averages) for individual menisci [in cylindrical (r-θ-z) coordinates][232,233,246,250,275-283] 117
Table 0-3: Representative IE material properties (inter-subject weighted averages) for knee ligaments and tendons (including meniscal attachments) 118
Table 0-4: Comparison of "a few" full-joint lower-body ex-vivo loading devices/setups (from the 80's to present time) 128
Table 0-5: Rig kinematic and kinetic parameters for walking experimental simulation (subject = K07, limb = right, sex = male, age = 68 years, height = 1.78m, BW = 743N) 180

Table 0-6: Rig kinematic and kinetic parameters for walking experimental simulation (subject = K07, limb = left, sex = male, age = 68 years, height = 1.78m, BW = 743N) 181
Table 0-7: Summary of applied muscle forces & their repeatability [intra-subject AVG ± SD (CV%)] of knee specimen (limb = left, sex = male, age = 68 years, height = 1.78m, BW = 743N); x-y-z coordinates relative to rig origin 187
Table 0-8: Gait variability literature search (some studies had data for >1 load or variability type) 189

List of figures

Figure 1-1: Overall study design flowchart. Adapted from Wikimedia Commons[18-21]. 3
Figure 2-1: Lower-body locomotor system: Hip, thigh, knee, shank, ankle, foot (joints highlighted, while muscles and other soft tissues hidden). Adapted from Creative Commons[22]... 5
Figure 2-2: Full knee simplified anatomy: A. Extended (assembled) & B. Flexed (resected) views. Adapted from Wikimedia Commons[23,24]..... 6
Figure 2-3: General viscoelastic behaviours: Creep vs. stress-relaxation. Adapted from Wikimedia Commons[27]..... 8
Figure 2-4: A. Common right-handed anatomic coordinate systems for right knees (A.1. Gait analysis, A.2. MSK models, A.3. TKR implants), B. less-common right-handed coordinates for left knees (note triad rotates about the longitudinal z direction for left limbs), C. sample method for defining knee coordinates, and D. Grood & Suntay analogy to linked mechanical joints. Reproduced with permission from Benoit et al. 2006[36], Heinlein et al. 2009[41], Baker et al. 1999[44], Cappozzo et al. 2005[37] and Grood et al. 1983[31]..... 10
Figure 2-5: Load transmission during physical activities (inverse dynamics): For each segment, (applied) distal loads and inertial effects must be balanced by loads at the joint, which transfer to the adjacent segment via Newton's 3rd law..... 11
Figure 2-6: Healthy (A) and osteoarthritic (B) knees (P-F joint not shown). Taken from Wikimedia Commons[78]..... 13
Figure 2-7: Healthy knee and malalignments with overloaded compartments..... 14
Figure 2-8: Full-joint ex-vivo rig types. Reproduced with permission from Greaves et al. 2009[12], McWalter et al.2014[96], Baldwin et al.2012[25], Li et al.1999[122] and Lawless et al.2014[94]. 15
Figure 2-9: Static optimization routine (A) & finding joint reactions via inverse dynamics (B) in OpenSim. Adapted with permission from Kutzner et al. 2010[42]. 21
Figure 2-10: A. MR scanner & B. sample volumetric MR image (note slice thickness). Adapted from Wikimedia Commons[157] and with permission from Jordan et al. 2014[158]..... 22
Figure 2-11: A. Morphologic MRI (qDESS, 1st echo) & B. qMRI (T_2 relaxation) sample slices; note soft tissues presence..... 23

Figure 2-12: Possible pathways for T_2 relaxation response to loading healthy (A) and OA (B) cartilages (dominating effect depends on the situation). Images courtesy of Dr. Emily McWalter. 25
Figure 3-1: System development process 28
Figure 3-2: Statically approximate gait loading regime for 1.8m, 1kN (102kg) subject's right knee: A. Knee flexion (H-S = heel strike, F-E = full extension, T-O = toe-off, T-O* = toe-off surrogate, F-F = full flexion); B. simulated knee joint loads (with respect to knee anatomic coordinates, invalid instances for moment simulation grayed out); & C. primary muscle tension 31
Figure 3-3: MRI-safe loading rig system (simplified exploded view showing key DOFs via arrows, muscle cables not shown) 32
Figure 3-4: MR creep rig simplified "anatomy" (2D side translucent view) and key coordinate systems; all coordinate systems are right-handed (irrespective of whether joint is right or left) . 33
Figure 3-5: Simplified P&ID diagram of loading system's pneumatic circuit: 1. Air compressor, 2. Flow-control valve, 3. Pressure gauge, 4. Piston cylinder (same components for all actuators) 34
Figure 3-6: Major loading mechanisms used: Muscle tension, direct axial compression and bending generation via off-axis load (shifting the compressive force by a distance *r* simultaneously applies compression *F* and moment *M* at the knee) 35
Figure 4-1: Study I diagram: Input & output repeatability characteristics for each flexion considered. Adapted from Wikimedia Commons[18,19]..... 39
Figure 4-2: Anatomy of interest: A. Articular soft tissues (articular cartilages, menisci, ligaments), B. Muscles carrying considerable tension that are available ex vivo and in OpenSim. Reproduced with permission from Orozco et al. 2018[190]. 40
Figure 4-3: Key gait time points with corresponding intended flexions recreated in OpenSim... 41
Figure 4-4: Specimen preparation: A). Intact knee (line drawing), B). Prepared knee anatomic model (dissected/potted/sutured knee surrogate), C). Potting station, D). Prepared specimen with pressure sensors inserted (bovine open capsule) 42
Figure 4-5: Hamstring guides difficult posterior sensor insertion in extended and flexed mounted specimen configurations 43
Figure 4-6: Specimen preparation plan (open capsule) for pressure sensors insertion..... 43

Figure 4-7: Specimens tested at MR creep rig for different purposes 45
Figure 4-8: pliance-x pressure sensing system (except for sensors/cables, all components remain outside MR-creep rig) 46
Figure 4-9: Knee loading repeatability throughout gait (n=3 tests, AVG ± 2 SD): A. Applied forces, B. Applied moments at tibia end (in rig coordinates), C. Effective knee flexion. Key gait time points include heel-strike (H-S), full extension (F-E), approximate toe-off (T-O*) and full flexion (F-F). 49
Figure 4-10: Knee loading response repeatability throughout gait (n=3 tests, AVG ± 2 SD): A. Contact area, B. Contact force magnitudes (compressive), C. Centers of geometry & pressure, and D. Contact pressures magnitudes (compressive). Key gait time points include heel-strike (H-S), full extension (F-E), approximate toe-off (T-O*) and full flexion (F-F). Knee compartments considered are patello-femoral (P-F), and medial and lateral tibio-femoral (T-F,med and T-F,lat). 51
Figure 5-1: Simplified knee pathologies model & study motivation 54
Figure 5-2: Study II diagram: Experimental pipeline for evaluating associations between deformation & T_2. Adapted from Wikimedia Commons[18,20,21]. 55
Figure 5-3: Key load bearing regions in cartilages of interest (probing sites marked with a star). Adapted from Wikimedia Commons[198,199]. 56
Figure 5-4: Mechanical testing & imaging setup: A. MR relaxation rig, B. Potted cadaver specimen (with superimposed knee illustration), C. 3T MR scanner. Images courtesy of Madeline Martel and Chelsey Thorson, and adapted from Wikimedia Commons[199] 57
Figure 5-5: Registration flowcharts for morphologic masks (A) & T_2 relaxation maps (B); all conducted via mutual information 3D registration (avoiding joint coordinate axes setup later on) 60
Figure 5-6: T_2 relaxation time and thickness sampling: Sagittal slice with mask overlaid (A), mask contour with unit normals field (B), probing site (C) and its T_2 time depth distribution (D) 61
Figure 5-7: Deformation vs. T_2 relaxation metrics for patellar (blue) and tibial (orange) cartilages after outlier/influence point removal; regression equation only for significant (bolded p-values) potential correlations 66

Figure 5-8: Initial thickness vs. T_2 relaxation time, after logarithmic transformations, for patellar (blue) and tibial (orange) cartilages after outlier/influence point removal; regression equation only for significant (bolded p-values) potential correlation 67
Figure 0-1: Types of mechanical loading (main failure modes, internal resultants and stress distributions) 105
Figure 0-2: Complex loading: A) Combined loading resultants, B) Arbitrary non-uniform stress boundary conditions, and C) Full state of stress for generalized combined loading (stresses on back faces not shown). Images courtesy of Dr. Allan Dolovich and adapted from Wikimedia Commons[209]. 105
Figure 0-3: Knee "internal" physiologic loads (A) vs. "external" equivalent loads (B) – Two- and Three-dimensional (2D & 3D) views. Adapted with permission from Orozco et al. 2018[190] and Kutzner et al. 2010[42] 106
Figure 0-4: Common stress-strain curves for isotropic, homogeneous industrial materials; material comparison highlighted in blue. Based on Calister et al. 2014[26]..... 109
Figure 0-5: Transversely isotropic poroelasticity: Transverse isotropy + poroelasticity. Adapted from Wikimedia Commons[247] and with permission from Tweten et al. 2015[248]..... 111
Figure 0-6: Bone cross-section (C = cortical, T = trabecular, S = subchondral), E-BMD relations and stress-strain curves for different bones (note characteristic differences in E for different densities). Adapted with permission from Venäläinen et al. 2014[226], Helgason et al. 2008[256] and Hart et al. 2017[257]..... 113
Figure 0-7: Split line patterns for different soft tissue regions with relatively uniform collagen fiber orientations demonstrate the need for spatially varying single-phase material models to effectively describe tissue functions. Adapted with permission from Halonen et al. 2017[144] and Gu et al. 2011[228]. 115
Figure 0-8: Meniscus section, fiber distribution & stress-strain curve for bovine samples along circumferential direction. Note similar yet different stiffness is expected for human menisci. Adapted from Wikimedia Commons[274] and with permission from Danso et al. 2014[267]..... 116
Figure 0-9: Ligaments, fiber orientation & sample stress-strain curve. Reproduced with permission from Orozco et al. 2018[190] and Lee et al. 2002[284]. 117
Figure 0-10: Geometrically linear vs. nonlinear problem. Adapted from Wikimedia Commons[288,289]. 119

Figure 0-11: Generalized deformation gradient. Adapted from Wikimedia Commons[291,292]. ... 120
Figure 0-12: Tissue-level FEM [ex-situ (A), indentation (B)] and joint-level FEM [2D T-F joint (C), 3D T-F joint (D)]. Reproduced or adapted with permission from Wilson et al. 2005[243], Danso et al. 2015[227], Venäläinen et al. 2014[226], Kazemi et al. 2014[220]. 121
Figure 0-13: Gait & motion capture setup showing a few marker snapshots from different views. Adapted from Wikimedia Commons[307] and with permission from Cappozzo et al. 2005[37]. 124
Figure 0-14: Instrumented TKR & gait measurements (external joint reactions showing a multiaxial combined loading scenario). Reproduced with permission from Heinlein et al. 2009[41]. 126
Figure 0-15: Radiographic medical images (note soft tissues absence). Taken from Wikimedia Commons[310,311]. 133
Figure 0-16: (A) 2D slice with segmented patellar and tibial cartilages and (B) corresponding volumes. Segmentation courtesy of Natasha Bzowey. 134
Figure 0-17: Sample registration steps conducted on two different versions of the same image (green = base image, turquoise = object requiring registration) 135
Figure 0-18: All lower limb muscle forces estimated throughout gait for Subject01_walk1..... 137
Figure 0-19: Lower limb muscle forces throughout gait for Subject01_walk1 after exclusion based on magnitude..... 138
Figure 0-20: Relevant muscles for Subject01_walk1 after exclusion based on practical considerations 138
Figure 0-21: Calibration & input loading repeatability setup showing tensile (Omega LCM703-75) and compressive (FUTEKLTH350-FSH04307) load cells, and pressure sensors (novel pliance-x) 170
Figure 0-22: Average calibration curves & equations for tensile (A) & compressive (B) actuators 171
Figure 0-23: Expected similarities and differences between OpenSim MSK model-based estimates & OrthoLoad TKR measurements of knee loading; datasets agree for most highlighted gait time points (H-S, F-E, T-O*, F-F) with larger discrepancies for abduction/adduction bending moment 174

Figure 0-24: Sensor contact testing hardware: A. Steel puck, B. Nylon puck, C. Metal rod, D. Metal indenter, E. Rubber ball, F. 3DP patella with silicone cartilage, G. 3DP tibia with silicone cartilage and rubber menisci, H. Artificial femur 177
Figure 0-25: Muscle forces (F_bifemsh, F_semimem, F_vastLat) showed large variability for all gait time points 187
Figure 0-26: Intra-subject (A. Healthy) and inter-subject (B. Healthy, C. General pathologic, D. Varum and E. Valgum) loading condition variability bounds (AVG ± 2 SD) for left knee specimen used in study I (BW = 743N, height = 1.78m) 192
Figure 0-27: Ideal vs. actual knee flexion (effective values are AVG±2SD for n=3 repeated tests) 194
Figure 0-28: Ideal vs. effective applied forces (left knee), including healthy variability ranges (effective values are AVG±2SD for n=3 repeated tests). Applied forces include biceps femoris (F_bifemsh), semimembranosus (F_semimem) and vastus lateralis (F_vasLat) tensions, shearing force (F_sh,cable), and axial compression (F_fem,axial). 195
Figure 0-29: Ideal vs. effective applied moments (left knee) in rig coordinates, including general pathology & valgum ranges (effective values are AVG±2SD for n=3 repeated tests) 196
Figure 0-30: Steady contact pressure 2D distributions and pressure centers during gait & 3D thumbnails (last repeated trial) 200
Figure 0-31: Contact forces (A) and contact areas (B) vs. applied axial force magnitude trends during stance 201
Figure 0-32: Contact force magnitudes (A) and contact areas (B) vs. knee flexion data show linear and non-linear trends 202
Figure 0-33: Linear trends between contact areas & contact force magnitudes 202
Figure 0-34: Regional maximum (A) and average (B) contact pressures vs. applied axial force magnitude register linear trends for the T-F joint only 203
Figure 0-35: Largest anterior-posterior centroid (C_y) location variations seem independent from applied axial force magnitude changes during gait. 203
Figure 0-36: Anterior-posterior location of centers of (A) geometry, C_y, & (B) pressure, CP_y, vs. applied moment parallel to flexion/extension axis, M_x,applied, only register a nontrivial trend for lateral T-F pressure center excursions 204

Figure 0-37: Sample qDESS image (A) & T_2 relaxation time map (B) sagittal slice containing trochlea (unloaded and loaded K06) 218
Figure 0-38: Thickness (A) and T_2 relaxation time (B) for unloaded and loaded states (AVG±2SD) and diagram showing change directions of average thickness and T2 relaxation time with load 219
Figure 0-39: Individual and group changes in thickness (A) and T_2 relaxation time (B) measurements upon applied loading; note differences in sample size 220
Figure 0-40: Absolute (A) and normalized (B) changes in thickness and T_2 relaxation time due to applied loading register copious inter-subject variability (AVG±2SD) 221
Figure 0-41: Histograms for mechanical measures: A. Initial thickness [mm], B. Final thickness [mm], C. Thickness change [mm], D. Engineering strain 222
Figure 0-42: Histograms for T_2 relaxation measures: A. Initial T_2 time [ms], B. Final T_2 time [ms], C. T_2 change [ms], D. T_2 strain..... 223
Figure 0-43: Histograms for residuals of significant associations between initial thickness & corresponding T_2 time, after outlier/influence point removal: A. $(t)_0$ vs. $(T_2)_0$ or $|(t)_0|$ vs. $|(T_2)_0|$, B. $\log|(t)_0|$ vs. $|(T_2)_0|$, C. $|(t)_0|$ vs. $\log|(T_2)_0|$, D. $\log|(t)_0|$ vs. $\log|(T_2)_0|$..... 224
Figure 0-44: Q-Q plots for significant associations between initial thickness & corresponding T_2 time, after outlier/influence point removal: A. $(t)_0$ vs. $(T_2)_0$ or $|(t)_0|$ vs. $|(T_2)_0|$, B. $\log|(t)_0|$ vs. $|(T_2)_0|$, C. $|(t)_0|$ vs. $\log|(T_2)_0|$, D. $\log|(t)_0|$ vs. $\log|(T_2)_0|$..... 225
Figure 0-45: Residual plots for significant associations between initial thickness & corresponding T_2 time, after outlier/influence point removal: A. $(t)_0$ vs. $(T_2)_0$ or $|(t)_0|$ vs. $|(T_2)_0|$, B. $\log|(t)_0|$ vs. $|(T_2)_0|$, C. $|(t)_0|$ vs. $\log|(T_2)_0|$, D. $\log|(t)_0|$ vs. $\log|(T_2)_0|$..... 226
Figure 0-46: Deformation vs. T_2 relaxation metrics for patellar (blue) and tibial (orange) cartilages before outlier/influence point (delineated in black) removal; regression equation only for significant (bolded p-values) potential correlations..... 227
Figure 0-47: Initial thickness vs. T_2 relaxation time, after logarithmic transformations, for patellar (blue) and tibial (orange) cartilages before outlier/influence point (delineated in black) removal; regression equation only for significant (bolded p-values) potential correlations..... 228
Figure 0-48: Deformation vs. T_2 relaxation metrics for patellar (blue) and tibial (orange) cartilages after outlier/influence point removal; regression equation only for significant (bolded p-values) potential correlations..... 230

Figure 0-49: Initial thickness vs. T_2 relaxation time, after logarithmic transformations, for patellar (blue) and tibial (orange) cartilages after outlier/influence point removal; regression equation only for significant (bolded p-values) potential correlation 231
Figure 0-50: Significant best-fit models (after outlier/influence point removal) for initial T_2 relaxation time as a function of initial cartilage thickness do not exhibit major differences but rather all point towards an inverse relation between these parameters in tibial cartilages. 232
Figure 0-51: Normal operation (N1) mechanical testing setup: A) MR creep rig + Body 18 coil at MR scanner (Siemens Magnetom Skyra) – flange cutouts allow pneumatic/electric cables to pass through; B) MR creep rig without flex coil to show fiducials 235

List of terms, symbols & acronyms

N.B.:

1. Some of these may be combined and/or slightly adapted to fit the language.
2. Measurement unit definitions are excluded from this glossary.
3. Be aware of font changes (e.g., uppercase/lowercase, bolding); they can change meaning.

Symbol or abbreviation	**Term**	**Description (in this research context)**
2D	Two-D	Two dimensions, two-dimensional
3D	Three-D	Three dimensions, three-dimensional
<none>	Cartesian coordinates	3D system with orthogonal bases $\hat{x}, \hat{y}, \hat{z}$
<none>	Polar coordinates	2D system with orthogonal bases $\hat{r}, \hat{\theta}$
<none>	Cylindrical coordinates	3D system with orthogonal bases $\hat{r}, \hat{\theta}, \hat{z}$
<none>	Curvilinear coordinates	3D system with orthogonal bases $\hat{t}, \hat{n}, \hat{b}$
Ant	Anterior	Closer to the front of the body
Pos	Posterior	Closer to the back of the body
Med	Medial	Closer to the middle of the body
Lat	Lateral	Closer to the outer side of the body
Sup	Superior	Closer to the top of the body
Inf	Inferior	Closer to the bottom of the body
<none>	Coronal, frontal	Plane that sections the body into anterior and posterior regions
<none>	Sagittal, side	Plane that sections the body into medial and lateral regions
<none>	Transverse, axial	Plane that sections the body into superior and inferior regions
<none>	Distal	Farther from centre of body
<none>	Proximal	Closer to centre of body
AVG	Average, arithmetic mean	1st statistical moment; generalized mean with degree p=1
RMS	Root-means-square(d), quadratic mean	Generalized mean with degree p=2
SD	Standard deviation	~ 2nd statistical moment (variance, SD^2, is the true 2nd statistical moment)
CV%	Percent coefficient of variation	(SD/AVG)·100%
r	Pearson product-moment correlation coefficient	Parametric statistic
r_s	Spearman's rank correlation coefficient	Non-parametric statistic

ρ	Generic correlation coefficient	Either Pearson or Spearman coefficient
DF	Degree of freedom	# of free independent variables that can be altered before changing a dependent variable (statistics context)
DOF	Degree of freedom	Allowable motion (mechanics context)
PDE	Partial differential equation	Equation involving multivariate functions and their derivatives
BC	Boundary condition	Known value of a function at a given boundary
IC	Initial condition	Known value of a function at the beginning of a transient process
FE, FEM	Finite-element(s), finite-element method/modelling	Approximation tool for numerically solving PDEs
<varies>	(Mechanical) load	Applied displacement, force, moment pressure, stress or strain
F, P	Force	Influence that aims to move a body
p	Pressure	Force divided by normal (perpendicular) area
M, T	Moment, torque	Tendency to rotate created by an offset normal force
<varies>	Moment arm	Offset distance between the axis of rotation and the applied force
δ, u	Deflection, displacement	Difference in position
v	Velocity	1^{st} time derivative of displacement
a	Acceleration	2^{nd} time derivative of displacement
g	Gravitational acceleration	$9.81 m/s^2$ in most places on Earth
θ	Angle, angular deflection	Angular difference between 2 points
ω	Rotational velocity	1^{st} time derivative of angular displacement
α	Rotational acceleration	2^{nd} time derivative of angular displacement
L	Angular momentum	Product of mass moment of inertia and angular velocity
t	Time	Progression of events, physical dimension
<none>	Creep	Transient loading process where variable strain results from constant applied stress
<none>	Stress relaxation	Transient loading process where variable stress results from constant applied strain
<none>	Equilibrium, steady state	State of balance when the conditions of working system or process stabilize and do not change further
σ	Normal stress	Hydrostatic pressure on a given area (may refer to magnitude or tensor matrix)
τ	Shearing stress	Force divided by tangential area (may refer to magnitude or tensor matrix)

ε	Normal strain	Non-dimensional change in length (may refer to magnitude or tensor matrix)
γ	Shearing strain	Non-dimensional change in angle (may refer to magnitude or tensor matrix)
λ	Stretch ratio	Ratio of deformed to original length (may refer to magnitude or tensor matrix)
<none>	Tension	Form of axial loading
<none>	Compression	Form of axial loading
<none>	Torsion	Twisting loading mode
Sh	Shear	Cutting loading mode
Bend	Bending, flexion	Flexural loading mode
CP	Center of pressure	Average location of some pressure
C	Centroid, center of geometry	Average location of some area
A	Area	Space bounded by a planar closed curve
I	2^{nd} moment of area	Geometric resistance to bending (may refer to magnitude or tensor matrix)
I_G	Mass moment of inertia (about center of gravity, G)	Resistance to rotational motion (may refer to magnitude or tensor matrix)
t	Thickness	Shell width
m	Mass	Resistance to translational motion
ρ	Density	Ratio of mass to volume, $\rho = m/V$
E	Young's modulus, elastic modulus	Material property describing material's stiffness, given by the slope of the linear-elastic stress-strain region
ν	Poisson's ratio	Material property relating transverse to longitudinal deformations
k	(Bulk or structural) stiffness	Deflection resistance to load
S	Strength	Stress at rupture; also, loosely used in biomechanics field to refer to elastic modulus
φ	Porosity	Measure of empty space in a porous medium
e	Void ratio	Ratio of voids volume to the total porous medium volume, $e = \varphi/(1-\varphi)$
κ	Permeability	Flow conductivity through a porous medium
μ	Dynamic (absolute) viscosity	Fluid resistance to shear deformation
μ / ρ	Kinematic viscosity	Ratio of dynamic viscosity to density
Q, $\dot{V}$	Volumetric flow rate	1^{st} time derivative of a changing volume
q, Q/A	Volumetric flux	Volumetric flow rate per (normal) unit area
SF	Safety factor	Ratio of capability to duty (often referring to a system or component)

<none>	Yield	Permanent deformation onset
<none>	Failure	Material rupture or yielding
<none>	Fatigue	Fracture due to repeated usage
<none>	Isotropy	Random organization of material particles
<none>	Anisotropy	Preferential organization of material particles
FR	Fiber-reinforced	Composite (artificial or natural) material with increased strength and stiffness along fibers
<none>	Ductile	Able to sustain large elastic deformations
<none>	Brittle	Unable to sustain large elastic deformations, prone to sudden failure
IE	Isotropic elastic	Uniform linear-elastic material behaviour in all directions
TIE	Transversely isotropic elastic	Identical IE behaviour in 2 normal directions (defining a plane of isotropy), different from the IE behaviour in out-of-plane direction
(d)TIPE	(Depth-dependent) transversely isotropic poroelastic	(Staggered) TIE materials incorporating porous media behaviour
(d)FRPE	(Depth-dependent) fiber-reinforced poroelastic	(Staggered) composite poroelastic media consisting of a pororus IE matrix reinforced by fibers
vE	Viscoelastic	Transient elastic stiffness response of a material
μ_s	Static coefficient of friction	Ratio between max tangential, shearing force (required to start motion) and normal force. Do not confuse with friction factors (used in pipe flow)
<none>	WD-40 (Water Displacement - 40th Attempt)	Hydrocarbon-based lubricant, degreaser
PMMA	Poly(methyl methacrylate)	Acrylic, Plexiglas, Persplex (brittle polymer compound)
<none>	Dental stone	Gypsum (ceramic compound)
CAD	Computer-aided design	Geometric modelling software
3DP	3D printing	Additive manufacturing technique
CNC	Computer numerical control	Computer-controlled manufacturing
<none>	Potting	Process that fixes biological tissues to industrial hardware
SOP	Standard operating procedure	<self-explanatory>
ROI	Region of interest	<self-explanatory>

MSK	Musculoskeletal	Regarding the muscular and/or skeletal systems
<none>	Musculoskeletal modelling	Numerical technique for simulating rigid body mechanics
<none>	Gait	Walking pattern
<none>	Gait analysis	Kinematic and kinetic study of gait motion
<none>	Forward dynamics	Predicting unknown kinematics from known kinetics
<none>	Inverse dynamics	Predicting unknown kinetics from known kinematics
Flex-Ext	Flexion-extension	Sagittal projection of the knee joint 3D rotation
Abd-Add	Abduction-adduction	Coronal projection of the knee joint 3D rotation
Int-Ext	Internal-external rotation	Transverse projection of the knee joint 3D rotation
BW	Body weight	<self-explanatory>
GRF	Ground reaction force	Physical activity load BCs at the ground
H-S	Heel-strike	Gait time point when the swinging leg's heel makes contact with the ground
F-E	Full-extension	Gait time point when the single leg supporting the entire body is compressed fully extended
T-O	Toe-off	Gait time point when the supporting leg stops making contact with the ground
F-F	Full-flexion	Gait time point when the swinging leg is flexed the most
F-A	Fully axial	F-E configuration but loaded up to 1BW only (used for estimating the knee centre)
<none>	In-vivo (adj), in vivo (adv)	In a living organism
<none>	In-vitro (adj), in vitro (adv)	In a glass (test tube) or in a controlled lab experiment
<none>	Ex-vivo (adj), ex vivo (adv)	Out of a living organism, dead, expired
<none>	In-situ (adj), in situ (adv)	In site (within intact tissues)
<none>	Ex-situ (adj), ex situ (adv)	Out of site (outside intact tissues)
<none>	Cortical	Compact bone
<none>	Trabecular	Spongy bone
<none>	Sesamoid	Bone encapsulated by tendons
<none>	Subchondral	Tissue region below cartilage
P-F	Patello-femoral	Joint comprised of patella and femur articulating surfaces
T-F	Tibio-femoral	Joint comprised of tibia and femur articulating surfaces

T-Fi	Tibio-fibular	Joint comprised of tibia and fibula contacting surfaces
Pat	Patella	Knee cap
Fem	Femur	Thigh bone
Tib	Tibia	Bigger shank bone
<none>	Fibula	Smaller shank bone
<none>	Articular cartilage	Soft tissue present on the ends of the bones and provides smooth surfaces for relative motion in the joint
<none>	Meniscus	Knee cartilage that facilitates smooth motion, shock absorption and joint stability
Vas lat	Quadriceps	Vastus lateralis (lateral) muscles connected to the superior patella
Semimem, Bifemsh	Hamstrings	Semimembranosus (medial), biceps femoris short head (lateral) muscles connected to the posterior tibia condyles
PT	Patellar tendon	Knee tendon connecting patella and tibia
ACL	Anterior cruciate ligament	Knee ligament connecting posterior femur and anterior tibia at the intercondylar notch
PCL	Posterior cruciate ligament	Knee ligament connecting anterior femur and posterior tibia at the intercondylar notch
MCL	Medial collateral ligament	Knee ligament connecting femur and tibia (medial side)
LCL	Lateral collateral ligament	Knee ligament connecting femur and tibia (lateral side)
MPFL	Medial patello-femoral ligament	Knee ligament connecting femur and patella (medial side)
LPFL	Lateral patello-femoral ligament	Knee ligament connecting femur and patella (lateral side)
PFL	Popliteo-fibular ligament	Knee ligament connecting femur and fibula
ALC	Anterior lateral capsule	Knee long capsule connecting femur and tibia (lateral side)
TL	Transverse ligament	Knee ligament connecting the anterior medial and lateral meniscal horns
<none>	Collagen	Macromolecule making up a portion of articular soft tissues (often in the form of fibers)
OA	Osteoarthritis	Whole-joint disease marked by soft tissue breakdown
<none>	Varum	Malalignment overloading knee’s medial T-F compartment

<none>	Valgum	Malalignment overloading knee's lateral T-F compartment
TKR	Total knee replacement (device)	Artificial knee implant installed during arthroplasty procedure
<none>	Fiducial	Registration or reference marker
HR	High resolution	<self-explanatory>
SNR	Signal-to-noise ratio	$(AVG)_{signal}/(SD)_{noisy\ background}$
FOV	Field of view	<self-explanatory>
RF	Radiofrequency	Lowest frequency range of the electromagnetic spectrum
TR	Repetition time	Time between successive RF pulses
TE	Echo time	Time between RF emission and receipt of its echo
CT	Computed tomography	Medical imaging modality that creates 3D images via X-rays
DXA, DEXA	Dual-energy X-ray absorptiometry	Medical imaging modality that creates 2D images of bones via X-rays to estimate their mineral density
RSA	Roentgen stereo(photo)grammetric analysis	Stereo X-rays used to study 3D geometries from two planar images
(q)MRI	(Quantitative) magnetic resonance imaging	(Quantitative) medical imaging that creates 3D images via magnetic fields
(q)DESS	(Quantitative) double-echo steady state	Imaging sequence that can be used to measure transverse relaxation via exponential curve fitting
$T_{1\rho}$	$T_{1\rho}$ relaxation time	Spin-lattice relaxation time
T_2	T_2 relaxation time	Transverse relaxation time
ε_{T2}	T_2 strain	Change in T_2 normalized by initial T_2 relaxation signal
λ_{T2}	T_2 stretch ratio	Ratio of final T_2 signal compared to initial T_2 relaxation signal
DAQ	Data acquisition	<self-explanatory>
<none>	novel pliance-x	Capacitive pressure sensing system
<none>	MR relaxation rig	Custom MRI-safe displacement-control testing system
<none>	MR creep rig	Custom MRI-safe load-control testing system

1. Introduction

Relating tissue- and joint-level knee structure and function during physical activities is a non-trivial task with clinical implications. Furthermore, the role of physiologically realistic loading conditions on knee function is key, since excessive loading, musculoskeletal (MSK) disorders and/or injuries likely contribute to irreversible joint diseases. Due to in-vivo and experimental limitations, studying healthy or pathologic knee biomechanics using ex-vivo models loaded to a physiologic state is an useful approach. This can be achieved via physiologic loading simulators and medical imaging; however, their potential for examining the effects of daily physical activities on joint biomechanics responses has been limited.

1.1. Motivation (Problem)

Among multiple pathologies affecting knees, osteoarthritis (OA) is a multifactorial joint disease marked by tissues degradation, articular pain, and limited motion or even impairment, eventually leading to joint destruction. It affects >10% of North America and Europe (obese and elderly populations at high risk[1-5]), representing significant long-term suffering and economic impact. For Canada, between 2010 and 2040, CA$550 billion are estimated as direct costs and CA$909 billion as indirect costs for OA alone[6]. Annually, these financial burdens together with related MSK complications' amount to thousands and billions of US$/year respectively for individuals and countries worldwide[7-9]. Moreover, its pathogenesis remains unclear and there is no cure.

1.2. Current practices & limitations

Quantitative magnetic resonance imaging (qMRI) is a promising non-invasive technique, which can potentially monitor tissue health, injuries or diseases at early stages[10,11], which is likely a key to having any success in treating such conditions. Some potential treatments are currently limited by a lack of objective measures to assess their outcomes, for which there may be reluctance to even developing them until such measures are adopted. Fortunately, in addition to MRI's ability to distinguish between different soft tissues due to inherent high contrast, qMRI measures local tissue properties (e.g., T_2 and $T_{1\rho}$ relaxation times) that preliminary studies have shown are associated with tissue constitution (biochemical content and structure) and function (mechanical properties)[10-16]. Hence, alongside three-dimensional morphologic information from MRI, qMRI

is an ideal tool for examining the knee's physiologic state and detecting any changes due to injuries or diseases.

While there are several techniques to carry out qMRI in cartilage[10,11], relatively few studies have linked these metrics to mechanical properties, mainly through ex-situ compression or in-situ indentation (tissue levels), which require disrupting the intact knee in an invasive attempt to load tissues physiologically. Unfortunately, this loaded state is not always representative of the in-vivo condition during daily physical activities. Moreover, due to nonlinear deformations and heterogeneous tissue properties, their results cannot extend to joint level simply via superposition, for which more comprehensive experimental mechanical tests are needed.

Currently, loading simulators are common practice to study knee kinematics, kinetics and tissue's loaded state (for normal or pathologic conditions), as well as to assess surgical repair techniques or implant designs. While several ex-vivo apparatuses can emulate dynamic activities realistically, these are rarely compatible with MRI (since nearby metals react adversely[17]). Moreover, due to experimental limitations, many in- or ex-vivo setups either flex or compress the whole knee (sometimes to low or sub-physiologic levels), neglecting its multiaxial combined loading scenario, which involves axial compression, shearing, bending, torsion (e.g., during walking). Ideally, the knee could be studied non-invasively under physiologic loads, for which new experimental tools must be developed.

1.3. Research objectives

The aim of this project was to determine if qMRI properties could characterize soft tissue local contact deformations under physiologically realistic full-joint loading conditions. Hence, we developed, assessed and implemented tools and techniques and meeting the following objectives:

1. Develop a MRI-safe, multiaxial mechanical testing station for realistically simulating the effects of physical activities in ex-vivo knees.
2. Evaluate the new testing system's repeatability in terms of applied knee loading and intra-articular contact response (affected by both specimen and loading device variability).
3. Determining if cartilage deformations are linked to T_2 relaxation times in full-joint human cadaver knees loaded in a nearly physiologic state.

All of these milestones could be accomplished via a single study (Figure 1-1). First, MSK modelling can be conducted to estimate an experimental loading regime for realistic walking simulation, adjusting for test specimen anthropometrics. Such experimental conditions can be used to design an MRI-safe load-control testing system, which can be used to enforce this loading regime in intact ex-vivo knees. Once prepared specimens are in a physiologically loaded state, MR images can be acquired to assess morphology and T_2 relaxation times. Correlation of these mechanical and imaging variables can be used to assess soft tissue deformations and T_2 relaxation time changes due to applied loads. After imaging, knee capsules can be opened to insert pressure sensors in the articular surfaces and measure their contact response, as well as assess precision regarding loading and response aspects of mechanical testing via repeated tests.

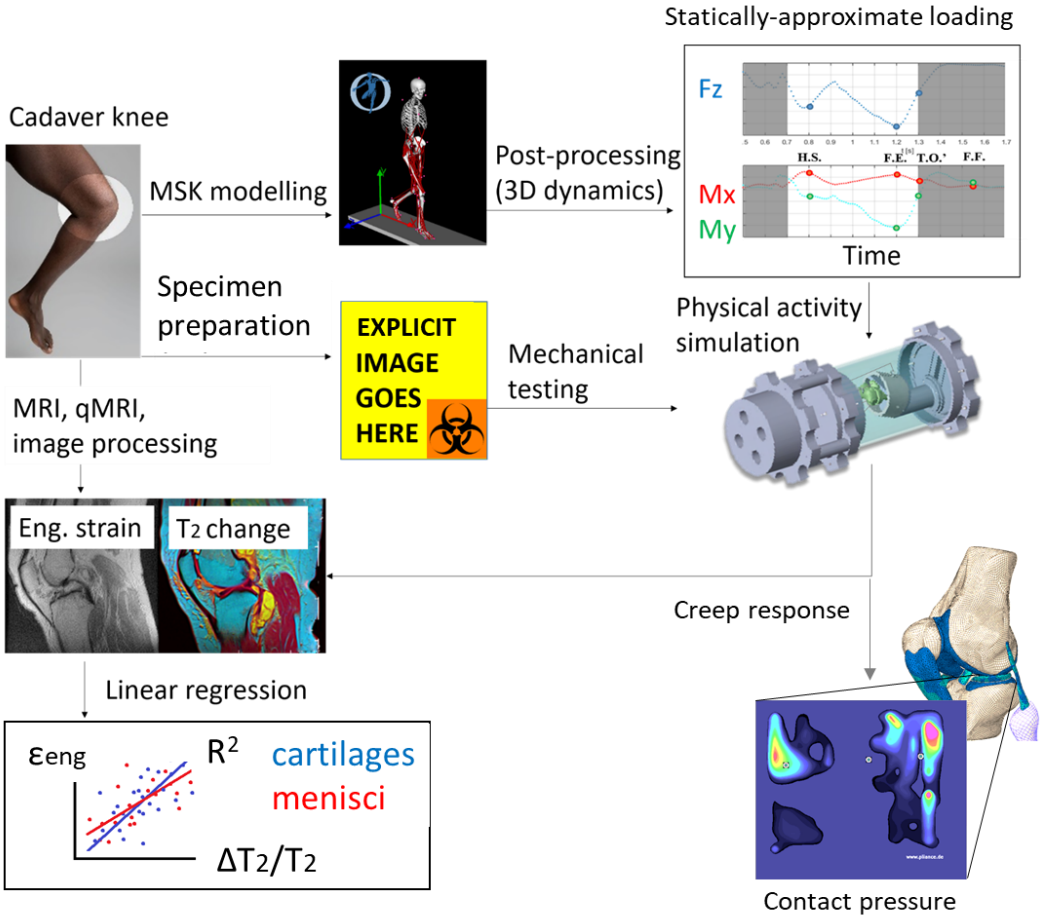

Figure 1-1: Overall study design flowchart. Adapted from Wikimedia Commons[18-21].

However, due to the Covid19 pandemic, accomplishing the proposed objectives required dividing the original plan (imaging six ex-vivo knees loaded physiologically and subsequently conducting contact testing) into two studies focusing on mechanical and imaging aspects. In study I, characterizing the loading system repeatability (objective 2) through loading and open-capsule contact assessment, previously meant to be conducted for all six specimens, had to be conducted only for one cadaveric knee. Hence, only the intra-specimen repeatability was evaluated. Objective 3, meant for the same specimens as in study I, had to be accomplished from previously acquired imaging data for other specimens, leading to study II. In this proof-of-concept correlations study (deformation vs. T_2 relaxation), morphologic and T_2 relaxation time maps were previously acquired (by colleagues) for six other knees unloaded and compressed axially via a MRI-safe displacement-controlled rig.

1.4. Thesis "mechanics" & scope

In this slightly unconventional thesis, Chapter 1 sets the stage for the entire research project. Then, Chapter 2 provides background on knee composition, loading and epidemiology. This chapter also introduces synthesizes the current state of the field, including relevant experimental tests, computational simulations, and medical imaging. Chapter 3 presents the full lifecycle development of a MRI-compatible testing system for loading ex-vivo joints physiologically. Chapter 4 continues by describing the implementation of this system to simulate walking instants on cadaver knees, including a repeatability evaluation of loading and contact response (study I). Chapter 5 describes the imaging of knee soft tissues' deformation due to physiologic loading, including the development and outcomes of a custom algorithm to relate deformation and imaging responses (study II). Chapter 6 integrates the results, strengths and limitations of the individual pilot studies. Additionally, recommendations for addressing current limitations and future research directions are suggested, prior to summarizing the entire project in Chapter 7. Supplementary materials for all these chapters are provided in appendices A1 through A6.

2. Background & literature review

2.1. Anatomy, physiology & epidemiology background

This section describes the different parts composing the lower-body MSK system, regarding the morphology (geometry), composition (material constitution discussed in appendix A2.1.2), arrangement and function (boundary and loading conditions are also discussed further in next sections). Following a brief overview of walking, knee joint components are described in detail, as well as their normal behaviour. Section 0 contrasts this section by discussing abnormal knee function.

2.1.1. Lower-body locomotor system

The human MSK system is composed of all tissues (such as bones, muscles, tendons) used to achieve a desired movement. These components work together and form joints (an arrangement of bodies, which move or remain fixed relative to each other), such as the spine, pelvis, hip, knee and ankle joints, for the lower body (Figure 2-1). Some of these articulations are actually compounded by multiple joints (e.g., all the small connections between all the bones in your ankle), and their movements are produced and guided by muscles and tendons/ligaments that connect many of these tissues (bone-tendon-muscle or bone-ligament-bone) sometimes by crossing over other joints.

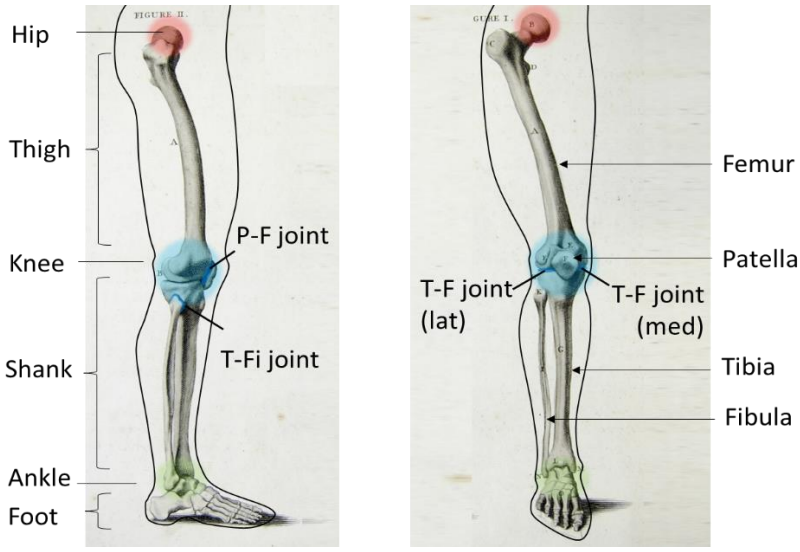

Figure 2-1: Lower-body locomotor system: Hip, thigh, knee, shank, ankle, foot (joints highlighted, while muscles and other soft tissues hidden). Adapted from Creative Commons[22].

2.1.2. Joint of interest: The knee

The knee is composed of several joints: Patello-femoral (P-F) and tibio-femoral (T-F), while the tibio-fibular (T-Fi) is a related joint. Although the fibula is often ignored, it is considered as a relevant component in this research since a major knee ligament (which is key to normal knee function) connects the femur to the fibula. The joints of interest, with major implications on knee normal/abnormal function, however, are the P-F, and medial and lateral T-F joints. Since all these bones can translate and/or rotate in any direction (in three dimensions) with respect to each other, each of these joints (Figure 2-2) has six degrees of freedom (DOF). However, muscles, tendons, ligaments and passive soft tissues (e.g., synovial capsule, skin) partially restrain their DOFs, resulting in a unique motion characteristic of knees. Although the knee joint is more complex than that, it is often approximated overall as a translating hinge for its predominant flexion/extension and gliding capabilities.

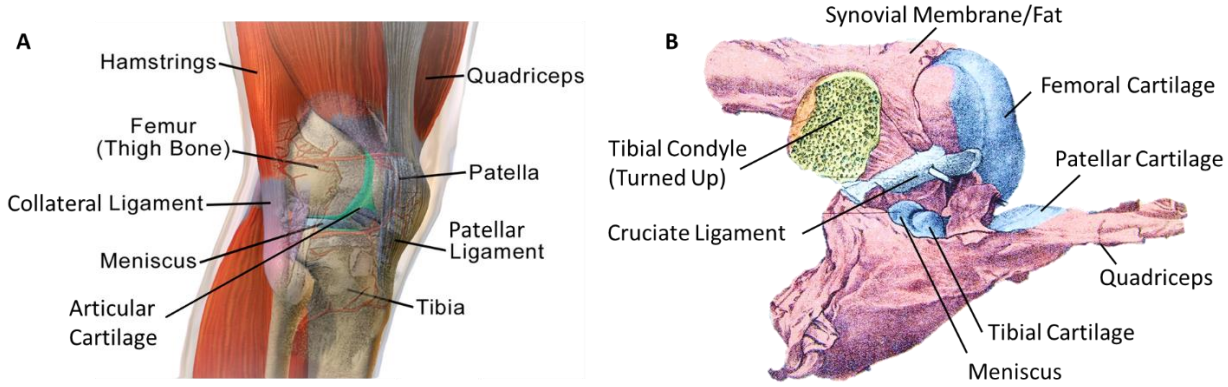

Figure 2-2: Full knee simplified anatomy: A. Extended (assembled) & B. Flexed (resected) views. Adapted from Wikimedia Commons[23,24].

2.1.2.1. Bones

The knee is composed of four primary bones (patella, femur, tibia and fibula), whose primary roles involve providing structural support and transmitting loads to achieve motion. The patella is a sesamoid (embedded within the tendon) ellipsoidal bone that is connected to the femur and tibia via ligaments and tendons. However, the patella only makes contact with the femur's trochlear groove (~saddle joint) as it is positioned too proximal to touch the tibia. The femur is the longest bone in the human body and is characterized by a complex morphology; at the proximal end, the femoral head contacts the pelvis acetabulum, making up the hip joint (~ball and socket joint); whereas at the distal end, the slender segment (with pseudo-triangular cross

section) transitions into the trochlea at the anterior side and femoral condyles. The femur's intercondylar groove is connected to the tibia's intercondylar eminence via ligaments, and the convex femoral condyles make contact with the condyles of the tibial plateau (~rocker joint). The tibia is another interestingly shaped long bone. Similar to the femur, the tibia also gets wider closer to the knee and rather slender away from it. The (proximal) tibial plateau is made up of the medial and lateral tibial condyles, which exhibit minor differences (the lateral compartment being slightly smaller and more circular than the medial side being elongated along the anterior-posterior direction). Lastly, the tibia's proximal lateral region makes contact with the fibula (not considered part of the knee) and its connection is reinforced by ligaments.

2.1.2.2. Articular soft tissues (cartilage & menisci)

Bone articulating surfaces are covered by articular cartilages, which facilitate motion due to their low friction and lubricating properties, and protect subchondral surfaces from wear due to repeated motion. Patellar cartilage shields the posterior medial and lateral sides of the patella, whereas the contacting femoral cartilage spans continuously from the anterior trochlea to the posterior side of each femoral condyle. For the tibia, separate cartilages cover each plateau.

Making it one of the most interesting joints in the human body, the knee has a unique component that differentiates it from any other joint, as no other articulation has this tissue - the meniscus. Each knee comes equipped with two menisci separating the outer portions (away from the knee centre) of each tibial cartilage plate from the femoral cartilage, while allowing cartilage-cartilage contact at each condyle's central region. So, their unique shape is a circumferentially curved wedge extrusion. Moreover, while carrying out their function, menisci are compressed axially and they develop hoop stresses along their circumferential direction. Ligaments tie the anterior and posterior horns of each meniscal body to tibial attachment sites, while the transverse ligament further reinforces their anterior attachment, so that menisci are able to distribute (static and dynamic) loads.

2.1.2.3. Other soft tissues (ligaments, tendons, muscles & capsules)

Bones and soft tissues are able to stay in place while performing physical activities thanks to ligaments (attaching bones to bones) and tendons (attaching bones to muscles), which guide motion. Furthermore, ligaments stabilize joints while tendons transmit the forces the muscles

carry to execute motion. Patellar and quadriceps tendons connect the patella to the tibia and quadriceps muscle groups, while medial and lateral P-F ligaments aid the retinaculum in stabilizing the gliding patella. For the T-F joint, anterior and posterior cruciate ligaments attach the femur and tibia internally, whereas medial and lateral collateral ligaments peripherally attach the femur to the tibia and fibula respectively. Knee flexion/extension and internal/external rotations are achieved by means of quadriceps (e.g., rectus femoris, vastus medialis, intermedius and lateralis) and their antagonist muscle groups, the hamstrings (semimembranosus, semitendinosus, and short- and long-headed biceps femoris) and triceps surae elements crossing the knee (medial and lateral gastrocnemius). The soleus is part of the triceps surae but does not cross the knee. Lastly, the popliteo-fibular ligament and anterior lateral capsule reinforce the T-Fi joint[25], while the synovial capsule (containing the lubricating synovial fluid) encompasses the entire knee joint.

2.1.2.4. Material behaviour of knee tissues

The material composition of these tissues is rather complex (Appendix A2.1.2.2), from space-varying density and elastic modulus fields for bones to multi-phasic (porous solid-liquid phases) soft tissues reinforced by fibers, resulting in time-varying mechanical responses. Anelasticity refers to the time-varying elastic response of materials not only to dynamic but also static loading. As such, there are two kinds of transient responses, depending on the input conditions. Creep is the gradually increasing deformation to constant input loading, while stress relaxation is the gradual decrease in stress to constant input displacement[26] (Figure 2-3).

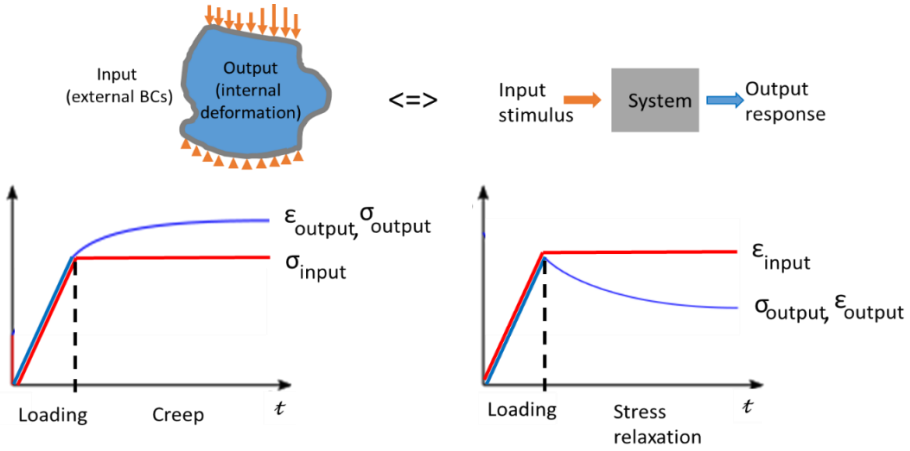

Figure 2-3: General viscoelastic behaviours: Creep vs. stress-relaxation. Adapted from Wikimedia Commons[27]

For most industrial materials, these transient effects are negligible (except for creep when operating temperature is ≳40% of metals' absolute melting temperature[26]); however, some polymers and biological materials (anisotropic natural composites) experience substantial viscoelastic effects (either creep or stress relaxation) at room temperature or higher (e.g., body temperature). Viscoelasticity is a special anelastic case marked by elastic behaviour and viscous flow characteristics[26], whether polymers are in fact composed of fluid and solid phases or simply resemble their characteristics. Viscoelastic processes eventually do stabilize at steady state and their duration depends on loading and material constitution.

2.1.3. Knee function

2.1.3.1. Coordinate systems

There are different ways of expressing the location of different features or sites of interest in the knee joint (prior, during and after physiologic loading). One approach is to describe their location by means of a fixed (global) coordinate system, which is often located on the ground[28,29]. Alternatively, local coordinate systems may be defined at the knee, so that they follow this joint as it flexes/extends, and there are different methods for doing this (Figure 2-4 A, B)[30-35]. In terms of the origin (the knee center), this may be fixed to the tibia at the intercondylar eminence or to the femur at the intercondylar notch, and moves together with either of these two bones. Defining the knee center is non-trivial, as there are many options for specifying knee coordinate directions. To define the femur and tibia axes, one can choose anatomic (along the long bone slender segment)[36] or mechanical axes (connecting the joint centers of each end of the bone)[37]. These can be expressed as vectors (with respect to a fixed coordinate system) to specify a right-handed coordinate system (most often for the right leg), by finding the cross-product between the femur and tibia axes to obtain the knee flexion/extension axis (normal to both bone vectors). Alternatively, the flexion axis is sometimes defined as being parallel to the most posterior sides of each femoral condyle, and/or to go through their most medial and lateral peaks[31,38]. The flexion axis can then be crossed with one of the bone axes (defining the knee's axial direction, i.e. knee's internal/external rotation axis) to obtain a perpendicular (abduction/adduction) axis. Finally, if the femur or tibia longitudinal axis is not perpendicular to the flexion/extension axis (because of the way axes were defined), a third cross-product is required between one of these axes and the abduction/adduction axis to complete the orthogonal

triad. This is, however, how real knees (in-vivo or ex-vivo) are described in most gait analysis studies only (Figure 2-4 C), as different approximations are used for MSK models and instrumented knee implants. For instance, for OpenSim MSK models (rigid body models for predicting human body motion/loading), in general, the anatomic coordinates are located at the femoral intercondylar notch but follow the tibia axial direction[39,40], whereas for OrthoLoad instrumented total knee replacement (TKR) free database, the origin is located at the center of the tibial plateau implant and is oriented with this bone as well[41,42]. Anatomic coordinates defined on real knees (especially in vivo) are seen as the common reference standard (Figure 2-4 D) with respect to other knee coordinates; however, they are not free from uncertainty. There are errors (mostly precision, as their notion of accuracy is debatable) associated with the definition of the bones' mechanical axes alone[30,32,33,43]. Further, knee axes (and ultimately rotations) may be compromised as they are estimated by markers placed on the skin and subject to skin motion artifacts[36,43], as well as subject to kinematic cross-talk when the adopted anatomic directions do not match rotation axes, leading to spurious knee rotations[32] (slightly delving into accuracy).

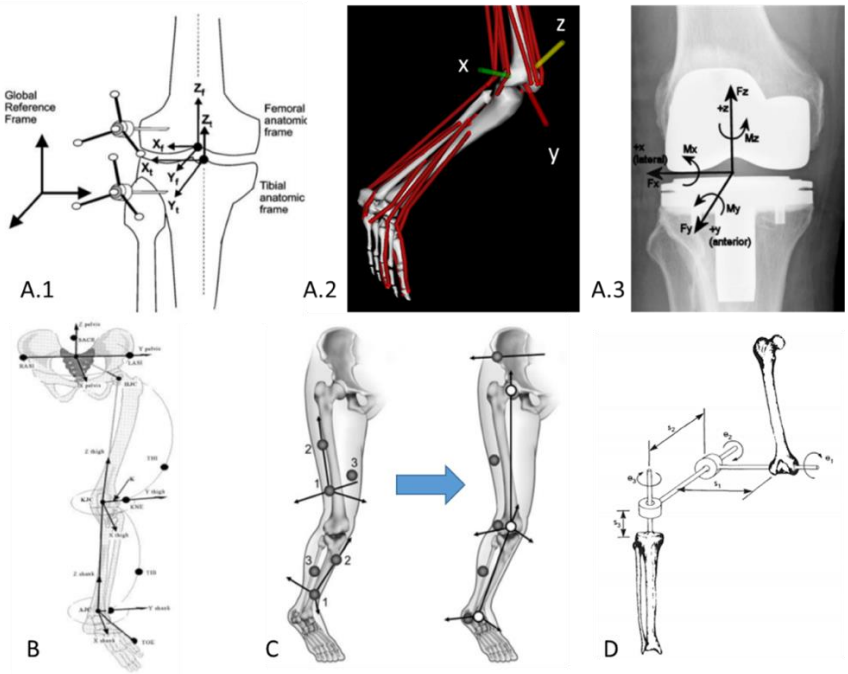

Figure 2-4: A. Common right-handed anatomic coordinate systems for right knees (A.1. Gait analysis, A.2. MSK models, A.3. TKR implants), B. less-common right-handed coordinates for left knees (note triad rotates about the longitudinal z direction for left limbs), C. sample method for defining knee coordinates, and D. Grood & Suntay analogy to linked mechanical joints. Reproduced with permission from Benoit et al. 2006[36], Heinlein et al. 2009[41], Baker et al. 1999[44], Cappozzo et al. 2005[37] and Grood et al. 1983[31].

2.1.3.2. Healthy behaviour

In walking (gait), the entire lower-body MSK system is always involved. From the moment the foot makes contact with the ground, loading develops due to the subject's body weight (BW), concentrated at their center of gravity, and the ground reaction forces. This load transmission through the entire lower body, from the sole through the foot to the ankle joint, from the ankle through the shank to the knee joint, from the knee joint through the thigh to the hip joint, and so on, is the basis for gait analysis (Figure 2-5).

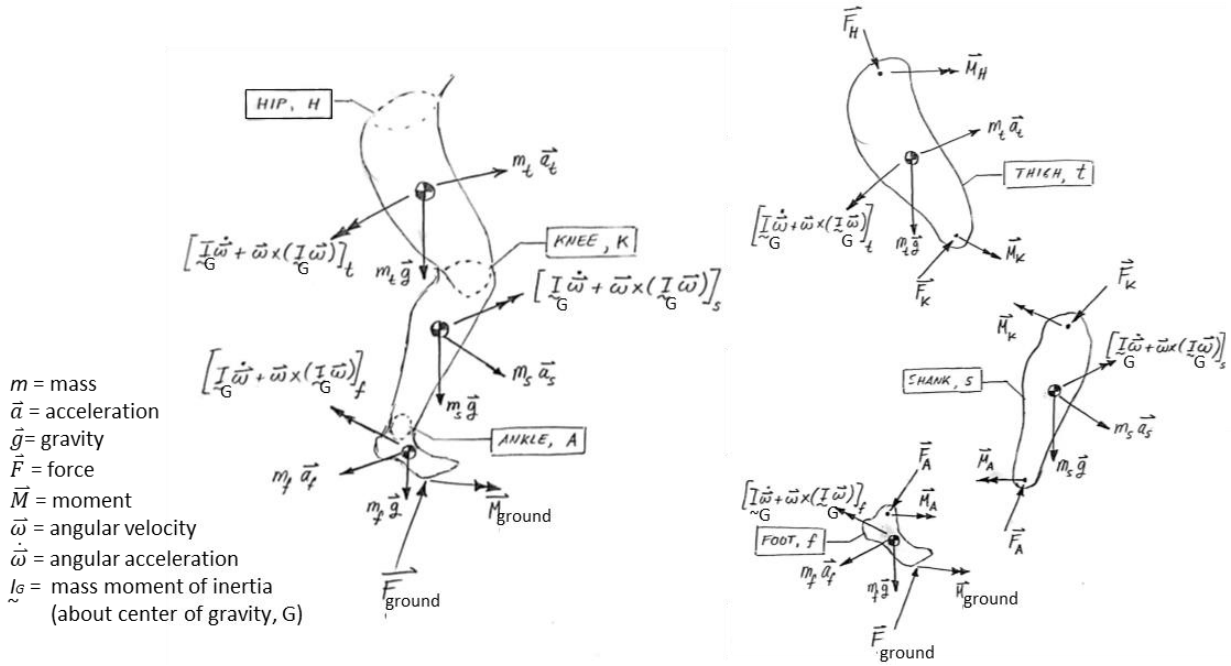

Figure 2-5: Load transmission during physical activities (inverse dynamics): For each segment, (applied) distal loads and inertial effects must be balanced by loads at the joint, which transfer to the adjacent segment via Newton's 3rd law.

In general, throughout physical activity, some of the loading generated by muscle forces transfers as strain energy into all the components involved (developing stress and strain), and it ultimately produces movement (translational and/or rotational motion, velocity, accelerations). For healthy gait, in general, there is always one limb in contact with the ground throughout this activity (unlike during running, which has a short aerial phase[45]). Although the magnitudes depend on subject characteristics and instant throughout gait, it is normal among healthy subjects for the medial T-F compartment to bear more load (e.g. 53.9% of 1st compressive peak) than the

lateral side (46.1% of 1st compressive peak) during stance due to an adduction moment produced by the BW acting through the center of gravity[39,46,47], and for the lateral patella to experience higher loading than the medial side when the knee is flexed (~70º) in swing[48,49]. During this process, the knee is subjected to some degree of internal/external [AVG ± SD: (14.4 ± 4.1)°] and abduction/adduction rotations [AVG ± SD: (8.3 ± 2.5)°], but flexion/extension has the predominant range of motion [AVG ± SD: (61.1 ± 5.0)°][50,51].

This general walking behavior is expected to vary between individuals[50,52] due to subject-specific characteristics (e.g., sex, unique anthropometrics, morphologic features and/or fitness level), leading to normal inter-subject variability ranges in knee functions[51,53,54]. Moreover, due to changes within subjects themselves (e.g., aging, metabolic changes, fatigue and/or fitness level), there is normal intra-subject variability in knee function[53,54]. Abnormal gait, however, consists of any significant deviation from this normal behaviour and can be a product of different disorders, pathologies and/or injuries, which can further amplify variability ranges[46], as discussed below.

Similar to how tissue morphology and mechanical properties vary from subject to subject and some within the same subject, so do gait (or other physical activity) patterns. This means that every single kinematic or kinetic aspect of motion and resulting loading varies within and between subjects. Due to experimental limitations, repeated measures and cross-sectional studies respectively report intra- and inter-subject variability only for a few of these aspects (mainly joint moments and flexion angles) for discrete time points throughout gait, (mostly during the stance phase only)[40,46,51-63]. Heel-strike (when the foot makes contact with the ground), full-extension (when the supporting leg is extended and compressed the most), toe-off (just before the foot leaves the ground) and full-flexion (when the knee is flexed the most), however, are all important instants during gait, which should be studied entirely. For comparing patterns (and sometimes their variability) across participants, loading data is often normalized to BW, height and percentage of the gait cycle. It is important to note that this variation is not due to pathology, as there is variability for both normal and abnormal patterns, usually pathologic variability being larger than normal variability). For instance, for normal gait, abduction/adduction moment standard deviation varies between individuals as 0.359, 0.412 and 0.440 %BW·ht at heel-strike, full-extension and toe-off respectively[40,51-54,56-61], whereas, for pathologic gait, this force varies between individuals as 1.50, 1.91 and 3.30 %BW·ht for the same gait time points[46,62,63].

2.1.3.3. Pathologic behaviour

Most knees can be afflicted by different diseases, tissue mechanical failure, damage or pain from compromised tissue function (e.g., malalignments), and/or a combination of any of the aforementioned conditions[64-67]. Just like in other mechanical systems, where the performance (or function) of its components depends on their own integrity (or health) as well as of others, it is not unusual for abnormal conditions and/or multiple pathologies to facilitate and foster each other, resulting in damage worse than if caused individually. Their consequences range from short-term adverse effects to long-term irreversible joint destruction.

OA is a multifactorial whole-joint disease, characterized by soft tissue breakdown and bone malformations (Figure 2-6), leading to limited joint mobility and further damage that may alter the loading environment and accelerate the disease[10,16,46,68,69]. OA mostly affects the knees and hips of $\gtrapprox$ 10% of North America and Europe, with elderly (30% afflicted, 2:1 women-men ratio) and obese populations at high risk[1-5], but also affecting injured athletes. Unfortunately, there is no cure for OA, and current treatments include pain-relieving medication, physical therapies, bracing, and/or surgical interventions (e.g., TKRs)[2,41,42,68,70]. However, complications with such measures surface as disease or injury advances, thus early detection is needed[10,11,70,71]. While it is known that mechanical loading[2,46,64,72], injuries (e.g., ligament/meniscus yielding or tearing)[62,66] and other conditions (e.g., patellar tilt/dislocation and varum/valgum malalignments)[67,73] are key disease risk factors[2,46,72,74], some evidence suggests OA may be potentially associated to other complications (e.g., P-F pain)[48,75,76]. However, the disease pathways and their inter-relations are far from being understood[77] and early detection is currently challenging.

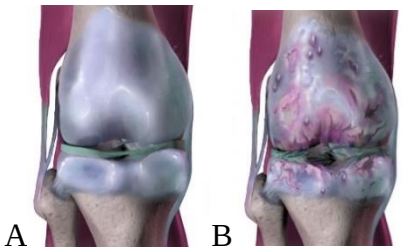

Figure 2-6: Healthy (A) and osteoarthritic (B) knees (P-F joint not shown). Taken from Wikimedia Commons[78].

Since knee MSK pathologies are strongly associated to loading[2,64,72,79], any alterations in a healthy knee may lead to abnormal and adverse loading, potentially causing more damage[16,46,74].

For instance, malalignments in which mechanical axes do not line up with the knee center, alter knee T-F loading conditions[55,67]. Genu varum is a condition where the compression line of action (for both legs) passes through the medial T-F joint, whereas, in genu valgum, these axes pass through the lateral T-F joint (Figure 2-7). Thus, these disrupt the normal medial/lateral T-F load distribution (medial side bearing more compression than the lateral side), which overloads and prematurely wears medial and lateral compartments respectively in varum and valgum, thereby offloading the other compartments[67]. Therefore, it is clear that studying loading under physiologic conditions is essential in experimental settings.

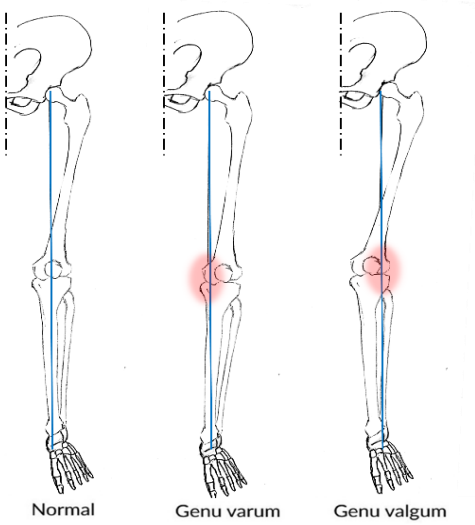

Figure 2-7: Healthy knee and malalignments with overloaded compartments

2.2. Review of experimental tests & techniques in biomechanics

There are different approaches to study different aspects of the biomechanical behaviour separately, each with specific advantages and limitations. These tests can be classified as in-vivo (with live subjects, e.g., gait analysis and instrumented implant measurements), ex-vivo (outside live subjects, thereby involving cadaveric tissues in these mechanical tests), in-situ (inside intact physiologic sites, e.g., indentation testing), ex-situ (outside the physiologic environment, e.g., tissue-level compression tests) and in-vitro (inside a laboratory-simulated environment, e.g., full-joint testing) depending on the region of interest (ROI). Unfortunately, due to experimental limitations and joints' complexity, it is not possible to incorporate all physiologic aspects simultaneously. Since ex-situ and in-vivo (Appendix A2.2) tests are not relevant to this particular project (focusing on full-joint ex-vivo testing), they will not be discussed much further.

2.2.1. Ex-vivo (ex-situ & in-situ) studies

Tissues can be loaded statically (stress relaxation, creep) or dynamically (impact, fatigue, physiologic loading), in either displacement- or load-control, in ex-vivo mechanical biomechanical testing (explant testing, indentation and full-joint testing). Although these tests have different purposes, these general classifications they can be regarded, in the order presented, as adding more physiologic realism (and complexity) to mechanical testing.

Since the ~1980's, at least 39 different full-joint loading devices have been developed[12,13,16,25,80-133] (Appendix A2.1.4, Figure 2-8). In these setups, entire intact or dissected joints are placed in the apparatus that applies mechanical loads to multiple tissues, aiming to simulate what the human body does during physical activities. Thus, these physical activity simulators can also be used to test the performance of implants (e.g., TKRs), prosthetic limbs, surgical practices (e.g., resections), or evaluate dynamic activity responses of the entire joint or individual components[90,91,134]. Loading devices can be classified by function (uniaxial compression, flexion via muscle activation, multiaxial rigs, robotic arms, robotic platforms and miscellaneous), transient behaviour (stress relaxation, creep, impact/fatigue dynamic simulation) or medical imaging compatibility [MRI, computer tomography (CT), and planar or stereo X-rays (e.g., Roentgen stereo(photo)grammetric analysis, RSA)]. Also, these can be further classified as "open" or "closed" kinetic chain when the distal end of the joint is free or restrained.

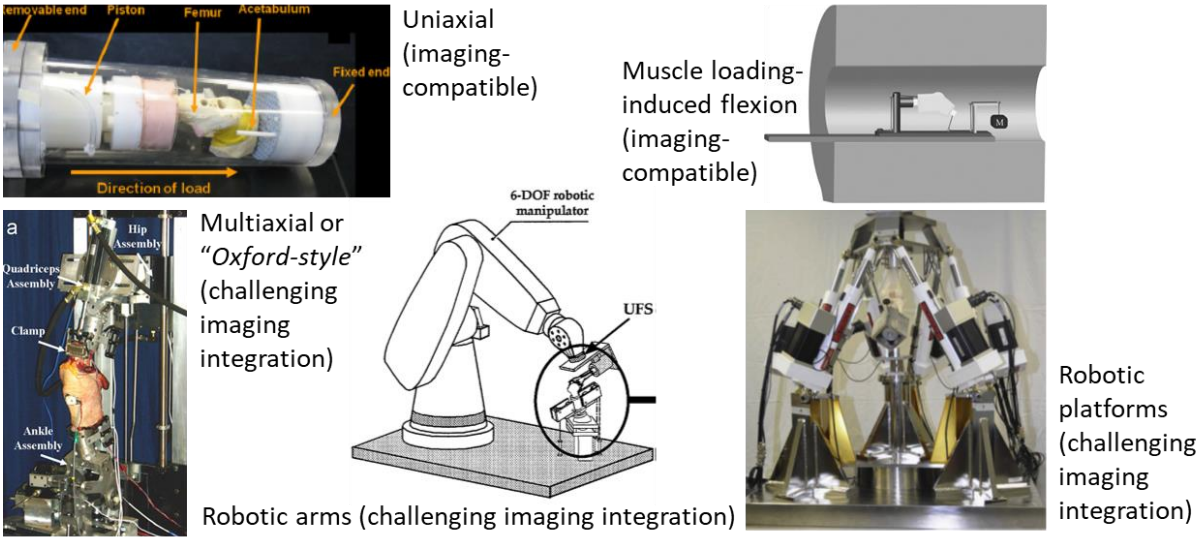

Figure 2-8: Full-joint ex-vivo rig types. Reproduced with permission from Greaves et al. 2009[12], McWalter et al.2014[96], Baldwin et al.2012[25], Li et al.1999[122] and Lawless et al.2014[94].

The most important criteria that experimental testing devices should exhibit for assessing articular tissue structure and function include medical imaging compatibility, high physiologic realism and high repeatability. Here, each of these characteristics is defined and the most promising machines (regarding individual criteria) presented.

Most loading rigs are compatible with MRI[12,13,16,82,84,85,92,93,96,102,103,105-108,110,111,118,123,124], CT[16,83,92,117,118] and (single or dual) planar X-ray[114,116,118,121,122,133] (Appendix A2.1.4); however, the fully 3D complex structure and composition of bones and soft tissues can only be imaged via CT and MR and respectively, each with their own challenges. For example, the small bore size of some CT and MR scanners imposes a physical constraint on the size of the loading rigs, which may contribute to studies being conducted on smaller animal specimens[16,92,93,102,103,105-107,116,117], rather than on actual human joints. Furthermore, MRI has the added complication of material compatibility, minimizing the usage of metallic components. Lastly, irrespective of imaging modality, in these tests, loaded tissues are to be imaged for extended periods, for which load-control systems are preferred over displacement-control setups, as tissues can be loaded more accurately and more consistently to a desired load target. As expected, all these imaging-imposed restrictions considerably limit the loading capacity and functionality of existing loading simulators.

Physiologic realism aspects include the integrity of the ex-vivo specimens, the active joint DOFs, load magnitudes and different load components making up a multiaxial combined loading scenario, all of which together mimic the in-vivo situation. Oxford-style multiaxial rigs, robotic arms and robotic platforms are expected to display high realism; however, not all of them keep the joints intact, instead it is easier for other simpler devices[12,13,83-88,92,93,96,97,102-108,110,111,118,120,130,132] to maintain the joint capsules closed (Appendix A2.1.4). It should be noted that this list may be limited by the available records, as some studies have been conducted on implants or TKRs, which does not mean that those rigs cannot work with intact specimens. In terms of joint mobility, approximately half of the existing loading devices allow/activate all knee DOFs (including the popular KKS and Oxford rigs, and the less-known Purdue Knee Simulator, Tuebingen Knee Simualtor, QKR, AMTI VIVO, Hexapod and Rotopod R-2000 platforms) [25,86-90,92,94,95,98-101,110-113,115-117,119-122,125-127,130,131], while a few allow two translations and one rotation[82,93,109,114,123,124,133], and the rest mostly apply axial displacement[12,13,16,83-85,105-107] or

flexion only[96,97,118]. The highest compressive loads reported have been delivered by robotic platforms (20kN), multiaxial (5kN) and a few uniaxial setups (2kN). Some devices also incorporate other loading modes, including shear, bending, torsion and muscle action; unfortunately, few incorporate all those simultaneously[25,86-88,90,98-101,116,119,121,122,125-127,133] (similar to the in-vivo state) and deliver large loads[25,90,98-101,116,119,121,122,125-127,133], while remaining imaging-compatible[116,121,122,133]. A good strategy that is often employed to increase realism is to incorporate bending by compressing flexed joints, which can be achieved with uniaxial devices capable of delivering high loads (e.g., a remarkable case[109] can reach 18kN in this configuration).

Repeatability is one of the most important and perhaps most nuanced criteria. Characterizing and comparing experimental precision among studies is nontrivial, since there are so many ways of grouping and analyzing data. For example, repeated tests can be conducted over time (e.g., several days), over space (e.g., different regions within the same specimen) by a single or different observers, leading to intra- and inter-observer precision. Also, the specimen may be removed in between tests to further evaluate testing reproducibility. Then, there is the question of which variable of interest is to characterize repeatability of the test inputs or responses, which may involve kinematic or kinetic field variables (scalar, vector or tensor functions of space and time). Since these variables exhibit a transient field behaviour, studies often sample the temporal or spatial minimum, mean or maximum field values. However, as precision also varies for different BCs, some studies also distinguish the minimum, mean and maximum standard deviation (variance as a variable itself). Lastly, each loading device is unique and performs slightly different functions and only few studies assess repeatability, while others do but are not clear as to what kind of variance they measure, and most simply do not explore precision. That being said, a few researchers have reported repeatability for their devices. These register wide ranges of moderate to high repeatability for all knee translations (0.05 to 1.2mm SD[111,116,131]), rotations (2.28 to 66.7 CV%[92] or 0.33 to 2º SD[111,116]), applied shearing (7.72 to 50.9N CV%[92]) and compressive (0.23 to 6.96 CV%[12,92,103,109] or 1 to 46.6N SD[104,113]) forces and cartilage displacements (2.7 CV%[13] or 65 to 132 μm SD[106]).

In general, due to medical imaging, biomechanics simulations are often compromised. Currently, MRI-safe rigs do not simulate dynamic physical activities realistically (i.e., an intense multiaxial combined loading in a physiologic state), no matter what functional family they belong to.

Usually, these rigs are small, compact devices capable of delivering small forces (due to the weak plastic components) or they are much bulkier (to compensate for mechanical integrity and supply large forces). In terms of function, they either activate muscles and flex the joint or they supply large compressive forces in a uniaxial setting, but not both. This is only achieved by robotic arms, multiaxial or miscellaneous rigs; however, these are considerably cumbersome and impractical for CT or MRI integration. Equally important as reaching a physiologic loaded state is to do it consistently, for which testing devices' repeatability should be reported (rarely done), even if it is low. Since testing repeatability is mostly limited by specimen repositioning or mode of load delivery, specimen preparation/mounting protocols should be implemented in load-control devices, to consistently image near-to-physiologic states. As shown, there is a compromise between medical imaging and physiologic loading realism, as well as a lacking repeatability assessment of most loading simulators. Full-joint ex-vivo testing does seems a promising alternative for exploring the effects of physical activity on the tissue- and joint-level responses of the knee in healthy or pathologic cases; however, a device that is able to integrate the previously discussed experimental criteria is needed.

In general, full-joint loading devices share the advantage that the knee is in its natural state (as close as possible to in-vivo conditions). However, although disadvantages depend on the device family, it is common for physiologic realism, medical imaging compatibility, and simplicity/cost-effectiveness to be conflicting objectives. As a result, most MRI studies (ex-vivo or in-vivo) are carried out without loads or under simplified axial loading, often of low magnitude[15,16,90,93,118,123,135]. At the expense of testing realism, loading simplification (either uniaxial compression at zero or low flexions, or muscle-activated high flexions) further leads to disregarding either the P-F or T-F joint. On the other hand, when incorporating more realistic loading conditions (axial compression, shear, bending, torsion at low or high flexions), this is often done by advanced simulators that recreate these effects as external joint loads only, while ignoring muscle tension sometimes. Moreover, the few that simulate physical activates realistically (including muscle action), involve complex robotic, hydraulic, pneumatic and control systems, which difficult medical imaging. Ideally, ex-vivo loading equipment should be compatible with current imaging modalities (to allow observation and measurement of tissues' loaded state), preserve the knee capsule integrity (to study both intact T-F and P-F joints), and

simulate a physiologic, multiaxial loading scenario[41,42]. A common limitation to all these tests is the use of cadaveric tissues, subject to decomposition potentially affecting mechanical properties of soft tissues (not as much for fresh-frozen, but definitely if embalmed); thus, fresh samples or full specimens have a short, finite testing life. One freeze-thaw cycle does not affect human cartilage[136,137] (even if frozen for 60 days[138]); however, soft tissues deteriorate significantly beyond three cycles[139,140]. Also, it seems cartilage can only be stored for a maximum of six days at 4ºC before mechanical properties change[141].

In general, experimental measurements are regarded as more accurate than analytical or numerical models, and therefore considered closer to the "ground truth" (which perhaps will always remain distant in the biomechanics field). Whereas models are effective for simulating aspects that are not practically feasible in reality, many rely on physical measurements[90,142]. The choice of experimental stream is further nuanced. Without a perfect solution, the most ideal test would exhibit high repeatability, physiologic realism (regarding loading and specimen integrity) and medical imaging compatibility. In-vivo testing enables imaging the real tissue in its natural physiologic state; however, load magnitude and repeatability are surpassed by ex-vivo methods (even considering sample/specimen repositioning errors)[90]. However, in the end, a combination of modelling, in-vivo and ex-vivo testing is usually required in order to explore structure-function relations in tissues.

2.3. Review of computational techniques in biomechanics

The purpose of this section is to give sufficient background on numerical simulations (widely used tools in the biomechanics field), so that the reader appreciates how nuanced, complex and costly they can be, and why, for the objectives of this project, an experimental approach was preferred in order to incorporate all these complex mechanisms in a physiologically realistic manner. However, due to complexity of MSK systems (morphology, loading conditions and material properties), not all physiologic conditions can be simulated experimentally (hence, the need for these computer models). Furthermore, among the cases that can be experimentally reproduced, estimating certain mechanical parameters (e.g., internal forces, stress and strain fields, material properties) requires combining experimental data (or approaches) with computational methods. Among these, the finite element method (Appendix A2.1.4) stands out

as one of the most advanced and complicated simulation tools for describing the mechanical behaviour of loaded bodies (from machine components to articular soft tissues). This technique is so powerful it can be extended to simulating subject-specific pathologies[79,143] and evaluating treatments[144]; however, it is limited by computational costs and requires full-joint experimental validation[142]. Since the FEM is not the focus of this thesis, it will not be discussed further.

2.3.1. MSK modelling

This technique involves modelling the MSK system limbs as rigid bodies and can be used to determine joint loads, from gait analysis kinematic (position/orientation, and translational/rotational velocity and acceleration) and kinetic (force plate) measurements, as described in Appendix A2.2.1. MSK models include a rigid skeleton and discrete muscle-tendon actuators (e.g., 92 lower-body muscle groups with predefined insertion points and elongations), whose dimensions and inertias can be adjusted based on subject anthropometrics. Modelling extends to joints themselves[39,40,61], whose DOFs are restricted to simplify the analysis while still preserving their main function (e.g., translating hinge models for the knee in OpenSim).

MSK models are especially useful for handling dynamically indeterminate systems, due to the presence of muscles (redundant mechanical supports crossing over joints), and can be used to obtain joint contact forces[39,40,56,60]. There are different ways to reduce such an indeterminate system to a determined one (e.g., energy methods[145], reduction methods, imposing additional constraints[146-149]), but muscular optimization is often used in MSK modelling[56,150-154]. Although dynamic optimization methods exist, muscle tensions are often approximated by static optimization for gait[155], which yields one of the possible static-equivalent muscle loading configurations that satisfies the 3D Newton-Euler governing equations of motion. Muscle optimization is based on the assumption that the human body has adapted to best carry out physical tasks and, when performing these activities, total muscle stress or energy expenditure is minimized[150,156]. Thus, model anthropometry, kinematics and kinetics can be combined to estimate muscle tension, by setting the chosen metric of efficient muscle performance as an objective function and the individual muscle tensions as free variables (Figure 2-9A). Once, all muscle loads are known, they can be combined with model anthropometry, kinematics and

kinetics and the inverse dynamic approach can be used to get not only external joint loads, but also internal contact forces (Figure 2-9B).

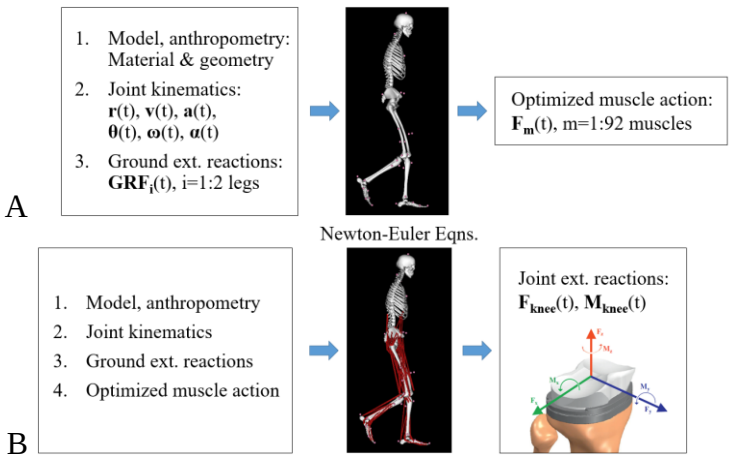

Figure 2-9: Static optimization routine (A) & finding joint reactions via inverse dynamics (B) in OpenSim. Adapted with permission from Kutzner et al. 2010[42].

In general, the main advantage of modelling is the ability predict the effects of changing different conditions or properties of a system, which otherwise would be expensive, challenging or simply not possible via experimental testing. However, verification (self-consistency, precision) and validation (realism, accuracy) are necessary conditions for any reliable model predictions, which represent additional considerations, opportunities and challenges depending on the modelling approach. MSK modelling is especially useful at handling indeterminate systems, via optimization methods, and at predicting internal joint forces. Required verification mainly consists of physical intuition (e.g., optimized muscle tensions must be positive since tensile, zero hip moment reaction since modelled as ball/socket, zero support reactions for the "pelvis-ground" joint since these are not connected). MSK-modeled internal joint and muscle loads can be validated by comparing the external joint reactions they produce against gait analysis measurements conducted on the same participants. Minor limitations are related to physical realism, as the joint DOFs are often restricted, it is not possible to incorporate all muscle fibers (whose forces are only estimates), and tissues' internal deformation cannot be determined from this technique alone (for which FE models are needed). However, perhaps most importantly, it is not currently possible to validate internal forces for the healthy. It is only possible to model and validate internal forces acting on knee implants (e.g., instrumented TRKs) of participants with advanced OA, alongside their characteristic pathologic gait patterns[46].

2.4. Review of medical imaging

Medical imaging allows acquiring visualizing tissues inside the human body, via 2D or 3D pictures or videos, avoiding risky surgical procedures formerly required for such examinations, facilitating assessing health state, injuries or diseases non-invasively. Since treatments are likely more successful if such pathologies are detected at early stages[10,11], considerable financial resources and (clinical and research sectors) efforts are spent in non-invasive monitoring and predictive diagnosis (for subject-specific health or medical conditions) via medical imaging and image processing (discussed separately in Appendix A2.4).

In contrast to photography, where light is manipulated in order to produce bi-dimensional images, medical imaging can use X-radiation, mechanical waves or magnetic fields to reveal the interior structure of biological materials. Hence, specialized equipment (Figure 2-10A), software and human resources are required for acquiring, processing and interpreting such images. Another unique characteristic of these imaging techniques is that a series of slices can be collected in order to obtain a full 3D description (Figure 2-10B) of specific tissues in the field of view (FOV). As shown next, there are different imaging modalities, each with different characteristics [e.g., resolution, signal-to-noise (SNR) ratio] and purposes, for which they can be classified as morphologic or quantitative (further describing tissues from numerical and spatial information in the images), although there are some hybrid sequences that can extract morphologic and quantitative information.

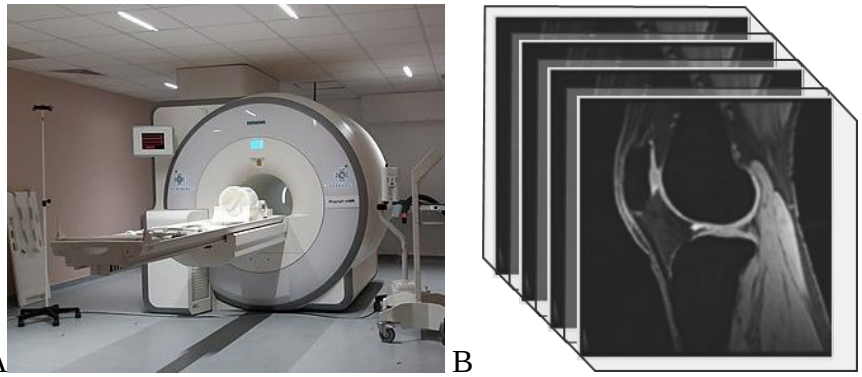

A B

Figure 2-10: A. MR scanner & B. sample volumetric MR image (note slice thickness). Adapted from Wikimedia Commons[157] and with permission from Jordan et al. 2014[158].

2.4.1. MRI and qMRI

Among different modalities available (Appendix A2.4.1), magnetic resonance imaging (MRI) uses strong magnetic fields to excite hydrogen nuclei present in water contained in biological tissues. As such, it has superior soft tissue contrast. In contrast to morphologic MRI (Figure 2-11A), which can be used to image soft tissue morphology, quantitative MRI (qMRI) can be used to non-invasively approximately assess cartilage and meniscus structure, biochemical content and mechanical response, by measuring MRI properties, which depend on tissue health and integrity (Figure 2-11B). This can be done for every voxel in the imaging volume; thus, it can be used to potentially track tissue changes from early stages. Preliminary studies of T_1, $T_{1\rho}$ and T_2 relaxation times (qMRI metrics), as well as delayed gadolinium-enhanced MRI of cartilage (dGEMRIC) have shown correlations between soft tissue's biochemical content (water, collagen, glycosaminoglycan) and mechanical behaviour[10-16].

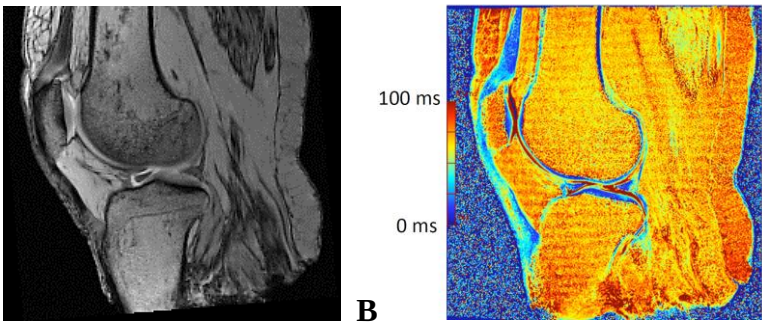

Figure 2-11: A. Morphologic MRI (qDESS, 1st echo) & B. qMRI (T_2 relaxation) sample slices; note soft tissues presence

The process of obtaining images via MRI is fairly involved. To produce images, transmitter coils are used to produce a small magnetic field, B_1, at some angle from the (larger) main magnetic field, B_0, along the scanner bore. This secondary radiofrequency (RF) pulse is applied at the Larmor frequency of the spinning protons preferentially aligned with B_0, in order to tilt the proton spin axis along the B_1 direction. The RF pulses are turned off and, as the protons precess back to their B_1 orientation, they induce a decaying voltage with a characteristic frequency in the receiver coils. The system's gradients can be applied along the slice select, phase encode and frequency encode directions at specific times [respectively coincident with RF pulses, between these pulses and the data acquisition (DAQ) periods, coincident with DAQ times] in order to

localize the signal. These data are saved as frequency maps (k-space) which are then converted to the image domain via an inverse Fourier transform (Figure 2-11A). To obtain quantitative parameters, such as T_1 and T_2 relaxation times, a series of images are acquired with varying contrast and signal models can be fit. T_2 relaxation time is the time it takes for the transverse magnetization to decay to 37% of its initial value. T1 relaxation time is the time it takes for the magnetization to return to its initial maximum (aligned with B_0).

Widely varied associations exist between qMRI metrics and tissue biochemical composition. For the case of T_2 relaxation time (transverse relaxation time) this metric is mostly correlated with water content ($r = 0.77$ in average)[159] and fiber organization ($r = 0.91$ in average $\pm$ 0.02 SD)[160], and different tissues register characteristic and distinct T_2 relaxation time ranges, which enables creating HR images that can help distinguish different tissues with greater ease. However, accurately measuring MRI properties of specific tissues requires optimizing imaging sequences specifically for them. In general, T_2 times for healthy cartilages and menisci are, in average, around 40ms[15,161-163] and 10ms[164,165] respectively. However, these values can change due to loading state, pathology, subject-specific features or sequences used (leading to intra- and inter-subject variation in qMRI properties).

Upon prolonged compression, water escapes soft tissues and that can produce a drop in T_2 relaxation time, as it is directly related to water presence[10]. However, T_2 relaxation also is directly related to collagen fiber anisotropy (especially transverse fiber alignment) and inversely related to soft tissue isotropy. As a result, a few studies showed T_2 times are highest at superficial layers of articular cartilage, followed by deep layers and lowest for (random, isotropic) intermediate layers[160,166]; however somewhat different T_2 time distributions have been found depending on tissue strain and orientation about B_0[167,168]. Hence, depending on the soft tissue, compressing the soft tissue may lead to some of these random fibers to deform and align themselves such that T_2 time decreases. Therefore, the net change in T_2 relaxation times would depend on the specific soft tissue deformation and fiber alignment with respect to the magnetic field (Figure 2-12A).

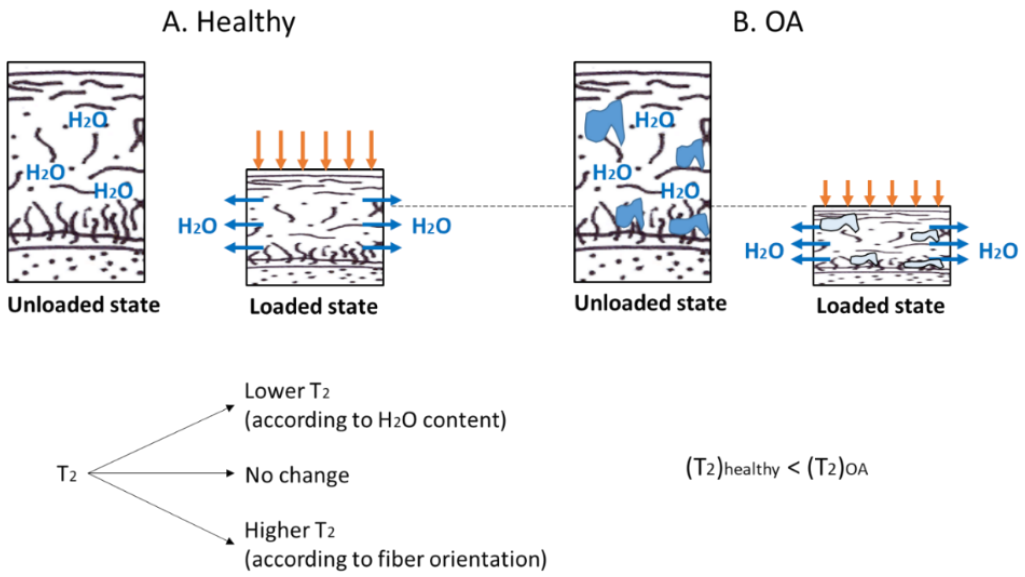

Figure 2-12: Possible pathways for T_2 relaxation response to loading healthy (A) and OA (B) cartilages (dominating effect depends on the situation). Images courtesy of Dr. Emily McWalter.

Lastly, it should be noted that, unlike bone density, qMRI parameters are only compared within participants[169]. However, as long as the expected difference between groups is large, T_2 relaxation times could be compared between participant groups. Further, qMRI metrics cannot be compared for the same subject if they were calculated from different pulse sequences. Given all this considerations, clinical applicability of MSK qMRI is currently limited; however, it is the best research tool for imaging soft tissues and evaluating their composition, structure and mechanical response non-invasively. Hence, it can be used to track injuries or diseases (e.g., OA) at early stages, which likely leads to more successful treatments[10,11], for which qMRI shows promise.

A major advantage of medical images is that they are non-invasive tools that allow researchers and clinicians to look inside biological tissues. This is especially useful for diagnosing, monitoring and/or treating injuries and diseases. Each imaging modality has its purpose and, in some cases, it may be more advantageous to use one over another, but in general CT and MRI are the best tools respectively for bone and soft tissue HR imaging. Radiography has the added advantages of inexpensive and fast image acquisition, which makes it clinically applicable. Furthermore, this modality can be extended to quantitatively measure bones' density and stiffness fields. On the other hand, MRI's inherent high contrast allows better distinguishing the

different soft tissues in the knee, while qMRI provides objective measures that has been associated with biochemical content, structure and mechanical function that can be used to track injuries or diseases at early stages. These imaging-mechanical associations, however, have been found mostly through explant testing (unconfined compression)[170-174] or indentation[14,175-179], without involving full joints in a physiologically loaded state. Alternatively, when entire loaded knees are involved, either only mechanical (e.g. thickness, strain, bulk stiffness, equilibrium and dynamic moduli, contact stress, contact area, indentation force, energy dissipation or cyclic loading phase) [47,180-182] or qMRI[15,161,162] (e.g. T_1, T_{1rho}, T_2, and dGEMRIC) aspects are considered, with a few exceptions where both of these responses are examined separately without aiming to correlate them[183-185].

In general, however, the major drawback of all imaging modalities is that each is so application-dependent that multiple are required to get a complete "picture" of the situation. Hence, one cannot image all the different issues solely with one image unfortunately. Also, pictures may become corrupted by different kinds of artifacts (e.g., ring artifacts in CT, metal-induced and susceptibility artifacts in MRI, and partial volume effects in both). Furthermore, while there are no known risks for (q)MRI, tissues are exposed to X-radiation in these scans, which should be considered for in-vivo imaging. MRI and qMRI are expensive and complex techniques, however, which require tissue-specific tuning in order to obtain usefully images. Also, unlike with radiography, associations between MR parameters and tissue characteristics vary significantly across studies (often registering moderate to low correlation strengths). So far, this suggests that there might not be one-to-one associations between qMRI and tissue characteristics, but rather each qMRI parameter likely depends on multiple tissue characteristics, and so sets of imaging and tissue properties are rather required to completely describe the state of a particular tissue. Hence, large robust sets of MR, compositional and/or mechanical data must be collected and processed to reveal the relatively unexplored soft tissue structure-function links, which is likely a non-trivial, costly and necessary goal with clinical implications.

2.5. Summary of gaps & connection to project

Throughout this chapter, the following research gaps were identified:

- The majority of experimental and FE studies focus on the stance phase of gait, omitting the high flexions and deformations the knee feels during swing.
- Most of these experimental and numerical simulations are limited to the T-F joint only, and, whereas studies examining the patella do exist, rarely both P-F and T-F joints are studied together and their interactions explored.
- Numerical studies (MSK and FE modelling) require full-joint experimental validation of their kinematic, kinetic and deformation characteristics (especially lacking for the latter).
- Mechanical loading plays a vital role of knee function (healthy or pathologic); yet current experimental studies are limited mechanically:
    - Current MRI-compatible simulators are mostly limited to either axial compression or knee flexion (but not both), failing to represent the multiaxial, combined loading scenario resulting from physiologic activities. This is especially challenging due to the imaging constraints (metal incompatibility, bore size) and load magnitudes.
    - As such, some ex-vivo (and definitely most in-vivo) setups are further limited in terms of the magnitude of the applied loads/flexions.
- Important characteristics of full-joint physiologic simulators include medical imaging compatibility, high physiologic realism and high repeatability; however, repeatability is rarely considered (or at least reported).
    - Load-control is also preferred (over displacement-control) for imaging the knee's loaded state and avoid soft tissues' viscoelastic offloading upon fixed displacements.
- Preliminary qMRI-mechanics associations have only been evaluated at tissue or indentation levels (not under full-joint realistic loading conditions), and when full joints are considered, qMRI and mechanical responses are examined separately.

These are the gaps that this whole project aims to address, by integrating them into the objectives of a design and two scientific studies surrounding knee biomechanics responses to full-joint physiologically realistic loads.

3. Development of a novel MRI-safe physiologic loading device for ex-vivo joints

3.1. System development

To study the effects of physical activities on healthy and/or diseased knee joints in a physiologically realistic context with (q)MRI, an entire MRI-safe, multiaxial loading system was developed and tested, all the way from inception to reality (Figure 3-1). This required determining physiologic loads experienced by a knee throughout walking (relevant daily physical activity) in order to define the equipment operating conditions and design requirements. MSK modelling was used to estimate gait physiologic loading, which was processed by a custom code for suitable experimental application. This made it possible to analyze the pneumatic and mechanical (functional, structural) aspects, and develop computer-aided design (CAD) models and blueprints for each component and the overall assembly, all of which had to be built. Hence, this system consisted of software to estimate such loading and the hardware to enforce it. Such simulated loads were also assessed against measurements (instrumented TKRs) before implementing them experimentally once calibrating the equipment.

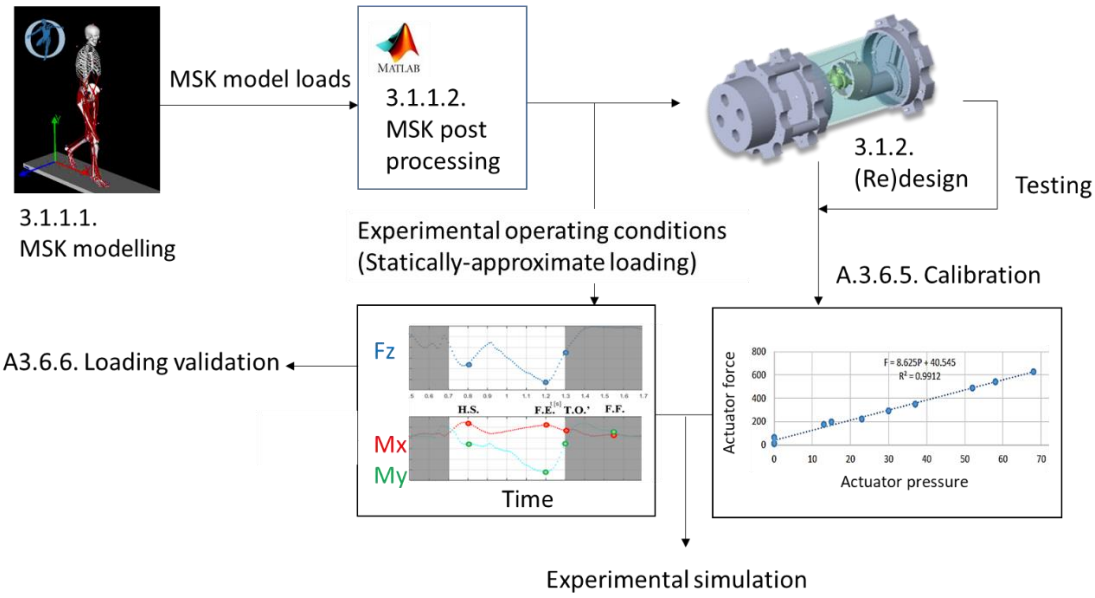

Figure 3-1: System development process

3.1.1. Software (MSK biomechanics)

3.1.1.1. MSK modelling

Since a physiologically realistic gait simulation (including muscle actuation) was desired, a lower body open-source MSK model (OpenSim 2.4.0, Stanford, Stanford, CA: https://opensim.stanford.edu) with 23 DOFs and 92 different muscle-tendon actuators was used to estimate knee full loading conditions (model details in Appendix A3.1). Muscle forces (whose magnitudes and directions change during walking) were estimated via static optimization, which requires subject's geometric and inertial information, as well as kinematic (limbs' position, velocity and acceleration) and kinetic (ground force reactions) data. Anthropometric characteristics, such as limbs' dimensions and properties, BW, and additional constraints (e.g., which muscle groups are available ex-vivo and should remain active during this simulation) were adjusted in the model to calculate knee joint loads throughout gait. Specific steps (Appendix A3.1, A3.2) were taken in OpenSim to:

1. determine experimentally relevant muscle groups for ex-vivo actuation (carrying considerable forces relative to other muscles) and determine their magnitudes,
2. simulate knee joint loads only due to these relevant muscles (via inverse dynamics), and
3. normalize knee loading (relative to BW and height) to later scale and match experimental conditions for specific purposes (e.g., rig design purposes, mechanical testing).

For design purposes, the anthropometry of the MSK model [Gait2392_simbody.osim based on an average of five healthy males' measurements, AVG ± SD: (688 ± 76)N BW, (1.77 ± 0.03)m tall, (26 ± 3)years, 100% males] was adjusted via a global scaling factor to represent a 1kN BW, 1.8m tall subject (the heaviest and tallest person whose knee loads could be simulated by the loading device, i.e., the design limit of this equipment). On the other hand, for experimental testing (study I), the normalized loads were scaled to match the BW and height of the ex-vivo specimen. As this system would be often used with ex-vivo specimens unrelated to the subjects in the OpenSim simulations, even after scaling these to match specimen's anthropometrics, the loading regime is just an arbitrary physiologic loading estimate (loading similar to what any ex-vivo subject could have felt during gait).

3.1.1.2. MSK processing

Since knees loaded to each gait time point configuration (gait "snapshot") are to be scanned for long periods while physical activities occur over short times, a custom biomechanics program was developed (MATLAB, The Mathworks, Natick, MA: https://www.mathworks.com) to convert simulated loads into achievable experimental conditions. In general, this custom code was written to:

1. convert the knee loading MSK estimates to statically approximate loads,
2. select only certain loads for simulation (due to experimental considerations), and
3. calculate the corresponding actuator forces and loading device configuration.

The goal was to obtain a statically approximate loading regime (also the loading conditions of the device components) that would recreate the same knee soft tissue deformation felt during physical activity. However, due to experimental limitations, not all physiologic loads could be applied (e.g., not all muscles can be actuated). Hence, the custom biomechanics code I (Appendix A3.2) must take the knee external loads (three forces and three moments as a function of gait cycle) and muscle tension estimates obtained from OpenSim as inputs, use coordinate transformations to select only certain components for simulation (axial force, two bending moments, and quadriceps and hamstrings tensile forces), and calculate the loading device forces and configuration (component placement) necessary to produce (or balance) the selected knee loads. Since loads and knee flexion change throughout walking, this procedure must be carried out for every instant in the gait cycle.

The major simplifications to the physiologic loading regime (conducted to facilitate experimental testing while trying to preserve its most salient features and effects on knee response) included omission of shear forces, torque and certain muscle groups. Shear forces were omitted from this analysis since they are negligible compared to axial compression[42]. Although being significant, torque was omitted too, as the current design cannot incorporate it yet (in load-control) as part of a combined loading scenario. Finally, only vastus lateralis, semimembranosus and (short head) biceps femoris were considered for experimental testing, since other muscles carry negligible tension (as per statically optimized values) or are not always available ex vivo. The gastrocnemius does carry a significant force; however its distal end is not available for knee

specimens cut mid shank, which presents a major design challenge if this muscle were to be actuated (not possible with the current design). Hence, the loading rig configuration was determined in order to approximately recreate the desired, simplified knee external loads (due to the vastus lateralis, semimembranosus, biceps femoris and gastrocnemius) but without the gastrocnemius; rather compensating via actuator forces.

As mentioned, for initial design purposes, the custom code was used to simulated the loads experienced by a 1.8m, 102kg (1kN BW) person walking at 1.2m/s (Figure 3-2), before considering other physical activities (e.g., running, stair climbing, etc.).

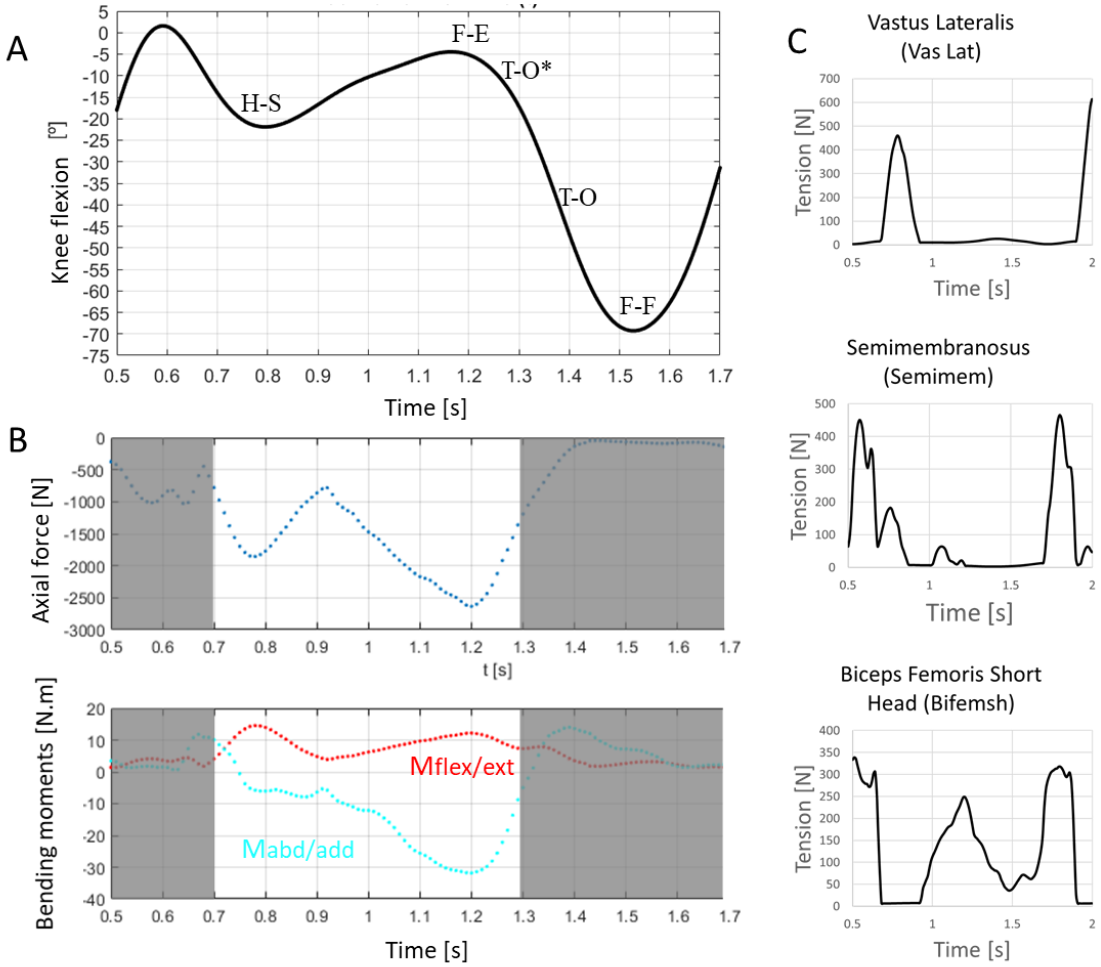

Figure 3-2: Statically approximate gait loading regime for 1.8m, 1kN (102kg) subject's right knee: A. Knee flexion (H-S = heel strike, F-E = full extension, T-O = toe-off, T-O* = toe-off surrogate, F-F = full flexion); B. simulated knee joint loads (with respect to knee anatomic coordinates, invalid instances for moment simulation grayed out); & C. primary muscle tension

Physiologic activity simulation would then be achieved by flexing/loading the knee specimen by means of the loading device corresponding to statically approximate representations of gait time points: Heel-strike (H-S), full extension (F-E), approximate toe-off (T-O*) and full flexion (F-F).

3.1.2. Hardware (pneumatic device) – a.k.a. "MR creep rig"

This loading device (Figure 3-3, Appendix A3.3) consists of a rig that can be disassembled to mount a cadaver knee, which gets loaded by air-controlled compressive and tensile actuators connected, via pneumatic hoses, to an air compressor. Key functionality included enclosing, loading and flexing knee specimens corresponding to any instant of the gait cycle (including stance and swing phases), measuring such loads, and facilitating soft tissue qMRI, which requires the MR coils to be very close to the ROI. The device must also meet the following criteria:

1. Only possess MRI-compatible materials (essentially no metals, especially ferromagnetic),
2. the rig, pneumatic hoses and coils must fit within the MR scanner bore (Ø450mm max),
3. the knee capsule must be kept intact to emulate the in-vivo knee joint environment, and
4. constant loads (not constant displacements) must be applied to account for viscoelasticity.

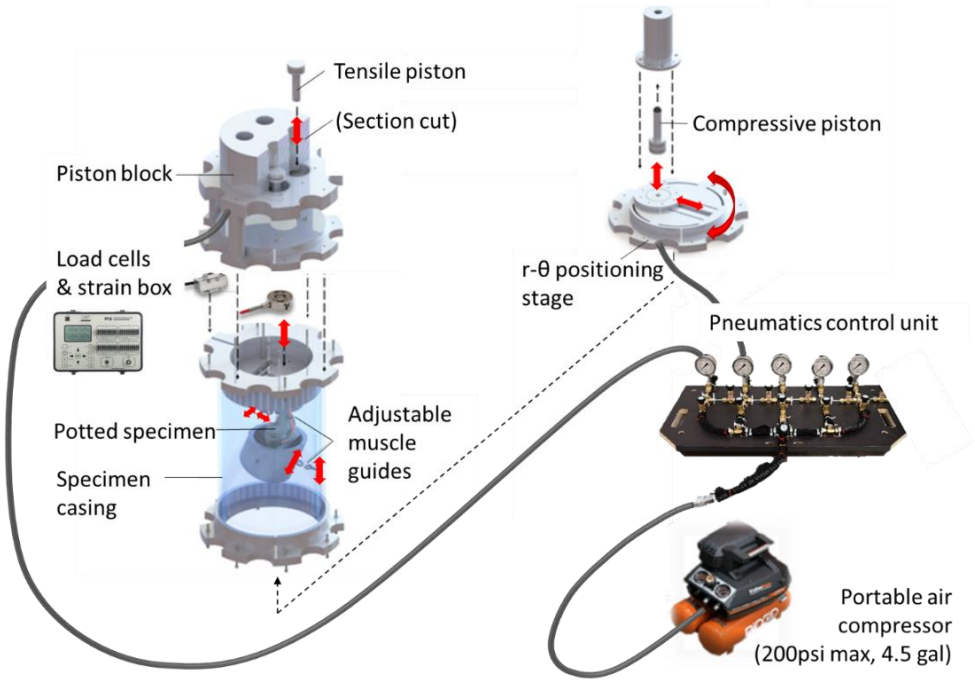

Figure 3-3: MRI-safe loading rig system (simplified exploded view showing key DOFs via arrows, muscle cables not shown)

The loading rig alone consists of > 200 components (>50 different parts) arranged as four major sub-assemblies (Figure 3-4):

1. *Top assembly* containing all tensile pistons in a cylinder block (similar to a car engine);
2. *Middle (specimen case) assembly*, the main structural component enclosing
3. the *potted specimen assembly*, containing cable guides to control muscle direction; and
4. *Bottom assembly*, composed of a compressive actuator and a *r-θ* table (similar to a *x-y* positioning stage but in polar coordinates).

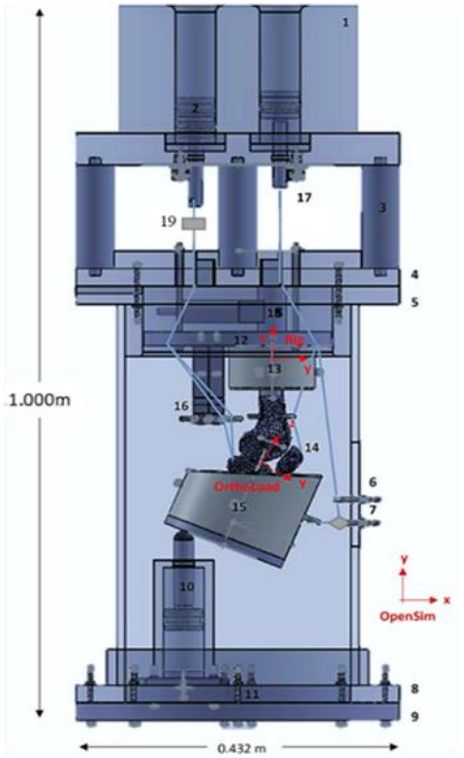

Top assembly:

1. Cylinder block, 2. Tensile actuators, 3. Column, 4. Fixed plate

Middle (specimen case) assembly:

5. Top flange, 6. Specimen cylinder, 7. Pulley + c-eyebolt (cable guide), 8. Bottom flange

Bottom assembly:

9. Fixed ring table, 10. Compressive actuator, 11. Rotating (r-θ) table

Potted specimen assembly:

12. Potting adapter, 13. Femur pot, 14. Knee specimen, 15. Tibia pot, 16. Hamstrings cable guides; 17. Muscle cable, 18. Compressive & 19. Tensile load cells (for calibration only)

Figure 3-4: MR creep rig simplified "anatomy" (2D side translucent view) and key coordinate systems; all coordinate systems are right-handed (irrespective of whether joint is right or left)

An extensive structural analysis was required to design this system and ensure all of its components (mostly plastics, as large as a tire rim or smaller than a coin) withstood the most demanding operating/loading conditions. A detailed CAD model was developed (SolidWorks, Dassault Systèmes, S.A., Suresnes, FR: https://www.solidworks.com) to keep track of design changes. A failure mode and effects analysis (FMEA)-like approach was adopted for each part, involving linear/nonlinear elasticity theory (Appendix A2.1) analytical solutions for simple problems, e.g., statically indeterminate problems solved via Castigliano's principles, as well as

FEM (Appendix A2.1.4) for more complex situations. This meant sometimes checking for different failure modes separately (e.g., bolt's axial loading and transverse shear) as well as combined (e.g., beams under compression and bending possibly leading to buckling), depending on the load cases. FEM (ANSYS APDL or Workbench, ANSYS, Inc., Canonsburg, PA: https://www.ansys.com) was essential for complex 3D geometry (often using the CAD files), diverse materials (mostly plastics, rubber, wood) and non-uniform loading. The average and minimum safety factors against all aspects considered were ~16.9 and 1.09 for structural parts (excluding threaded interfaces and the prepared specimen), and ~12.0 and 1.80 for pneumatic components. Further considerations were necessary for functionality (e.g., fine tolerancing following standards and handbooks), manufacturing [e.g., design-for-manufacturing (DFM) changes for better computer numerical control (CNC) machining or 3D printing (3DP)] and implementation (e.g., controlling friction via lubricants) in order to produce the blueprints (Appendix A3.3.3), fabricate the components and assemble this machine.

To load ex-vivo specimens in load control (creep) and avoid viscoelastic offloading with respect to fixed displacements, pneumatics were used similarly to previous studies[12,13,16,83,93,123] but extended to a multiaxial setting (Figure 3-5). Air delivered by the compressor (RIDGID OF45200SS, RIDGID, Elyria, OH: https://www.ridgid.com) was split among five actuators, whose pressure can be fine-tuned via flow-control valves: Three for applying muscle tension (connected to the specimen via cables), one for balancing knee flexion (connected to the specimen's tibia pot), and one for applying compression and bending moments via off-axis loading[117]. The directions of all these tensile cables were controlled via adjustable muscle guides.

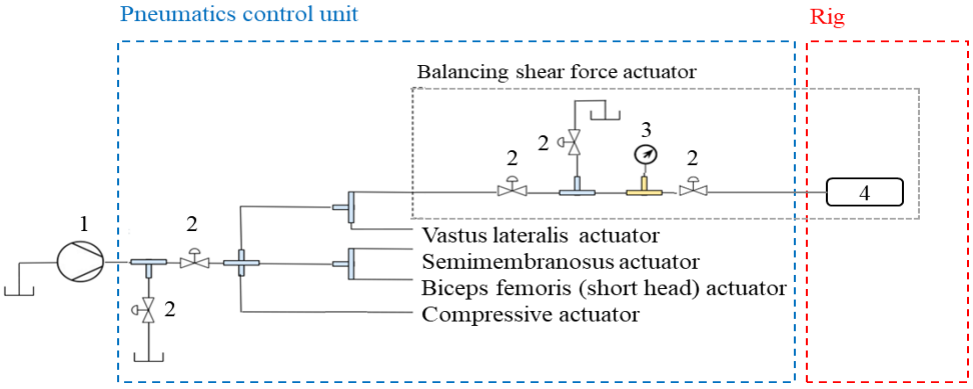

Figure 3-5: Simplified P&ID diagram of loading system's pneumatic circuit: 1. Air compressor, 2. Flow-control valve, 3. Pressure gauge, 4. Piston cylinder (same components for all actuators)

Delivering bending moments with the same physiologic force that compresses the knee (Figure 3-6) brings a major practical challenge, which is the reason why a particular time point T-O* is simulated as an estimate of the actual T-O. Since the axial force magnitude varies throughout gait, applying moments when the off-axis compressive force is close to zero requires very large moment arms that may not be practically achievable. Hence, moments can only be simulated as long as the axial force remains large enough, which occurs up to ~T-O*, just before T-O.

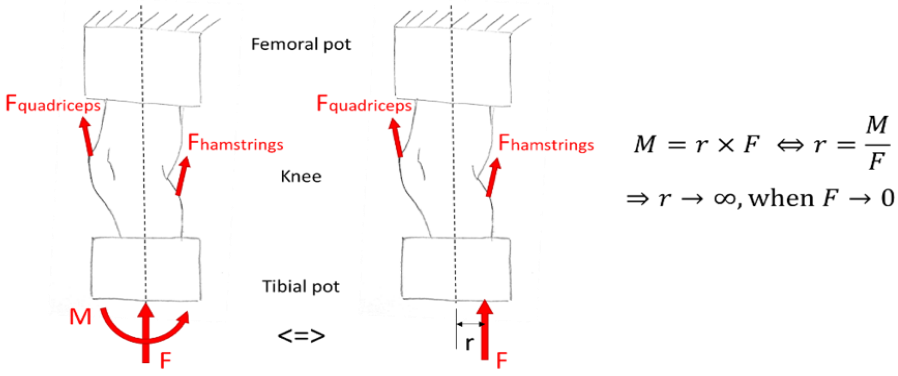

Figure 3-6: Major loading mechanisms used: Muscle tension, direct axial compression and bending generation via off-axis load (shifting the compressive force by a distance *r* simultaneously applies compression *F* and moment *M* at the knee)

To control the level of force applied in relation to the system pressure, tensile and compressive actuators were calibrated (Appendix A3.5.5) by mounting tensile (LCM703-75, Omega Engineering, Norwalk, CT: https://www.omega.ca/en/; ±1N resolution, ±0.05% repeatability) and compressive (LTH350-FSH04307, FUTEK Advanced Sensor Technology, Irvine, CA: https://www.futek.com; ±1N resolution, ±0.5%rated output non-repeatability) load cells along their line of action. Calibration curves were especially necessary since these sensors could not be used inside MR scanners. Thus, pressures required to achieve desired loads (calibration predictions) were double checked against live load cell readings, showing that calibration curves were reliable.

For validating whether the statically approximate MSK loading estimates (Figure 3-2) were within the same range as TKR measurements and were thus representing in-vivo physiologic conditions, percent relative differences between them were calculated for key time points throughout gait, H-S, F-E, T-O* and F-F (Appendix A3.5.6). Validating muscle forces is challenging and was outside the project scope, as the reference standard for in-vivo

measurements (electromyography) is affected by many signals (not just muscle action), for which they are limited to show muscle activation patterns with some degree of uncertainty.

3.2. Discussion

Individually, there are several loading rigs available that excel at integrating with medical imaging systems, exhibiting physiologic realism and displaying high testing repeatability (section 2.2.1, Appendix A2.2). However, the challenge is to achieve that high performance across all relevant experimental criteria. Among some of the most innovative designs that incorporate these aspects collectively, the rig developed by Chen et al.[92] can activate all six knee DOFs in a load-control test and achieve loads as high as 700N for axial compression and 350N of muscle tension with high repeatability (3.22 to 6.96 and 7.72 to 50.9 CV% for axial and shearing forces respectively). The rig cannot vary abduction/adduction moments or shearing forces and can only fit porcine stifle joints; however, it is compatible with both MR and CT scanners. Martin et al.[110,111] also developed a design that is MRI-compatible and capable of simulating static (either in stress relaxation or creep) or dynamic (fatigue) activities. This device can position intact human knee specimens with high repeatability (1.2mm translation and 0.9º rotation SD) and compress them up to a maximum of 1.5kN. The spine tester by Si-hoe et al.[117] is another outstanding device that accepts dissected porcine and bovine spine segments and can apply three translations and rotations. However, what is unique about this CT device is that although being a stress-relaxation rig, they devised a way to determine a series of stepwise compressive displacements (which likely depends on the specimen constitution) that lead to a pseudo-equivalent creep test. Additionally, they are able to achieve large-magnitude compression (5kN), shear (1kN) and bending moments (15N.m) via off-axis compression. Unfortunately, the corresponding repeatability has not been measured yet.

As it will be demonstrated by the end of this thesis, the functionality of the MRI-safe loading system developed is comparable to the most advanced lower-body ex-vivo testing technologies that exist up to date. In terms of physiologic realism, the rig is large enough to contain human knees or bovine stifles (with intact or open knee capsules) and can simultaneously activate all six joint DOFs. Loads can be as large as 2.5kN for axial compression, 1kN for shearing and muscle forces and 30N.m for bending moments, and they can be applied simultaneously thereby approximating joints' multiaxial physiologic loaded state. As shown in study I (section 0), a

repeatability assessment of loading input and response characteristics was conducted and the system was found to possess high repeatability. Moreover, the MSK biomechanics programs developed allow exploiting mechanical testing potential of this equipment and simulating physiologic loads during physical activities, such as gait (including stance and swing phases), which were validated against TKR measurements and showed reasonable agreement (Appendix A3.5.6). Lastly, in practical terms, this pneumatic system is portable, does not occupy excessively large amounts of space, and neither does it consume large amounts of energy, as the compressor only needs to run to charge the tanks, after which the system can operate without (or even disconnected from) the compressor.

3.3. Conclusion

In comparison to current experimental loading devices and previous studies focused on stance, the MRI-safe creep loading system developed in this project addresses some of their limitations and further improves upon their functions. This simulator allows imaging specimens under near-to-physiologic loading conditions throughout the entire cycle of walking or other activities. Physiologic simulation involves an intense multiaxial combined loading scenario (including axial compression, bending moments and muscles actuation), which simultaneously loads all T-F and P-F tissues, just like physical activities do. In terms of specifications, this simulator operates in load control without complex control systems, which are harder to troubleshoot and fix, to achieve a realistic simulation. Additionally, this rig has been tested extensively and allows simulating various physical activities for healthy or pathologic human knees (or other joints and/or species). All in all, this novel and versatile loading system compares with the most sophisticated technologies in terms of medical imaging integration, physiologic realism and testing repeatability!

4. Study I: Human knee mechanical loading & response repeatability – What may be going on inside knees at different gait phases? (Preliminary findings from a static approach)

4.1. Introduction

Our knees are subjected to physical activities of daily living, injuries (e.g., lesions, tears) and/or diseases without cure (e.g., OA), costing thousands to billions of US$/year for individuals and countries[7,8], yet their loading response is not well understood in healthy nor pathologic cases. Since abnormal/excessive mechanical loading, obesity, malalignment (e.g., varum, valgum), disorders or simply aging are key risk factors leading to further complications[2,46,72,74], healthy or pathologic knees must be studied under realistic loading conditions to better represent the knee physiologic state, which is heavily influenced by such mechanical factors. Ex-vivo testing provides a controlled path for evaluating such effects on knee behavior in situ, which could be combined with medical imaging (MRI) to assess soft tissues' current state, and determine how to detect diseases at an early stage[10,11]. Unfortunately, due to joints' complexity (geometry, mechanical properties and loading), current experimental devices are either often limited to uniaxial compression (sometimes only applying low loads[15,105,120]) or can only load individual tissues[186-189], while others simply do not facilitate MRI integration[89,90,97,113]. Hence, a MRI-safe physiologically relevant loading device was recently developed to address all those limitations; however, its repeatability is to be determined before it can be implemented. Thus, the objective of this study was to determine the repeatability of our novel loading device by testing this system with a full-joint cadaver knee several times and measuring applied loads and contact responses.

4.2. Methods

4.2.1. Study overview

The novel, MRI-safe, physiologically relevant knee loading system developed in Chapter 3 was used to assess repeatability. Also, once its testing repeatability was determined, it was compared to gait variability data to check whether the simulated state (with its repeatability error) was within healthy or pathologic ranges. In addition to being used in the development phase (for calibration), an anatomic model was also used to conduct mock-up pressure sensing tests, and later so was a bovine stifle joint to account for real ex-vivo specimen conditions. For

repeatability purposes, a human ex-vivo knee was loaded repeatedly according to an approximately statically equivalent regime pertaining to key points in the gait cycle (three tests for each knee configuration). For each of the three repeated trials, loading input and knee response parameters were measured at steady state, so that their standard deviation (SD) for each gait cycle point was determined (Figure 4-1). To accomplish all this, the following resources were required:

- Specimens: Anatomic model (life-size polymer knee model), bovine stifle, human knee;
- Lab equipment: MR creep loading system and related custom computer codes, load cells and DAQ system for measuring tensile and compressive forces (and estimate bending moments), and a pressure sensing system.

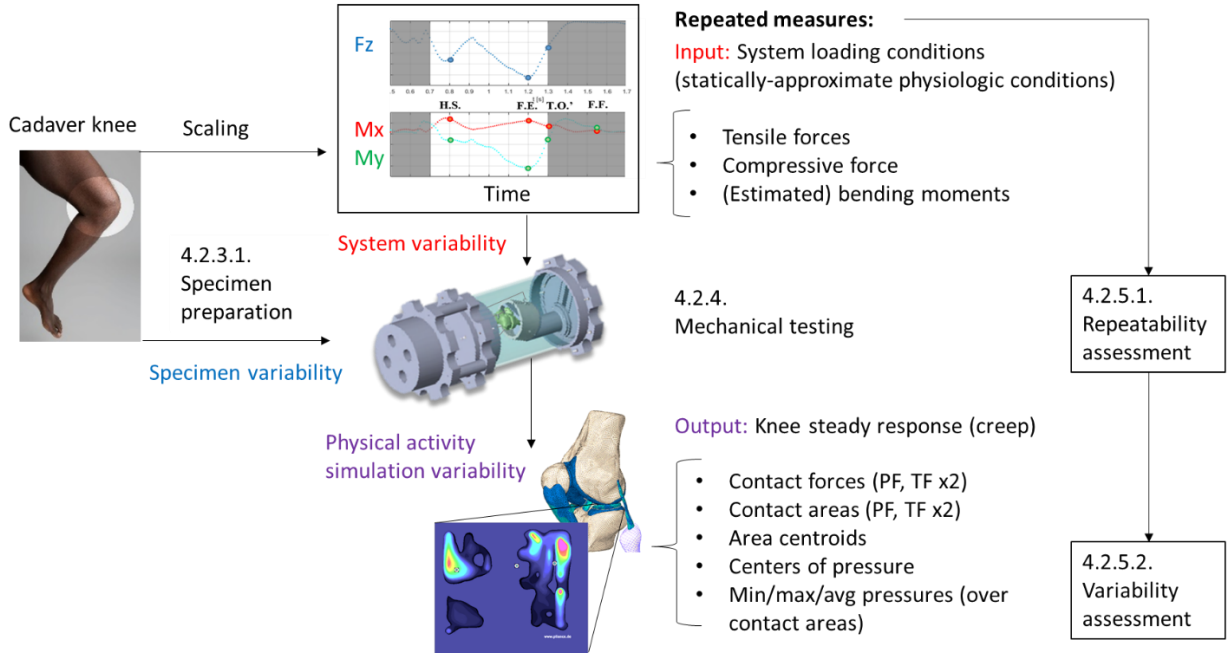

Figure 4-1: Study I diagram: Input & output repeatability characteristics for each flexion considered. Adapted from Wikimedia Commons[18,19].

4.2.2. Study scope

4.2.2.1. Anatomy & loads of interest

Articular soft tissues (cartilages, menisci) and their response, as opposed to bones', were the primary focus of this project (Figure 4-2A). In contrast to other studies which focused on loading knee compartments separately, in this study the full knee (i.e. both T-F and P-F joints) was loaded in a physiologically realistic way approximating walking. Unfortunately, since this was an experimental ex-vivo study, not all muscles were available for actuation neither all that were available could be activated. Thus, after performing a muscle force magnitude assessment (statically optimized tensions obtained via OpenSim), the muscle groups available ex vivo that carried considerable tension (with respect to the others) during gait and could be used to control the knee flexion were identified as the vastus lateralis, semimembranosus and (short head) biceps femoris (Figure 4-2B). All other muscle activations were excluded.

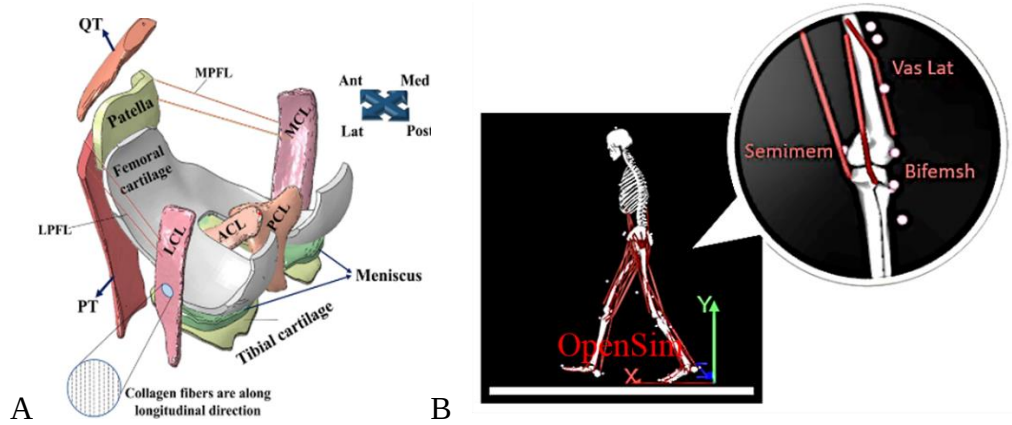

A B

Figure 4-2: Anatomy of interest: A. Articular soft tissues (articular cartilages, menisci, ligaments), B. Muscles carrying considerable tension that are available ex vivo and in OpenSim. Reproduced with permission from Orozco et al. 2018[190].

4.2.2.2. Gait time point discretization

Since mechanical testing and imaging is expensive and time-consuming, not all points in the gait cycle could be simulated experimentally, but rather only the most important ones, as done in other studies[108]. For gait (Figure 4-3), the most representative instants to consider are: Heel-strike, full-extension, toe-off and full-flexion. As explained in the next sections, due to experimental limitations, a surrogate for toe-off (T-O*: time point occurring 0.1s before T-O) was simulated.

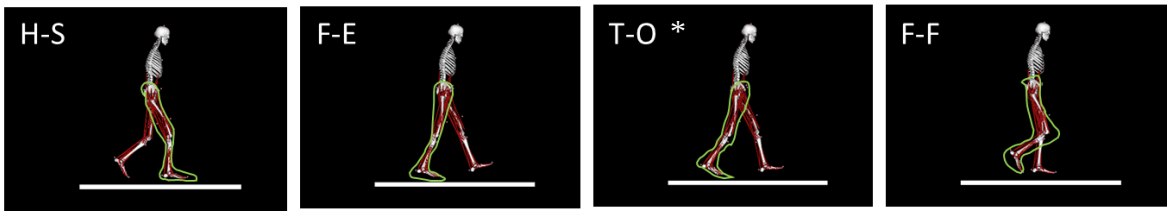

Figure 4-3: Key gait time points with corresponding intended flexions recreated in OpenSim

4.2.3. Specimens

One fresh-frozen healthy specimen (Figure 4-4A), with no history of MSK disorders or surgery, was used for this repeatability study (743N BW, 1.78m tall, 68 years, male, left knee, Science Care, Inc., Phoenix, AZ). This specimen was kept frozen at -20ºC and thawed before testing; testing took place within one week, in order to preserve specimens integrity as much as possible[141]. Specimen procurement and testing were carried out according to an institution approved ethics protocol (Appendix A1).

4.2.3.1. Specimen preparation

The loading rig design allows integration not only with MR scanners, but also with pressure sensing systems, which requires inserting sensors inside the knee capsule to measure loading response repeatability. As such, the loading device can operate in either intact- or open-capsule configurations, depending on the application.

Intact-capsule general preparation

Specimens were carefully prepared while trying to preserve as many tissues as possible (not only the joint capsule) to be as close as to the in-vivo scenario as possible, while still being able to actuate the knee. In general, knees had to be cut at ˜15cm above and below an estimate of the knee joint center (midpoint between femoral condyles) and all tissues resected at those ends until the bone was exposed. Bone ends were then be potted in dental stone (nylon bolts drilled through bones were used as glue anchors) and sealed with Poly(methyl methacrylate) (PMMA) caps (Figure 4-4B). To apply muscle loading, tendons needed to be exposed by carefully resecting the skin close to the quadriceps and hamstrings muscle groups (keeping the knee capsule intact). Since tissue is stronger at the muscle insertion sites, Ø0.05” (1.27mm) polypropylene cables

were sutured using a 3-loop pulley knot[191] to tendons, whereas the other end attached to Ø1/8" (3.175mm) nylon cables connected to the tensile actuators. Finally, absorbent pads were wrapped around the knee in order to hydrate the specimen (to better preserve its integrity) and prevent leaking into the rest of the machine (Figure 0-21). To ensure specimen preparation (alignment, potting, suturing) repeatability, the specific protocols and tools developed for this purpose (Figure 4-4C, Appendix A3.3) must be used, including a specimen misalignment calculator to measure and account for deviations introduced during potting.

Figure 4-4: Specimen preparation: A). Intact knee (line drawing), B). Prepared knee anatomic model (dissected/potted/sutured knee surrogate), C). Potting station, D). Prepared specimen with pressure sensors inserted (bovine open capsule)

Open-capsule preparation adaptations

For this study (aiming to characterize load response repeatability), additional steps were taken after intact-capsule preparation in order to open the knee compartments and be able to insert/fix the pressure sensors (Figure 4-4D). This was not straightforward due to the presence of the hamstring guides (Figure 4-5), which prevented inserting the sensors through the posterior side of the knee (i.e. how they are designed to be used). However, once the specimen was prepared according to the standard procedure (which protects the knee capsule), the knee capsule had to be open by cutting vertically inclined slits on the anterior side of the knee (Figure 4-6), so that ligaments/other passive tissues were not destroyed in the process. As these slits became deeper, they also became more horizontal in order to access the T-F compartments. To fix these sensors, shallow horizontal slits (mostly removing skin/fat) were also carved on the posterior side

(without cutting the hamstrings), so that a cable could be used to pull the sensors through the slits and fix them to surrounding passive tissues by the posterior region. This was much easier than suturing them near the sides/front, where many other ligaments/tissues interfere. The patella sensor was easier to insert, just accessing the joint from another inclined slit near the proximal side of the patella (without cutting the vastus lateralis), while another inclined slit was used to fix the sensor to the adjacent tissue (patellar tendon and retinaculum).

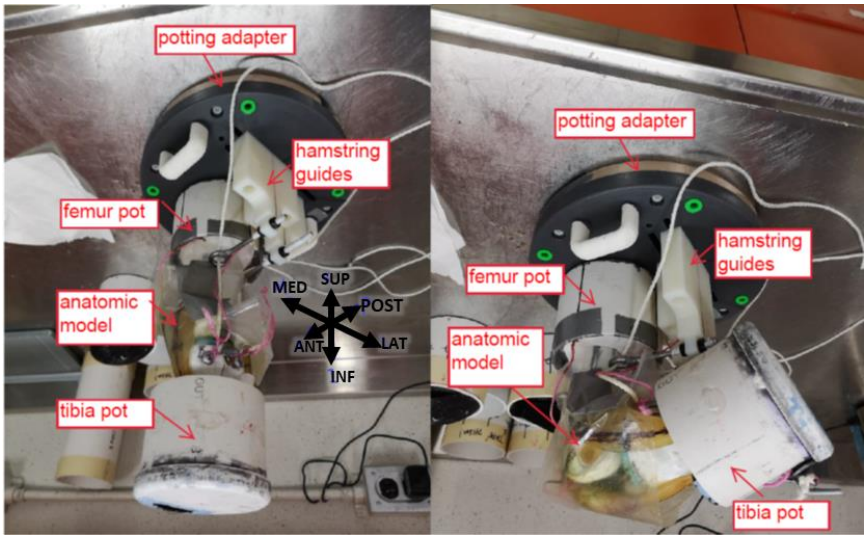

Figure 4-5: Hamstring guides difficult posterior sensor insertion in extended and flexed mounted specimen configurations

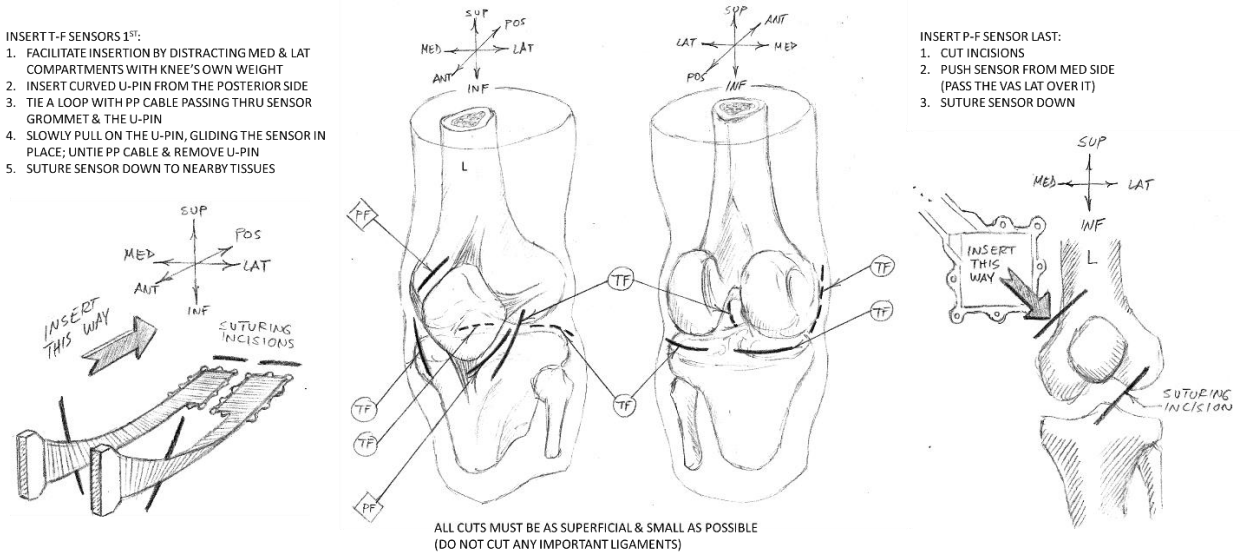

Figure 4-6: Specimen preparation plan (open capsule) for pressure sensors insertion

Since knee testing is commonly carried out over several days (especially due to testing duration), the rig was modified to also be used as a self-contained cooler. This allowed the specimen to remain within the rig between test days improving the repeatability of experiments while preserving the specimen from expiring. This way, the specimen, rig components and pressure sensors could be left overnight without removing them from the rig (which also helped preserving high repeatability). To do this, an array of icepacks and flexible insulating material was left on the outside of the rig, as well as a few icepacks inside to provide more refrigeration whenever possible.

4.2.4. Mechanical testing

To determine the experimental conditions for gait simulation specific to each specimen (Appendix A4.3.1), the location of muscle insertions must be measured. The rig kinematic configuration (muscle guides location and compressive piston location) was then determined via the MSK biomechanics code II, which automates these calculations for all gait time points. As mentioned in Chapter 3, kinetic parameters must be scaled by BW and height to determine the experimental loading regime (Table 4-1). In this study, valgum effects on walking were simulated by reversing the position of the compressive actuator for healthy gait along the medial-lateral direction. This approximation was assessed by comparing the ranges of applied loading to healthy and pathologic ranges, which indicated we were close to genu valgum (Appendix A4.6).

Table 4-1: Rig kinematic and kinetic parameters for valgum-like walking experimental simulation (subject = K07, limb = left, sex = male, age = 68 years, height = 1.78m, BW = 743N)

Kinematic parameters	**Relative to**	H-S (%gait ~= 14.7%)	F-E (%gait ~= 49.0%)	T-O* (%gait ~= 57.2%)	F-F (%gait ~= 76.0%)
r_piston [mm]	r-θ table origin	60.2	2.1	25.2	N/A
θ_piston [mm]	r-θ table origin	-108.5	135	-107.7	N/A
x_vas [mm]	knee centre	Fixed to femur	Fixed to femur	Fixed to femur	Fixed to femur
l_vas [mm]	knee centre	Fixed to femur	Fixed to femur	Fixed to femur	Fixed to femur
x_bif [mm]	rig origin	N/A	-14.4	-14.4	-14.4
l_bif [mm]	guide front face	N/A	25.5	16.5	19.1
x_sem [mm]	rig origin	28.7	N/A	N/A	N/A
l_sem [mm]	guide front face	14.8	N/A	N/A	N/A
h_tib pot guide [mm]	slot endpoint	27.3	6.2	21.2	N/A
∡_sag,pulley [º]	eyebolt knot	~0	~45	~0	~45
θ_flex,ideal [º]	femur axis	21.7	5.1	17.2	69.3
Kinetic parameters					
F_fem,axial [N]		1312	1958	849	N/A
F_sh,cable [N]		212	394	178	N/A
F_bifemsh [N]		N/A	185	108	42
F_semimem [N]		118	N/A	N/A	N/A
F_vasLat [N]		343	N/A	N/A	N/A

N/A (not applicable) refers to negligible loads or guide positions which are therefore no longer needed

To apply this loading regime as closely as possible, for each gait time point, the knee must be loaded quasi-statically in two load steps:

1. Muscle pre-tension (joint stability): Loading one tensile actuator at a time starting with one hamstring group (the one with lower tension), the quadriceps group, the other hamstring group (the one with greater tension), and finally the shearing force balancing cable. By alternating actuators this way, the knee develops mechanical stability, as its joint DOFs are progressively constrained by muscle activation (acting like redundant supports).
2. Joint compression, flexion & bending: Once the knee is stable, the compressive piston can be progressively loaded until reaching the target load for that gait time point. Since, the piston is offset with respect to the knee center, flexion and bending occur simultaneously with compression.

Due to experimental limitations including unique specimen characteristics, potting/alignment imperfections and friction (still present despite the use of lubricants and friction-reducing adaptations), while close, the resulting (effective) loads and rig configuration (Table 4-1) are somewhat different than the theoretical (ideal) loading scenario (Figure 3-2). This was determined prior to testing (calibration, repeatability) by using the whole system with an anatomic model (to test and conduct calibration protocols), a bovine stifle joint (to test pressure sensors and repeatability protocols in a similar physiologic context). After, these proof of concept trials (Figure 4-7), the human specimen was used for actual data collection (repeatability), as indicated in the testing protocols (Appendix A4.3.1).

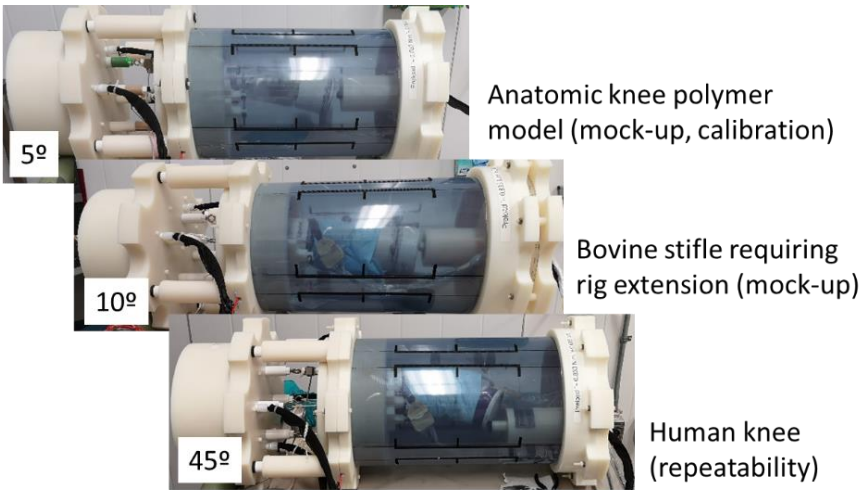

Figure 4-7: Specimens tested at MR creep rig for different purposes

Due to experimental limitations (test duration and degradation of the specimen – usually limited to about one week of testing), each of these physiologic scenarios was experimentally simulated three times (in addition to a pre-conditioning loading phase to reach viscoelastic equilibrium). For all trials, input load conditions were measured by tensile (LCM703-75, Omega Engineering, Norwalk, CT: https://www.omega.ca/en/; ±1N resolution, ±0.05% repeatability) and compressive (LTH350-FSH04307, FUTEK Advanced Sensor Technology, Irvine, CA: https://www.futek.com; ±1N resolution, ±0.5%rated output non-repeatability) load cells connected to a DAQ unit (P3 strain indicator and recorder, Vishay Micro-Measurements, Raleigh, NC: www.vishaymg.com; ±1s temporal resolution), and/or pressure gauge (3548K118, McMASTER-CARR, Elmhurst, IL: https://www.mcmaster.com/; ±1.5% accuracy) readings and calibration curves (Figure 0-22 in Appendix A3.5.5), whereas knee contact response was measured via a pressure sensing system (pliance-x, novel, München, DE: https://www.novel.de; ±0.01MPa load resolution and ±0.097 to 8.450 CV% load repeatability[192], ±6.25 and 7.29mm^2 area resolution (S2016 and S2014 mat), ±0.02s temporal resolution) (Figure 4-8). Actual knee flexion was estimated via goniometer measurements outside the rig parallel to the specimen's sagittal plane, similarly to as is performed on live subjects. Force and pressure sensors were calibrated prior to rig calibration and mechanical testing. Load cells were calibrated by loading them with known weights (10kg blocks), while pressure sensor calibration was more involved. Pressure sensors were first calibrated by the vendor (loading sensors via their proprietary trublu pneumatic calibration device) over low (0 to 1.275MPa) and high pressure ranges (0 to 2.550MPa), which were checked in the lab via simple tests (Appendix A1.1).

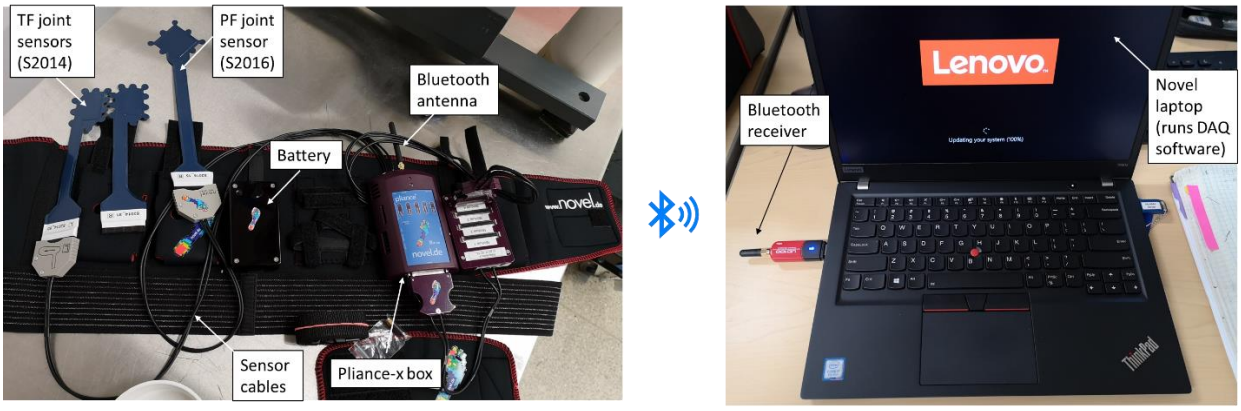

Figure 4-8: pliance-x pressure sensing system (except for sensors/cables, all components remain outside MR-creep rig)

4.2.5. Statistical analysis

4.2.5.1. Repeatability of gait experimental simulation (loading & response parameters)

Intra-subject repeatability for loading and responses (Table 4-2) was determined for the human specimen. For each of the four simulated gait time points, three identical repeated trials were conducted without dismounting the specimen from the rig nor allowing for substantial viscoelastic restitution between trials, throughout which load input and response data were recorded. These repeated trials (10min creep) were conducted, after a pre-conditioning loading phase (30min creep) in order to reach viscoelastic equilibrium, under the same (constant) applied loads required to simulate each gait time point. For each parameter measured, the sample mean, sample standard deviation and coefficient of variation expressed as a percentage (CV%) were calculated to gauge the repeatability of the loading input and output response throughout the overall simulation, as recommended for evaluating precision errors of individual subjects[193]:

$$CV\% = \frac{s}{\bar{X}} \times 100\%, \tag{4-1}$$

$$\bar{X} = \sum_{i=1}^{n} \frac{X_i}{n} \tag{4-2}$$

$$s = \sqrt{\sum_{i=1}^{n} \frac{(X_i - \bar{X})^2}{n-1}}, \tag{4-3}$$

where X_i = ith repeated measurement (from a total of n), $\bar{X}$ = sample mean, and s = sample SD.

Table 4-2: Input and steady-state output measures considered for repeatability assessment

Input:

Metric	Definition	Mathematical expression
Muscle tensions	Statically optimized muscle forces for vastus lateralis, semimembranosus and biceps femoris (short head)	F_{vasLat}, $F_{semimem}$, $F_{bifemsh}$
Shearing force	Balancing force required at the tibia end to keep the flexed knee in equilibrium (i.e. a shear support reaction at this bone end)	$F_{sh,cable}$
Axial compression	Axial support reaction at the femur fixed end (depends on but not equal to the force applied by the compressive piston at the tibia pot)	$F_{fem,axial}$
Applied bending moments	Moments along the x and y directions (in rig coordinates) applied with respect to the tibia end's centre (not at the tibia pot end, nor relative to the rig centre)	$M_{x,applied}$, $M_{y,applied}$
Knee flexion	Smallest angle between the femur and tibia mechanical axes on the sagittal plane[i]	θ_{flex}

Output:

Contact areas	Total area of active pressure sensor cells (equal-sized), adding up to n active cells	$A_{contact} = \iint_{A_{contact}} dA \approx \sum_{i=1}^{n_{active\ cells}} A_{cell_i} = A_{cell} \cdot n_{active\ cells}$
Contact forces	Portion of the total contact force supported by a particular knee compartment	$F_{contact} = \iint_{A_{contact}} p(x,y)dA \approx \sum_i \sum_j p(x_i,y_j)A_{cell}$
Centers of geometry	Average location of the contact area with respect to the sensor's coordinate system origin (which varies based on sensor)	$\langle C_x = \frac{\iint_{A_{contact}} xdA}{A_{contact}} \approx \frac{\sum_i x_i A_{cell}}{A_{contact}}$, $C_y = \frac{\iint_{A_{contact}} ydA}{A_{contact}} \approx \frac{\sum_j y_j A_{cell}}{A_{contact}} \rangle$
Centers of pressure	Average location of the contact force with respect to the sensor's coordinate system origin (which varies based on sensor)	$\langle CP_x = \frac{\iint_{A_{contact}} xp(x,y)dA}{F_{contact}} \approx \frac{\sum_i \sum_j x_i p(x_i,y_j) A_{cell}}{F_{contact}}$, $CP_y = \frac{\iint_{A_{contact}} yp(x,y)dA}{F_{contact}} \approx \frac{\sum_i \sum_j y_i p(x_i,y_j) A_{cell}}{F_{contact}} \rangle$
Regional minimum, maximum, and average pressures	Minimum (non-zero), maximum and mean pressure values over the contact areas (not over time, since they are at steady state)	p_{min}, p_{max}, p_{avg}

4.3. Results

By implementing the tools developed in this project (MR creep rig and associated codes), in combination with other systems (e.g., load cells and pressure sensing DAQ systems), and following the methods described earlier, it was possible to load the knee specimen in a physiologically realistic way. Additionally, it was possible to obtain the following results regarding repeatability and knee load response (Appendix A4.4, A4.5).

[i] Whereas knee flexion is mostly part of the specimen response to muscle loading (the effective flexion, $\theta_{flex,eff}$), it can also be regarded as an angular displacement BC (the ideal flexion one tries to enforce via loading, $\theta_{flex,ideal}$). To facilitate understanding, its steady value is reported as an input parameter as a whole-joint BC (similar to other input parameters), separating it from the different contact pressure responses of each knee compartment.

From repeated testing, it was determined that the MR creep rig is able to deliver compressive forces (1.23 to 2.91 CV%), balancing shear forces (6.46 to 37.0 CV%), bending moments (1.23 to 42.8 CV%) and achieve knee flexions (1.95 to 26.5 CV%) with high repeatability (Table 4-3, Figure 4-9). Certain parameters characterizing steady knee load response (Table 4-4, Figure 4-10) showed adequate repeatability (0.467 to 11.3 CV% for contact area, 0.029 to 3.32 CV% for centroids and 0.029 to 21.1 CV% for pressure centres), while others were not as consistent (0.708 to 54.8 CV% for contact forces and 0 to 172 CV% for contact pressures). The repeatability assessment for muscle forces is more involved and thus discussed separately (Appendix A4.5.1), as are the complex contact pressure distribution features and their interrelations (Appendix A4.7).

Table 4-3: Summary of (input) kinematic & kinetic testing parameters & repeatability [intra-subject AVG ± SD (CV%)] of knee specimen (limb = left, sex = male, age = 68 years, height = 1.78m, BW = 743N); x-y-z coordinates relative to rig origin

Parameter	H-S (%gait ~= 14.7%, θ_flex,ideal = 21.7º)	F-E (%gait ~= 49.0%, θ_flex,ideal = 5.1º)	T-O* (%gait ~= 57.2%, θ_flex,ideal = 17.2º)	F-F (%gait ~= 76.0%, θ_flex,ideal = 69.3º)
θ_flex,eff [º]	30 ± 1 (1.95%)	10 ± 3 (26.46%)	18 ± 3 (14.70%)	48 ± 3 (6.25%)
F_sh,cable [N]	336 ± 124 (36.99%)	320 ± 21 (6.46%)	206 ± 32 (15.34%)	N/A
F_fem,axial [N]	-828 ± 24 (2.91%)	-1638 ± 20 (1.23%)	-823 ± 22 (2.70%)	N/A
Mx_appied [N.m]	-20.2 ± 0.7 (3.66%)	-27.8 ± 11.9 (42.76%)	-17.1 ± 5.4 (31.77%)	N/A
My_appied [N.m]	15.8 ± 0.5 (2.91%)	2.4 ± 0.03 (1.23%)	6.3 ± 0.2 (2.70%)	N/A

Key gait time points include heel-strike (H-S), full extension (F-E), approximate toe-off (T-O*) and full flexion (F-F).

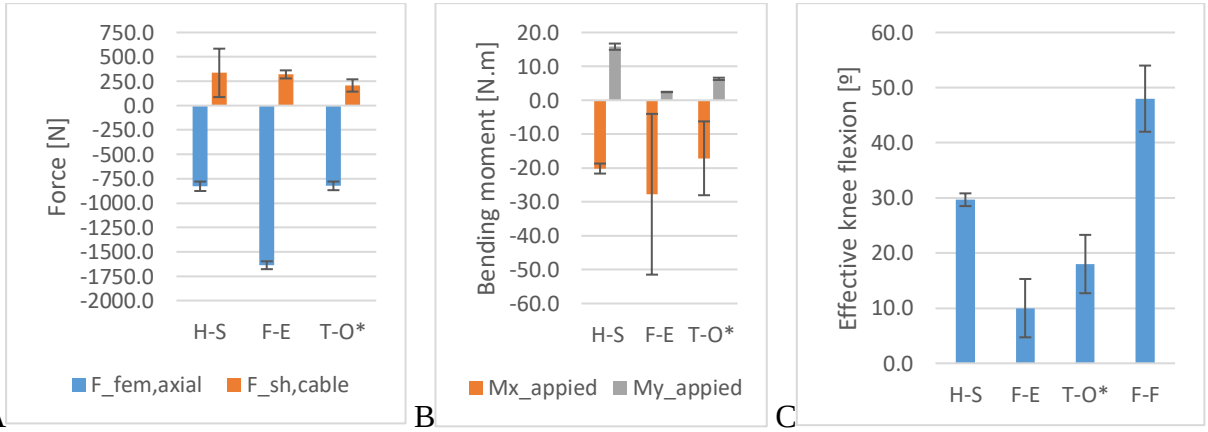

Figure 4-9: Knee loading repeatability throughout gait (n=3 tests, AVG ± 2 SD): A. Applied forces, B. Applied moments at tibia end (in rig coordinates), C. Effective knee flexion. Key gait time points include heel-strike (H-S), full extension (F-E), approximate toe-off (T-O*) and full flexion (F-F).

Table 4-4: Summary of (output) load response parameters & repeatability [intra-subject AVG ± SD (CV%)] of a knee specimen (limb = left, sex = male, age = 68 years, height = 1.78m, BW = 743N); x-y local coordinates relative to individual pressure sensors' origin

Parameter	H-S (%gait ~= 14.7%, θ_flex,ideal = 21.7º)			F-E (%gait ~= 49.0%, θ_flex,ideal = 5.1º)			T-O* (%gait ~= 57.2%, θ_flex,ideal = 17.2º)			F-F (%gait ~= 76.0%, θ_flex,ideal = 69.3º)		
	PF	TF,med	TF,lat	PF	TF,med	TF,lat	PF	TF,med	TF,lat	PF	TF,med	TF,lat
A_contact [mm^2]	1545.8 ± 7.2 (0.467%)	816.5 ± 7.3 (0.893%)	770.3 ± 4.2 (0.546%)	1241.7 ± 25.3 (2.034%)	592.9 ± 22.3 (3.756%)	648.8 ± 12.6 (1.946%)	1504.2 ± 7.2 (0.480%)	782.5 ± 4.2 (0.538%)	750.9 ± 19.3 (2.569%)	925.0 ± 34.8 (3.762%)	357.2 ± 33.4 (9.352%)	260.0 ± 29.5 (11.331%)
F_contact [N]	205 ± 2 (0.926%)	122 ± 10 (8.258%)	112 ± 61 (54.799%)	111 ± 5 (4.149%)	141 ± 5 (3.253%)	190 ± 56 (29.499%)	180 ± 2 (1.292%)	121 ± 1 (0.708%)	94 ± 2 (1.664%)	68 ± 4 (5.680%)	24 ± 2 (10.336%)	14 ± 2 (13.706%)
<C_x,	20.4 ± 0.1 (0.353%)	11.8 ± 0.05 (0.418%)	10.8 ± 0.3 (3.075%)	22.4 ± 0.04 (0.197%)	12.7 ± 0.1 (0.810%)	10.0 ± 0.1 (0.875%)	20.7 ± 0.1 (0.334%)	12.0 ± 0.02 (0.127%)	10.3 ± 0.2 (1.840%)	23.6 ± 0.3 (1.301%)	12.9 ± 0.3 (2.378%)	10.3 ± 0.3 (3.316%)
C_y> [mm]	20.1 ± 0.01 (0.056%)	21.9 ± 0.04 (0.200%)	21.9 ± 0.3 (1.526%)	19.7 ± 0.2 (0.917%)	23.0 ± 0.2 (0.811%)	23.0 ± 0.2 (0.860%)	20.0 ± 0.01 (0.029%)	22.4 ± 0.1 (0.399%)	21.3 ± 0.1 (0.655%)	19.9 ± 0.2 (1.188%)	22.1 ± 0.3 (1.535%)	21.7 ± 0.3 (1.321%)
<CP_x,	21.5 ± 0.1 (0.336%)	14.9 ± 0.2 (1.441%)	8.7 ± 1.8 (21.096%)	23.1 ± 0.03 (0.109%)	16.4 ± 0.2 (1.274%)	6.6 ± 0.5 (8.220%)	21.8 ± 0.05 (0.210%)	15.0 ± 0.01 (0.038%)	8.5 ± 0.2 (1.961%)	23.4 ± 0.1 (0.495%)	13.6 ± 0.3 (2.292%)	10.2 ± 0.3 (3.400%)
CP_y> [mm]	19.9 ± 0.01 (0.029%)	26.4 ± 0.4 (1.574%)	24.4 ± 2.4 (9.935%)	18.9 ± 0.2 (0.931%)	28.1 ± 0.3 (1.033%)	31.2 ± 0.7 (2.184%)	19.7 ± 0.03 (0.163%)	26.4 ± 0.1 (0.544%)	26.9 ± 0.1 (0.541%)	19.8 ± 0.1 (0.556%)	24.5 ± 0.4 (1.722%)	21.4 ± 0.2 (0.918%)
p_min [MPa]	0.004 ± 0.006 (172.267%)	0.050 ± 0 (0%)	0.050 ± 0 (0%)	0.033 ± 0.015 (44.036%)	0.050 ± 0 (0%)	0.050 ± 0 (0%)	0.027 ± 0.024 (90.732%)	0.050 ± 0 (0%)	0.050 ± 0 (0%)	0.037 ± 0.023 (62.941%)	0.050 ± 0 (0%)	0.050 ± 0 (0%)
p_max [MPa]	0.230 ± 0 (0%)	1.650 ± 0.221 (13.375%)	1.157 ± 1.208 (104.451%)	0.140 ± 0 (0%)	1.813 ± 0.225 (12.409%)	2.550 ± 0 (0%)	0.173 ± 0.006 (3.331%)	1.123 ± 0.040 (3.598%)	1.653 ± 0.098 (5.936%)	0.220 ± 0 (0%)	0.190 ± 0 (0%)	0.067 ± 0.006 (8.660%)
p_avg [MPa]	0.132 ± 0.0003 (0.244%)	0.153 ± 0.011 (7.383%)	0.149 ± 0.081 (54.492%)	0.090 ± 0.002 (2.129%)	0.244 ± 0.017 (6.894%)	0.300 ± 0.084 (27.976%)	0.120 ± 0.001 (0.914%)	0.159 ± 0.0005 (0.313%)	0.128 ± 0.002 (1.581%)	0.076 ± 0.002 (2.339%)	0.069 ± 0.001 (1.249%)	0.053 ± 0.001 (2.401%)

Key gait time points include heel-strike (H-S), full extension (F-E), approximate toe-off (T-O*) and full flexion (F-F).

Knee compartments considered are patello-femoral (P-F), and medial and lateral tibio-femoral (T-F,med and T-F,lat).

Figure 4-10: Knee loading response repeatability throughout gait (n=3 tests, AVG ± 2 SD): A. Contact area, B. Contact force magnitudes (compressive), C. Centers of geometry & pressure, and D. Contact pressures magnitudes (compressive). Key gait time points include heel-strike (H-S), full extension (F-E), approximate toe-off (T-O*) and full flexion (F-F). Knee compartments considered are patello-femoral (P-F), and medial and lateral tibio-femoral (T-F,med and T-F,lat).

4.4. Discussion

The repeatability of the physical activity simulator developed in this project was found to be similar to that of existing technologies, while the contact response, obtained by successfully implementing this system along with other tools and methodologies, registered a mix of high repeatability and variability throughout gait. In this section, we first present repeated measures outcomes (1st input, then response), followed by practical implications of these findings.

The MR creep rig consistently delivers repeatable compressive and shearing forces, which further impact bending moments' repeatability, as it was found that only some portion of loading repeatability can be controlled, while other aspects also depend on subject variability. Bending moment magnitudes depend on both compressive force and its offset, while moment directions only depend on offset, which might be purposely set via the r-θ stage or be inadvertently influenced by knee flexion. Moments parallel to the abduction/adduction axis applied to the tibia are expected to be more repeatable than moments applied parallel to the flexion/extension axis (also repeatable under certain conditions). For the first case, moment repeatability only depends on that of the compressive force, since the compressive piston r-θ position and all muscle guides (five mobile guides with eight DOFs tot) were held fixed between repeated trials (for which their SDs are all zero and thus only reported in Appendix A4.3.1). For the second case, it may seem this moment only depends on the large axial compression forces (since the moment arm seems to be held constant); however, additional moment arm offsets (which varied between trials) develop due to flexion variability. Hence, a portion of the knee input loading (and its repeatability) are influenced by the joint's mechanical response (and its repeatability). Nevertheless, repeated measurements further showed that the loading device precision (for axial compression and shear forces) is in the same order of magnitude as other existing loading simulators (0.23 to 6.96 CV% for axial compression and 7.72 to 50.9 CV% for shear forces)[12,92,103,109]. Interestingly, knee flexion repeatability is close to intra-subject healthy normal variability (2.7º SD)[50] and variance of similar experimental setups (0.71 to 1.26º SD)[92,111], further evidencing simulation realism.

Regarding the high repeatability in knee load response, it is surprising that certain contact parameters (e.g., contact area, and centers of geometry and pressure), which depend on the geometry of large deformations and specimen variability, remain fairly consistent over repeated

trials. It is not that surprising, however, that centroids are close to (yet remain different from) centers of pressure, as seen previously in other studies[194], despite the uneven contact areas and pressure distributions (Appendix A4.7). Because of the way contact areas are defined (based on active sensor cells), the spatial domains of contact areas and pressure distributions are very similar, and any differences between them would be attributed to the pressure weighting in CP. However, it is surprising that the repeatability in C and CP is that high, when repeatability of the heterogeneous pressure distributions was considerably low at times, and when pressure sensors' SNR was lower under small loads (causing C and CP to fluctuate excessively and preventing steady-state stabilization, especially under uniform distributed loads).

As a result of these input and response behaviours, certain gait characteristics are more repeatable than others in this type of experimental simulation. The most repeatable loading parameters include compressive and shearing forces, specimen flexion and abduction/adduction moment, while the flexion/extension moment repeatability is lower due to specimen variability. In terms of response, contact areas, centers of geometry and centers of pressure seem more forgiving to variations in applied loading, while special care should be taken when measuring and interpreting contact forces and pressures (whose magnitudes may be larger than reported in this study, as explained in Appendix A4.7), which were found to be very sensitive to loading. Lastly, in this experimental simulation, the H-S, T-O* and F-F configurations are more repeatable than F-E as per input loading (in terms of the combined loading as a whole), while T-O* and F-F are more repeatable with respect to the overall intra-articular contact response.

4.5. Conclusion

In this study, we showed experimentally how knee soft tissues could deform throughout walking under valgum influence, by simulating different gait instants and measuring applied loads and contact responses. These experimental tests were verified against repeated testing, showcasing high repeatability relative to current ex-vivo setups; therefore, providing a unique opportunity for experimentally studying knees (or other joints) in different conditions. Results further showed there seems to be an interdependence between loading input and response repeatability, for which certain parameters and simulated gait configurations are more repeatable than others.

5. Study II: Are loading-induced changes in knee cartilage morphology related to T_2 relaxation times?

5.1. Introduction

Certain injuries, diseases and MSK conditions specifically target knee soft tissues, whose condition may be tracked non-invasively from early stages by means of qMRI[10,11]. Considerable preliminary research has been conducted to find associations between qMRI parameters (such as T_2 relaxation), biochemical content and mechanical behaviour[14,15,195-197], some studies ultimately aiming to link cartilage health to their complex mechanical response[167,182], as well as understanding the relations between tissue- and joint-level biomechanics (Figure 5-1). However, these preliminary studies have been carried out at the tissue level (either via explant or indentation testing)[170-17414,186-190], ignoring what would happen to such associations in full joints under true physiologic loading. The logical hypothesis would be that if qMRI can be used for tracking mechanical response at the tissue level, it should also extend to predicting the entire knee's complex intra-articular response (including small and large deformations). Therefore, we must ask the research question: Can T_2 relaxation time (widely used qMRI metric with clinical potential) predict deformation behaviour in axially loaded cadaver knee specimens? Hence, the purpose of this preliminary study was to determine if there were T_2-deformation associations in cartilages of full-joint human cadaver knees under physiologically relevant loading conditions.

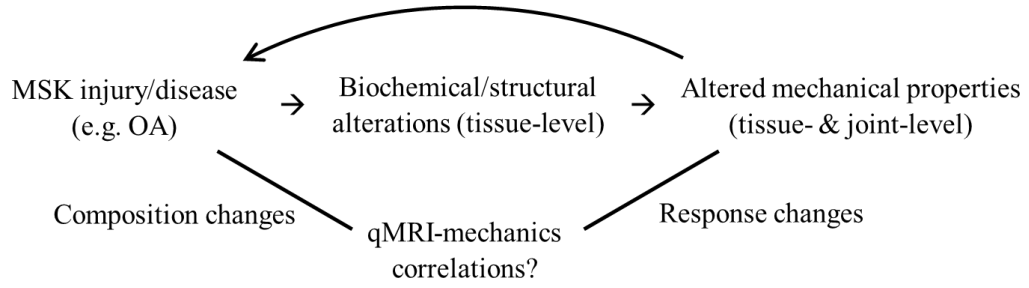

Figure 5-1: Simplified knee pathologies model & study motivation

5.2. Methods

5.2.1. Study overview

Six fresh-frozen knees were prepared and scanned in a MR scanner in unloaded and axially loaded states by means of a displacement-controlled rig (Figure 5-2). These images were processed (segmentation, registration) to estimate mechanical (cartilage thickness, displacement and engineering strain) and qMRI (T_2 times, change in T_2 times and normalized change in T_2 time) parameters across key load bearing sites in the tibial and patellar cartilage, via a custom algorithm, in order to determine if there were any correlations between analogous deformation-T_2 relaxation metrics. To evaluate these potential associations, the following resources were required:

- Specimens: 6 human knees;
- Lab (ENGR 2C50) equipment: MR relaxation (displacement-control) rig [different from the (load-control) rig used in chapters 3 and 4], MRI-safe load cell and DAQ system;
- Imaging-related resources: 3T MRI scanner (MAGNETOM Skyra, Siemens Healthineers, Erlangen, Germany), image processing software (Analyze14, Analyze Direct, Overland Park, USA), and qMRI-mechanics algorithm.

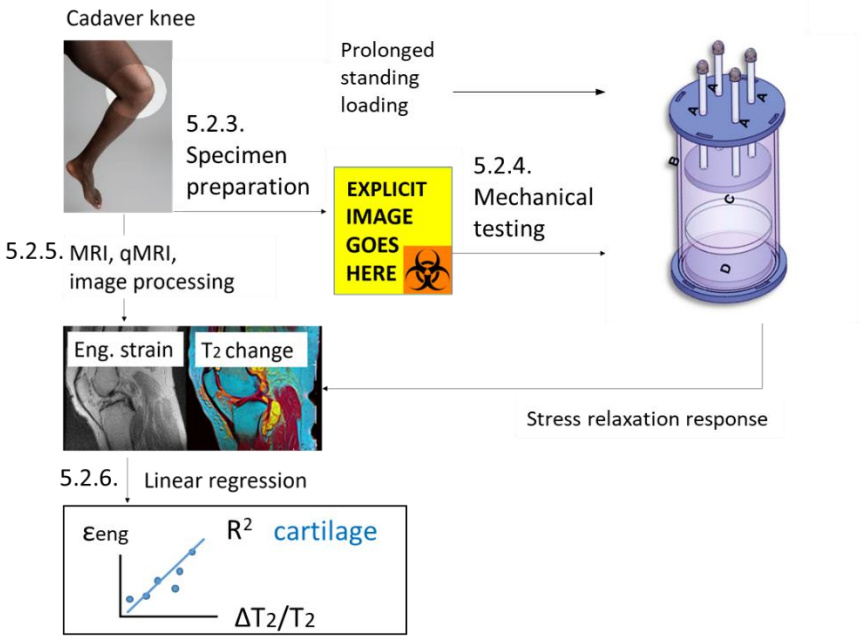

Figure 5-2: Study II diagram: Experimental pipeline for evaluating associations between deformation & T_2. Adapted from Wikimedia Commons[18,20,21].

5.2.2. Study scope

5.2.2.1. Tissues, regions & sites of interest

Tibial and patellar cartilage were selected for representing the T-F and P-F joints. Femoral cartilage was excluded, due to its relatively higher stiffness (and resulting much smaller deformations, which require higher image resolution for analysis[12,13,16,47]). Key load bearing regions (Figure 5-3) were selected for measuring qMRI and deformation characteristics. To ensure repeatability, these sites of interest were identified in images according to predefined guidelines (Appendix A1.1).

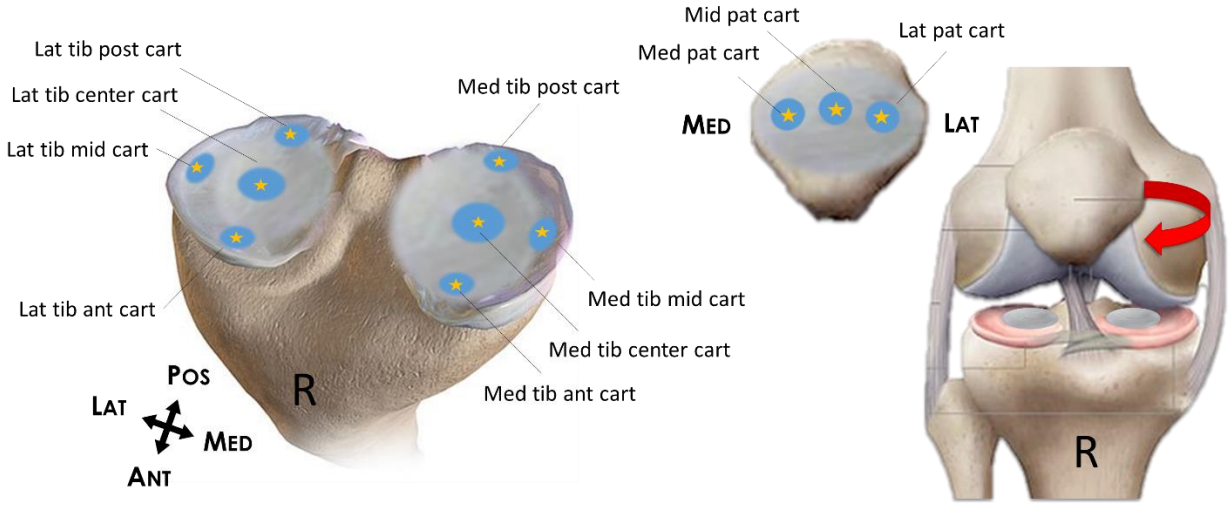

Figure 5-3: Key load bearing regions in cartilages of interest (probing sites marked with a star). Adapted from Wikimedia Commons[198,199].

5.2.3. Specimens & preparation

Six fresh frozen, healthy specimens without history of MSK disorders or surgery (Table 5-1) were tested, for which institutional ethics approval was obtained (Appendix A1). Each of these knees [AVG ± SD: (687 ± 76)N BW, (1.63 ± 0.08)m tall, (70 ± 9)years old, 50% females/males, 50% left/right knees, Science Care, Inc., Phoenix, AZ] were prepared according to specific procedures (removing tissues to expose and pot bone ends, while keeping the knee capsule intact) for full-joint stress relaxation testing. Knees were prepared by several different researchers (including the author).

Table 5-1: Specimen bank for study II

Specimen ID	Left/right	Sex	Age	Height [m]	Body weight [N]
K01	L	M	72	1.73	667
K02	R	M	56	1.73	823
K03	R	M	67	1.60	623
K04	R	F	82	1.63	623
K05	L	F	67	1.57	667
K06	L	F	78	1.55	721
AVG±SD:			70±9	1.63±0.08	687±76

5.2.4. Mechanical testing

A custom MRI-safe displacement-controlled rig (different from the load-control rig developed in this thesis project) was used to compress ex-vivo knees, which were imaged inside a 3T MR scanner (MAGNETOM Skyra, Siemens Healthineers, Erlangen, Germany) in unloaded and loaded conditions (Figure 5-4). During these tests, carried out by a fellow researcher, fully extended knees were compressed in stress-relaxation (≤1BW peak, ~0.5 to 0.75BW at steady state), simulating prolonged standing, for which loading concentrated on the T-F compartments while leaving the P-F joint unloaded (which is not necessarily true during standing).

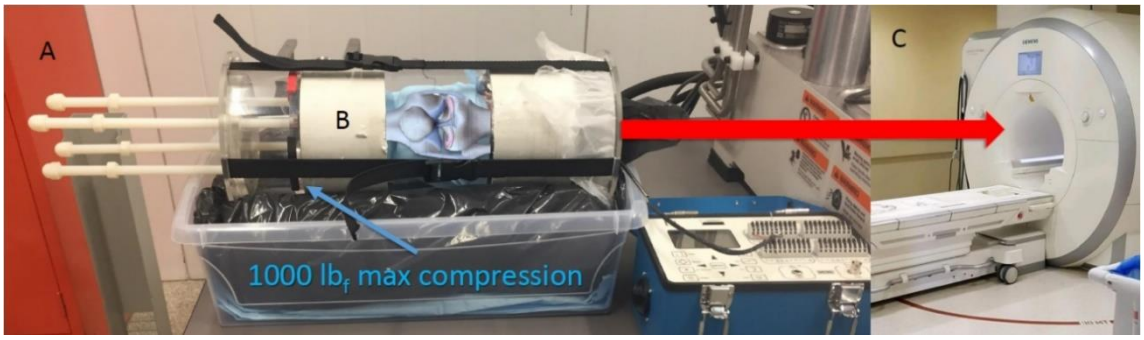

Figure 5-4: Mechanical testing & imaging setup: A. MR relaxation rig, B. Potted cadaver specimen (with superimposed knee illustration), C. 3T MR scanner. Images courtesy of Madeline Martel and Chelsey Thorson, and adapted from Wikimedia Commons[199].

This was achieved by placing the potted specimen inside an acrylic cylinder [1.5ft (457mm) long, Ø7in (178mm) outer, Ø6.5in (165mm) inner] between two rigid disks, to apply a uniform displacement to bone ends, prior to closing the rig by tying low-stretch straps. Forces were recorded with an MRI-safe load cell placed adjacent to the bottom disk, while the other disk was displaced by tightening nuts on four long threaded rods. Hence, in these tests, applied loading

was not only limited by the structural integrity of the rig [max 1 kip (4.45 kN)] but also by the non-ferromagnetic load cell rating [max 0.250 kip (1.11 kN)].

5.2.4.1. Experimental loading protocols

To acquire the unloaded scans, each knee was placed in the rig without tightening the bolts. After this, the knee was loaded by the bolts in preparation for imaging the loaded state. Due to the viscoelastic behaviour of cartilage, load decreased over time when holding the displacement constant, which would result in motion in the image. Hence, the loaded images were not acquired until equilibrium at 0.5BW was achieved (after ~ 110 min). This was verified by obtaining five coronal T_1 weighted images every 10 minutes and creating a subtraction image from the previous time frame. Once there was little to no anatomical features in the subtraction image (i.e. essentially a noise-only image) the loaded data acquisition commenced.

5.2.5. Imaging & processing

To measure mechanical deformations and characterize tissue integrity, morphologic and quantitative image volumes were acquired for each loading configuration at steady state using a Siemens Body 18 Flex Coil wrapping the rig, as described in the testing protocols (Appendix A5.3). This task was conducted by a fellow MRI researcher/developer.

5.2.5.1. Imaging sequences (data acquisition)

Morphology: qDESS images [160x160mm^2 FOV, 256x256 matrix (0.625x0.625 mm^2 planar resolution), 3mm slice thickness, 36 slices, 22 ms TR, 6 and 38 ms TE, diffusion gradient 31.32 mT/m·ms] were acquired for all knees prior to loading, and after reaching stress relaxation equilibrium. To evaluate tissue morphology, the 1st echo (with a mixture of T_1 and T_2 contrast) was used.

T_2 relaxation time maps: Data for T_2 relaxation time mapping were obtained for both loading conditions (unloaded and loaded) using a product multi-echo spin echo sequence at five different echo times [160x160mm^2 FOV, 384x384 matrix, (0.417x0.417mm^2 planar resolution), 3mm slice thickness, 31 slices, 2700 ms TR, 13.8, 27.6, 41.4, 55.2, 69.0 ms TE]. T_2 relaxation maps were obtained using the manufacturer's built-in T_2 relaxation mapping post-processing tool (a standard mono-exponential fitting approach).

5.2.5.2. Pre-processing

Segmentation

Tibial and patellar cartilage were manually segmented (Analyze14.0, AnalyzeDirect, Overland Park, KS), for each specimen (loads 0 and 1) in a slice-by-slice manner, from qDESS sagittal acquired images (directly obtained from the MR scanner). Segmentation was carried out by a fellow researcher and checked by an expert with 20 years of segmentation experience.

Image Resampling

Acquired morphology was resampled (re-oriented + re-sliced) via a 3D multi-planar reformation algorithm (Horos3.3.6, Horos Project, www.horosproject.org) along anatomical planes (coronal, sagittal, transverse) for locating key sites in load bearing regions consistently according to predefined guidelines. This operation changed the resolution for qDESS volumes. All planar resolutions for each knee and resampled images were slightly different, due to small rotation differences, which altered the FOV, while the planar matrix size remained the same (719x777 for sagittal resampling, and 720x388 for coronal and transverse resampling). Resampled slice thickness was set to 1mm for all specimens to prevent loss of resolution due to this processing step (1mm was the finest slice spacing Horos allowed for the interpolation used), while the slice size was large enough to contain the original volume acquired but in the desired orientation.

Registration

A semi-automatic mutual information 3D registration protocol (Analyze14.0, AnalyzeDirect, Overland Park, KS) was employed to align cartilage masks and T_2 relaxation time maps with respect to resampled qDESS images (Figure 5-5). Accurately registering binary masks (Figure 5-5A) required a previous "dummy" registration step (converting morphological images into their resampled version via the same registration algorithm to obtain the transformation matrix exclusively), unlike with T_2 relaxation images, which had substantial spatial information to conduct this automatic registration solely based on the resampled morphology target (Figure 5-5B), This apparently redundant step was necessary because the geometric information in binary masks (just the patellar or tibial cartilages) was not enough to obtain good results by applying the registration algorithm directly. This overall process was conducted for each

specimen's loading state (unloaded and loaded), totaling four actual (and two dummy) registrations per specimen.

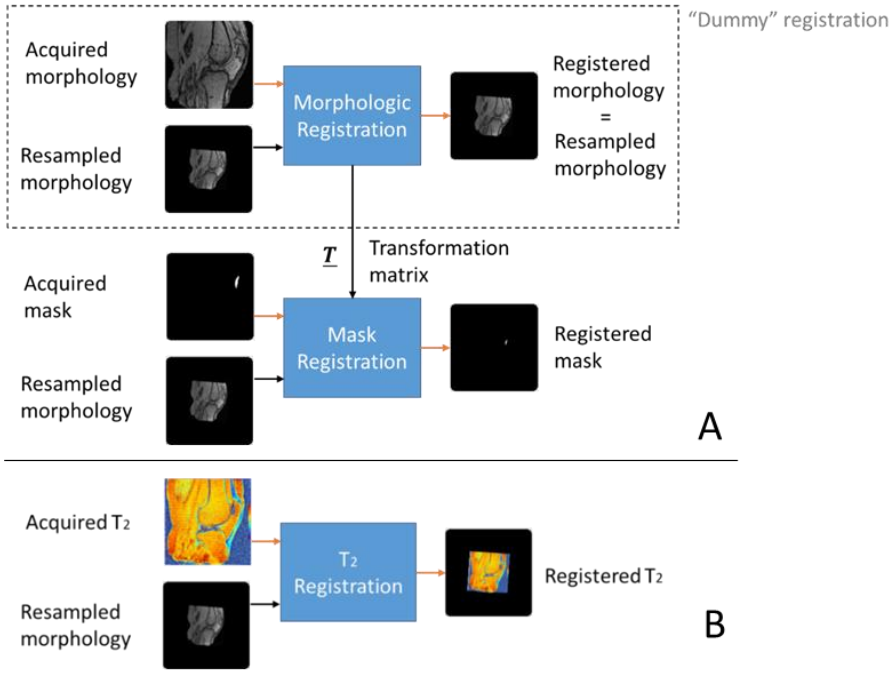

Figure 5-5: Registration flowcharts for morphologic masks (A) & T_2 relaxation maps (B); all conducted via mutual information 3D registration (avoiding joint coordinate axes setup later on)

5.2.5.3. qMRI-mechanics algorithm (data processing)

This study explored the potential of T_2 relaxation time maps to measure deformations in 2D, before assessing its performance in 3D. Hence, a custom semi-automatic algorithm was developed (MATLAB, the Mathworks, Natick, MA) to carry out the following steps (Figure 5-6) for patellar and tibial cartilage of all specimens in unloaded and loaded configurations:

1. Create mask contour, *s*, delineating tissue of interest.
2. Create boundary's unit normal directions field, $\hat{n}(s)$.
3. Find boundary pixel closest to user input (ideally coincides with mask boundary) via k-nearest neighbour search.
4. Sample the average T_2 relaxation time through a line across the mask (along the normal direction) and measure its distance (cartilage thickness, t).

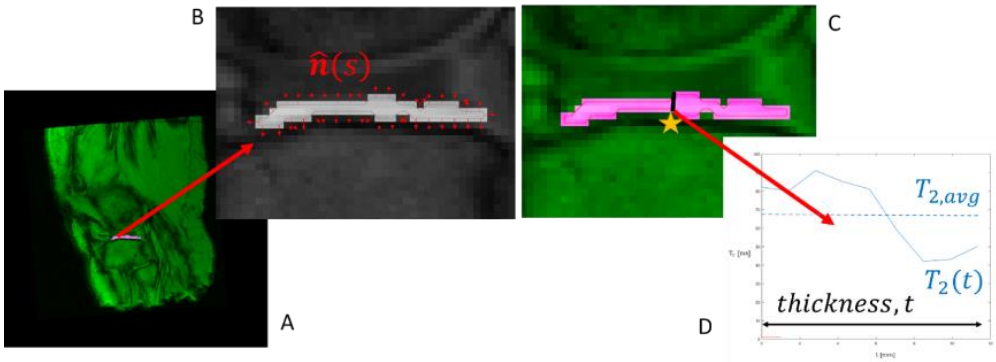

Figure 5-6: T_2 relaxation time and thickness sampling: Sagittal slice with mask overlaid (A), mask contour with unit normals field (B), probing site (C) and its T_2 time depth distribution (D)

5.2.5.4. Post-processing

Thresholding

Voxel exclusion (set to remove T_2 times > 150ms for all specimens[200,201]) was used to filter out unusually bright pixels present especially near boundaries but also within tissues, not representative of cartilage tissue properties (likely due to partial voluming of adjacent fluid). For the qMRI-mechanics custom program, thresholding was conducted at this stage. Aside from this, no other data was excluded.

Analogous T_2 relaxation & deformation metrics

To characterize the qMRI-related and mechanical aspects of knee loading, the following parameters were computed based on soft tissues' T_2 relaxation time and thickness measurements (Table 5-2):

Table 5-2: T_2 relaxation and deformation variable definitions

Metric	Definition	Mathematical expression
Original (initial) thickness	Undeformed cartilage thickness	$(t)_0$
Deformed (final) thickness	Deformed cartilage thickness	$(t)_f$
Thickness change	Loading-induced thickness normal displacement	$\Delta t = \delta = (t)_f - (t)_0$
Nominal engineering strain	Normalized thickness change, normal component of the strain tensor (for small deformations)	$\varepsilon_{eng} = \frac{\Delta t}{(t)_0} = \lambda - 1, \lambda = \frac{(t)_f}{(t)_0}$
Original tissue's (initial) T_2 relaxation time	Spatial average of T_2 relaxation signal across the undeformed cartilage thickness (normal to the subchondral surface)	$(T_2)_0 = \frac{1}{(t)_0}\int_{(t)_0} T_2(t)dt$
Deformed tissue's (final) T_2 relaxation time	Spatial average of T_2 relaxation signal across the deformed cartilage thickness (normal to the subchondral surface)	$(T_2)_f = \frac{1}{(t)_f}\int_{(t)_f} T_2(t)dt$
T_2 change	Loading-induced change in average T_2 relaxation signal	$\Delta T_2 = (T_2)_f - (T_2)_0$
T_2 strain	Normalized T_2 change	$\varepsilon_{T2} \equiv \frac{\Delta T_2}{(T_2)_0} = \lambda_{T2} - 1, \lambda_{T2} \equiv \frac{(T_2)_f}{(T_2)_0}$

5.2.6. Statistical analysis: qMRI-mechanics correlations (exploratory)

Analogous pairs of deformation and T_2 relaxation time metrics were plotted against each other, yielding four plots used to evaluate associations between those variables: Unloaded thickness vs. corresponding T_2 time, deformed thickness vs. corresponding T_2 time, thickness change vs. T_2 change, and engineering strain vs. T_2 strain. For each of these scatter plots, correlations were assessed separately for patellar and tibial cartilage, due to their different composition, loading and function. While it remains unknown whether deformation produces certain T_2 relaxation signal change or tissue integrity (characterized by T_2 relaxation time) dictates the amount of deformation, mechanical metrics were set as independent variables and T_2 relaxation variables as dependent, since different loads were applied in these tests and the T_2 relaxation response measured.

Pearson product-moment correlation coefficient, *r*, was used to assess association strength only for tibial cartilage (only correlations with $n > 30$ data points after thresholding), while Spearman's rank correlation coefficient, r_s, was used for patellar and tibial cartilages ($n < 30$). These correlations were determined significant if $p < 0.05$ by means of a 2-tailed *t* test for significance (H_0: No correlation; H_1: Either positive or negative correlation) using the statistic

$$t = \frac{|\rho|}{\sqrt{\frac{1-\rho^2}{DF}}}, \tag{5-1}$$

where $DF = n - 2$, and $\rho = r$ or r_s.[202] Correlation strength was classified as very strong, strong, moderate, weak or very weak depending on the magnitude of the correlation coefficient (Table 5-3). Furthermore, variables could be either positively or negatively correlated, as indicated by the positive or negative sign of the correlation coefficient.

Table 5-3: Adopted correlations strength ranges (positive/negative sign of correlation coefficient denotes correlation direction)[203]

Correlation coefficient magnitude range	Correlation strength
$0.80 < \|\rho\| \leq 1.00$	Very strong
$0.60 < \|\rho\| \leq 0.80$	Strong
$0.40 < \|\rho\| \leq 0.60$	Moderate
$0.20 < \|\rho\| \leq 0.40$	Weak
$0.00 < \|\rho\| \leq 0.20$	Very weak

As a preliminary assessment of the appropriateness of parametric or non-parametric methods, the sample distributions of all variables in Table 5-2 (for loaded and unloaded T-F and P-F joints) were examined for normality (1st by looking at histograms with $\sqrt{n}$ bins, later via more advanced methods, as described below) and these variables plotted against each other. Upon inspection of each of the scatter plots clouds for presence of any nontrivial linear trends, potential nonlinear trends were found among initial metrics, changes and strains. Logarithmic transformations allowed further exanimating this type of trends, but their domain was limited to positive real numbers. Hence, these transformations were only applied to deformation and T_2 relaxation time magnitudes (rather than to signed metrics). Thus, for each of the four scatter plots (deformation vs. corresponding T_2 relaxation metrics), there were four combinations of transformed scatter plots in addition to the original plot comparing signed metrics (Appendix A5.5): Abscissa vs. ordinate magnitudes, logarithm of abscissa magnitude vs. ordinate magnitude, abscissa magnitude vs. logarithm of ordinate magnitude, and logarithm of abscissa magnitude vs. logarithm of ordinate magnitude. Least squares fitting was conducted only for potential correlations determined to be statistically significant. Correlation strength, significance and normality assessments were conducted for all transformed variables to verify that associations were meaningful, and assumptions for linear regressions had been met, described by the following criteria[202,204,205] (Appendix A5.5.2):

- Abscissa normality (histogram, mean, variance, skewness, kurtosis, median, min, max)
- Ordinate normality (histogram, mean, variance, skewness, kurtosis, median, min, max)
- Residuals normality (Q-Q plot, histogram, mean, variance, skewness, kurtosis, median, min, max)
- Residuals homoscedasticity (residuals plot)
- Linear trend between abscissa and ordinate mean
- Significance (H_0: No correlation; H_1: Either positive or negative correlation)
- Correlation strength (r or r_s)

5.3. Results

5.3.1. Estimated knee deformation & T_2 relaxation response during prolonged standing

By implementing the testing and imaging protocols, the acquired morphologic qDESS and quantitative T_2 relaxation time images showed that, in general, cartilage is thicker in the unloaded configuration compared to the loaded state (Table 5-4), except for the medial patellar site, and the lateral middle, medial and lateral posterior, and medial central tibial sites. On the other hand, T_2 time is generally longer in the unloaded state compared to the loaded tissue, except for the medial and middle patellar sites, and the medial posterior and lateral central tibial sites, while the medial central tibial cartilage T_2 time almost remains constant. As such, despite the high inter-subject variation, the distribution of thickness resembles the majority of the T_2 time distribution over the probing sites (Figure 0-38).

Table 5-4: Thickness and T_2 relaxation values for unloaded & loaded cartilage sites of all 6 knees [inter-subject AVG ± SD (100%·SD/AVG)]; only uncorrupted measurements shown

	Initial metrics (unloaded, 0%BW)			**Final metrics (loaded, 50%BW)**		
Site	$(t)_0$ [mm]	$(T_2)_0$ [ms]	n	$(t)_f$ [mm]	$(T_2)_f$ [ms]	n
Pat cart (mid)	3.22 ± 0.97 (30.18%)	55.4 ± 9.6 (17.29%)	4	2.35 ± 1.50 (63.97%)	64.8 ± 7.7 (11.89%)	6
Pat cart (med)	1.58 ± 0.60 (37.80%)	60.4 ± 9.7 (16.09%)	6	1.84 ± 0.81 (43.75%)	79.5 ± 27.9 (35.16%)	6
Pat cart (lat)	2.71 ± 1.80 (66.33%)	79.9 ± 6.2 (7.81%)	5	2.33 ± 1.29 (55.31%)	72.3 ± 5.4 (7.42%)	5
Tib ant cart (med)	1.27 ± 0.76 (60.27%)	44.2 ± 13.1 (29.57%)	5	1.16 ± 0.33 (28.15%)	37.9 ± 9.8 (25.79%)	6
Tib ant cart (lat)	1.31 ± 0.70 (53.21%)	45.0 ± 12.7 (28.31%)	4	0.88 ± 0.29 (33.15%)	41.9 ± 13.9 (33.24%)	5
Tib mid cart (med)	1.13 ± 0.39 (34.71%)	53.7 ± 5.9 (11.03%)	5	0.91 ± 0.38 (41.90%)	33.6 ± 3.8 (11.31%)	3
Tib mid cart (lat)	1.15 ± 0.42 (36.71%)	54.4 ± 5.1 (9.31%)	6	1.35 ± 0.72 (53.39%)	49.2 ± 12.4 (25.19%)	5
Tib pos cart (med)	1.20 ± 0.52 (42.95%)	55.3 ± 7.5 (13.61%)	6	1.33 ± 1.00 (75.04%)	64.4 ± 34.1 (52.97%)	5
Tib pos cart (lat)	1.78 ± 1.35 (75.97%)	75.9 ± 59.5 (78.44%)	2	2.73 ± 1.90 (69.50%)	49.4 ± 5.0 (10.10%)	3
Tib central cart (med)	2.05 ± 0.70 (34.21%)	42.7 ± 12.2 (28.70%)	5	1.17 ± 0.44 (38.07%)	42.7 ± 12.4 (29.13%)	5
Tib central cart (lat)	3.42 ± 0 (0%)	22.0 ± 0 (0%)	1	2.81 ± 1.43 (50.97%)	37.6 ± 9.4 (24.93%)	5

The resulting absolute and normalized changes ("strains") in thickness and T_2 relaxation due to loading (Table 5-5) show the same trend (Appendix A5.5.1), in average (fewer data remaining after thresholding), as unloaded and loaded thickness and T_2 relaxation time for all sites, except for the T_2 time at the lateral anterior tibial cartilage. Opposite change directions are also found only between thickness displacement and engineering strain for the lateral patellar, and medial and lateral anterior tibial cartilage sites. Additionally, inter-subject variance further amplifies for absolute and normalized changes for both deformation and qMRI metrics.

Table 5-5: Changes in thickness and T_2 relaxation time due to loading for different cartilage sites [inter-subject AVG ± SD (100%·SD/AVG)]; only including data after thresholding

Site	Δt [mm]	ΔT2 [ms]	ε_eng [m/m]	ε_T2 [s/s]	n
Pat cart (mid)	-0.07 ± 0.50 (700.08%)	8.1 ± 13.6 (167.60%)	-0.02 ± 0.2 (976.91%)	0.18 ± 0.32 (174.16%)	4
Pat cart (med)	0.26 ± 1.01 (391.53%)	19.0 ± 26.0 (136.34%)	0.3 ± 0.7 (206.63%)	0.32 ± 0.39 (123.10%)	6
Pat cart (lat)	-0.38 ± 0.96 (252.05%)	-7.5 ± 8.7 (114.88%)	0.1 ± 0.7 (1289.11%)	-0.09 ± 0.10 (114.52%)	5
Ant tib cart (med)	-0.03 ± 0.68 (2246.91%)	-4.8 ± 16.2 (336.16%)	0.2 ± 0.5 (313.97%)	-0.05 ± 0.30 (645.47%)	5
Ant tib cart (lat)	-0.29 ± 1.05 (364.43%)	5.0 ± 21.5 (427.55%)	0.1 ± 0.8 (1565.09%)	0.17 ± 0.53 (311.31%)	3
Mid tib cart (med)	-0.31 ± 0.36 (116.17%)	-20.3 ± 1.8 (8.67%)	-0.2 ± 0.3 (115.63%)	-0.38 ± 0.01 (2.06%)	3
Mid tib cart (lat)	0.14 ± 1.12 (824.42%)	-5.4 ± 15.6 (289.67%)	0.4 ± 1.2 (278.21%)	-0.09 ± 0.27 (316.26%)	5
Pos tib cart (med)	0.24 ± 0.71 (296.95%)	9.5 ± 36.8 (388.42%)	0.2 ± 0.5 (307.19%)	0.21 ± 0.72 (348.11%)	5
Pos tib cart (lat)	3.65 ± 0 (0%)	-70.2 ± 0 (0%)	4.4 ± 0 (0%)	-0.60 ± 0 (0%)	1
Central tib cart (med)	-0.88 ± 0.74 (84.29%)	0.02 ± 14.3 (86074.39%)	-0.4 ± 0.3 (68.93%)	0.04 ± 0.31 (717.89%)	5
Central tib cart (lat)	-0.42 ± 0 (0%)	5.6 ± 0 (0%)	-0.1 ± 0 (0%)	0.26 ± 0 (0%)	1

5.3.2. T_2-deformation correlations (exploratory)

A moderate negative correlation ($r = -0.402$, $p = 0.019$) was found between thickness and T_2 relaxation time in unloaded tibial cartilage (Figure 5-7). No other correlations were found among other variables compared in this study. In search for presence of any other (stronger) associations among initial metrics, logarithmic transformations were conducted (Figure 5-8); however, correlation strength did not vary much ($r = -0.402$, -0.351, -0.467 and -0.403 for different transformation combinations) and neither did p-values. Whereas outlier or influence point removal (Appendix A5.5.3) changed correlation strength ($r = -0.437$, $p = 0.011$) and equations, this did not alter the overall results and conclusions, i.e. only initial cartilage thickness and corresponding T_2 relaxation signal were correlated moderately.

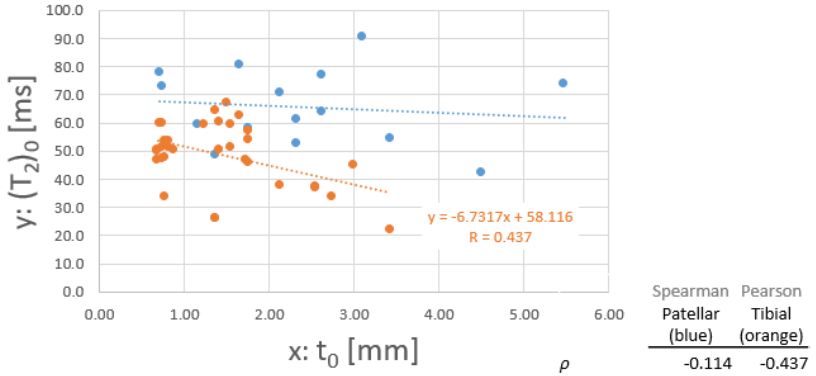

	Spearman Patellar (blue)	Pearson Tibial (orange)
ρ	-0.114	-0.437
p-value	0.685	**0.011**
n	15	33

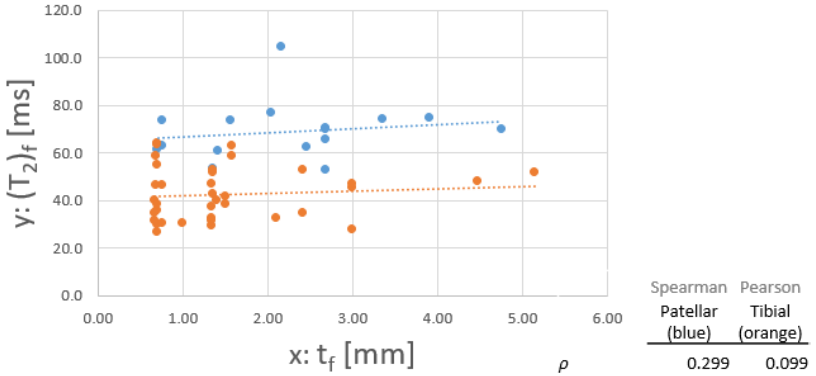

	Spearman Patellar (blue)	Pearson Tibial (orange)
ρ	0.299	0.099
p-value	0.260	0.567
n	16	36

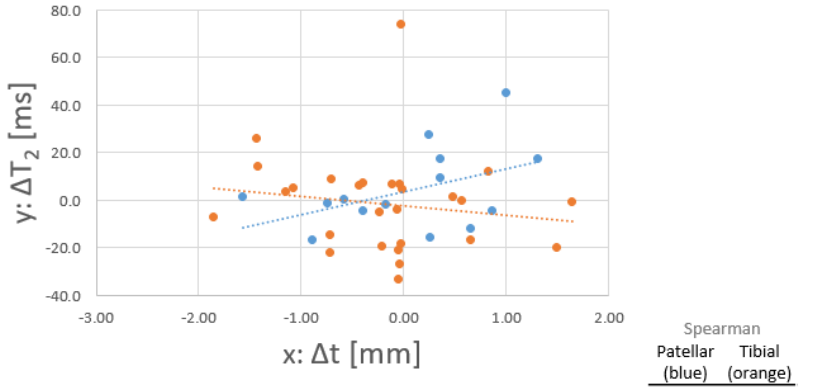

	Spearman Patellar (blue)	Tibial (orange)
r_s	0.341	-0.188
p-value	0.233	0.347
n	14	27

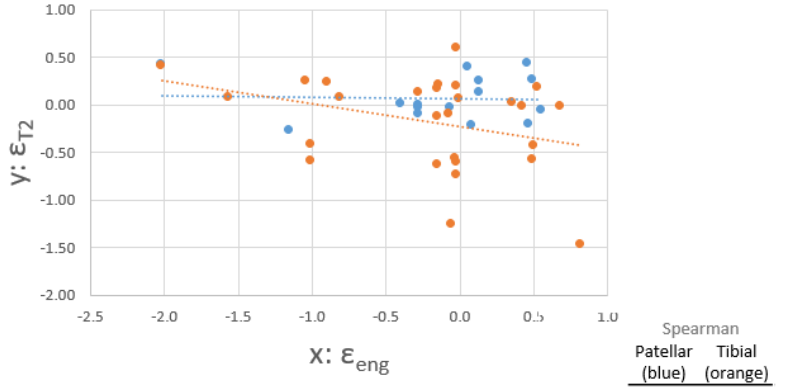

	Spearman Patellar (blue)	Tibial (orange)
r_s	0.091	-0.325
p-value	0.746	0.098
n	15	27

Figure 5-7: Deformation vs. T_2 relaxation metrics for patellar (blue) and tibial (orange) cartilages after outlier/influence point removal; regression equation only for significant (bolded p-values) potential correlations

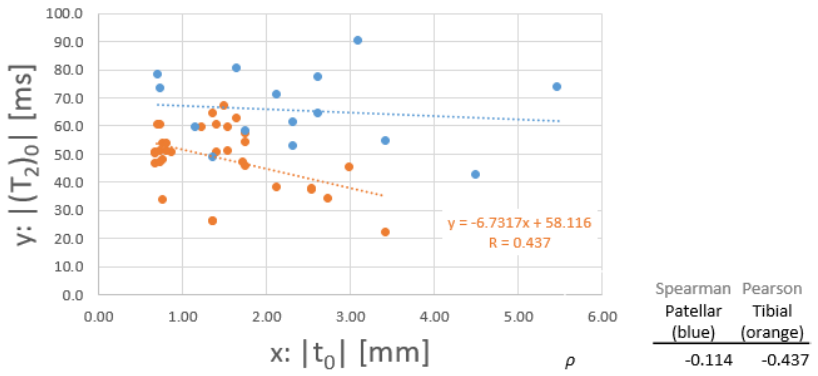

Spearman	Patellar (blue)	Tibial (orange)
ρ	-0.114	-0.437
p-value	0.685	**0.011**
n	15	33

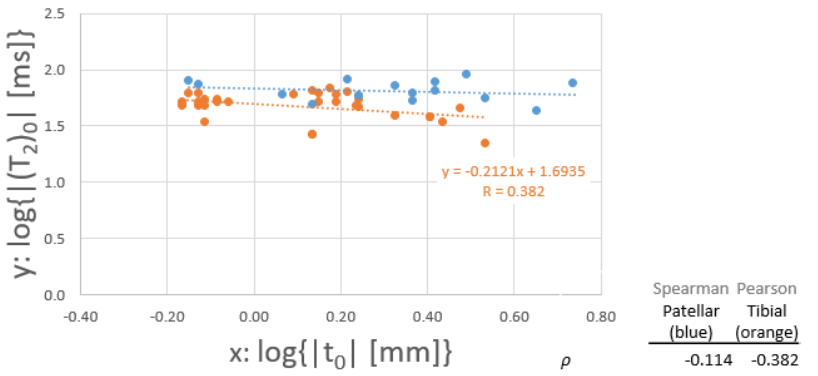

Spearman	Patellar (blue)	Tibial (orange)
ρ	-0.114	-0.382
p-value	0.685	**0.028**
n	15	33

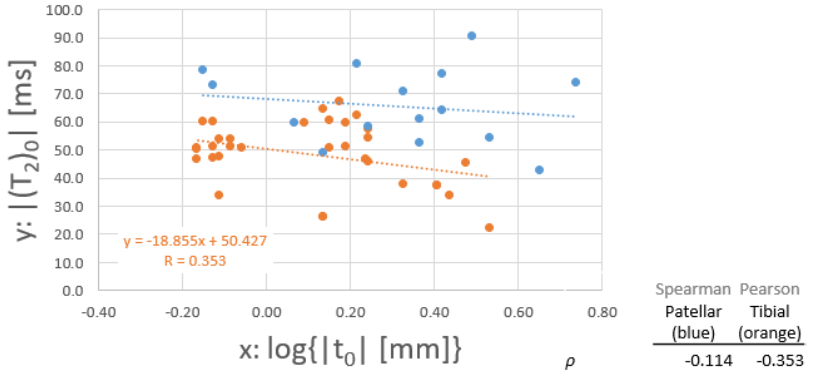

Spearman	Patellar (blue)	Tibial (orange)
ρ	-0.114	-0.353
p-value	0.685	**0.044**
n	15	33

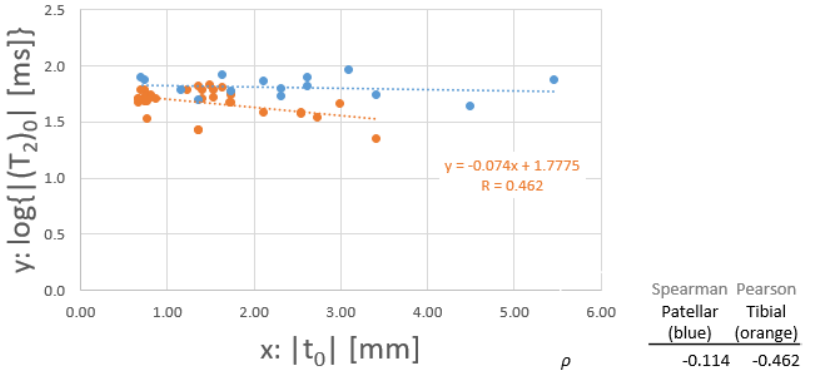

Spearman	Patellar (blue)	Tibial (orange)
ρ	-0.114	-0.462
p-value	0.685	**0.007**
n	15	33

Figure 5-8: Initial thickness vs. T_2 relaxation time, after logarithmic transformations, for patellar (blue) and tibial (orange) cartilages after outlier/influence point removal; regression equation only for significant (bolded p-values) potential correlation

5.4. Discussion

5.4.1. Knee deformation and T_2 relaxation response to loading

Cartilage responses fell within reasonable healthy ranges, demonstrating physiologic realism of the experimental simulation conducted, as evidenced by generally higher thickness and T_2 times for the unloaded state relative to the loaded case. For instance, participants' unloaded tibial cartilages (AVG±SD) have been previously measured to be 1.35 to 1.71mm thick[184], whereas, for a standing individual (~0.5BW compression per knee), cartilage was as fine as 1mm and as thick as 2.5mm[47,163]. Published in-vivo measurements exhibit some inter-subject variation but their average magnitudes are smaller and mostly compressive for the same loading conditions as in this study. When averaging over the entire cartilages, engineering strains are -15.8 to -1.8%[47,180,181,184], whereas these are -5.9 to 1.8% when inspecting central, anterior, middle and posterior sub-compartments[180,183]. Even when examining the minimum principal, maximum principal and shearing strain tensor components, their respective peak values only reach −8.1, 9.5 and 8.5% over entire cartilages[182]. Only one study[47] was found to measure strains as large as in study II for a healthy standing participant (-39 and -30% maximum for medial and lateral compartments).

T_2 relaxation measurements are still realistic in this ex-vivo study but somewhat higher than those reported in the literature. Previous in-vivo healthy studies have reported 30.16 to 30.38ms for bulk cartilages without bearing loading, and 29.30 to 29.94ms upon the application of 50%BW[161]. On the other hand, regional examinations (anterior, middle and posterior sites) yielded 17.7 to 25.3ms for unloaded, and 17.2 to 25.2ms for loaded cases[162]. Alternatively subdividing the cartilage thickness (superficial and deep layers) leads to 31.18 to 47.86ms for unloaded, 29.96 to 43.37ms for loaded (120N)[i] cases[15], which are closer to study II responses, although load conditions are different. In terms of changes, the ample ranges in study II encompass changes measured in the literature, including -2.9 to -1.4% for entire medial and lateral cartilages[161], and -7.6 to -2.2% for anterior, middle and posterior regions[183]. Previous studies also found a mix of positive and negative changes, such as decreasing T_2 in load-bearing

[i] In all these other studies, knees were loaded to 50%BW > 120N compression.

regions and increasing T_2 in adjacent regions[185], and general decreases and decreases respectively in superior and deep layers for both medial and lateral cartilages of healthy and OA populations[184].

Cartilage mechanical and qMRI responses demonstrate that the physiologic standing simulation was an overall realistic representation of this physiologic activity; however, variability is remarkably high, for which we are unsure it could all be attributed to differences between specimens, especially for deformation measures. Unlike this study's large SDs suggest, published healthy inter-subject variability ranges only between 0.27 to 0.57mm for unloaded and loaded thickness[163,184], 7.70 to 14.09% for engineering strain[183,184], 0.9 to 2.8% for true strain components[182], 1.81 to 6.06ms for unloaded and loaded T_2[15,161], and 4.7 to 10.1% for T_2 strain SDs[183]. The substantial variability observed in study II for both cartilage deformation and T_2 relaxation response may however be due to natural variation between individuals, as well as mechanical testing variability, specimen alignment differences and/or image acquisition/processing limits. Due to the nature of viscoelastic relaxation, it is more difficult to consistently achieve the same loaded state (involving high loads) using a displacement-control setup, which may considerably reduce testing repeatability. Specimen misalignment may have also introduced bending moments on the T-F joint, since mechanical axes alignment was not accurately enforced during specimen preparation (Appendix A5.3). As a result, for some but not all specimens, certain regions could have been overloaded and exuding water (potentially registering thickness and T_2 reductions), possibly leaving other load-bearing areas unloaded and absorbing water (potentially registering thickness and T_2 increases). Lastly, imaging thin cartilage and their deformations is challenging (especially at the current resolution), potentially limiting thickness accuracy and associated precision, coincidentally lower than that of T_2 relaxation measurements, which are likely not affected as much by this. Also, site selection and image registration methods have implications on thickness measurements, as discussed later in this chapter.

Therefore, although cartilage thickness and T_2 times generally agree with the literature (corresponding to load bearing under 50%BW), both generally higher in the unloaded state compared to the loaded condition, precision error is too large to trust the magnitude of these changes. These changes are expected from a physical standpoint, since, after compressing the

cartilage for a long time, not only cartilage thickness would decrease in load-bearing regions but also T_2 times (as synovial fluid exudes out of the collagen matrix), once again suggesting that cartilage deformation could be correlated with T_2 changes.

5.4.2. T_2-deformation correlations

In this study, only significant correlations (moderately negative) were found between thickness and T_2 relaxation time in the unloaded tibial cartilages, as suggested by their similar distributions over cartilage sites (Figure 0-38); however, this was not the case for any of the variables influenced by loading (i.e. deformed thickness and T_2 time, thickness and T_2 change, and engineering and T_2 strains). It does make sense that no T_2-deformation associations were found in the patellar cartilage, as this tissue remained relatively unloaded during the entire testing process, but the absence of T-F load response associations and the wide variability ranges (mechanical and qMRI) brings in the question whether study limitations interfere when detecting potential correlations between tissue integrity, composition and mechanical behaviour. Along these lines, Spearman's coefficient almost found a weak negative correlation among engineering and T_2 strains ($p = 0.098$. Figure 5-7), whose significance is the highest among all variables compared according to this coefficient, possibly hiding relationships between strains. Unfortunately, thresholding and outlier/influence point removal reduced sample sizes, for which it was not possible to inspect these correlations via the Pearson coefficient.

The considerably large variability ranges in the mechanical response suggest that loading repeatability may have been low enough that another variable was introduced throughout mechanical testing (i.e. slightly different compression magnitudes), effectively decreasing even further the number of independent measurements at a given load in this study. This further opposes a fundamental principle in multilevel statistical modelling, as more tests (or observations) must be performed per every new independent variable introduced. Hence, since none of these interactions (which could have taken place experimentally) were accounted for, it is no surprise that it was difficult for univariate linear regressions to fit the data, whether it is due to imprecise mechanical testing or imaging limitations. As mentioned earlier, another explanation lies on the measurement of the load response, instead of on the experimental conditions enforcement. For instance, morphologic resolution limits the accuracy of thickness measures, for which most of these were truncated due to round-off and different measurements

binned together as the same, for which many data points seem organized as columns in Figure 5-8. If a single pixel (0.2mm isotropic resolution) represents 20% of thinnest cartilage thickness (~1mm) producing tibial cartilage measurement errors of 4.4% (in average) and 6.7% (max) for one knee[47], then the current resolution (0.625x0.625x3mm^3) is expected to develop errors within the ~20 to ~90% range registered at 0.547x0.547x1.5mm^3 when measuring 1mm thicknesses or ~10% (in average) for 2 or 3mm cartilages[206]. Hence, thicker regions could have been less affected. Also, due to the way sites were defined, the custom algorithm may have probed slightly different locations in the same load-bearing regions in unloaded and loaded states, instead of the same material point. Hence, it would be understandable if the accuracy among changes and strains, as well as their correlations, become affected. However, this limitation should not affect the correspondence between deformed morphology and T_2 times for the loaded case; those associations may be only limited by loading repeatability and morphologic resolution. In light of these implications, it is somewhat remarkable that this preliminary study found a moderate negative T_2-thickness correlation in unloaded tibial cartilages and almost found a correlation association between tibial engineering and T_2 strains, highlighting the strength of this method.

In general, there are relatively few studies that relate qMRI and mechanical responses for human knee cartilages (and a few others looking at other human or animal soft tissues). Some studies in this area examine cartilage thickness changes separately from loading-induced qMRI changes involving full in-vivo knees (at 50% compression)[183,184], while others do aim assessing if or how strongly various mechanical and qMRI metrics are related at the tissue level[14,163,167,170-179]. In these studies, loading effects are evaluated mostly ex vivo (explant unconfined compression or indentation testing, but not full-joint physiologic simulation) for healthy or pathologic conditions, leading to interesting findings. In general, preliminary research has found that local T-F cartilage thickness decreases upon tissue compression, and so do T_2 relaxation times; however, qMRI-mechanics correlations are noticeably diverse, varying from weak to very strong associations[14,170,175,176,178,179,144-146,147]. Among these, one study suggested a potential relation between engineering and T_2 strain magnitudes in canine humeral cartilages via explant stress relaxation. Unfortunately, with such a few data points, no correlation strength assessment was carried out[167]; however, clearly defined trends (close to linear) are observed between these variables, as hinted by study II.

5.4.2.1. Physical interpretation possibilities

Since T_2 relaxation time (and qMRI parameters in general) are affected in different amounts by several factors, such as water content and collagen fiber organization, the inverse T_2-thickness trend found could be due to spatial variations in these factors across the irregular cartilage thickness or other non-compositional reasons. Due to the limited data, however, this section only reports the observations and a few possible explanations supported by literature.

Due to the positive association between T_2 relaxation time and water content, longer T_2 times within thinner cartilage would imply there may be more water per volume compared to the thicker regions. From the positive association between tissue anisotropy and T_2 times, collagen fibers may be organized more tangentially in thinner regions and more randomly in thicker cartilages, especially in intermediate layers. Due to the T_2-thickness correlation strength, if these potential differences in tissue hydration and fiber reinforcement exist between thin and thick cartilage, it is most likely they are simply subtle.

Similar T_2 distributions throughout tissue thickness have been previously observed for unloaded bovine cartilage (patellar)[160,166] and in unloaded and loaded canine cartilage (humeral)[167] explants. Some differences exist (e.g., max T_2 taking place at different cartilage depths) but the overall distributions remain comparable to those measured in study II. Fiber distributions have also been examined in relation to T_2 distributions[160,167], which were shown to change with sample orientation relative to the main magnetic field (due to the magic angle effect) and mechanical loading, suggesting fibers become more random with tissue compression in a study[167].

If the observed T_2 distributions are a result of tissue composition, however, why are these trends not observed in the unloaded patella? Or why would these correlations vanish with externally applied loading, when the structure is the same (although probably exhibiting some load-induced changes)? While it is true that there were fewer patellar data points and applied loading may have varied across specimens, maybe these trends are caused simply by resolution or partial volume artifacts, which change the T_2 values near the boundaries of different tissues. In either case, compositional cause or not, future studies could investigate collagen organization and water content (involving histology sections and component staining across the variable cartilage

thickness) to uncover the meaning of this inverse trend between thickness and T_2 times, since study II seems to be the first aiming to correlate healthy human cartilage (finite, large) deformation to T_2 relaxation in a full-joint, physiologic context.

5.5. Conclusion

Cartilage mechanical and T_2 relaxation responses fell within expected ranges for healthy knees, while exhibiting large inter-subject variability. In general, cartilage were thicker and their T_2 times longer prior to loading them, which agrees with expected synovial fluid transport during compression. Among these measurements, a moderate negative correlation was found between unloaded tibial cartilage thickness and its T_2 time, possibly linked to fiber reinforcement and hydration variation with cartilage thickness. So far, no other statistically significant correlations were found by this study for tibial or patellar cartilages, and logarithmic transformations and outlier/influence point removal did not change these findings. Future research is likely needed to determine whether any other correlations exist and whether the cause behind correlations is in fact compositional in nature. Although this proposed method was tested with T2 relaxation times only, it could be extended to any other qMRI sequence, as results suggest this method may be more general in nature and able to detect composition-structure-function relationships (such as a potential association between T_2 thickness distribution and tibial cartilage composition).

6. Integrated discussion

6.1. Research direction reminder

Aging, injuries, diseases (e.g., OA) and other MSK conditions affect the knee, which is composed of highly anisotropic composites operating in unison under a complex combined loading regime during daily physical activities. To address complications and costs associated with a damaged knee, this whole joint (healthy or pathologic) must be studied under a true physiologically realistic loading scenario, which has not been possible in many cases. qMRI offers a potential non-invasive evaluation of tissue constitution (biochemical content and structure) and function (mechanical properties), which preliminary research has suggested are related. However, few studies have been able to investigate this (often via explant or indentation testing), as research is limited by the lacking MRI-safe testing setups that can place full knees in a physiologically realistic loaded state. As such, links between tissue- and joint-level mechanical behaviour and qMRI response (and their dependence or implications on joint health) remain unclear; those are what this project aimed to uncover. Hence, the overall objective was to develop, evaluate and implement entire systems and methodologies to simulate physical activities ex vivo, while allowing qMRI, to determine how repeatable such a novel methodology is, how physiologic loading affects soft tissue mechanical (e.g., contact mechanics, deformations) and qMRI responses, and how closely (or whether) they are related.

6.2. Key findings overview

In study I, the custom load-control system developed was determined to have moderate to high testing repeatability, comparable among existing loading devices (Appendix A2.2). This was achieved by simulating different phases throughout gait and measuring the resulting contact responses under simulated valgum malalignment (introduced by a medial/lateral shift in the compressive actuator placement). It was further discovered that some of the repeatability of the input loading conditions (flexion/extension moment) depends not only on the loading device, but also on the subject characteristics. Hence, certain loading and response parameters (compressive and shearing forces, knee flexion, abduction/adduction moment, contact area, centroids and centers of pressure), and certain gait configurations (T-O* and F-F) registered larger repeatability than others.

Meanwhile, in study II, cartilage thickness and T_2 relaxation measurements fell within healthy ranges, and both of these variables decreased after loading, as expected from synovial fluid discharge after compressing the T-F tissues, demonstrating the physiologic realism of this experimental (prolonged standing) simulation. However, there was large inter-subject variability for both cartilage deformation and T_2 relaxation response that greatly surpassed other studies', which could have been due to natural inter-subject variation, specimen misalignment and/or low repeatability of the displacement-control testing system used. Despite mechanical testing, imaging and image processing limitations, a significant moderately negative correlation was found between unloaded tibial cartilage thickness and corresponding T_2 times, which may have constitution implications regarding fiber alignment and tissue hydration over articular cartilage variable thickness or simply be a consequence of imaging limitations. Additionally, there may be a relationship between engineering and T_2 strain magnitudes, also as suggested by a preliminary study[167]; however, there was not enough data in study II to detect significant correlations.

6.3. Linking pilot studies

Relating these preliminary studies is not that simple, as each examines different aspects of knee biomechanics under different experimental conditions for different specimens; however, it is still possible to gain some insight into how to connect tissue- and joint-level biomechanics from this attempt. Although both studies involve physiologically realistic experimental simulations, which have been substantially verified and validated, each study simulates a different physical activity and has a different focus. Study I aims to approximately describe knee physiologic loading (during creep) by measuring a few fragments of the applied BCs (knee external loads and muscle forces), stress field (normal contact stress component) and contact response (contact force, contact area, and centers of pressure and geometry) for key discrete time points in walking (throughout stance and swing). On the other hand, study II aims to relate knee load responses (during stress relaxation), characterized by few aspects of deformation (thickness, thickness change and engineering strain) and transverse relaxation (T_2 time, T_2 change and T_2 strain), arising from simulated 2-leg stance by examining the tissue structure. If the same conditions were examined by both studies, however, then their outcomes could be combined to reveal material constitution [e.g., determining linear-elastic isotropic mechanical properties from generalized ellipsoidal Hertzian contact or via more advanced constitutive relations for (porous)

hyperelastic continua[105] or composites], which are likely related to microstructure measured by qMRI. Unfortunately, this is not presently possible because the closest experimental conditions are too far apart: F-E contact measurements (2.5BW axial compression, lateral tibial plateau overloading due to valgum, sensor inside the joint) vs. prolonged standing deformation (0.5BW axial compression, larger deformation in the medial as opposed to the lateral tibial condyle). Hence, future research (Appendix A6.3) should try to match these conditions as much as possible between contacts measurements and qMRI (as explained in more detail in section A1.1 and Appendix A6.1). Moreover, experimental biomechanics simulations require following very accurate and precise procedures related to a specimen preparation, test execution and data acquisition, since even the slightest errors and variability tend to propagate and manifest greatly in mechanical and qMRI responses, like the valgum misalignment effect in study I or the large variability ranges in study II. Repeatability is especially important, as there may be considerable natural inter-subject variation already. Also, instruments/systems exhibiting both fine resolution and large range are needed to capture physiologic activity features (e.g., large focal contact pressures, fine cartilage deformations) and ensure high testing and measurement accuracy.

6.4. Suggested future studies & directions

Although there may be other aspects, issues or opportunities that have not been considered yet (Appendix A1.1), the following suggestions as well as some additional guidelines (Appendix A6.2) are provided, based on the current findings. We also think it is worth to continue this research, despite the complexity and costs, as results are promising and delve into unexplored areas in biomechanics, which was only possible after finally addressing multiple key limitations of the field. Thanks to this, many vital research questions with clinical implications that could not be answered before can now be investigated (after addressing current limitations of course).

6.4.1. Study I improvements

For study I, the current limitations and future recommendations are associated to the physiologic loading regime, mechanical testing, and study design aspects. In order to better simulate dynamic physical activities, it may be better to find kinematic data that fits the test specimen anthropometrics more closely. Fortunately, in this study, anthropometric differences were not that large, for which minor scaling was used to match model and test conditions; however, for

more distant cases, maybe more complex scaling methods (for each individual limb) are required in addition to more representative kinematic data. Muscular dynamic optimization and dynamic load balance (including inertial effects) could also be integrated in the MSK biomechanics custom program to obtain better representative muscle forces (of higher magnitude compared to the often negligible statically optimized values). In addition, so that no inadvertent loading effects are introduced, any medial/lateral adjustments necessary for left/right knees in this custom algorithm should be automatically accounted for. Also, the user should have the option to simulate different abnormal conditions (e.g., varum, valgum). To improve the physiologic realism, one should consider the effects of key loads omitted during mechanical testing, especially the gastrocnemius tension and external joint torque, both of which have significant effects on the joint response. The absence of gastrocnemius actuation during mechanical testing may in fact explain why the P-F joint is relatively unloaded throughout gait instants, especially near the transition from stance to swing (T-O*). Including these effects, however, is nontrivial and likely requires major hardware modifications to enforce these desired (more accurate) loading conditions, as described in Appendix A6.2. However, at this stage of development, we believe that the current experimental simplifications probably do not have as much influence on test repeatability as they do on physiologic realism.

In terms of hardware, tensile pistons should be recalibrated due to their complex sudden loading behavior, which includes hysteresis. To avoid these sudden effects, more O-rings / lubricant combinations could be tested or, as a last resort, pistons and cylinders resized to reduce breakout friction. The current cylinders, pistons, sealing and lubrication configuration may be kept if a pressure regulator is installed in order to fine tune pressure delivery. To be able to produce complete calibration curves for any of these pneumatic actuator configurations, faster-sampling DAQ systems should be used, due to the high-speed piston retraction right after overcoming the breakout friction (taking place within fractions of a second). Additionally, the calibration ranges of the T-F pressure sensors should be increased to avoid truncation of contact pressure peaks. Lastly, minor improvements include addressing air leaks at low pressures, which do not prevent achieving the target loads, but are an inconvenience during mechanical testing. However, to truly help the operator achieve the desired physiologic state, an adequate pressure regulator should be installed right downstream from the air compressor outlet, as this resolves issues associated with

compressor leaks (at low pressures), and low pressures delivery and measurement. This component should enable better control for tuning the pressures delivered to each actuator, which would further improve the repeatability of the system.

6.4.2. Study II improvements

Limitations and proposed strategies for addressing them involve mechanical testing, image acquisition/processing and design of study II. Despite the high physiologic realism of the mechanical tests, which simulate prolonged standing, axial loading varied by knee. Hence, in order to achieve a physiologically realistic loading environment consistently, resulting in consistent mechanical and qMRI responses, this study should be conducted with the MRI safe load control system developed in study I, as originally intended. Then, to accurately measure the large and fine deformations that take place when cartilage is subject to a physiologic loading state, higher-resolution morphologic images must be obtained. In order to best preserve these valuable (and more expensive) data, unusually bright pixels in T_2 relaxation time maps should be addressed by implementing better de-noising methods (e.g., wavelet filtering, which can even approximately repair corrupted pixels), instead of thresholding exclusion, to preserve more data points. Also, binary masks should be generated specifically to accurately define cartilage morphology, possibly involving morphologic repair operations (e.g., erosion, dilation), which is important since masks affect thickness measurements and any correlations between them and qMRI parameters. Standard registration was performed similarly to previous studies to align the entire knee; however, for improvement, a more sophisticated registration algorithm could be adopted to better align unloaded and loaded cartilages based on the subchondral bones' alignment, since individual tissues displace or deform differently. This process may require segmenting the tibia and patella for each loading conditions to obtain the required transformation matrices, so that the exact same subchondral site is probed over different loading conditions. This Lagrangian approach is likely more accurate (and precise) than defining bone landmarks to generate local anatomic coordinates to define probing site locations, which would be as limited as the current approach based on bone and soft tissue landmark identification. Finally, the qMRI mechanics algorithm should be extended to a 3D scenario and implemented throughout the entire soft tissue volumes (which would drastically increase sample sizes within each knees), possibly including menisci and their axial, radial and circumferential deformations.

6.5. Contributions & research significance

The research and/or clinical novelty and value of this project is related to the development of tools and methods, as well as data acquisition. In comparison to current experimental loading devices and previous studies (focused on stance), the MRI-safe creep loading system developed in this project addresses some of their limitations and further improves upon their functions. This loading rig allows simulating and imaging physiologic loading effects throughout the entire cycle of gait (including stance and swing) or other activities. Physiologic simulation involves an intense multiaxial combined loading scenario (including axial compression, bending moments and muscles actuation), which simultaneously loads all T-F and P-F tissues, just like physical activities do. In terms of specifications, this simulator operates in load control without complex control systems, which are harder to troubleshoot and fix, to achieve a realistic simulation. Also, this rig has been tested extensively and allows simulating various physical activities for healthy or pathologic human knees (or other joints and/or species) with high repeatability. Lastly, in practical terms, this versatile simulator is portable, does not occupy large amounts of space, and neither does it consume large amounts of energy, as the compressor only needs to run to charge the tanks, after which the system can operate without (or disconnected from) the compressor.

The contact and deformation datasets obtained using this hardware (MR rig, potting equipment) and software (MSK biomechanics code, knee misalignment calculator, qMRI-mechanics algorithm, contact data processing routine) are also very useful and actively sought after in the biomechanics field for validating knee joint models, such as but not limited to FE simulations. Despite the present limitations, the equilibrium contact data obtained in study I gives a glimpse of what the knee tissues look like inside throughout walking (stance and swing) subject to valgum, which has never been done before experimentally under such realistic conditions, while study II shows how the knee deforms under 2-leg stance and how their structure might be related to qMRI parameters. The ex-vivo datasets gathered in both studies supplements the available experimental measurements on full-joint human knee loading response, including knee flexion kinematics during swing (ex-vivo healthy, ACL- and PCL-deficient)[73], T-F tissue deformations during simulated 2-leg stance (in-vivo healthy)[47,182], and T-F contact stress fields for 1-leg stance (ex-vivo healthy)[114], stair descent or squatting (ex-vivo healthy)[133].

7. Concluding remarks

The overall goal of this research was relating tissue structure and joint function in whole cadaver knees under physiologically relevant loads. This required developing a MRI-safe simulator and collecting/processing valuable experimental data to answer the main research queestion: How does physiologic loading affect knee's soft tissues (i.e., contact, deformation and T_2 relaxation responses)? The objectives and conclusions for each study are as follows:

Design study: Developing a realistic MRI-safe loading simulator for ex-vivo joints

1. A custom MRI-safe, load-control testing station (involving MSK software + mechanical and pneumatic hardware) was designed, fabricated, calibrated, tested and evaluated extensively.
2. This versatile device is capable of achieving a multiaxial, combined loading scenario representing physiologic activities, involving axial compression, bending and muscle tension.
3. The performance of this device is comparable to existing simulators, including imaging integration and physiologic realism (preserving the synovial capsule, activating all DOFs).

Study I: Assessing repeatability of loads applied by the simulator and resulting contact response

1. The loading device registered moderate to high loading repeatability.
2. The knee contact response to the applied loading and subject characteristics was more complex, with some parameters displaying high repeatability and others high variability.
3. It was discovered that loading conditions and repeatability are partially tied to knee response and its variability; hence, some parameters and gait phases are more repeatable than others.

Study II: Determining if there are T_2-deformation associations for whole knees in compression

1. Decreasing cartilage thickness and T_2 relaxation responses to applied compression agreed within expected ranges across multiple studies in the biomechanics literature.
2. A moderate negative correlation was found between cartilage thickness and T_2 relaxation time for unloaded tibial cartilages, which may be related to tissue composition.

In conclusion, as shown in this thesis, thanks to the novel tools and methods developed and experimental data acquired, by combining modelling, mechanical testing and medical imaging, it is possible to connect tissue- and joint-level biomechanics in healthy or pathologic knees.

References

1 Bender, B. *et al.* Prevalence and Impact of Chronic Joint Symptoms—Seven States, 1996. *JAMA* **279**, 1940-1941, doi:10.1001/jama.279.24.1940 (1998).

2 Felson, D. T. *et al.* Osteoarthritis: new insights. Part 1: the disease and its risk factors. *Ann Intern Med* **133**, 635-646, doi:200010170-00016 [pii] 10.7326/0003-4819-133-8-200010170-00016 (2000).

3 Hootman, J. M. & Helmick, C. G. Projections of US prevalence of arthritis and associated activity limitations. *Arthritis & Rheumatism* **54**, 226-229, doi:10.1002/art.21562 (2006).

4 Lawrence, R. C. *et al.* ESTIMATES OF THE PREVALENCE OF ARTHRITIS AND SELECTED MUSCULOSKELETAL DISORDERS IN THE UNITED STATES. *Arthritis & Rheumatism* **41**, 778-799 (1998).

5 Pendleton, A. *et al.* EULAR recommendations for the management of knee osteoarthritis: report of a task force of the Standing Committee for International Clinical Studies Including Therapeutic Trials (ESCISIT). *Annals Of Rheumatic Diseases* **59**, 936-944 (2000).

6 Bombardier, C., Hawker, G. & Mosher, D. The Impact of Arthritis in Canada: Today and Over the Next 30 Years. (Arthritis Alliance of Canada, 2011).

7 March, L. M. & Bachmeier, C. J. M. Economics of osteoarthritis: A global perspective. *Bailliere's Clinical Rheumatolog* **11**, 817-834 (1997).

8 Salmon, J. H. *et al.* Economic impact of lower-limb osteoarthritis worldwide: a systematic review of cost-of-illness studies. *Osteoarthritis and Cartilage* **24**, 1500-1508, doi:10.1016/j.joca.2016.03.012 (2016).

9 Chen, A., Gupte, C., Akhtar, K., Smith, P. & Cobb, J. The Global Economic Cost of Osteoarthritis: How the UK Compares. *Arthritis* **2012**, 1-6, doi:10.1155/2012/698709 (2012).

10 Matzat, S. J., Kogan, F., Fong, G. W. & Gold, G. E. Imaging Strategies for Assessing Cartilage Composition in Osteoarthritis. *Current Rheumatology Reports* **16**, doi:10.1007/s11926-014-0462-3 (2014).

11 Matzat, S. J., van Tiel, J., Gold, G. E. & Oei, E. H. Quantitative MRI techniques of cartilage composition. *Quant Imaging Med Surg* **3**, 162-174, doi:10.3978/j.issn.2223-4292.2013.06.04qims-03-03-162 [pii] (2013).

12 Greaves, L. L., Gilbart, M. K., Yung, A., Kozlowski, P. & Wilson, D. R. Deformation and recovery of cartilage in the intact hip under physiological loads using 7T MRI. *Journal of Biomechanics* **42**, 349-354, doi:10.1016/j.jbiomech.2008.11.025 (2009).

13 Greaves, L. L., Gilbart, M. K., Yung, A. C., Kozlowski, P. & Wilson, D. R. Effect of acetabular labral tears, repair and resection on hip cartilage strain: A 7T MR study. *Journal of Biomechanics* **43**, 858-863, doi:10.1016/j.jbiomech.2009.11.016 (2010).

14 Samosky, J. T. *et al.* Spatially-localized correlation of dGEMRIC-measured GAG distribution and mechanical stiffness in the human tibial plateau. *Journal of Orthopaedic Research*® **23**, 93-101, doi:10.101 6/j.orthres.2004.05.008 (2005).

15 Schoenbauer, E. *et al.* Cartilage evaluation with biochemical MR imaging using in vivo Knee compression at 3T-comparison of patients after cartilage repair with healthy volunteers. *J Biomech* **48**, 3349-3355, doi:10.1016/j.jbiomech.2015.06.016S0021-9290(15)00353-X [pii] (2015).

16 Song, Y., Greve, J. M., Carter, D. R., Koo, S. & Giori, N. J. Articular cartilage MR imaging and thickness mapping of a loaded knee joint before and after meniscectomy. *Osteoarthritis and Cartilage* **14**, 728-737, doi:10.1016/j.joca.2006.01.011 (2006).
17 Dedini, R. D. *et al.* MRI issues for ballistic objects: information obtained at 1.5-, 3- and 7-Tesla. *The Spine Journal* **13**, 815-822, doi:10.1016/j.spinee.2013.02.068 (2013).
18 Gunnarsson, G.-T. License: https://creativecommons.org/licenses/by-sa/4.0/deed.en (Wikimedia Sverige, 2016).
19 nbe, H. License: https://creativecommons.org/licenses/by-sa/4.0/deed.en (Wikimedia Commons, 2017).
20 Dilmen, N. License: https://creativecommons.org/licenses/by-sa/3.0/deed.en (Wikimedia Commons, 2016).
21 Dilmen, N. License: https://creativecommons.org/licenses/by-sa/3.0/deed.en (Wikimedia Commons, 2012).
22 liverpoolhls. License: https://creativecommons.org/licenses/by-sa/2.0/ (Creative Commons).
23 BruceBlaus. License: https://creativecommons.org/licenses/by/3.0/deed.en (Wikimedia Commons, 2013).
24 Health, U. o. L. F. o. License: https://creativecommons.org/licenses/by/2.0/deed.en (Wikimedia Commons, 2013).
25 Baldwin, M. A. *et al.* Dynamic finite element knee simulation for evaluation of knee replacement mechanics. *Journal of Biomechanics* **45**, 474-483, doi:10.1016/j.jbiomech.2011.11.052 (2012).
26 Callister, W. D. & Rethwisch, D. G. *Materials Science and Engineering: An Introduction*. 9th Ed. edn, (John Wiley & Sons, 2014).
27 Officer781. License: https://creativecommons.org/licenses/by-sa/4.0/deed.en (Wikimedia Commons, 2019).
28 Mow, V. C. & Huiskes, R. *Basic Orthopaedic Biomechanics and Mechano-Biology*. 3rd edn, (Lippincott Williams & Wilkins, 2004).
29 Kinzel, G. L., A. S. Hall, J. & Hillberry, B. M. MEASUREMENT OF THE TOTAL MOTION BETWEEN TWO BODY SEGMENTS - I. ANALYTICAL DEVELOPMENT*. *Journal of Biomechanics* **5**, 93-105 (1972).
30 Kedgley, A. E., McWalter, E. J. & Wilson, D. R. The effect of coordinate system variation on in vivo patellofemoral kinematic measures. *The Knee* **22**, 88-94, doi:10.1016/j.knee.2014.11.006 (2015).
31 Grood, E. S. & Suntay, W. J. A Joint Coordinate System for the Clinical Description of Three-Dimensional Motions: Application to the Knee. *Journal of Biomechanical Engineering* **105**, 136-144 (1983).
32 Kadaba, M. P., Ramakrishnan, H. K. & Wootten, M. E. Measurement of Lower Extremity Kinematics During Level Walking. *Journal of Orthopaedic Research* **8**, 383-392 (1990).
33 Lafortune, M. A., Cavanagh, P. R., III, H. J. S. & Kalenak, A. THREE-DIMENSIONAL KINEMATICS OF THE HUMAN KNEE DURING WALKING*. *Journal of Biomechanics* **25**, 347-357 (1992).
34 Pennock, G. R. & Clark, K. J. AN ANATOMY-BASED COORDINATE SYSTEM FOR THE DESCRIPTION OF THE KINEMATIC DISPLACEMENTS IN THE HUMAN KNEE. *Journal of Biomechanics* **23**, 1209-1218 (1990).

35 Morrison, J. B. THE MECHANICS OF THE KNEE JOINT IN RELATION TO NORMAL WALKING. *Journal of Biomechanics* **3**, 51-61 (1970).
36 Benoit, D. L. *et al.* Effect of skin movement artifact on knee kinematics during gait and cutting motions measured in vivo. *Gait & Posture* **24**, 152-164, doi:10.1016/j.gaitpost.2005.04.012 (2006).
37 Cappozzo, A., Della Croce, U., Leardini, A. & Chiari, L. Human movement analysis using stereophotogrammetry. *Gait & Posture* **21**, 186-196, doi:10.1016/j.gaitpost.2004.01.010 (2005).
38 Klets, O. *et al.* Comparison of different material models of articular cartilage in 3D computational modeling of the knee: Data from the Osteoarthritis Initiative (OAI). *Journal of Biomechanics* **49**, 3891-3900, doi:10.1016/j.jbiomech.2016.10.025 (2016).
39 Lerner, Z. F., DeMers, M. S., Delp, S. L. & Browning, R. C. How tibiofemoral alignment and contact locations affect predictions of medial and lateral tibiofemoral contact forces. *Journal of Biomechanics* **48**, 644-650, doi:10.1016/j.jbiomech.2014.12.049 (2015).
40 Moissenet, F., Chèze, L. & Dumas, R. A 3D lower limb musculoskeletal model for simultaneous estimation of musculo-tendon, joint contact, ligament and bone forces during gait. *Journal of Biomechanics* **47**, 50-58, doi:10.1016/j.jbiomech.2013.10.015 (2014).
41 Heinlein, B. *et al.* ESB clinical biomechanics award 2008: Complete data of total knee replacement loading for level walking and stair climbing measured in vivo with a follow-up of 6–10 months. *Clinical Biomechanics* **24**, 315-326, doi:10.1016/j.clinbiomech.2009.01.011 (2009).
42 Kutzner, I. *et al.* Loading of the knee joint during activities of daily living measured in vivo in five subjects. *Journal of Biomechanics* **43**, 2164-2173, doi:10.1016/j.jbiomech.2010.03.046 (2010).
43 Andriacchi, T. P., Alexander, E. J., Toney, M. K., Dyrby, C. & Sum, J. A Point Cluster Method for In Vivo Motion Analysis: Applied to a Study of Knee Kinematics. *Journal of Biomechanical Engineering* **120**, 743-749 (1998).
44 Baker, R., Finney, L. & Orr, J. A new approach to determine the hip rotation profile from clinical gait analysis data. *Human Movement Science*, 655-667 (1999).
45 Nilsson, J. & Thorstensson, A. Ground reaction forces at different speeds of human walking and running. *Acta Physiologica Scandinavica* **136**, 217-227 (1989).
46 Astephen, J. L., Deluzio, K. J., Caldwell, G. E. & Dunbar, M. J. Biomechanical changes at the hip, knee, and ankle joints during gait are associated with knee osteoarthritis severity. *Journal of Orthopaedic Research* **26**, 332-341, doi:10.1002/jor.20496 (2008).
47 Halonen, K. S. *et al.* Deformation of articular cartilage during static loading of a knee joint – Experimental and finite element analysis. *Journal of Biomechanics* **47**, 2467-2474, doi:10.1016/j.jbiomech.2014.04.013 (2014).
48 Farrokhi, S., Keyak, J. H. & Powers, C. M. Individuals with patellofemoral pain exhibit greater patellofemoral joint stress: a finite element analysis study. *Osteoarthritis and Cartilage* **19**, 287-294, doi:10.1016/j.joca.2010.12.001 (2011).
49 Akbarshahi, M., Fernandez, J. W., Schache, A. G. & Pandy, M. G. Subject-specific evaluation of patellofemoral joint biomechanics during functional activity. *Medical Engineering & Physics* **36**, 1122-1133, doi:10.1016/j.medengphy.2014.06.009 (2014).

50 Desloovere, K. *et al.* Range of motion and repeatability of knee kinematics for 11 clinically relevant motor tasks. *Gait & Posture* **32**, 597-602, doi:10.1016/j.gaitpost.2010.08.010 (2010).
51 Eng, J. J. & Winter, D. A. KINETIC ANALYSIS OF THE LOWER LIMBS DURING WALKING: WHAT INFORMATION CAN BE GAINED FROM A THREE-DIMENSIONAL MODEL? *J Biomech* **28**, 733 758 (1995).
52 Lim, Y. P., Lin, Y.-C. & Pandy, M. G. Muscle function during gait is invariant to age when walking speed is controlled. *Gait & Posture* **38**, 253-259, doi:10.1016/j.gaitpost.2012.11.020 (2013).
53 Winter, D. A. KINEMATIC AND KINETIC PATTERNS IN HUMAN GAIT: VARIABILITY AND COMPENSATING EFFECTS. *Human Movement Science* **3**, 51-76 (1984).
54 Chehab, E. F., Andriacchi, T. P. & Favre, J. Speed, age, sex, and body mass index provide a rigorous basis for comparing the kinematic and kinetic profiles of the lower extremity during walking. *Journal of Biomechanics* **58**, 11-20, doi:10.1016/j.jbiomech.2017.04.014 (2017).
55 Leitch, K. M., Birmingham, T. B., Dunning, C. E. & Robert Giffin, J. Changes in valgus and varus alignment neutralize aberrant frontal plane knee moments in patients with unicompartmental knee osteoarthritis. *Journal of Biomechanics* **46**, 1408-1412, doi:10.1016/j.jbiomech.2013.01.024 (2013).
56 Knarr, B. A. & Higginson, J. S. Practical approach to subject-specific estimation of knee joint contact force. *Journal of Biomechanics* **48**, 2897-2902, doi:10.1016/j.jbiomech.2015.04.020 (2015).
57 Schache, A. G. & Baker, R. On the expression of joint moments during gait. *Gait & Posture* **25**, 440-452, doi:10.1016/j.gaitpost.2006.05.018 (2007).
58 Lee, M., Kim, J., Son, J. & Kim, Y. Kinematic and kinetic analysis during forward and backward walking. *Gait & Posture* **38**, 674-678, doi:10.1016/j.gaitpost.2013.02.014 (2013).
59 Lencioni, T. *et al.* Are Modular Activations Altered in Lower Limb Muscles of Persons with Multiple Sclerosis during Walking? Evidence from Muscle Synergies and Biomechanical Analysis. *Frontiers in Human Neuroscience* **10**, doi:10.3389/fnhum.2016.00620 (2016).
60 Meireles, S. *et al.* Knee contact forces are not altered in early knee osteoarthritis. *Gait & Posture* **45**, 115-120, doi:10.1016/j.gaitpost.2016.01.016 (2016).
61 Meireles, S., De Groote, F., Van Rossom, S., Verschueren, S. & Jonkers, I. Differences in knee adduction moment between healthy subjects and patients with osteoarthritis depend on the knee axis definition. *Gait & Posture* **53**, 104-109, doi:10.1016/j.gaitpost.2017.01.013 (2017).
62 Samaan, M. A. *et al.* Cyclops lesions are associated with altered gait patterns and medial knee joint cartilage degeneration at 1 year after ACL-reconstruction. *Journal of Orthopaedic Research* **35**, 2275-2281, doi:10.1002/jor.23530 (2017).
63 Patterson, M. R., Delahunt, E. & Caulfield, B. Peak knee adduction moment during gait in anterior cruciate ligament reconstructed females. *Clinical Biomechanics* **29**, 138-142, doi:10.1016/j.clinbiomech.2013.11.021 (2014).

64 Wilson, D. R., McWalter, E. J. & Johnston, J. D. The Measurement of Joint Mechanics and their Role in Osteoarthritis Genesis and Progression. *Rheumatic Disease Clinics of North America* **34**, 605-622, doi:10.1016/j.rdc.2008.05.002 (2008).
65 Arumalla, N. & Coakley, G. Septic arthritis: time to rethink service delivery? *The Lancet Infectious Diseases* **20**, 266-267, doi:10.1016/S1473-3099(19)30563-8 10.1016/S1473-3099(19)30574-2 10.1016/S1473-3099(19)30419-0 10.1136/bmj.l1 (2020).
66 Teichtahl, A. J. *et al.* Meniscal extrusion and bone marrow lesions are associated with incident and progressive knee osteoarthritis. *Osteoarthritis and Cartilage* **25**, 1076-1083, doi:10.1016/j.joca.2017.02.792 (2017).
67 Sharma, L. *et al.* The Role of Knee Alignment in Disease Progression and Functional Decline in Knee Osteoarthritis. *JAMA* **286 (#2)**, 188-195 (2001).
68 Breedveld, F. C. Osteoarthritis--the impact of a serious disease. *Rheumatology (Oxford)* **43 Suppl 1**, i4-8, doi:10.1093/rheumatology/keh10243/suppl_1/i4 [pii] (2004).
69 Poole, A. R. An introduction to the pathophysiology of osteoarthritis. *Frontiers in Bioscience* **4**, 662-670 (1999).
70 Stamenović, D., Kojić, M., Stojanović, B. & Hunter, D. Pneumatic Osteoarthritis Knee Brace. *Journal of Biomechanical Engineering* **131**, doi:10.1115/1.3072890 (2009).
71 Wang, X.-H. *et al.* The impact of variations in input directions according to ISO 14243 on wearing of knee prostheses. *PLoS One* **13**, 1-15, doi:10.1371/journal.pone.0206496 10.1371/journal.pone.0206496.g001 (2018).
72 Toivanen, A. T. *et al.* Obesity, physically demanding work and traumatic knee injury are major risk factors for knee osteoarthritis--a population-based study with a follow-up of 22 years. *Rheumatology* **49**, 308-314, doi:10.1093/rheumatology/kep388 (2009).
73 Ali, A. A. *et al.* Validation of predicted patellofemoral mechanics in a finite element model of the healthy and cruciate-deficient knee. *Journal of Biomechanics* **49**, 302-309, doi:10.1016/j.jbiomech.2015.12.020 (2016).
74 Andriacchi, T. P. *et al.* A Framework for the in Vivo Pathomechanics of Osteoarthritis at the Knee. *Annals of Biomedical Engineering* **32**, 447-457 (2004).
75 Utting, M. R., Davies, G. & Newman, J. H. Is anterior knee pain a predisposing factor to patellofemoral osteoarthritis? *The Knee* **12**, 362-365, doi:10.1016/j.knee.2004.12.006 (2005).
76 Borotikar, B. S. & Sheehan, F. T. In vivo patellofemoral contact mechanics during active extension using a novel dynamic MRI-based methodology. *Osteoarthritis and Cartilage* **21**, 1886-1894, doi:10.1016/j.joca.2013.08.023 (2013).
77 Liukkonen, M. K. *et al.* Application of a semi-automatic cartilage segmentation method for biomechanical modeling of the knee joint. *Computer Methods in Biomechanics and Biomedical Engineering* **20**, 1453-1463, doi:10.1080/10255842.2017.1375477 (2017).
78 BruceBlaus. License: https://creativecommons.org/licenses/by-sa/4.0/deed.en (Wikimedia Commons, 2017).
79 Liukkonen, M. K. *et al.* Simulation of Subject-Specific Progression of Knee Osteoarthritis and Comparison to Experimental Follow-up Data: Data from the Osteoarthritis Initiative. *Scientific Reports* **7**, doi:10.1038/s41598-017-09013-7 (2017).
80 Espinosa, A. & McWalter, E. J. Novel multiaxial, MRI-compatible loading rig to simulate daily activities: A design overview. *AB BME 2016* (2016).
81 Espinosa, A., Johnston, J. D. & McWalter, E. J. DESIGN OF A NOVEL MRI-SAFE PHYSICAL ACTIVITY SIMULATOR FOR CADAVER KNEES. *13th IWOAI* (2019).

82 Nebelung, S., M., P., C., K. & D., T. SERIAL T1ρ MAPPING TO STUDY CARTILAGE TISSUE FUNCTIONALITY AND ITS RELATION TO DEGENERATION. *13th IWOAI* (2019).
83 Dullaert, K. *et al.* Influence of tibialis posterior muscle activation on foot anatomy under axial loading: A biomechanical CT human cadaveric study. *Foot and Ankle Surgery* **23**, 250-254, doi:10.1016/j.fas.2016.07.003 (2017).
84 Martel, M. M., Thorson, C. S. & McWalter, E. J. Quantitative magnetic resonance imaging (qMRI) of the meniscus in the knee joint in the unloaded and loaded conditions. *18th AB BME* (2017).
85 Thorson, C. S., Martel, M. M. & McWalter, E. J. Quantitative MRI of cadaver knee articular cartilage in axial compression using a custom MRI-safe loading rig. *18th AB BME* (2017).
86 Naghibi Beidokhti, H. *et al.* The influence of ligament modelling strategies on the predictive capability of finite element models of the human knee joint. *Journal of Biomechanics* **65**, 1-11, doi:10.1016/j.jbiomech.2017.08.030 (2017).
87 Rachmat, H. H., Janssen, D., Verkerke, G. J., Diercks, R. L. & Verdonschot, N. In-situ mechanical behavior and slackness of the anterior cruciate ligament at multiple knee flexion angles. *Medical Engineering & Physics* **38**, 209-215, doi:10.1016/j.medengphy.2015.11.011 (2016).
88 Barink, M., Meijerink, H., Verdonschot, N., van Kampen, A. & de Waal Malefijt, M. Asymmetrical total knee arthroplasty does not improve patella tracking: a study without patella resurfacing. *Knee Surgery, Sports Traumatology, Arthroscopy* **15**, 184-191, doi:10.1007/s00167-006-0158-y (2006).
89 Fitzpatrick, C. K. *et al.* Validation of a new computational 6-DOF knee simulator during dynamic activities. *Journal of Biomechanics* **49**, 3177-3184, doi:10.1016/j.jbiomech.2016.07.040 (2016).
90 Maletsky, L. *et al.* In Vitro Experimental Testing of the Human Knee: A Concise Review. *Journal of Knee Surgery* **29**, 138-148, doi:10.1055/s-0035-1566739 (2016).
91 Forlani, M. *A NEW TEST RIG FOR IN-VITRO EVALUATION OF THE KNEE JOINT BEHAVIOUR* PhD. thesis, UNIVERSITÀ DEGLI STUDI DI BOLOGNA, (2015).
92 Chen, L., Gordon, K. & Hurtig, M. Design and validation of a cadaveric knee joint loading device compatible with magnetic resonance imaging and computed tomography. *Medical Engineering & Physics* **36**, 1346-1351, doi:10.1016/j.medengphy.2014.06.017 (2014).
93 Freutel, M. *et al.* Medial meniscal displacement and strain in three dimensions under compressive loads: MR assessment. *Journal of Magnetic Resonance Imaging* **40**, 1181-1188, doi:10.1002/jmri.24461 (2014).
94 Lawless, I. M., Ding, B., Cazzolato, B. S. & Costi, J. J. Adaptive velocity-based six degree of freedom load control for real-time unconstrained biomechanical testing. *Journal of Biomechanics* **47**, 3241-3247, doi:10.1016/j.jbiomech.2014.06.023 (2014).
95 Ding, B., Stanley, R. M., Cazzolato, B. S. & Costi, J. J. Real-time FPGA control of a hexapod robot for 6-dof biomechanical testing. *IECON 2011-37th Annual Conference on IEEE Industrial Electronics Society*, 252-257 (2011).
96 McWalter, E. J., O'Kane, C. M., FitzPatrick, D. P. & Wilson, D. R. Validation of an MRI-based method to assess patellofemoral joint contact areas in loaded knee flexion in

vivo. *Journal of Magnetic Resonance Imaging* **39**, 978-987, doi:10.1002/jmri.24240 (2014).
97 Shalhoub, S. & Maletsky, L. P. Variation in patellofemoral kinematics due to changes in quadriceps loading configuration during in vitro testing. *Journal of Biomechanics* **47**, 130-136, doi:10.1016/j.jbiomech.2013.09.019 (2014).
98 Wünschel, M. *et al.* Differences in knee joint kinematics and forces after posterior cruciate retaining and stabilized total knee arthroplasty. *The Knee* **20**, 416-421, doi:10.1016/j.knee.2013.03.005 (2013).
99 Wünschel, M., Müller, O., Lo, J., Obloh, C. & Wülker, N. The Anterior Cruciate Ligament Provides Resistance to Externally Applied Anterior Tibial Force But Not to Internal Rotational Torque During Simulated Weight-Bearing Flexion. *Arthroscopy: The Journal of Arthroscopic & Related Surgery* **26**, 1520-1527, doi:10.1016/j.arthro.2010.04.069 (2010).
100 Müller, O., Lo, J., Wünschel, M., Obloh, C. & Wülker, N. Simulation of force loaded knee movement in a newly developed in vitro knee simulator / Simulation von belastungsabhängigen Kniebewegungen in einem neuartigen Knie-Simulator für In-vitro-Studien. *Biomedizinische Technik/Biomedical Engineering* **54**, 142-149, doi:10.1515/bmt.2009.015 (2009).
101 Lo, J., Müller, O., Wünschel, M., Bauer, S. & Wülker, N. Forces in anterior cruciate ligament during simulated weight-bearing flexion with anterior and internal rotational tibial load. *Journal of Biomechanics* **41**, 1855-1861, doi:10.1016/j.jbiomech.2008.04.010 (2008).
102 Shiomi, T. *et al.* Influence of medial meniscectomy on stress distribution of the femoral cartilage in porcine knees: a 3D reconstructed T2 mapping study. *Osteoarthritis and Cartilage* **20**, 1383-1390, doi:10.1016/j.joca.2012.07.015 (2012).
103 Shiomi, T. *et al.* Loading and knee alignment have significant influence on cartilage MRI T2 in porcine knee joints. *Osteoarthritis and Cartilage* **18**, 902-908, doi:10.1016/j.joca.2010.05.002 (2010).
104 Siston, R. A., Maack, T. L., Hutter, E. E., Beal, M. D. & Chaudhari, A. M. W. Design and Cadaveric Validation of a Novel Device to Quantify Knee Stability During Total Knee Arthroplasty. *Journal of Biomechanical Engineering* **134**, doi:10.1115/1.4007822 (2012).
105 Butz, K. D., Chan, D. D., Nauman, E. A. & Neu, C. P. Stress distributions and material properties determined in articular cartilage from MRI-based finite strains. *Journal of Biomechanics* **44**, 2667-2672, doi:10.1016/j.jbiomech.2011.08.005 (2011).
106 Chan, D. D., Neu, C. P. & Hull, M. L. Articular cartilage deformation determined in an intact tibiofemoral joint by displacement-encoded imaging. *Magnetic Resonance in Medicine* **61**, 989-993, doi:10.1002/mrm.21927 (2009).
107 Chan, D. D., Neu, C. P. & Hull, M. L. In situ deformation of cartilage in cyclically loaded tibiofemoral joints by displacement-encoded MRI. *Osteoarthritis and Cartilage* **17**, 1461-1468, doi:10.1016/j.joca.2009.04.021 (2009).
108 Netravali, N. A., Koo, S., Giori, N. J. & Andriacchi, T. P. The Effect of Kinematic and Kinetic Changes on Meniscal Strains During Gait. *Journal of Biomechanical Engineering* **133**, doi:10.1115/1.4003008 (2011).
109 Quenneville, C. E., Fraser, G. S. & Dunning, C. E. Development of an Apparatus to Produce Fractures From Short-Duration High-Impulse Loading With an Application in

the Lower Leg. *Journal of Biomechanical Engineering* **132**, doi:10.1115/1.4000084 (2010).
110 Martin, K. J., Neu, C. P. & Hull, M. L. Quasi-Steady-State Displacement Response of Whole Human Cadaveric Knees in a MRI Scanner. *Journal of Biomechanical Engineering* **131**, doi:10.1115/1.2978986 (2009).
111 Martin, K. J., Neu, C. P. & Hull, M. L. An MRI-Based Method to Align the Compressive Loading Axis for Human Cadaveric Knees. *Journal of Biomechanical Engineering* **129**, 855-862, doi:10.1115/1.2800765 (2007).
112 Yildirim, G., Walker, P. S. & Boyer, J. Total knees designed for normal kinematics evaluated in an up-and-down crouching machine. *Journal of Orthopaedic Research* **27**, 1022-1027, doi:10.1002/jor.20839 (2009).
113 Aubin, P. M., Cowley, M. S. & Ledoux, W. R. Gait Simulation via a 6-DOF Parallel Robot With Iterative Learning Control. *IEEE TRANSACTIONS ON BIOMEDICAL ENGINEERING* **55**, 1237-1240 (2008).
114 Papaioannou, G. *et al.* Patient-specific knee joint finite element model validation with high-accuracy kinematics from biplane dynamic Roentgen stereogrammetric analysis. *Journal of Biomechanics* **41**, 2633-2638, doi:10.1016/j.jbiomech.2008.06.027 (2008).
115 Withrow, T. J., Huston, L. J., Wojtys, E. M. & Ashton-Miller, J. A. Effect of Varying Hamstring Tension on Anterior Cruciate Ligament Strain During in Vitro Impulsive Knee Flexion and Compression Loading. *The Journal of Bone and Joint Surgery-American Volume* **90**, 815-823, doi:10.2106/jbjs.f.01352 (2008).
116 Clary, C. W. *Design and Validation of a Knee Loading Rig to Perform Clinical Injury Assessments in vitro* MSc. thesis, University of Kansas, (2006).
117 Si-hoe, K. M. Radio-Translucent 3-Axis Mechanical Testing Rig for the Spine in Micro-CT. *Journal of Biomechanical Engineering* **128**, 957, doi:10.1115/1.2375136 (2006).
118 Fellows, R. A. *et al.* Magnetic resonance imaging for in vivo assessment of three-dimensional patellar tracking. *Journal of Biomechanics* **38**, 1643-1652, doi:10.1016/j.jbiomech.2004.07.021 (2005).
119 Maletsky, L. P. & Hillberry, B. M. Simulating Dynamic Activities Using a Five-Axis Knee Simulator. *Journal of Biomechanical Engineering* **127**, 123-133, doi:10.1115/1.1846070 (2005).
120 Fujie, H., Sekito, T. & Orita, A. A Novel Robotic System for Joint Biomechanical Tests: Application to the Human Knee Joint. *Journal of Biomechanical Engineering* **126**, 54-61, doi:10.1115/1.1644567 (2004).
121 Li, G. *et al.* Kinematics of the knee at high flexion angles: an in vitro investigation. *Journal of Orthopaedic Research* **22**, 90-95 (2004).
122 Li, G. *et al.* The importance of quadriceps and hamstring muscle loading on knee kinematics and in-situ forces in the ACL. *J Biomech* **32**, 395-400 (1999).
123 Herberhold, C. *et al.* In situ measurement of articular cartilage deformation in intact femoro patellar joints under static loading. *Journal of Biomechanics* **32**, 1287}1295 (1999).
124 Herberhold, C. *et al.* An MR-Based Technique for Quantifying the Deformation of Articular Cartilage During Mechanical Loading in an Intact Cadaver Joint. *Magnetic Resonance in Medicine* **39**, 843-850 (1998).
125 Zavatsky, A. B. A KINEMATIC-FREEDOM ANALYSIS OF A FLEXED-KNEE-STANCE TESTING RIG. *J Biomech* **30**, 277-280 (1997).

126 Petersilge, W. J., Oishi, C. S., Kaufman, K. R., Irby, S. E. & Colwell, C. W. The effect of trochlear design on patellofemoral shear and compressive forces in total knee arthroplasty. *Clinical Orthopaedics and Related Research* **309**, 124-130 (1994).
127 Shoemaker, S. C., Adams, D., Daniel, D. M. & Woo, S. L.-Y. Quadriceps/anterior cruciate graft interaction: An in vitro study of joint kinematics and anterior cruciate ligament graft tension. *Clinical Orthopaedics and Related Research* **294**, 379-390 (1993).
128 Shelley, F. J., Anderson, D. D., Kolar, M. J., Miller, M. C. & Rubash, H. E. Physical Modelling of Hip Joint Forces in Stair Climbing. *Proceedings of the Institution of Mechanical Engineers, Part H: Journal of Engineering in Medicine* **210**, 65-68, doi:10.1243/pime_proc_1996_210_391_02 (1996).
129 Shelley, F. J., Anderson, D. D., Kolar, M. J., Miller, M. C. & Rubash, H. E. A device to model the hip during stair climbing, including consideration of the extensor, abductor and adductor muscle groups. *ASME Advances in Bioengineering* **20**, 173-175 (1991).
130 Xerogeanes, J. W. *et al.* Effect of knee flexion on the in situ force distribution in the human anterior cruciate ligament. *Knee Surg, Sports Traumatol, Arthroscopy* **3**, 9-13 (1995).
131 Fujie, H. *et al.* The Use of Robotics Technology to Study Human Joint Kinematics: A New Methodology. *Journal of Biomechanical Engineering* **115**, 211-217 (1993).
132 Grood, E. S., Stowers, S. F. & Noyes, F. R. Limits of Movement in the Human Knee. *The Journal ofBone and Joint Surgery* **70-A**, 88-97 (1988).
133 Gu, W. & Pandy, M. G. Direct Validation of Human Knee-Joint Contact Mechanics Derived From Subject-Specific Finite-Element Models of the Tibiofemoral and Patellofemoral Joints. *Journal of Biomechanical Engineering* **142**, doi:10.1115/1.4045594 (2020).
134 Jerban, S., Chang, E. Y. & Du, J. Magnetic resonance imaging (MRI) studies of knee joint under mechanical loading: Review. *Magnetic Resonance Imaging* **65**, 27-36, doi:10.1016/j.mri.2019.09.007 (2020).
135 Yung, A. C., Nickmanesh, R., Kozlowski, P. & Wilson, D. R. DESS T2 mapping in Knee Cartilage at Supine and Standing Positions in an Upright MR Scanner. *ISMRM 24th Annual Meeting & Exhibition* (2016).
136 Szarko, M., Muldrew, K. & Bertram, J. E. Freeze-thaw treatment effects on the dynamic mechanical properties of articular cartilage. *BMC Musculoskeletal Disorders* **11**, 231-238 (2010).
137 Qu, C. *et al.* Effects of Freeze–Thaw Cycle with and without Proteolysis Inhibitors and Cryopreservant on the Biochemical and Biomechanical Properties of Articular Cartilage. *Cartilage* **5**, 97-106, doi:10.1177/1947603513515998 (2013).
138 Kwan, M. K., Hacker, S. A., Woo, S. L.-Y. & Wayne, J. S. The Effect of Storage on the Biomechanical Behavior of Articular Cartilage—A Large Strain Study. *Journal of Biomechanical Engineering* **114**, 149-153 (1992).
139 Peters, A. E., Comerford, E. J., Macaulay, S., Bates, K. T. & Akhtar, R. Micromechanical properties of canine femoral articular cartilage following multiple freeze-thaw cycles. *Journal of the Mechanical Behavior of Biomedical Materials* **71**, 114-121, doi:10.1016/j.jmbbm.2017.03.006 (2017).
140 Lewis, P. B. *et al.* Multiple freeze-thaw cycled meniscal allograft tissue: A biomechanical, biochemical, and histologic analysis. *Journal of Orthopaedic Research* **26**, 49-55, doi:10.1002/jor.20473 (2008).

141 Changoor, A., Fereydoonzad, L., Yaroshinsky, A. & Buschmann, M. D. Effects of Refrigeration and Freezing on the Electromechanical and Biomechanical Properties of Articular Cartilage. *Journal of Biomechanical Engineering* **132**, doi:10.1115/1.4000991 (2010).
142 Kazemi, M., Dabiri, Y. & Li, L. P. Recent Advances in Computational Mechanics of the Human Knee Joint. *Computational and Mathematical Methods in Medicine* **2013**, 1-27, doi:10.1155/2013/718423 (2013).
143 Venäläinen, M. S. *et al.* Quantitative Evaluation of the Mechanical Risks Caused by Focal Cartilage Defects in the Knee. *Scientific Reports* **6**, doi:10.1038/srep37538 (2016).
144 Halonen, K. S. *et al.* Workflow assessing the effect of gait alterations on stresses in the medial tibial cartilage - combined musculoskeletal modelling and finite element analysis. *Scientific Reports* **7**, doi:10.1038/s41598-017-17228-x (2017).
145 Beer, F. P., Johnston, E. R., DeWolf, J. T. & Mazurek, D. F. *Mechanics of Materials*. 7th Ed. edn, (McGraw-Hill Education, 2015).
146 Abbott, B. C. & Wilkie, D. R. THE RELATION BETWEEN VELOCITY OF SHORTENING AND THE TENSION-LENGTH CURVE OF SKELETAL MUSCLE. *Journal of Physiology* **120**, 2I4-223 (1953).
147 Delp, S. L. *et al.* An interactive graphics-based model of the lower extremity to study orthopaedic surgical procedures. *IEEE TRANSACTIONS ON BIOMEDICAL ENGINEERING* **37**, 757-767, doi:10.1109/10.102791 (1990).
148 Hill, A. V. The mechanics of active muscle. *Proceedings of the Royal Society B: Biological Sciences* **38**, 57-76 (1953).
149 Hurwitz, D. E., Foucher, K. C. & Andriacchi, T. P. A new parametric approach for modeling hip forces during gait. *Journal of Biomechanics* **36**, 113-119, doi:http://dx.doi.org/10.1016/S0021-9290(02)00328-7 (2003).
150 Crowninshield, R. D. & Brand, R. A. A physiologically based criterion of muscle force prediction in locomotion. *Journal of Biomechanics* **14**, 793-801, doi:https://doi.org/10.1016/0021-9290(81)90035-X (1981).
151 Pandy, M. G. & Anderson, F. C. Dynamic Simulation of Human Movement Using Large-Scale Models of the Body. *Phonetica* **57**, 219-228, doi:10.1159/000028475 (2000).
152 Röhrle, H., Scholten, R., Sigolotto, C., Sollbach, W. & Kellner, H. Joint forces in the human pelvis-leg skeleton during walking. *Journal of Biomechanics* **17**, 409-424, doi:https://doi.org/10.1016/0021-9290(84)90033-2 (1984).
153 Seireg, A. & Arvikar, R. J. The prediction of muscular load sharing and joint forces in the lower extremities during walking. *Journal of Biomechanics* **8**, 89-102, doi:https://doi.org/10.1016/0021-9290(75)90089-5 (1975).
154 Simonsen, E. B. *et al.* Bone-on-Bone Forces during Loaded and Unloaded Walking. *Cells Tissues Organs* **152**, 133-142, doi:10.1159/000147692 (1995).
155 Anderson, F. C. & Pandy, M. G. Static and dynamic optimization solutions for gait are practically equivalent. *Journal of Biomechanics* **34**, 153-161, doi:https://doi.org/10.1016/S0021-9290(00)00155-X (2001).
156 Pedotti, A., Krishnan, V. V. & Stark, L. Optimization of muscle-force sequencing in human locomotion. *Mathematical Biosciences* **38**, 57-76, doi:https://doi.org/10.1016/0025-5564(78)90018-4 (1978).
157 Romainbehar. License: https://creativecommons.org/publicdomain/zero/1.0/deed.en (Wikimedia Commons, 2019).

158 Jordan, C. D. *et al.* Variability of CubeQuant T1ρ, quantitative DESS T2, and cones sodium MRI in knee cartilage. *Osteoarthritis and Cartilage* **22**, 1559-1567, doi:10.1016/j.joca.2014.06.001 (2014).
159 Raya, J. G., Ruiz, A. & Ferizi, U. Revisiting the experriimental base of compositional biomarkers: A meta-analysis study. *ISMRM 2017* (2017).
160 Nieminen, M. T. *et al.* T2 Relaxation Reveals Spatial Collagen Architecture in Articular Cartilage: A Comparative Quantitative MRI and Polarized Light Microscopic Study. *Magnetic Resonance in Medicine* **46**, 487-493 (2001).
161 Souza, R. B. *et al.* The effects of acute loading on T1rho and T2 relaxation times of tibiofemoral articular cartilage. *Osteoarthritis and Cartilage* **18**, 1557-1563, doi:10.1016/j.joca.2010.10.001 (2010).
162 Souza, R. B. *et al.* Response of knee cartilage T1rho and T2 relaxation times to in vivo mechanical loading in individuals with and without knee osteoarthritis. *Osteoarthritis and Cartilage* **22**, 1367-1376, doi:10.1016/j.joca.2014.04.017 (2014).
163 Maher, S. A. *et al.* Clinical platform for understanding the relationship between joint contact mechanics and articular cartilage changes after meniscal surgery. *Journal of Orthopaedic Research* **35**, 600-611, doi:10.1002/jor.23365 (2017).
164 Son, M. *et al.* Regional variation in T1ρ and T2 times in osteoarthritic human menisci: correlation with mechanical properties and matrix composition. *Osteoarthritis and Cartilage* **21**, 796-805, doi:10.1016/j.joca.2013.03.002 (2013).
165 McWalter, E. J., Gold, G. E., Alley, M. T. & Hargreaves, B. A. T2 and T2* Relaxometry in the Meniscus using a Novel, Rapid Multi-Echo Steady State Sequence. *ISMRM 2013* (2013).
166 Berberat, J. E., Nissi, M. J., Jurvelin, J. S. & Nieminen, M. T. Assessment of interstitial water content of articular cartilage with T1 relaxation. *Magnetic Resonance Imaging* **27**, 727-732, doi:10.1016/j.mri.2008.09.005 (2009).
167 Alhadlaq, H. A. & Xia, Y. The structural adaptations in compressed articular cartilage by microscopic MRI (μMRI) T2 anisotropy. *Osteoarthritis and Cartilage* **12**, 887-894, doi:10.1016/j.joca.2004.07.006 (2004).
168 Zheng, S. & Xia, Y. The collagen fibril structure in the superficial zone of articular cartilage by μMRI. *Osteoarthritis and Cartilage* **17**, 1519-1528, doi:10.1016/j.joca.2009.05.013 (2009).
169 Matzat, S. J., McWalter, E. J., Kogan, F., Chen, W. & Gold, G. E. T2 Relaxation time quantitation differs between pulse sequences in articular cartilage. *Journal of Magnetic Resonance Imaging* **42**, 105-113, doi:10.1002/jmri.24757 (2015).
170 Kurkijärvi, J. E., Nissi, M. J., Kiviranta, I., Jurvelin, J. S. & Nieminen, M. T. Delayed gadolinium-enhanced MRI of cartilage (dGEMRIC) andT2characteristics of human knee articular cartilage: Topographical variation and relationships to mechanical properties. *Magnetic Resonance in Medicine* **52**, 41-46, doi:10.1002/mrm.20104 (2004).
171 Lammentausta, E. *et al.* T2 relaxation time and delayed gadolinium-enhanced MRI of cartilage (dGEMRIC) of human patellar cartilage at 1.5 T and 9.4 T: Relationships with tissue mechanical properties. *Journal of Orthopaedic Research* **24**, 366-374, doi:10.1002/jor.20041 (2006).
172 Lammentausta, E. *et al.* Quantitative MRI of parallel changes of articular cartilage and underlying trabecular bone in degeneration. *Osteoarthritis and Cartilage* **15**, 1149-1157, doi:10.1016/j.joca.2007.03.019 (2007).

173 Nissi, M. J. *et al.* Estimation of mechanical properties of articular cartilage with MRI – dGEMRIC, T2 and T1 imaging in different species with variable stages of maturation. *Osteoarthritis and Cartilage* **15**, 1141-1148, doi:10.1016/j.joca.2007.03.018 (2007).
174 Raya, J. G. *et al.* Change of Diffusion Tensor Imaging Parameters in Articular Cartilage With Progressive Proteoglycan Extraction. *Investigative Radiology* **46**, 401-409 (2011).
175 Baldassarri, M. *et al.* Relationship between cartilage stiffness and dGEMRIC index: Correlation and prediction. *Journal of Orthopaedic Research* **25**, 904-912, doi:10.1002/jor.20378 (2007).
176 Juras, V. *et al.* In vitro determination of biomechanical properties of human articular cartilage in osteoarthritis using multi-parametric MRI. *Journal of Magnetic Resonance* **197**, 40-47, doi:10.1016/j.jmr.2008.11.019 (2009).
177 Keenan, K. E. *et al.* T1ρ Dispersion in Articular Cartilage. *Cartilage* **6**, 113-122, doi:10.1177/1947603515569529 (2015).
178 Rautiainen, J. *et al.* Multiparametric MRI assessment of human articular cartilage degeneration: Correlation with quantitative histology and mechanical properties. *Magnetic Resonance in Medicine* **74**, 249-259, doi:10.1002/mrm.25401 (2015).
179 Tang, S. Y. *et al.* Local tissue properties of human osteoarthritic cartilage correlate with magnetic resonance T1rho relaxation times. *Journal of Orthopaedic Research* **29**, 1312-1319, doi:10.1002/jor.21381 (2011).
180 Cotofana, S. *et al.* In vivo measures of cartilage deformation: patterns in healthy and osteoarthritic female knees using 3T MR imaging. *European Radiology* **21**, 1127-1135, doi:10.1007/s00330-011-2057-y (2011).
181 Wang, H. *et al.* An MRI-compatible loading device to assess knee joint cartilage deformation: Effect of preloading and inter-test repeatability. *Journal of Biomechanics* **48**, 2934-2940, doi:10.1016/j.jbiomech.2015.08.006 (2015).
182 Chan, D. D. *et al.* In vivo articular cartilage deformation: noninvasive quantification of intratissue strain during joint contact in the human knee. *Scientific Reports* **6**, doi:10.1038/srep19220 (2016).
183 Nishii, T., Kuroda, K., Matsuoka, Y., Sahara, T. & Yoshikawa, H. Change in knee cartilage T2 in response to mechanical loading. *Journal of Magnetic Resonance Imaging* **28**, 175-180, doi:10.1002/jmri.21418 (2008).
184 Subburaj, K. *et al.* Association of MR relaxation and cartilage deformation in knee osteoarthritis. *Journal of Orthopaedic Research* **30**, 919-926, doi:10.1002/jor.22031 (2012).
185 Szomolányi, P. *et al.* Evaluation of compression properties of human knee cartilage - In-vivo study at 7T MRI. *IEEE 11th International Conference on Measurement* (2017).
186 Neu, C. P., Hull, M. L., Walton, J. H. & Buonocore, M. H. MRI-based technique for determining nonuniform deformations throughout the volume of articular cartilage explants. *Magnetic Resonance in Medicine* **53**, 321-328, doi:10.1002/mrm.20343 (2005).
187 Zevenbergen, L. *et al.* Functional assessment of strains around a full-thickness and critical sized articular cartilage defect under compressive loading using MRI. *Osteoarthritis and Cartilage* **26**, 1710-1721, doi:10.1016/j.joca.2018.08.013 (2018).
188 Nebelung, S., J., T., C., K. & D., T. PRECISE PRESSURE-CONTROLLED LOADING TO QUANTIFY CARTILAGE AND MENISCUS FUNCTIONALITY BASED ON ADVANCED MRI TECHNIQUES. *13th IWOAI* (2019).

189 Danso, E. K. *et al.* Structure-function relationships of human meniscus. *Journal of the Mechanical Behavior of Biomedical Materials* **67**, 51-60, doi:10.1016/j.jmbbm.2016.12.002 (2017).
190 Orozco, G. A., Tanska, P., Mononen, M. E., Halonen, K. S. & Korhonen, R. K. The effect of constitutive representations and structural constituents of ligaments on knee joint mechanics. *Scientific Reports* **8**, doi:10.1038/s41598-018-20739-w (2018).
191 Duffy, D. J., Millard, R. P., Breur, G. J., Moore, G. E. & Main, R. P. Ex vivo biomechanical comparison of barbed suture and standard polypropylene suture for acute tendon laceration in a canine model. *Veterinary and Comparative Orthopaedics and Traumatology* **28**, 263-269, doi:10.3415/vcot-14-11-0174 (2015).
192 Lai, C. H. Y. & Li-Tsang, C. W. P. Validation of the Pliance X System in measuring interface pressure generated by pressure garment. *Burns* **35**, 845-851, doi:10.1016/j.burns.2008.09.013 (2009).
193 Glüer, C.-C. *et al.* Accurate Assessment of Precision Errors: How to Measure the Reproducibility of Bone Densitometry Techniques. *Osteoporosis International* **5**, 262-270 (1995).
194 Elebute, I. O. *Repeatability of an Integrative Method to Assess Knee Joint Mechanics and Cartilage Health under Load* MSc. thesis, University of Saskatchewan, (2020).
195 Menezes NM, Gray ML, Hartke JR & D., B. T2 and TI rho MRI in articular cartilage systems. *Magn Reson Med*, 503-509 (2004).
196 Nieminen, M. T. *et al.* Quantitative MR Microscopy of Enzymatically Degraded Articular Cartilage. *Magnetic Resonance in Medicine* **43**, 676–681 (2000).
197 Wayne, J. S. *et al.* MR Imaging of Normal and Matrix-depleted Cartilage: Correlation with Biomechanical Function and Biochemical Composition. *Radiology* **228** (2003).
198 Andrewmeyerson. License: https://creativecommons.org/licenses/by-sa/4.0/deed.en (Wikimedia Commons, 2016).
199 Rodríguez, M. License: https://creativecommons.org/licenses/by-sa/4.0/deed.en (Wikimedia Commons, 2019).
200 Gold, G. E. *et al.* Musculoskeletal MRI at 3.0 T: Relaxation Times and Image Contrast. *American Journal of Roentgenology* **183**, 343–351 (2004).
201 Jordan, C. D., Saranathan, M., Bangerter, N. K., Hargreaves, B. A. & Gold, G. E. Musculoskeletal MRI at 3.0T and 7.0T: A comparison of relaxation times and image contrast. *European Journal of Radiology* **82**, 734-739, doi:10.1016/j.ejrad.2011.09.021 (2013).
202 Glantz, S. A. *Primer of Biostatistics*. 7th Ed. edn, (McGraw-Hill Medical, 2012).
203 Evans, J. D. *Straightforward Statistics for the Behavioral Sciences*. (Brooks/Cole Publishing Company, 1996).
204 Prescott, R. J. Editorial: Avoid being tripped up by statistics: Statistical guidance for a successful research paper. *Gait & Posture* **72**, 240-249, doi:10.1016/j.gaitpost.2018.06.172 (2019).
205 Navidi, W. *Statistics for Engineers and Scientists*. (McGraw-Hill Science/Engineering/Math, 2010).
206 Koo, S., Gold, G. E. & Andriacchi, T. P. Considerations in measuring cartilage thickness using MRI: factors influencing reproducibility and accuracy. *Osteoarthritis and Cartilage* **13**, 782-789, doi:10.1016/j.joca.2005.04.013 (2005).

207 Budynas, R. G. *Advanced Strength and Applied Stress Analysis*. 2nd Ed. edn, (McGraw-Hill Companies, 1999).
208 Budynas, R. G. & Nisbett, J. K. *Shigley's Mechanical Engineering Design*. 10th Ed. edn, (McGraw-Hill Education, 2015).
209 Martinez, D. D. L. License: https://creativecommons.org/licenses/by-sa/3.0/deed.en (Wikimedia Commons, 2006).
210 Chandrupatla, T. R. & Belegundu, A. D. *INTRODUCTION TO FINITE ELEMENTS IN ENGINEERING*. 3rd edn, (Prentice Hall, 2002).
211 Strzelecki, T. & Strzelecki, M. Relation Between Filtration and Soil Consolidation Theories. *Studia Geotechnica et Mechanica* **37**, 105-114, doi:10.1515/sgem-2015-0012 (2015).
212 Bartel, D. L., Davy, D. T. & Keaveny, T. M. *Orthopaedic Biomechanics: Mechanics and Design in Musculoskeletal Systems*. 1st edn, (Pearson/Prentice Hall, 2006).
213 Johnson, F., Scarrow, P. & Waugh, W. Assessment of loads in the knee joint. *Medical & Biological Engineering & Computing* **19**, 237-243 (1981).
214 Schipplein, D. & Andriacchi, T. P. Interaction Between Active and Passive Knee Stabilizers During Level Walking. *Journal of Orthopaedic Research* **9**, 113-119 (1991).
215 Mott, P. H. & Roland, C. M. Limits to Poisson's ratio in isotropic materials. *Physical Review B* **80**, doi:10.1103/PhysRevB.80.132104 (2009).
216 Rivlin, R. S. LARGE ELASTIC DEFORMATIONS OF ISOTROPIC MATERIALS IV. FURTHER DEVELOPMENTS OF THE GENERAL THEORY. *Proceedings of the Royal Society* **241**, 379-397 (1947).
217 Mooney, M. A Theory of Large Elastic Deformation. *Journal of Applied Physics* **11**, 582-592, doi:10.1063/1.1712836 10.1063/1.1710039 10.1063/1.1723785 10.1063/1.1723791 (1940).
218 Ogden, R. W. Large deformation isotropic elasticity — on the correlation of theory and experiment for incompressible rubberlike solids. *Proceedings of the Royal Society* **326**, 565-584 (1972).
219 Pence, T. J. & Gou, K. On compressible versions of the incompressible neo-Hookean material. *Mathematics and Mechanics of Solids* **20**, 157–182 (2015).
220 Kazemi, M. & Li, L. P. A viscoelastic poromechanical model of the knee joint in large compression. *Medical Engineering & Physics* **36**, 998-1006, doi:10.1016/j.medengphy.2014.04.004 (2014).
221 Young, W. C. & Budynas, R. G. *Roark's Formulas for Stress and Strain*. 7th edn, (McGraw-Hill, 2002).
222 Bursac, P. M., Obitz, T. W., Eisenberg, S. R. & Stamenovic, D. Confined and unconfined stress relaxation of cartilage: appropriateness of a transversely isotropic analysis. *Journal of Biomechanics* **32**, 1125-1130 (1999).
223 Ashby, M. F. *Materials Selection in Mechanical Design*. (Butterworth-Heinemann, 2011).
224 ASM. in *Volume 1: Properties and Selection: Irons Steels and High Performance Alloys* (ASM International, Metal Park, 2005).
225 Arjmand, H. *et al.* Mechanical Metrics of the Proximal Tibia are Precise and Differentiate Osteoarthritic and Normal Knees: A Finite Element Study. *Scientific Reports* **8**, doi:10.1038/s41598-018-29880-y (2018).

226 Venäläinen, M. S. *et al.* Importance of Material Properties and Porosity of Bone on Mechanical Response of Articular Cartilage in Human Knee Joint—A Two-Dimensional Finite Element Study. *Journal of Biomechanical Engineering* **136**, 121005, doi:10.1115/1.4028801 (2014).
227 Danso, E. K. *et al.* Characterization of site-specific biomechanical properties of human meniscus—Importance of collagen and fluid on mechanical nonlinearities. *Journal of Biomechanics* **48**, 1499-1507, doi:10.1016/j.jbiomech.2015.01.048 (2015).
228 Gu, K. B. & Li, L. P. A human knee joint model considering fluid pressure and fiber orientation in cartilages and menisci. *Medical Engineering & Physics* **33**, 497-503, doi:10.1016/j.medengphy.2010.12.001 (2011).
229 Mow, V. C., Kuei, S. C., Lai, W. M. & Armstrong, C. G. Biphasic Creep and Stress Relaxation of Articular Cartilage in Compression: Theory and Experiments. *Journal of Biomechanical Engineering* **102**, 73-84 (1980).
230 Kazemi, M., Li, L. P., Buschmann, M. D. & Savard, P. Partial Meniscectomy Changes Fluid Pressurization in Articular Cartilage in Human Knees. *Journal of Biomechanical Engineering* **134**, doi:10.1115/1.4005764 (2012).
231 Li, L. P., Cheung, J. T. M. & Herzog, W. Three-dimensional fibril-reinforced finite element model of articular cartilage. *Medical & Biological Engineering & Computing* **47**, 607-615, doi:10.1007/s11517-009-0469-5 (2009).
232 Klets, O. *et al.* Estimation of the Effect of Body Weight on the Development of Osteoarthritis Based on Cumulative Stresses in Cartilage: Data from the Osteoarthritis Initiative. *Annals of Biomedical Engineering* **46**, 334-344, doi:10.1007/s10439-017-1974-6 (2017).
233 Tanska, P., Mononen, M. E. & Korhonen, R. K. A multi-scale finite element model for investigation of chondrocyte mechanics in normal and medial meniscectomy human knee joint during walking. *Journal of Biomechanics* **48**, 1397-1406, doi:10.1016/j.jbiomech.2015.02.043 (2015).
234 Kazemi, M., Li, L. P., Savard, P. & Buschmann, M. D. Creep behavior of the intact and meniscectomy knee joints. *Journal of the Mechanical Behavior of Biomedical Materials* **4**, 1351-1358, doi:10.1016/j.jmbbm.2011.05.004 (2011).
235 Dabiri, Y. & Li, L. P. Altered Knee Joint Mechanics in Simple Compression Associated with Early Cartilage Degeneration. *Computational and Mathematical Methods in Medicine* **2013**, 1-11, doi:10.1155/2013/862903 (2013).
236 Asadi, R. & Ataie-Ashtiani, B. A comparison of finite volume formulations and coupling strategies for two-phase flow in deforming porous media. *Computers and Geotechnics* **67**, 17-32, doi:10.1016/j.compgeo.2015.02.004 (2015).
237 Asadi, R., Ataie-Ashtiani, B. & Simmons, C. T. Finite volume coupling strategies for the solution of a Biot consolidation model. *Computers and Geotechnics* **55**, 494-505, doi:10.1016/j.compgeo.2013.09.014 (2014).
238 Helmig, R., Flemisch, B., Wolff, M., Ebigbo, A. & Class, H. Model coupling for multiphase flow in porous media. *Advances in Water Resources* **51**, 52-66, doi:10.1016/j.advwatres.2012.07.003 (2013).
239 Li, L. P., Soulhat, J., Buschmann, M. D. & Shirazi-Adl, A. Nonlinear analysis of cartilage in unconfined ramp compression using a fibril reinforced poroelastic model. *Clinical Biomechanics* **14**, 673-682 (1999).

240 Li, L. P., Buschmann, M. D. & Shirazi-Adl, A. A fibril reinforced nonhomogeneous poroelastic model for articular cartilage: inhomogeneous response in unconfined compression. *Journal of Biomechanics* **33**, 1533-1541 (2000).
241 Li, L. P., Shirazi-Adl, A. & Buschmann, M. D. Alterations in Mechanical Behaviour of Articular Cartilage due to Changes in Depth Varying Material Properties--a Nonhomogeneous Poroelastic Model Study. *Computer Methods in Biomechanics and Biomedical Engineering* **5**, 45-52, doi:10.1080/10255840290008088 (2002).
242 Wilson, W., van Donkelaar, C. C., van Rietbergen, B., Ito, K. & Huiskes, R. Stresses in the local collagen network of articular cartilage: a poroviscoelastic fibril-reinforced finite element study. *Journal of Biomechanics* **37**, 357-366, doi:10.1016/s0021-9290(03)00267-7 (2004).
243 Wilson, W., van Donkelaar, C. C., van Rietbergen, B. & Huiskes, R. A fibril-reinforced poroviscoelastic swelling model for articular cartilage. *Journal of Biomechanics* **38**, 1195-1204, doi:10.1016/j.jbiomech.2004.07.003 (2005).
244 Julkunen, P. *et al.* Stress–relaxation of human patellar articular cartilage in unconfined compression: Prediction of mechanical response by tissue composition and structure. *Journal of Biomechanics* **41**, 1978-1986, doi:10.1016/j.jbiomech.2008.03.026 (2008).
245 Korhonen, R. K., Julkunen, P., Li, L. & van Donkelaar, C. C. Computational Models of Articular Cartilage. *Computational and Mathematical Methods in Medicine* **2013**, 1-2, doi:10.1155/2013/254507 (2013).
246 Mononen, M. E. *et al.* Effect of superficial collagen patterns and fibrillation of femoral articular cartilage on knee joint mechanics—A 3D finite element analysis. *Journal of Biomechanics* **45**, 579-587, doi:10.1016/j.jbiomech.2011.11.003 (2012).
247 Kapitola, P. License: https://creativecommons.org/licenses/by-sa/2.5/deed.en (Wikimedia Commons, 2018).
248 Tweten, D. J., Okamoto, R. J., Schmidt, J. L., Garbow, J. R. & Bayly, P. V. Estimation of material parameters from slow and fast shear waves in an incompressible, transversely isotropic material. *Journal of Biomechanics* **48**, 4002 - 4009 (2015).
249 Venäläinen, M. S. *et al.* Effect of bone inhomogeneity on tibiofemoral contact mechanics during physiological loading. *Journal of Biomechanics* **49**, 1111-1120, doi:10.1016/j.jbiomech.2016.02.033 (2016).
250 Ali, A. A. *et al.* Combined measurement and modeling of specimen-specific knee mechanics for healthy and ACL-deficient conditions. *Journal of Biomechanics* **57**, 117-124, doi:10.1016/j.jbiomech.2017.04.008 (2017).
251 Shirazi, R. & Shirazi-Adl, A. Computational biomechanics of articular cartilage of human knee joint: Effect of osteochondral defects. *Journal of Biomechanics* **42**, 2458-2465, doi:10.1016/j.jbiomech.2009.07.022 (2009).
252 Boskey, A. L. Bone composition: relationship to bone fragility and antiosteoporotic drug effects. *BoneKEy Reports* **2**, doi:10.1038/bonekey.2013.181 (2013).
253 Hayes, W. in *Basic orthopaedic biomechanics* 93-142 (Raven Press, 1991).
254 Öhman, C. *et al.* Compressive behaviour of child and adult cortical bone. *Bone* **49**, 769-776, doi:10.1016/j.bone.2011.06.035 (2011).
255 Morgan, E. F. & Keaveny, T. M. Dependence of yield strain of human trabecular bone on anatomic site. *Journal of Biomechanics* **34**, 569–577 (2001).

256 Helgason, B. *et al.* Mathematical relationships between bone density and mechanical properties: A literature review. *Clinical Biomechanics* **23**, 135-146, doi:10.1016/j.clinbiomech.2007.08.024 (2008).
257 Hart, N. H. *et al.* Mechanical basis of bone strength: influence of bone material, bone structure and muscle action. *Journal of Musculoskeletal and Neuronal Interactions* (2017).
258 Lai, W. M., Hou, J. S. & Mow, V. C. A Triphasic Theory for the Swelling and Deformation Behaviors of Articular Cartilage. *Journal of Biomechanical Engineering* **113**, 245-258, doi:10.1115/1.2894880 (1991).
259 Linn, F. C. & Sokoloff, L. Movement and composition of interstitial fluid of cartilage. *Arthritis and Rheumatism* **8**, 481-494 (1965).
260 Maroudas, A. in *Adult articular cartilage* 215-290 (Pitman Medical Publishing, 1979).
261 Maroudas, A., Bayliss, M. T. & Venn, M. F. Further studies on the composition of human femoral head cartilage. *Annals of the Rheumatic Diseases* **39**, 514-523 (1980).
262 Mow, V. C., Holmes, M. H. & Lai, W. M. FLUID TRANSPORT AND MECHANICAL PROPERTIES OF ARTICULAR CARTILAGE: A REVIEW. *Journal of Biomechanics* **17**, 377-394 (1984).
263 Muir, H. in *Adult articular cartilage* 145-214 (Pittman Medical, 1979).
264 Stockwell, R. A. & Scott, J. E. Distribution of Acid Glycosaminoglycans in Human Articular Cartilage. *Nature* **215**, 1376-1378, doi:10.1038/2151376a0 (1967).
265 Stockwell, R. *Biology of cartilage cells*. (Cambridge University Press, 1979).
266 Laasanen, M. S. *et al.* Biomechanical properties of knee articular cartilage. *Biorheology* **40**, 133–140 (2003).
267 Danso, E. K., Honkanen, J. T. J., Saarakkala, S. & Korhonen, R. K. Comparison of nonlinear mechanical properties of bovine articular cartilage and meniscus. *Journal of Biomechanics* **47**, 200-206, doi:10.1016/j.jbiomech.2013.09.015 (2014).
268 Nuki, G., Ferguson, J., Boyle, J. A. & Boddy, K. Rheological Simulation of Synovial Fluid by a Synthetic Polymer Solution. *Nature* **224**, 1118–1119 (1969).
269 Barnett, C. H. MEASUREMENT AND INTERPRETATION OF SYNOVIAL FLUID VISCOSITIES. *Annals of the Rheumatic Diseases* **17**, 229-233 (1958).
270 Xu, Y. *et al.* Computational synovial dynamics of a normal temporomandibular joint during jaw opening. *Journal of the Formosan Medical Association* **112**, 346-351, doi:10.1016/j.jfma.2012.02.015 (2013).
271 Jeon, O. H. & Elisseeff, J. Orthopedic tissue regeneration: cells, scaffolds, and small molecules. *Drug Delivery and Translational Research* **6**, 105-120, doi:10.1007/s13346-015-0266-7 (2015).
272 Ashhurst, D. E. The cartilaginous skeleton of an elasmobranch fish does not heal. *Matrix Biology* **23**, 15-22, doi:10.1016/j.matbio.2004.02.001 (2004).
273 Murphy, M. P. *et al.* Articular cartilage regeneration by activated skeletal stem cells. *Nature Medicine* **26**, 1583-1592, doi:10.1038/s41591-020-1013-2 (2020).
274 College, O. License: https://creativecommons.org/licenses/by/3.0/deed.en (Wikimedia Commons, 2013).
275 Halonen, K. S., Mononen, M. E., Jurvelin, J. S., Töyräs, J. & Korhonen, R. K. Importance of depth-wise distribution of collagen and proteoglycans in articular cartilage—A 3D finite element study of stresses and strains in human knee joint. *Journal of Biomechanics* **46**, 1184-1192, doi:10.1016/j.jbiomech.2012.12.025 (2013).

276 Mononen, M. E., Tanska, P., Isaksson, H. & Korhonen, R. K. A Novel Method to Simulate the Progression of Collagen Degeneration of Cartilage in the Knee: Data from the Osteoarthritis Initiative. *Scientific Reports* **6**, doi:10.1038/srep21415 (2016).
277 Donahue, H., Hull, T. L., M. L. Rashid, Jacobs, M. M. & R., C. A Finite Element Model of the Human Knee Joint for the Study of Tibio-Femoral Contact. *Journal of Biomechanical Engineering* **124**, 273-280, doi:10.1115/1.1470171 (2002).
278 Donahue, T. L. H., Hull, M. L., Rashid, M. M. & Jacobs, C. R. How the stiffness of meniscal attachments and meniscal material properties affect tibio-femoral contact pressure computed using a validated finite element model of the human knee joint. *Journal of Biomechanics* **36**, 19–34 (2003).
279 Wheatley, B. B., Fischenich, K. M., Button, K. D., Haut, R. C. & Haut Donahue, T. L. An optimized transversely isotropic, hyper-poro-viscoelastic finite element model of the meniscus to evaluate mechanical degradation following traumatic loading. *Journal of Biomechanics* **48**, 1454-1460, doi:10.1016/j.jbiomech.2015.02.028 (2015).
280 Yang, N., Nayeb-Hashemi, H. & Canavan, P. K. The Combined Effect of Frontal Plane Tibiofemoral Knee Angle and Meniscectomy on the Cartilage Contact Stresses and Strains. *Annals of Biomedical Engineering* **37**, 2360-2372, doi:10.1007/s10439-009-9781-3 (2009).
281 Łuczkiewicz, P., Daszkiewicz, K., Witkowski, W., Chróścielewski, J. & Zarzycki, W. Influence of meniscus shape in the cross sectional plane on the knee contact mechanics. *Journal of Biomechanics* **48**, 1356-1363, doi:10.1016/j.jbiomech.2015.03.002 (2015).
282 Hao, Z., Jin, D., Zhang, Y. & Zhang, J. A Finite Element 3D Model of in Vivo Human Knee Joint Based on MRI for the Tibiofemoral Joint Contact Analysis. *1st Digital Human Modeling* (2007).
283 Kang, K.-T., Kim, S.-H., Son, J., Lee, Y. H. & Chun, H.-J. In vivo evaluation of the subject-specific finite element model for knee joint cartilage contact area. *International Journal of Precision Engineering and Manufacturing* **16**, 1171-1177, doi:10.1007/s12541-015-0151-9 (2015).
284 Lee, M. & Hyman, W. Modeling of failure mode in knee ligaments depending on the strain rate. *BMC Musculoskeletal Disorders* **3**, 1-8 (2002).
285 Halonen, K. S. *et al.* Optimal graft stiffness and pre-strain restore normal joint motion and cartilage responses in ACL reconstructed knee. *Journal of Biomechanics* **49**, 2566-2576, doi:10.1016/j.jbiomech.2016.05.002 (2016).
286 Räsänen, L. P. *et al.* The effect of fixed charge density and cartilage swelling on mechanics of knee joint cartilage during simulated gait. *Journal of Biomechanics* **61**, 34-44, doi:10.1016/j.jbiomech.2017.06.041 (2017).
287 Beillas, P., Papaioannou, G., Tashman, S. & Yang, K. H. A new method to investigate in vivo knee behavior using a finite element model of the lower limb. *Journal of Biomechanics* **37**, 1019-1030, doi:10.1016/j.jbiomech.2003.11.022 (2004).
288 Anciv. License: https://creativecommons.org/licenses/by-sa/3.0/deed.en (Wikimedia Commons, 2013).
289 Anciv. License: https://creativecommons.org/licenses/by-sa/3.0/deed.en (Wikimedia Commons, 2013).
290 Wang, Z.-Q. & Wang, Y. A Natural Generalization of Linear Isotropic Relations with Seth-Hill Strain Tensors to Transversely Isotropic Materials at Finite Strains. *Mathematical Problems in Engineering* **2016**, 1-9, doi:10.1155/2016/7473046 (2016).

291 Lam, W. License: https://creativecommons.org/licenses/by-sa/2.0/deed.en (Wikimedia Commons, 2016).
292 taw, T. License: https://creativecommons.org/licenses/by-sa/4.0/deed.en (Wikimedia Commons, 2021).
293 Cook, R. D., Malkus, D. S. & Plesha, M. E. *CONCEPTS AND APPLICATIONS OF FINITE ELEMENT ANALYSIS*. 3rd Ed. edn, (John Wiley & Sons, 1989).
294 Hosseinitabatabaei, S., Ashjaee, N. & Tahani, M. Introduction of Maximum Stress Parameter for the Evaluation of Stress Shielding Around Orthopedic Screws in the Presence of Bone Remodeling Process. *Journal of Medical and Biological Engineering* **37**, 703-716, doi:10.1007/s40846-017-0267-8 (2017).
295 Abe, S. *et al.* Exercise loading history and femoral neck strength in a sideways fall: A three-dimensional finite element modeling study. *Bone* **92**, 9-17, doi:10.1016/j.bone.2016.07.021 (2016).
296 Ho, K.-Y., Keyak, J. H. & Powers, C. M. Comparison of patella bone strain between females with and without patellofemoral pain: A finite element analysis study. *Journal of Biomechanics* **47**, 230-236, doi:10.1016/j.jbiomech.2013.09.010 (2014).
297 Wang, Y., Fan, Y. & Zhang, M. Comparison of stress on knee cartilage during kneeling and standing using finite element models. *Medical Engineering & Physics* **36**, 439-447, doi:10.1016/j.medengphy.2014.01.004 (2014).
298 Pal, S. *et al.* Patellofemoral cartilage stresses are most sensitive to variations in vastus medialis muscle forces. *Computer Methods in Biomechanics and Biomedical Engineering* **22**, 206-216, doi:10.1080/10255842.2018.1544629 (2018).
299 Besier, T. F., Gold, G. E., Beaupré, G. S. & Delp, S. L. A Modeling Framework to Estimate Patellofemoral Joint Cartilage Stress In Vivo. *Medicine & Science in Sports & Exercise* **37**, 1924-1930, doi:10.1249/01.mss.0000176686.18683.64 (2005).
300 Dabiri, Y. & Li, L. MECHANICAL RESPONSE OF HUMAN KNEE JOINT TO SINUSOIDAL COMPRESSION – INFLUENCE OF FLUID PRESSURIZATION IN SOFT TISSUES. *ASME 2012 Summer Bioengineering Conference* (2012).
301 Dabiri, Y. & Li, L. A NUMERICAL MODEL OF MECHANICS OF OSTEOARTHRITIS IN HUMAN KNEE JOINT. *ASME 2012 International Mechanical Engineering Congress & Exposition* (2012).
302 Dabiri, Y. & Li, L. P. Influences of the depth-dependent material inhomogeneity of articular cartilage on the fluid pressurization in the human knee. *Medical Engineering & Physics* **35**, 1591-1598, doi:10.1016/j.medengphy.2013.05.005 (2013).
303 Dabiri, Y. & Li, L. Focal cartilage defect compromises fluid-pressure dependent load support in the knee joint. *International Journal for Numerical Methods in Biomedical Engineering* **31**, e02713, doi:10.1002/cnm.2713 (2015).
304 Li, G., Lopez, O. & Rubash, H. Variability of a Three-Dimensional Finite Element Model Constructed Using Magnetic Resonance Images of a Knee for Joint Contact Stress Analysis. *Journal of Biomechanical Engineering* **123**, 341-346, doi:10.1115/1.1385841 (2001).
305 Xu, K., Zi, P. & Ding, X. Gait Analysis of Quadruped Robot Using the Equivalent Mechanism Concept Based on Metamorphosis. *Chinese Journal of Mechanical Engineering* **32**, doi:10.1186/s10033-019-0321-2 (2019).
306 Hartley, C., Folland, J. P., Kerslake, R. & Brooke-Wavell, K. High-Impact Exercise Increased Femoral Neck Bone Density With No Adverse Effects on Imaging Markers of

Knee Osteoarthritis in Postmenopausal Women. *Journal of Bone and Mineral Research* **35**, 53-63, doi:10.1002/jbmr.3867 (2019).
307 6, A. License: https://creativecommons.org/licenses/by-sa/3.0/deed.en (Wikimedia Commons, 2011).
308 Morrison, J. Bioengineering analysis of force actions transmitted by the knee joint. *Biomedical Engineering* **3**, 164-170 (1968).
309 Harrington, I. J. A bioengineering analysis of force actions at the knee in normal and pathological gait. *Biomedical Engineering* **11**, 167-172 (1976).
310 Lebreton, D. C. License: https://creativecommons.org/licenses/by/2.0/deed.en (Wikimedia Commons, 2010).
311 LottieLattes. License: https://creativecommons.org/licenses/by-sa/4.0/deed.en (Wikimedia Commons, 2021).
312 Anderson, F. C. & Pandy, M. G. Dynamic Optimization of Human Walking. *Journal of Biomechanical Engineering* **123**, 381-390, doi:10.1115/1.1392310 (2001).
313 Herssens, N. *et al.* Do spatiotemporal parameters and gait variability differ across the lifespan of healthy adults? A systematic review. *Gait & Posture* **64**, 181-190, doi:10.1016/j.gaitpost.2018.06.012 (2018).
314 Frimenko, R., Goodyear, C. & Bruening, D. Interactions of sex and aging on spatiotemporal metrics in non-pathological gait: a descriptive meta-analysis. *Physiotherapy* **101**, 266-272, doi:10.1016/j.physio.2015.01.003 (2015).
315 Alcock, L., Vanicek, N. & O'Brien, T. D. Alterations in gait speed and age do not fully explain the changes in gait mechanics associated with healthy older women. *Gait & Posture* **37**, 586-592, doi:10.1016/j.gaitpost.2012.09.023 (2013).
316 Kobayashi, Y., Hobara, H., Heldoorn, T. A., Kouchi, M. & Mochimaru, M. Age-independent and age-dependent sex differences in gait pattern determined by principal component analysis. *Gait & Posture* **46**, 11-17, doi:10.1016/j.gaitpost.2016.01.021 (2016).
317 Bovi, G., Rabuffetti, M., Mazzoleni, P. & Ferrarin, M. A multiple-task gait analysis approach: Kinematic, kinetic and EMG reference data for healthy young and adult subjects. *Gait & Posture* **33**, 6-13, doi:10.1016/j.gaitpost.2010.08.009 (2011).
318 Boyer, K. A., Andriacchi, T. P. & Beaupre, G. S. The role of physical activity in changes in walking mechanics with age. *Gait & Posture* **36**, 149-153, doi:10.1016/j.gaitpost.2012.02.007 (2012).
319 Boyer, K. A., Johnson, R. T., Banks, J. J., Jewell, C. & Hafer, J. F. Systematic review and meta-analysis of gait mechanics in young and older adults. *Experimental Gerontology* **95**, 63-70, doi:10.1016/j.exger.2017.05.005 (2017).
320 Cofré, L. E., Lythgo, N., Morgan, D. & Galea, M. P. Aging modifies joint power and work when gait speeds are matched. *Gait & Posture* **33**, 484-489, doi:10.1016/j.gaitpost.2010.12.030 (2011).
321 Fan, Y., Li, Z., Han, S., Lv, C. & Zhang, B. The influence of gait speed on the stability of walking among the elderly. *Gait & Posture* **47**, 31-36, doi:10.1016/j.gaitpost.2016.02.018 (2016).
322 Hullfish, T. J. *et al.* Measuring clinically relevant knee motion with a self-calibrated wearable sensor. *Journal of Biomechanics* **89**, 105-109, doi:10.1016/j.jbiomech.2019.04.003 (2019).

323 Ko, S.-u., Tolea, M. I., Hausdorff, J. M. & Ferrucci, L. Sex-specific differences in gait patterns of healthy older adults: Results from the Baltimore Longitudinal Study of Aging. *Journal of Biomechanics* **44**, 1974-1979, doi:10.1016/j.jbiomech.2011.05.005 (2011).
324 Ko, S.-u., Stenholm, S., Metter, E. J. & Ferrucci, L. Age-associated gait patterns and the role of lower extremity strength – Results from the Baltimore Longitudinal Study of Aging. *Archives of Gerontology and Geriatrics* **55**, 474-479, doi:10.1016/j.archger.2012.04.004 (2012).
325 Jerome, G. J. *et al.* Gait characteristics associated with walking speed decline in older adults: Results from the Baltimore Longitudinal Study of Aging. *Archives of Gerontology and Geriatrics* **60**, 239-243, doi:10.1016/j.archger.2015.01.007 (2015).
326 Saxby, D. J. *et al.* Tibiofemoral contact forces during walking, running and sidestepping. *Gait & Posture* **49**, 78-85, doi:10.1016/j.gaitpost.2016.06.014 (2016).
327 Winter, D. A. *Biomechanics and Motor Control of Human Movement*. (John Wiley & Sons, 2009).
328 Hamill, J., Knutzen, K. M. & Derrick, T. R. *Biomechanical Basis of Human Movement*. 4th Ed. edn, (Lippincott Williams & Wilkins, 2015).
329 Bruns, J., Volkmer, M. & Luessenhop, S. Pressure distribution in the knee joint. Influence of flexion with and without ligament dissection. *Archives of Orthopedic and Trauma Surgery* **113**, 204-209 (1993).
330 Harrington, I. J. Static and dynamic loading patterns in knee joints with deformities. *JBJS* **65**, 247-259 (1983).
331 Johnson, F., Leitl, S. & Waugh, W. THE DISTRIBUTION OF LOAD ACROSS THE KNEE. A COMPARISON OF STATIC AND DYNAMIC MEASUREMENTS. *The Journal of Bone and Joint Surgery* **62**, 346-349 (1980).
332 Yang, N. H., Nayeb-Hashemi, H., Canavan, P. K. & Vaziri, A. Effect of frontal plane tibiofemoral angle on the stress and strain at the knee cartilage during the stance phase of gait. *Journal of Orthopaedic Research* **28**, 1539-1547, doi:10.1002/jor.21174 (2010).

Appendices

A1. Ethics certificate

UNIVERSITY OF SASKATCHEWAN

Biomedical Research Ethics Board (Bio-REB) 22-Jul-2021

Certificate of Re-Approval

Ethics Number:	16-158
Principal Investigator:	Emily McWalter Department: Department of Mechanical Engineering
Locations Where Research Activities are Conducted:	Canadian Light Source, Canada College of Kinesiology, Canada Royal University Hospital, Saskatoon, Canada
Student(s):	Alvaro Espinosa Maldonado Brennan Berryman Chelsey Thorson Ibukunoluwa Elebute Kirstin Olsen Lumeng Cui Madeline Martel
Funder(s):	Canada Foundation for Innovation College of Engineering Innovation Saskatchewan Natural Sciences and Engineering Research Council of Canada Office of the Vice-Provost, Faculty Relations
Sponsor:	
Title:	MRI and Mechanical Testing of Cadaver Knee Specimens
Approval Effective Date:	11-Jul-2021
Expiry Date:	11-Jul-2022
Acknowledgment Of:	
Review Type:	Delegated Review
IRB Registration Number:	Not Applicable

* This study, inclusive of all previously approved documents, has been re-approved until the expiry date noted above

CERTIFICATION

The University of Saskatchewan Biomedical Research Ethics Board (Bio-REB) has reviewed the above-named project.The project is acceptable on scientific and ethical grounds. The principal investigator has the responsibility for any other administrative or regulatory approvals that may pertain to this project, and for ensuring that the authorized project is carried out according to governing law. This approval is valid for the specified period provided there is no change to the approved project.

FIRST TIME REVIEW AND CONTINUING APPROVAL

The University of Saskatchewan Research Ethics Boards review above minimal projects at a full-board (face-to-face) meeting. If a project has been reviewed at a full board meeting, a subsequent project of the same protocol may be reviewed through the delegated review process. Any research classified as minimal risk is reviewed through the delegated (subcommittee) review process. The initial Certificate of Approval includes the approval period the REB has assigned to a study. The Status Report form must be submitted within one month prior to the assigned expiry date. The researcher shall indicate to the REB any specific requirements of the sponsoring organizations (e.g. requirement for full-board review and approval) for the continuing review process deemed necessary for that project.

REB ATTESTATION

In respect to clinical trials, the University of Saskatchewan Research Ethics Board complies with the membership requirements for Research Ethics Boards defined in Part 4 of the Natural Health Products Regulations and Part C Division 5 of the Food and Drug Regulations and carries out its functions in a manner consistent with Good Clinical Practices. Members of the Bio-REB who are named as investigators, do not participate in the discussion related to, nor vote on such studies when presented to the Bio-REB. This approval and the views of this REB have been documented in writing. The University of Saskatchewan Biomedical Research Ethics Board is constituted and operates in accordance with the current version of the Tri-Council Policy Statement: Ethical Conduct for Research Involving Humans (TCPS 2 2018).

Digitally Approved by Dr. Gordon McKay, Ph.D.
Chair, Biomedical Research Ethics Board
University of Saskatchewan

A2. Additional background

A2.1. Deformable body mechanics (from machines to biological systems under load)

The following is based on theory that is available in many engineering and/or applied mechanics textbooks. The specific references used here are: "Mechanics of Materials", "Advanced Strength and Applied Stress Analysis" and "Shigley's Mechanical Engineering Design"[145,207,208]. The reason for including this section is to provide sufficient background and set the proper context for this research (regarding knee loading response, advanced mechanical design and experimental biomechanical testing). This section provides an overview of mechanical loading modes and their manifestation in real-life biomechanics. This is followed by a sequel to the anatomy section, which further explores knee tissue composition. Lastly, the deformation response of these tissues to mechanical loads applied by physical activities is discussed.

The most basic description of an object's motion is through a *particle* (a mathematical point), which can translate in any direction. The next level involves considering the size of the objects in question via *rigid bodies* (each being a system of particles, where all particles are fixed relative to each other), for which one can also consider object's rotations. *Deformable bodies* (systems of particles, where particles can displace relative to each other) refers to yet another category, where one also considers the deformations that the object can experience throughout any process. As subtly hinted in this section's title, this description is so complete that it allows describing from the simplest mechanical components (e.g., springs deformed by some static weight) all the way to the cartilage inside your body carrying the impact as you run. However, to describe any of these motions or deformations, frames of reference are necessary.

A2.1.1. Loading

The following fundamental concepts involving (bio)mechanical loading, material constitution and deformation response are essential for this project, in particular due to loading rig-knee specimen interactions. Deformation is the result of loading applied to an object, for which this response depends on the properties of the object (geometry, material), as well as on the applied loads (e.g., mechanical, thermal, and/or electromagnetic). Regardless of what caused them, the main kinds of mechanical loading are direct axial, shear (abbreviated "sh"), bending (abbreviated "bend") and torsion (Figure 0-1)[145].

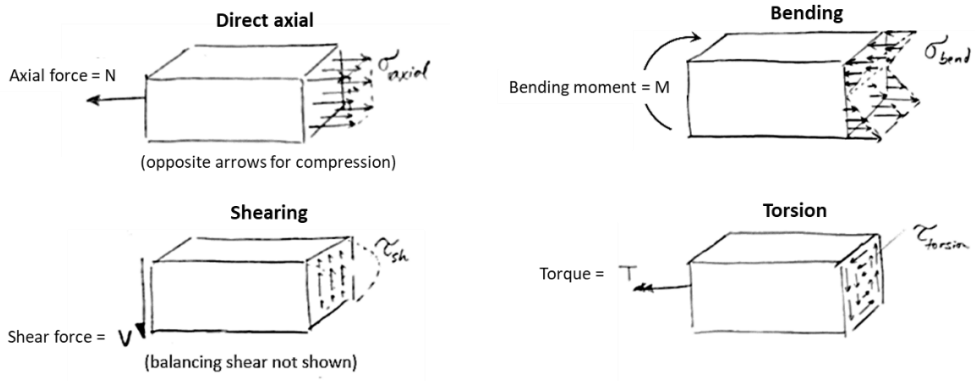

Figure 0-1: Types of mechanical loading (main failure modes, internal resultants and stress distributions)

Of course, more complicated loading may arise as a combination of these simpler cases (Figure 0-2A) or as a unique non-uniform loading (Figure 0-2B). In either situation, such externally applied loads are balanced by internal loads in the material, which result in the generalized stress state of every single element that composes the material (Figure 0-2C), making up an internal load-response tensor field[145,207,208].

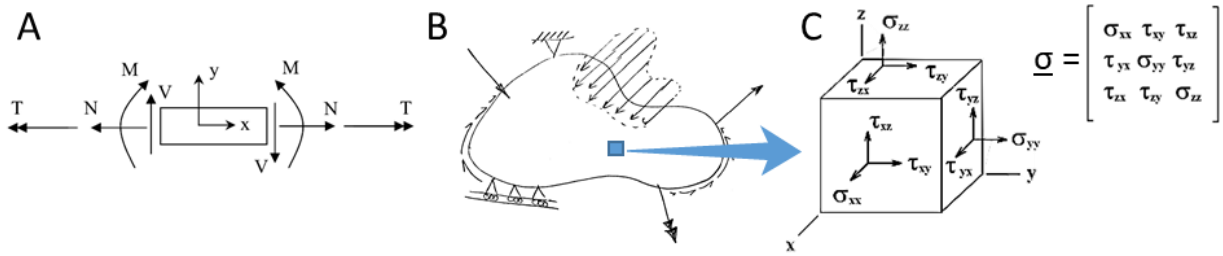

Figure 0-2: Complex loading: A) Combined loading resultants, B) Arbitrary non-uniform stress boundary conditions, and C) Full state of stress for generalized combined loading (stresses on back faces not shown). Images courtesy of Dr. Allan Dolovich and adapted from Wikimedia Commons[209].

Fundamental concepts in applied mechanics theory and all its ramifications (containing biomechanics) include *stress*, σ, and *strain*, ε (the latter expressing deformation and explained in detail by the end of this section). The (mechanical) stress tensor, $\underline{\sigma}$, describes all possible forces every face of any material element could experience in three dimensions, for which its most fundamental definition is force per unit area[207]. Stress is the intensive property equivalent of applied loading (extensive property) as shown in Figure 0-1. At the continuum level, no matter how complex, initial conditions (ICs) and/or boundary conditions (BCs) can only translate in either

normal, σ, or shearing stresses, τ, and every single solid mechanics problem can be described by the partial differential equations (PDEs) of motion, abbreviated as

$$\vec{\nabla} \cdot \underline{\sigma} + \frac{\vec{F}}{\forall} = \rho \frac{\partial^2 \vec{u}}{\partial t^2}, \tag{0-1}$$

alongside ICs, BCs and constitutive relations (section A2.1.2)[207,210]. Continuum mechanics is described by similar systems of equations incorporating fluid behaviour and solid/fluid interactions[211], therefore allowing the description of different time-dependent processes (in addition to inertial effects, $\rho \frac{\partial^2 \vec{u}}{\partial t^2}$, and transient specific body forces, $\vec{F}/\forall$). These equations can be solved only for idealized cases without numerical simulations, whose implementation is challenged by common biomechanics processes. To tackle the overwhelming task of handling such complicated BCs for every single tissue in the knee, a biomechanics approach considers an equivalent representation of all these internal forces as external joint loads. Six external reactions (forces and moments in three directions) are determined by a load balance[28,35,212-214], which satisfies translational and rotational equilibrium equations, and this method can be used to apply these external BCs to any tissue(s) of interest. For the knee, the ligament, articular soft tissue, muscle and contact forces can be reduced to forces and moments along the flexion/extension, abduction/adduction and internal/external rotation directions (Figure 0-3).

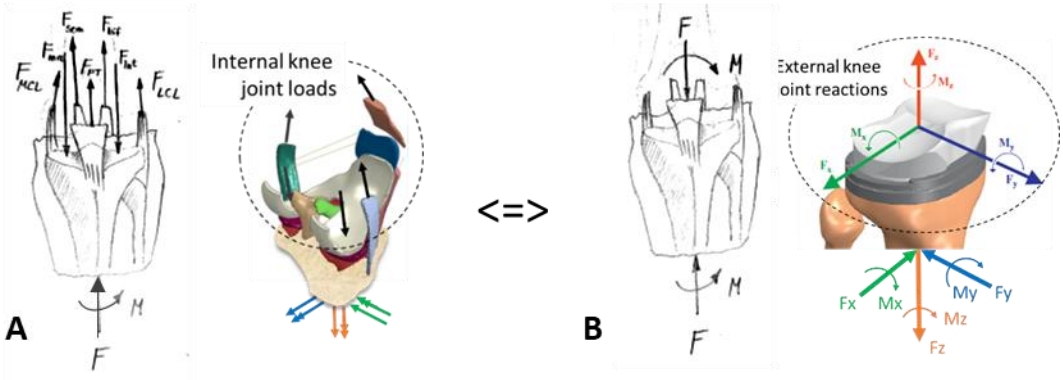

Figure 0-3: Knee "internal" physiologic loads (A) vs. "external" equivalent loads (B) – Two- and Three-dimensional (2D & 3D) views. Adapted with permission from Orozco et al. 2018[190] and Kutzner et al. 2010[42]

A2.1.2. Material constitution

The rationale for this section is to describe the multiple material behaviours interacting within biological tissues as well as in machine components to illustrate how both contribute to overall mechanical responses (e.g., in biomechanics testing or inside knee implants). The structure of this section is divided into a general description of common behaviours shared among most materials, after which specific characteristics of biological soft tissues is presented. At the end, the material composition of every tissue of the knee joint is described in depth.

A2.1.2.1. General material behaviour

The amount and type of deformation of every material depends on a fundamental quantity, stiffness. In its most basic expression, stiffness is the resistance to deformation due to applied loading[i], and it can describe any of the main loading modes (and their resulting deformation). Stiffness can refer to resistance due to the material itself via the elastic (Young's) modulus, *E*, or its rotational counterpart, the shear modulus of rigidity, $G = \frac{E}{2(1+\nu)}$, where $\nu = -\frac{\varepsilon_{transv}}{\varepsilon_{axial}} \in [-1,0.5]$[ii] is Poisson's ratio[215] (relating axial and transverse deformations), or due to geometric characteristics, such as cross-sectional area, *A*, 1st moment of area of a portion *A** of the cross section, $(Q_i)_{A*} = \iint_{A*} x_i dA$, 2nd moment of area of the entire cross section, $I_{ii} = \iint_A {x_j}^2 dA$, product moments of area, $I_{ij} = \iint_A x_i x_j dA$, polar moment of area, $J = I_{ii} + I_{jj}$, or other geometric properties derived from those, such as rigidity due to both material and geometry (e.g., *EA, JG, EI*)[145]. In some cases (common for the biomedical field), it is further extended to the (bulk) stiffness, *k*, of entire components (e.g., springs) or complex structures (e.g., articular cartilage). For some materials, this elongation resistance can be different for tensile and compressive cases but, in general, this material behavior is described by Hooke's law[26],

$$\sigma = E\varepsilon \Leftrightarrow \varepsilon = C\sigma, \qquad C = E^{-1}, \tag{0-2}$$

[i] Analogous (and complimentary) relative to how inertia is the resistance to altering rigid body motion (often due to external loading)

[ii] Thermodynamic bounds for isotropic materials

which is the basis for characterizing material isotropy, where this material behavior is uniformly observed in all possible directions, since their constituents are randomly oriented. There are corresponding expressions for other loading modes and directions, up to generalized Hooke's law for describing linear-elastic 3D isotropic behavior[145], and much more involved models for fully anisotropic materials. These are essentially described by the same equation as Hooke's law, but considering stress and strain as vectors (tensor components concatenated as one column vector) related by a stiffness matrix (or its inverse, the compliance matrix, C)[210]. Stress-strain relationships can be rewritten by expressing material properties in terms of specific strain energy (energy required to produce deformation per unit volume) and more advanced hyperelastic material descriptions require it to describe "exotic" materials or constituents of biological soft tissues (anisotropic composites)[38,216-220].

Failure is another important aspect of material behavior tied to elasticity, strength and ductility. Elasticity refers to thermodynamically reversible material deformation, prior to its permanent yielding threshold, beyond which the material enters its thermodynamically irreversible plasticity regime (Figure 0-4)[26]. Depending on the situation, material failure can refer to objects yielding or breaking and it is avoided (e.g., in mechanical design) as much as required (e.g., in manufacturing). Hence, failure can be characterized by the yield strength, S_{yield} (or corresponding strain, ε_{yield}) and via the ultimate or fracture strengths, $S_u \gtrapprox S_f$ (or corresponding strains, $\varepsilon_u < \varepsilon_f$). Strength, S, refers to materials' resistance to failure and it is defined as the stress level, beyond which yielding or fracture occurs. Which failure mechanism happens first depends on the material's ductility, the ability to delay yielding and sustain elastic deformation (characterized by ε_{yield})[208]. For brittle materials (with relatively lower ductility), such as ceramics, some metals and cortical bone, sudden fracture occurs shortly after 'yielding'[i] (i.e., they are almost the same event, and therefore $S_{yield} \approx S_u \approx S_f$ and $\varepsilon_{yield} \approx \varepsilon_u \approx \varepsilon_f$); however, for ductile metals, and especially

[i] Another way of defining brittle materials is by absence of yielding (but rather characterized by sudden failure). However, for materials in general, there is always a permanent deformation period. For ceramic and other similar materials, this period is negligible and failure happens almost immediately after the elastic regime, for which this negligible yielding is often ignored and thus the material categorized as brittle.

NB: Nature is not perfectly accurate with this process, there are always imperfections, variability; there are no perfectly brittle materials.

polymers and MSK soft tissues, yielding precedes fracture by a large amount (and so $S_{yield} < S_f \lessapprox S_u$, however especially $\varepsilon_{yield} << \varepsilon_u \lessapprox \varepsilon_f$). Hence, ductility also dictates which theory best predicts mechanical failure via a safety factor, $SF = \frac{S}{\sigma}$, often relating material strength to the applied stress[145,208]. Since failure modes are different, specific theories are required[221] for isotropic materials under static loading, isotropic materials subject to dynamic fatigue loads and/or failure of anisotropic materials, which exhibit different material properties in different directions, such as articular cartilages[222].

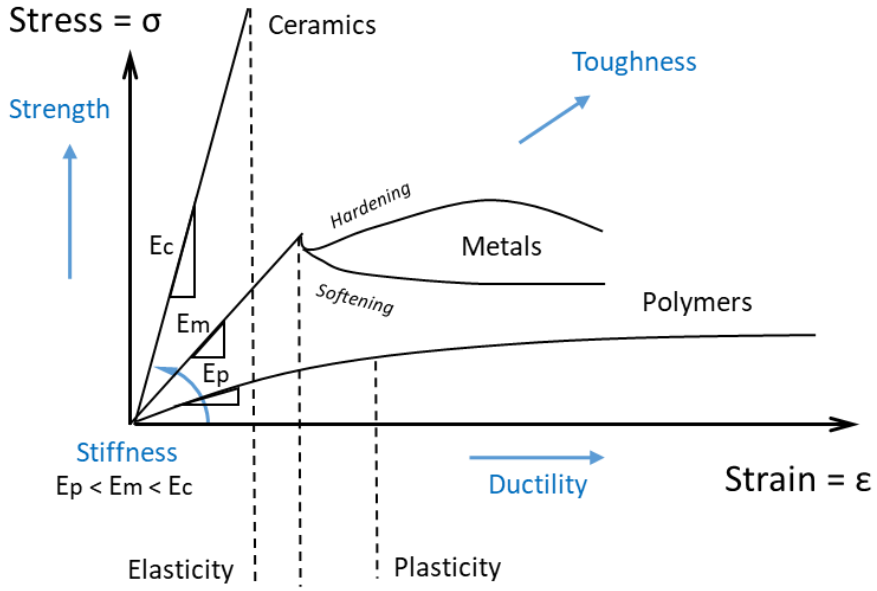

Figure 0-4: Common stress-strain curves for isotropic, homogeneous industrial materials; material comparison highlighted in blue. Based on Calister et al. 2014[26]

Each material is unique; however, material groups exhibit general trends in their properties (Figure 0-4). Stiffness and strength are in general highest for ceramics, high to intermediate for metals (which exhibit a wide range for both properties) and intermediate to lowest for polymers[223]. This may be the reason why the term strength is loosely used in the biomechanics field to refer to either *S* or *E*. Although these properties are associated in general, there are situations where this correspondence does not hold, as these properties really describe completely different aspects of material behaviour. In contrast, ductility, which is usually highest in polymers, followed by metals, and lowest for ceramics, is inversely related to stiffness[26]. Poisson's ratio is harder to predict, but it is generally between 0.3 and 0.4 for rigid materials

(e.g., ceramics, metals) and highest (i.e. between 0.4 and 0.5) for nearly incompressible materials (e.g., some polymers, especially rubbers, and MSK soft tissue estimates)[142,215]. Although different processes can be conducted to improve strength[224], stiffness and ductility are much harder to alter and most processing methods yield minimal changes in these properties.

A2.1.2.2. Biological materials (including bi-phasic, anisotropic, natural composites)

In contrast to the majority of industrial materials (ceramics, metals and polymers), whose properties are isotropic and uniform over the material, biological tissues exhibit substantial spatial variation in their properties[225,226] (and temporal response variation for soft tissues[227,228]), resulting in a complex heterogeneous (transient) material response. Transient effects are introduced by multiple constituents making up soft tissues (involving solid and fluid phases)[229], unlike most (single-phase) industrial materials. Alloys, wood and other composites are some exceptions; however, their multiple phases have the same solid state, so they exhibit negligible transient behaviour compared to MSK soft tissues (especially creep)[230]. Moreover, these multiple constituents (e.g., collagen matrices, collagen fibers, proteoglycans, blood vessels, bone marrow, synovial fluid), each of which is described by specific sets of constitutive relations, result in anisotropic behavior (especially in articular cartilage and menisci), similar to wood and other fiber-reinforced composites. Each tissue's unique complex behaviour is accompanied by substantial field variation in material properties. In fact, material variation is so large that different constitutive relations are needed for different bones and articular cartilage[144], and different material properties for specific regions (throughout the surface and depth) in same tissue[14,231]. As such, inter- and intra-sample variability is usually higher for natural anisotropic composites relative to uniform industrial materials.

For soft tissues, multiple phases lead to continuum mechanics theories and material models for porous media[142,144,228,232-235]. In addition to stress-strain relations for the solid phases, poroelastic constitutive relations include descriptions for the fluid phases[211], which can register distinct viscous behaviours and various degrees of coupling between phases[236,237] and scales[238]. Darcy's law can describe the mechanically-driven fluid transport through such media (i.e. consolidation)[211], such as cartilage or other rheological systems (e.g., soils), by means of the fluid viscosity, μ, and the permeability of the porous matrix, $\kappa(\vec{r})$,

$$\vec{q} = -\frac{\kappa}{\mu}\vec{\nabla}p, \tag{0-3}$$

where $\vec{q}(t) = \frac{Q(t)}{A(t)}\frac{\vec{v}(t)}{|\vec{v}(t)|}$ is volumetric flux, $Q(t) = \frac{dV}{dt}$ the volumetric flow rate, $A(t)$ the area normal to the flow, $p = p(\vec{r}, t)$ the pressure field across the porous object resulting from the tissue stress state and fluid content[211], $\frac{\vec{v}(t)}{|\vec{v}(t)|}$ the flow unit direction and $\vec{r}(t) = \langle x(t), y(t), z(t)\rangle$ describes flow particles' position over time, t. As shown, in these cases (such as knee's soft tissues), pressure-driven flow is directly related to permeability and limited by the fluid viscosity, for which fluid pressurization plays a significant role in the mechanical behavior of articular cartilage and meniscus[142,228]. As such, this equation does not describe fluid diffusion due to fixed charge density. Due to the reinforcing fibers of articular MSK soft tissues, poroelasticity blends with anisotropy, resulting in anisotropic cohesive poroelastic continua, or more specifically, fiber-reinforced poro(visco)elastic (FRP(v)E) soft tissues[239-245]. Articular cartilage can, however, be approximated (all phases as a whole) by transverse isotropy[222], an orthotropic special case, where two of the orientations register a similar behavior that differs from the 3rd direction, resulting in transversely isotropic poroelastic (TIPE) systems[38,222,232,246] (Figure 0-5). Menisci are sometimes even modelled simply as transversely isotropic elastic (TIE) materials, ignoring fluid flow across their surfaces[60,63,65-75].

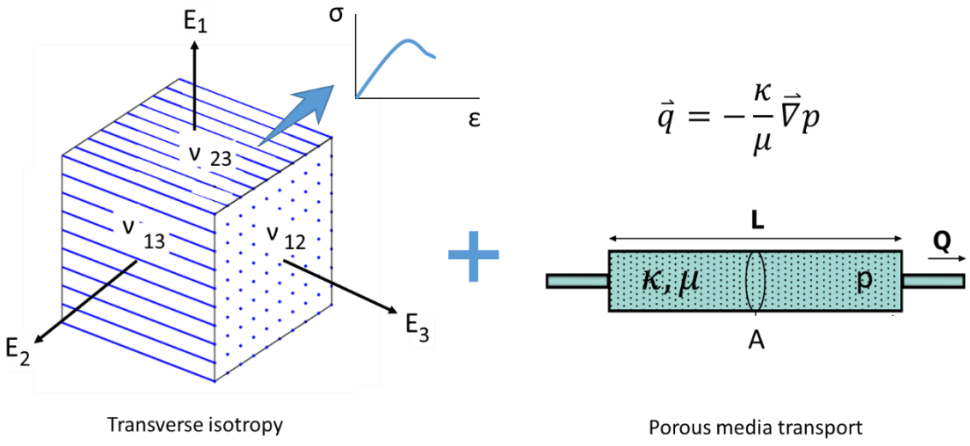

Figure 0-5: Transversely isotropic poroelasticity: Transverse isotropy + poroelasticity. Adapted from Wikimedia Commons[247] and with permission from Tweten et al. 2015[248]

Simpler material models can, however, still describe many biological tissues. Homogeneous single-phase isotropic elastic (IE) linear or nonlinear models are mostly used for 1D structures (e.g., ligaments, tendons), while heterogeneous or homogeneous single-phase IE linear models are used to describe 3D bone structures when their deformation is of interest[143,226,249], as blood vessels' and bone marrow's mechanical roles are likely negligible. However, it is also common to simplify bones as rigid when only focusing on articular soft tissues deformation[142,144,249-251].

Bone

Different constituents make up osseous structures and their specific composition varies based on bone type. In general, bones are made up of bone tissue and water. Bone tissue itself is composed of a hydroxyapatite (crystalline calcium phosphate) mineral phase and a fibrous organic matrix, whose mass is ~90% collagen (type I), and ~5% non-collagenous proteins and ~2% lipids making an amorphous substance[28,252]. Bones can be classified as cortical or trabecular, based on regional microstructure differences. Cortical bone is a very compact rigid shell that encapsulates trabecular (same constituents but organized much more sparsely developing pores) at the bone ends or bone marrow along long bone shafts[253], while subchondral bone refers to cortical bone regions that transition into the articular cartilage covering those regions. As such, despite the large variability, equivalent stiffness is higher in cortical bone (~22.4 GPa) compared to "spongy" trabecular bone (~1 GPa, accounting for porosity effects) in average, even though the microstructural stiffness (~19.4 GPa) is essentially the same for both, like Poisson's ratio (0.3 for all bones)[226]. Hence, ductility is effectively lower in cortical relative to trabecular bone (Figure 0-6); however, both cortical and trabecular bones exhibit space-varying stiffness and bone mineral density (BMD) fields, which exhibit moderate to strong correlations between them, leading to E-BMD relationships. Despite displaying minor degrees of anisotropy, bone is considered isotropic linear-elastic. Furthermore, effective stiffness progressively changes with aging, due to reformation (new bone mass growth, fostered by impact physiologic loading) and resorption (bone mass reduction due to bone inactivity and present in advanced ages) processes. Thus, it is difficult to characterize bone as either brittle or ductile, as its material properties change with space and time (although, in some cases, there might be a predominant behaviour). This further complicates which failure theories can best predict bone fragility, since despite experimental studies showing that bones fail at a consistent strain level (~10 000 and ~7 000

μstrain respectively for cortical[254] and trabecular[255] bones), this failure strain corresponds to different failure stresses (depending on where failure takes place).

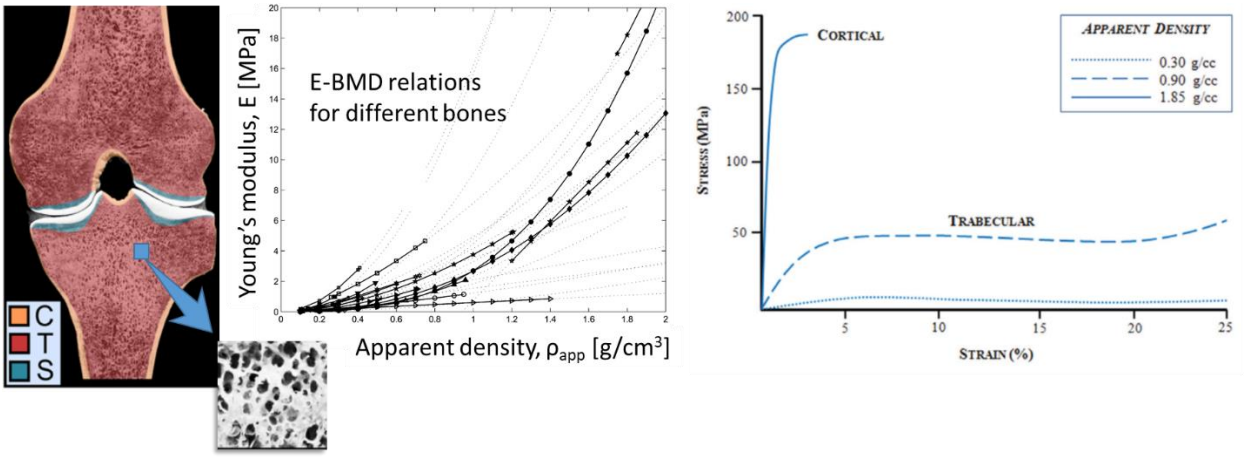

Figure 0-6: Bone cross-section (C = cortical, T = trabecular, S = subchondral), E-BMD relations and stress-strain curves for different bones (note characteristic differences in E for different densities). Adapted with permission from Venäläinen et al. 2014[226], Helgason et al. 2008[256] and Hart et al. 2017[257]

Articular cartilage

Articular cartilages are complex heterogeneous composite structures made up of different phases. Their composition includes water (68-85%wt), collagen (10-20%wt), and proteoglycans and chondrocyte cells (5-10%wt), which is clear why they are considered bi-phasic (or tri-phasic by some models) and expected to exhibit substantial viscoelasticity, due to such a high water content[229,258-265]. This collagen (type II) is arranged in the form of reinforcing fibers that are organized differently for specific cartilage regions. Independent of the subchondral bone, patellar, femoral and tibial cartilages display a characteristic stratified[i] fiber distribution across their thickness[266] (Figure 0-7). For deep regions (~56% of cartilage thickness), cartilage anchors to bone with fibers oriented normal to the subchondral surface, resulting in a transversely isotropic layer. In the intermediate layer (~32% of cartilage thickness) Adapted with permission from Venäläinen et al.2016[143] and Danso et al. 2014[267].

[i] There is substantial variability in layer thicknesses over different subjects, cartilages or topographical regions.

It is evident that regarding entire cartilage as IE materials (as often done) is a very coarse approximation that does not take the laminar structure into account nor the solid/fluid interactions. Whether they are linear or nonlinear (to account for the stress-strain toe region), such models are unable to describe the transient viscoelastic behaviour and could at most estimate cartilage's mechanical steady state. Moreover, it is clear to see why a TIPE description of the entire cartilage is still an approximation, for which depth-varying TIPE models (TIPE for each layer) or more advanced models (e.g., FRP(v)E) should be used when possible[38]. Bulk TIPE is perhaps only acceptable for the stiffer femoral cartilage[38,79,181], which is much thinner than other cartilages and thus likely registers less depth variation over such a fine thickness).

Unlike bone E-BMD relations, so far, there is greater discrepancy concerning the association between imaging parameters and mechanical properties of knee articular cartilage, as wide ranges of very strong ($0.81 \leq |\rho| \leq 0.97$)[14,170,175,176,178,179], strong ($0.62 \leq |\rho| \leq 0.8$)[14,171-173,175,176], moderate ($0.42 \leq |\rho| \leq 0.57$)[14,170-172,176,178] and weak ($0.24 \leq |\rho| \leq 0.4$)[170-172,176,177] correlations have been found (by the same or different studies). Hence, for soft tissues, material model properties are determined via optimization, i.e. adjusting them as free variables so that force or displacement response fits data from mechanical tests (e.g., ex-situ uniaxial compression or in-situ indentation). In average, articular cartilage is ~1000 times less rigid and more flexible than bone and nearly incompressible (Table 0-1). Cartilage permeability is considerably low, for which it takes a few hours for the knee to reach steady state under physiologic loads, as synovial fluid (non-Newtonian[268,269] but sometimes described by Newtonian properties[270]) diffuses and/or flows in/out cartilage surfaces due to fixed charge density and/or pressure gradients.

Table 0-1: Representative TIPE material properties (inter-subject weighted averages) for patellar, femoral and tibial cartilages [in curvilinear ($\hat{t}$-$\hat{n}$-$\hat{b}$) coordinates]

Solid:	**Patellar (pat)[38,232]**	**Femoral (fem)[38,232]**	**Tibial (tib) layers[38]**		
			Superficial	**Middle**	**Deep**
Eb [MPa]	16.00	16.00	24.00	16.97	8.49
Et [MPa]	16.00	16.00	24.00	16.97	8.49
En [MPa]	0.46	0.46	0.46	0.46	0.46
vbt = vtb	0.42	0.42	0.42	0.42	0.42
vbn = vnb	0.09	0.09	0.06	0.08	0.12
vtn = vnt	0.09	0.09	0.06	0.08	0.12
Solid-fluid interactions:					
e_o	4	4	4	4	4
κ [mm/s]	9.91E-09	9.91E-09	9.91E-09	9.91E-09	9.91E-09
Fluid[270]:					
$\mathscr{p}$ g [N/mm^3]	9.91E-06	9.91E-06	9.91E-06	9.91E-06	9.91E-06
μ [Pa.s]	0.008	0.008	0.008	0.008	0.008

Indentation testing, imaging, biochemical assays and histology are especially useful for characterizing regional (topographical) variation in cartilage fibers, which lead to somewhat different material properties in each of these regions[266]. In addition to depth variation, collagen fibers display specific orientations on the $\hat{b}$-$\hat{t}$ plane for each cartilage; femoral superficial fibers pointing to the center of the knee joint, tibial superficial fibers pointing towards the center of each T-F condyle and patellar fibers oriented vertically (Figure 0-7)[144,228,246]. The specific material properties in each region with common fiber orientations can only be accounted for via FRP(v)E models, the current most accurate model for individual cartilage constituents.

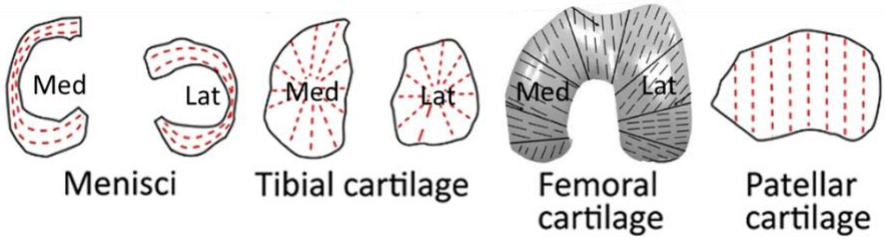

Figure 0-7: Split line patterns for different soft tissue regions with relatively uniform collagen fiber orientations demonstrate the need for spatially varying single-phase material models to effectively describe tissue functions. Adapted with permission from Halonen et al. 2017[144] and Gu et al. 2011[228].

Lastly and unfortunately, unlike bones and menisci, articular cartilage is not vascularized and its thick extracellular matrix greatly limits its regeneration[271,272]. Until recently, researchers claimed that (likely) there is no intrinsic process equivalent to bone reformation that could repair/regenerate damaged or lost cartilage; however, extrinsic micro-fracture surgery to activate skeletal stem cells seems to be the closest alternative to cartilage self-healing[273].

Menisci

Menisci composition resembles articular cartilage's: 60-70%wt water, 15-25%wt collagen (type I) and 1-2%wt proteoglycans[229,258-265], including blood vessels. Collagen fibers are mostly arranged circumferentially along each meniscus, although these randomly transition to fibers oriented radially and/or slightly vertically (Figure 0-8).

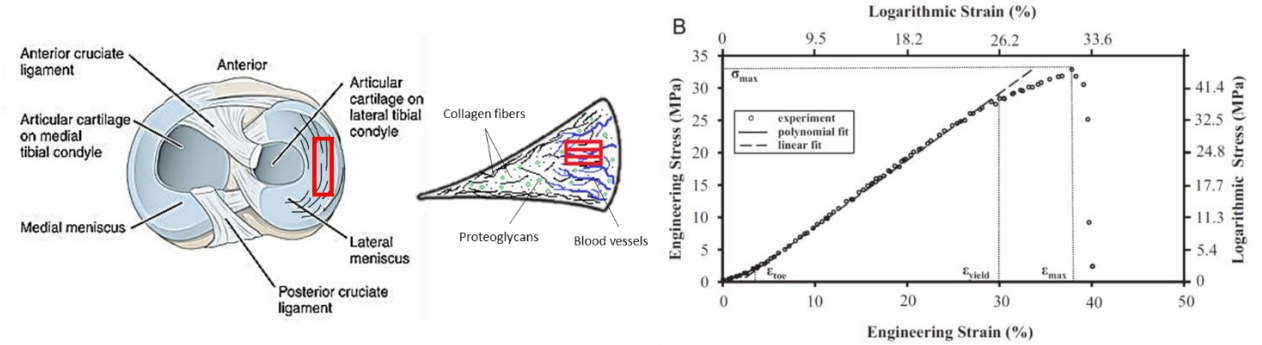

Figure 0-8: Meniscus section, fiber distribution & stress-strain curve for bovine samples along circumferential direction. Note similar yet different stiffness is expected for human menisci. Adapted from Wikimedia Commons[274] and with permission from Danso et al. 2014[267].

Meniscus (circumferential) stiffness is much higher than that of cartilage (only ~10 times lower than bone, Table 0-2) that menisci are often described as TIE materials, since a significant portion of the loading is likely borne by the solid matrix. While they still are very ductile, ductility is not as high as cartilage's. As a result, their Poisson's ratio is much smaller than cartilage's.

Table 0-2: Representative TIE material properties (inter-subject weighted averages) for individual menisci [in cylindrical ($\hat{r}$-$\hat{\theta}$-$\hat{z}$) coordinates][232,233,246,250,275-283]

E_r [MPa]	20.469
E_z [MPa]	20.469
E_θ [MPa]	140.213
$\nu_{rz} = \nu_{zr}$	0.249
$\nu_{r\theta} = \nu_{\theta r}$	0.196
$\nu_{z\theta} = \nu_{\theta z}$	0.196

Longitudinal soft tissues

Most of the remaining soft tissues consist of fibers oriented along one preferential (longitudinal) direction only, which results in ligaments connecting bones together and tendons connecting bones to muscles (Figure 0-9). These ligament and tendon structures are composed of water (65-70%wt), collagen (type I, 21-28%wt), elastin, proteoglycans and glycolipids[28].

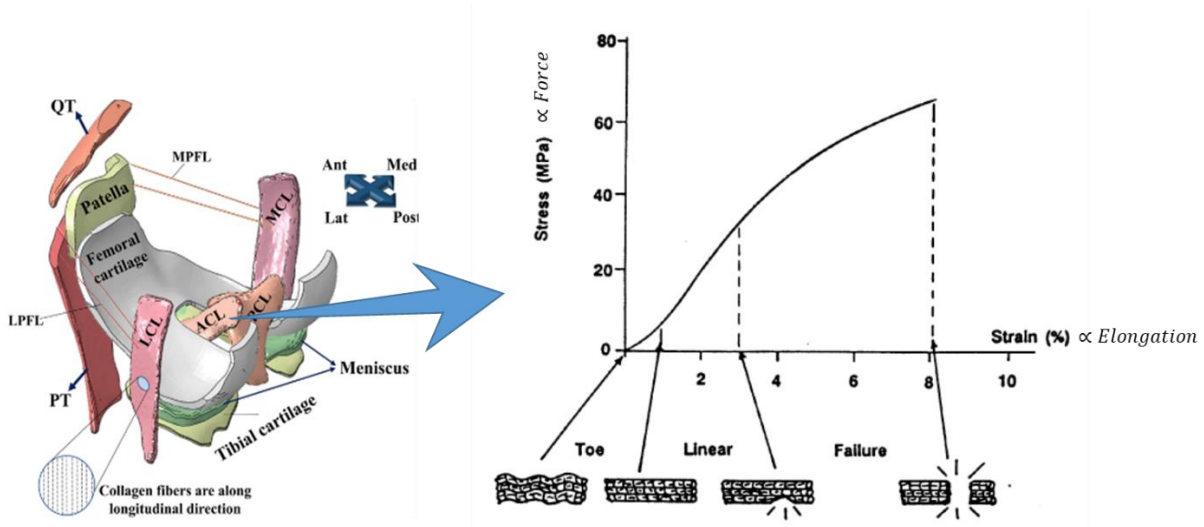

Figure 0-9: Ligaments, fiber orientation & sample stress-strain curve. Reproduced with permission from Orozco et al. 2018[190] and Lee et al. 2002[284].

As such, these tissues are mostly considered IE, characterized by bulk stiffness *k*, which can be linear/nonlinear (mostly just to describe zero stiffness in compression, while ignoring their stress-strain toe region). Additionally, some of these "cables" always feel tension, regardless of externally applied loads, which is accounted for by pre-strain (Table 0-3).

Table 0-3: Representative IE material properties (inter-subject weighted averages) for knee ligaments and tendons (including meniscal attachments)

Slender member:	Bulk stiffness, k (tensile) [N/mm]	Pre-strain
Meniscal attachment (each horn)[38,47,143,233,249,250,275-278,280,282,283,285,286]	1082.667	0.0000
Transverse ligament, TL[277,278,280]	666.667	0.0000
Patellar tendon, PT[144,190,285,287]	458.750	0.0000
Anterior cruciate ligament, ACL[38,47,144,190,233,285-287]	176.875	0.0433
Posterior cruciate ligament, PCL[38,47,144,190,233,285-287]	203.500	0.0433
Medial collateral ligament, MCL[25,38,47,144,190,233,285,286]	107.938	0.0350
Lateral collateral ligament, LCL[25,38,47,144,190,233,285,286]	96.188	0.0367
Medial patello-femoral ligament, MPFL[144]	49.000	0.0500
Lateral patello-femoral ligament, LPFL[144]	68.000	0.0500
Popliteo-fibular ligament, PFL[25]	30.400	0.0000
Anterior lateral capsule, ALC[25]	76.200	0.0000

To finish framing this complex picture, all these mechanical property space- and time-varying fields (for bones and soft tissues) vary between subjects, leading to subject-specific approaches, often imaging-based.

A2.1.3. Deformation

In addition to nonlinear transient response to loading input or material non-linearity, nonlinear effects may be present in soft tissues in the form of "large" deformations (even for linear materials during uniform loading), due to bones' relatively higher stiffness with respect to soft tissues. In contrast to "small" (infinitesimal) deformations, large (finite) deformations are very noticeable (Figure 0-10). In fact, the spatial domain changes so much that large deformations require different descriptions and analysis techniques. Lagrangian and Eulerian descriptions arise from this nonlinear phenomenon, as they respectively describe deformation from the moving point of view of material particles or from a point of view fixed in space regardless of which material points are inside or whether there is any material at all within its scope.

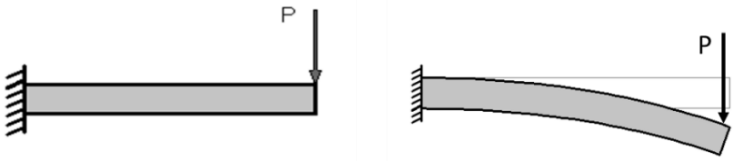

Figure 0-10: Geometrically linear vs. nonlinear problem. Adapted from Wikimedia Commons[288,289].

These two main modes of looking at deformation give rise to the different definitions of *strain*, ε, which in essence is a tensor describing unitary deformations. Just like with stress, there are normal and shearing strains in the linear and nonlinear regimes. In the non-linear regime, however, there is an entire family of normal strain measures, the Seth–Hill (or Doyle-Ericksen) family of strains[290]:

$$\varepsilon = \frac{\lambda^{2m}-1}{2m} = \begin{cases} \lambda - 1 = \dfrac{l-l_0}{l_0} = \varepsilon_{eng}, m = \dfrac{1}{2} \\ 1-\lambda^{-1} = \dfrac{l-l_0}{l} = \varepsilon_{true}, m = -\dfrac{1}{2} \\ \ln(\lambda) = \ln\left(\dfrac{l}{l_0}\right) = \varepsilon_{log}, m \to 0 \\ \dfrac{(\lambda^2-1)}{2} = \dfrac{l^2-{l_0}^2}{2{l_0}^2} = \varepsilon_{Lag}, m = 1 \\ \dfrac{(1-\lambda^{-2})}{2} = \dfrac{l^2-{l_0}^2}{2l^2} = \varepsilon_{Alm}, m = -1 \end{cases}, \qquad \lambda = \frac{l}{l_0}, \tag{0-4}$$

where l is the undeformed length measure, l_0 the deformed length measure, λ the stretch, and ε_{eng} is the engineering strain (or Biot strain), ε_{true} the true strain, ε_{log} the logarithmic strain (a.k.a. Hencky or natural strain[i]), ε_{Lag} the Green-Lagrangian strain and ε_{Alm} the Almansi strain.

There are even more strain variants, and this same equation can be extended, by the proper means, to a 3D context essentially by replacing strain and stretch with their tensor equivalents, and the term 1 with the identity matrix. For geometrically linear problems, all these different expressions give close estimates of "real strain". However, for large deformations, differences

[i] Sometimes even referred to as (the other) true strain

between these approximations are more noticeable and meaningful, as certain displacement-strain or strain-stress relationships only exist for certain types of strains.

In terms of techniques, these strain measures are computed via a deformation mapping, $\vec{x} = \vec{x}(\vec{X})$, and its gradient, F_{ij}, a Jacobian which describes one of the multiple (sometimes infinite) possible deformation processes that connect an undeformed object (described by specific material coordinates, $\vec{X}$) to its deformed version (Figure 0-11).

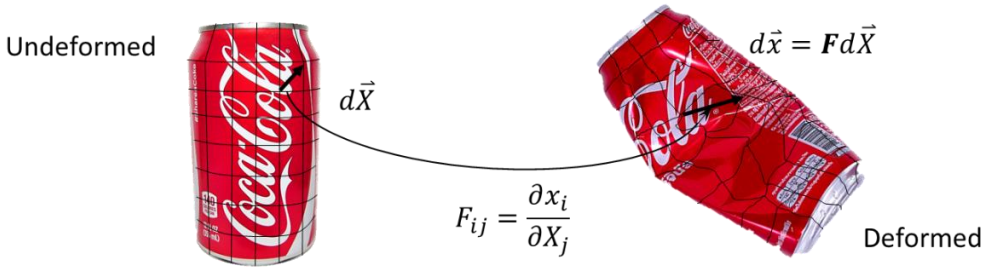

Figure 0-11: Generalized deformation gradient. Adapted from Wikimedia Commons[291,292].

Physiologic activities routinely involve complex and highly nonlinear processes. A perfect example of this are the large deformations present at the P-F and T-F contact interfaces, since contact pressures (normal contact stresses) and contact deformation depend on the applied compression, the geometry and material properties of the slave/master[i] contacting objects (articular cartilage and/or menisci), and the contact area between them. However, contact area and contacting objects' geometry themselves change as the object undergoes large deformations over short time periods (a few seconds or less) due to the bi-phasic nature of the contacting materials and the sudden dynamic nature of physical activities. Therefore, it is easy to see why both experimental and numerical approaches are often required (and sometimes combined) to study MSK systems throughout physiologic activities.

[i] The stiffer/larger tissue usually being the "master" body and the softer/smaller antagonist being the "slave"

A2.1.4. FE modelling

When used correctly, the finite element (FE) method is a powerful approximation tool used to numerically solve boundary value problems, including (but not limited to) equations (0-1), (0-2), (0-3) BCs and/or ICs, describing any continuum mechanics problem. As such, it is widely used in engineering practice, mechanical design, and biomechanics research, since these field problems often cannot be solved analytically, due to their geometric, compositional and/or functional complexity. In stress analysis, PDE(s) can be solved approximately via the principle of minimum stationary potential energy, which can be conducted over the entire domain (usually exhibiting complex field variations, which limits approximation accuracy) or individually over small elements (exhibiting less field variation and therefore easier to approximate locally[207,293]). Since subdividing complex problems facilitates estimating the PDE(s) solution, instead of solving the governing PDE(s) for the entire problem, the FEM does it for a small element within the domain. This is conducted individually for each of the elements making up the problem and the results are assembled to obtain an overall approximation of the field of interest (e.g., displacement, strain, stress, strain energy, fluid flow, pore pressure, contact pressure, etc.). Hence, the geometries of interest [whether they are samples (Figure 0-12A), complete tissues or machine components (Figure 0-12B), or entire (bio)mechanical systems (Figure 0-12C,D)] are subdivided by meshes into a discrete number of small elements. Advanced numerical methods are involved in executing this strategy and practical problems require a large number of elements, for which this technique can only be implemented effectively using computers.

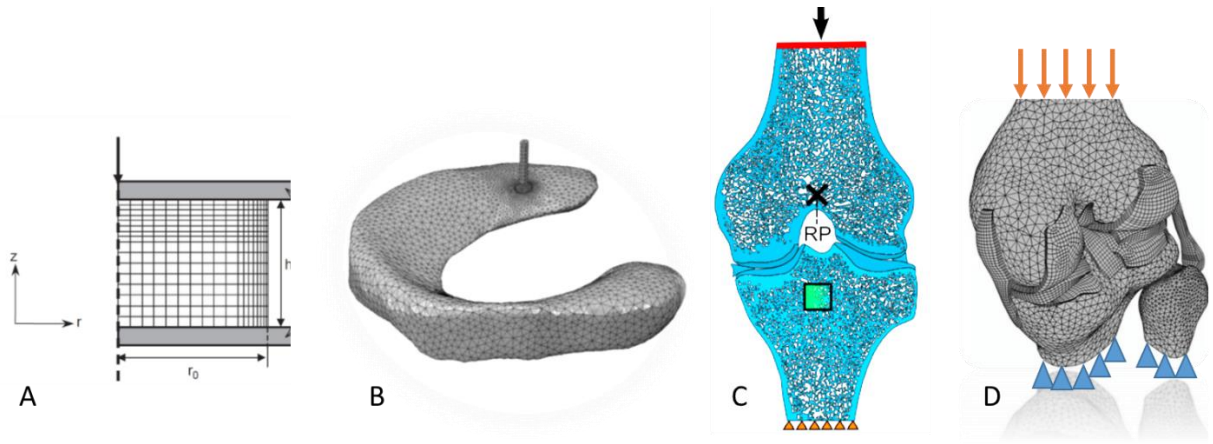

Figure 0-12: Tissue-level FEM [ex-situ (A), indentation (B)] and joint-level FEM [2D T-F joint (C), 3D T-F joint (D)]. Reproduced or adapted with permission from Wilson et al. 2005[243], Danso et al. 2015[227], Venäläinen et al. 2014[226], Kazemi et al. 2014[220].

Different finite element models can be developed for different purposes (each involving different simplifications, assumptions, functions, etc.); however, in general they all require geometric, material constitution and loading information. Usually, tissue 3D geometries are obtained via imaging (bones via CT or MRI, and soft tissues via MRI), and material information is either imaged for bones (e.g., E-BMD mapping) or estimated via soft tissue models (e.g., FRPE, TIPE, IE previously tuned via mechanical testing). Physiologic loading can be estimated via gait analysis and MSK models or simplified as uniaxial compression (sometimes of small magnitude[228] to avoid numerical instabilities) in creep or stress relaxation[220]. Once models are built, however, they can be used to test different conditions, such as the effects of focal defects on articular cartilages' stress and strain[143] and osteochondral regions' contact pressure and strain[251]. Similarly, the effects of meniscectomy on fluid and contact pressures in T-F joints have been explored[230,234]. FE procedures have become so advanced they can be used to simulate entire system pathologies, such as OA[79,276], as well as potential treatments[144]. Depending on the scope, FE models can include some or all relevant soft tissues, and even describe multi-scale interactions between these tissues and their components[233]. Of course with all this computational power comes a great computational cost, for which research also evaluates strategies to mitigate this, such as simplifying the bone[249], articular cartilage[38] or ligament[190] material descriptions. As one can imagine, soft tissue FEM is a vast field (and so is bone FEM), and therefore the present list merely includes some of the most detailed, state-of-the-art full-joint knee models (author's opinion); this is not a complete nor representative list.

The finite element technique can be used to simulate essentially any physical process and estimate any field of interest. Moreover, subject-specific models can be generated when incorporating the geometry and material properties extracted from medical images and can be used to predict bone reformation/resorption[294], fractures[295], or even diseases (e.g., T-F OA)[79]. For FE models, one can verify that the numerical solution is invariant to mesh size (h-convergence) or interpolation method (p-convergence) used to estimate it, as the true solution is a physical field independent of any observations or analyses concerning it.

Whether it is an experimental or numerical model, T-F and P-F joints should be considered, as OA develops significantly in both[79]; unfortunately, knee FE models[48,49,73,296-299] seldom do this

(at least not as much anymore); currently, with more technological advances, research rather focuses on the T-F joint [38,47,77,79,133,143,144,190,220,226,228,232-235,246,249,275,276,281,297,300-303]. Moreover, these models often stray away further from reality in terms of material (as explained previously) and load descriptions. To resume the discussion on material models, numerical power is challenged by soft tissue complexity (heterogeneous anisotropic bi-phasic materials subject to large deformations from contact mechanics); however, FE solutions are especially challenged by numerical issues arising from modelling nearly incompressible articular cartilage. These issues include loss of physical realism (volumetric and shear locking, hourglassing and other spurious modes), convergence issues and numerical instability, leading to singular or ill-conditioned systems with high sensitivity to minute changes in Poisson's ratio[142,304]. Despite having techniques for addressing those issues and accurate material descriptions [e.g., FRP(v)E and TIPE], these models are not clinically applicable[245] due to their high computational costs (running such models may take several weeks[142], assuming they are implemented correctly with powerful computer resources). To avoid some of these issues, models often involve low-magnitude axial compression[220], while a few incorporate large compressive forces[251], and physiologic loading or flexions representative of dynamic physical activities[79,144] (from gait analysis, instrumented TKRs or MSK modelling, including muscle actuation) in a physiologically realistic context. As a result, subject-specific FE studies frequently involve small sample sizes, with few exceptions[79,276,298]. However, most importantly, FE models' potential is limited by lacking experimental validation (kinematics, kinetics and deformation response) at joint-level (not just for tissues)[142] under realistic loading conditions. This is yet another reason why there is a pressing need in the biomechanics field for whole-knee physiologically realistic experimental data, such as a complete ex-vivo dataset for T-F and P-F joints in a physiologic, multiaxial loading scenario.

A2.2. Current in-vivo (in-situ) experimental biomechanics techniques

A2.2.1. Gait analysis (non-invasive)

This popular technique is used to measure mechanical aspects of walking but can be extended to other physical activities (e.g., running, sitting down, standing, etc.), which can be used to determine limbs or joint loading. Hence, this multipurpose technique can be combined with mechanical testing, numerical simulations and/or medical imaging[79,194], as discussed in the next sections. Gait analysis setups include force plates, motion capture devices, fiducial markers and (usually human[305]) test participants (Figure 0-13). Additionally, participant anthropometrics (BW, height, and relative size and position of individual limbs) are often recorded, separately from the physical activity trials, in order to further characterize participants' kinematics and kinetics. Force plates (of high sampling frequency, e.g., 2kHz <=> 0.5ms resolution[306], to capture as much of the impact characteristics) measure ground reaction forces (GRFs) that the participants exert on the ground while performing physical activities. Additionally, several high-speed cameras (e.g., 120Hz <=> 8.33ms resolution[36]) are positioned throughout the activity space to cover the range of distance travelled. These cameras detect fiducials mounted on the participant's limbs and/or joints to define limb axes and joints (via anatomic coordinates) and track their motion over time. These "human constellations" can then be used to estimate limb's (translational and rotational) position, velocity and acceleration over time.

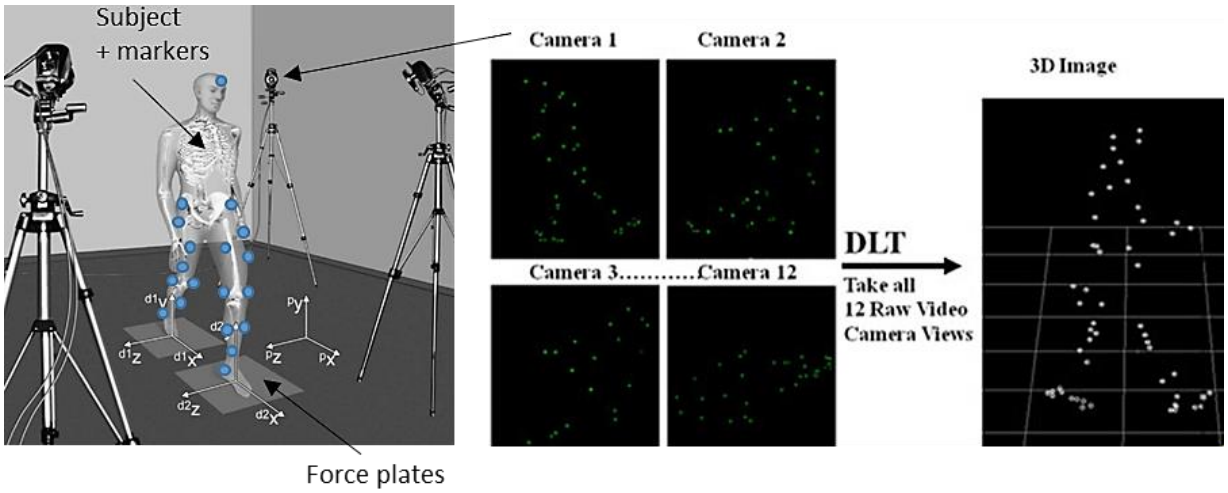

Figure 0-13: Gait & motion capture setup showing a few marker snapshots from different views. Adapted from Wikimedia Commons[307] and with permission from Cappozzo et al. 2005[37].

Joint loads can be determined via inverse dynamics, which first requires combining kinematic signals, syncing them with GRFs and filtering all of these signals beforehand. As opposed to forward dynamics, where kinematics are determined from known kinetic actuation, in inverse dynamics, kinematics are known and kinetics predicted. By measuring the GRFs, limb anthropometrics and kinematics, one can solve the Newton-Euler equations [a special case of equation (0-1) in Appendix A2.1 for 3D rigid bodies] for the feet and determine ankle joint loads (three moments and three forces required to maintain dynamic equilibrium). Then, the same procedure is repeated for the adjacent segment (i.e. determine the unknown support force and moment reactions at one end from the known segment kinematics and support reactions at the other end) until reaching the joint of interest[28,35,213,214,308,309]. Unfortunately, these indirect measurements of joint loading cannot be extended to contact forces, due to the presence of numerous ligaments, tendons and muscles (mechanical reinforcements, each consisting of countless loaded fibers) that lead to a dynamically indeterminate system. Thus, contact forces are measured directly (e.g., via pressure sensors) or estimated via finite element (FE) modelling, while some muscle forces estimated via MSK modelling. Knee joint external reactions can also be measured via instrumented knee implants; however, these represent an abnormal loading environment (explained in the next section).

Gait analysis is a very powerful tool that enables measurement of 3D kinematic and kinetic characteristics of the human body while performing physical activities. This is particularly useful for characterizing physiologic loading BCs, inertial terms and external joint loads (via inverse dynamics) non-invasively. Unfortunately, it is not possible to estimate internal joint loads from gait analysis alone, and gait measurements may be affected by skin motion and/or kinematic crosstalk artifacts.

A2.2.2. Instrumented TKRs (invasive)

Knee external reaction forces can be measured directly over time via telemetric total knee replacements instrumented with 6-DOF load cells, which record three forces and three moments over time with respect to anatomic coordinates centred at the tibial plateau[41,42] (Figure 0-14, Figure 2-4 A.3). These, however, cannot be converted into actual knee contact forces either, due to implants' altered morphology and mechanical properties, both affecting contact behaviour. Also, gait patterns are not normal, since participants no longer have normal knees due to their

implants often paired with late-stage OA[41,46]. They do, however, provide some experimental validation for knee external forces measured via gait analysis and there is free open-source longitudinal data for different participants conducting > 11 daily physical activities[42]. For all the physical activities involving the lower locomotor system (and especially for gait, stair ascending/descending and running), the knee axial force is much larger than the negligible joint's external shear forces and, among these, running registers the highest forces (due to impact), followed by stair descending, stair ascending and level walking[42,45]. However, even for walking at a low speed, knee axial forces are as high as ~3BW[41,42], due to bearing upper-body BW, limbs acceleration and muscles co-contraction.

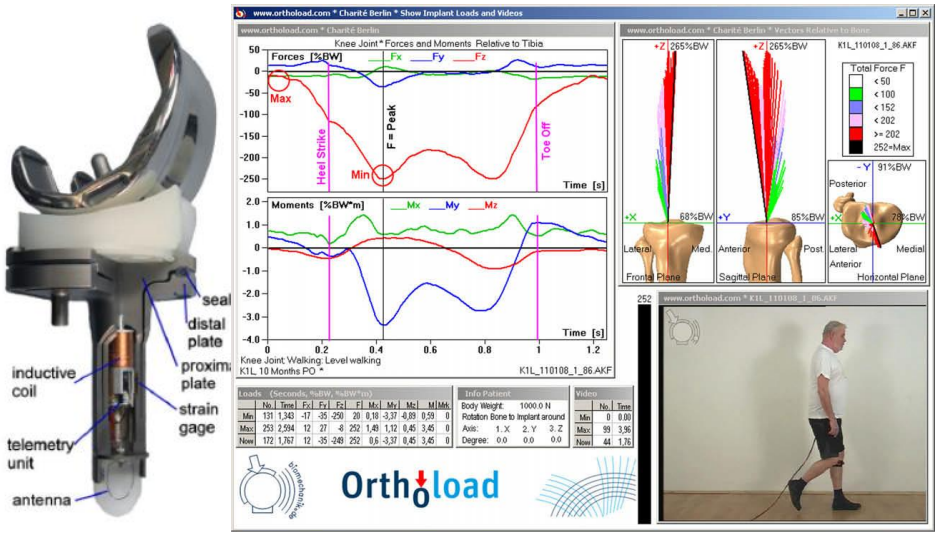

Figure 0-14: Instrumented TKR & gait measurements (external joint reactions showing a multiaxial combined loading scenario). Reproduced with permission from Heinlein et al. 2009[41].

So far, instrumented TKRs provide the only direct measurement of knee external loads, and so they are the current reference standard. However, this invasive technique can only be performed on people requiring knee replacements. Hence, knee loads correspond to altered loading due to the implant (different from healthy knee function) and altered contact mechanics (due to the implant components). Also, it is still not possible to estimate internal joint loads (nor the stress and strain fields in knee tissues) from these measurements alone.

A2.2.3. Simplified loading (non-invasive)

To measure load effects, rather than applied loads, joint loading can be combined with imaging. This can be achieved by means of an external apparatus for applying loads to people lying supine

or for people standing in an open-bore scanner, and via CT and (q)MRI sequences for imaging bone and soft tissues. Unfortunately, due to closed bore orientation and long scanning times for most MRI sequences, applied loads and joint flexions are limited in magnitude and no longer represent dynamic physical activities (especially short impact periods). Imaging the knees of living participants under simplified loading conditions (e.g., weight-bearing extended or non-weight-bearing flexed) allows seeing inside knee tissues and non-invasively evaluating the effects of physiologic loading and subject-specific characteristics in tissue- or joint-level response. These in-vivo measurements are restricted by low-magnitude loads (sometimes sub-physiologic) and imaging limitations (e.g., trade-offs between short scan times, spatial resolution, signal-to-noise ratio in MRI of soft tissues).

A2.3. Comparison of ex-vivo load devices used to existing technologies

Table 0-4 contains a synthesis of existing full-joint lower-body ex-vivo loading devices, including the MRI-safe creep rig developed in study I and the MRI-safe stress relaxation rig used in study II. Devices are compared based on the type of joint they can load, their loading mechanism and imaging compatibility.

Table 0-4: Comparison of "a few" full-joint lower-body ex-vivo loading devices/setups (from the 80's to present time)

Study	ROI	Simultaneous joint motions	Transient test	Loading	Power	Medical imaging compatibility
Espinosa MSc. Thesis (University of Saskatchewan) 2022; Espinosa et al, IWOAI 2019[81]; AB BME 2016[80] (current, study I)	Human knee (intact, open), bovine stifle (intact, open), can be adapted for other joints & implants	3 translations, 3 rotations	Creep	Axial compression (2.5kN max), bending (30N·m max), muscle actuation (1kN max, each); misalignments may develop shear, torsion	Pneumatics	MR
Gu et al, J. Biomech. Eng. 2020[133] (*DCKSA*)	Human knee (open)	2 translations, 1 rotation	Creep	Axial compression (1kN), flexion and muscle loading (315N) achieved via linear actuators mounted on a frame	Electro-mechanics	X-ray
Nebelung et al, IWOAI 2019[82]	Human femoral cartilage (dissected sample inserted in anatomic knee model)	2 translations, 1 rotation	Creep	Axial compression (0.95BW = 660N)	Pneumatics	MR
Dullaert et al, J Foot Ankle Surg 2017[83]	Human foot (intact)	1 translation	Creep	Axial compression (1BW = 700N), muscle actuation (150N) via hanging weights	Pneumatics	CT
Martel et al, AB BME 2017[84]; Thorson et al, AB BME 2017[85] (current, study II)	Human knee (intact)	1 translation	Stress relaxation	Axial compression (890N) achieved via screws & sliding plate	Mechanical /manual	MR
Naghibi Beidokhti et al, J. Biomech 2017[86]; Rachmat et al, Med Eng Phys 2016[87]; Barink et al, Knee Surg Sports Traumatol Arthrosc 2007[88]	Human knee (intact)	3 translations, 3 rotations	Stress relaxation	Muscle stabilization (20N max) via ropes, knee external loading (105N axial, 100N shear, 5.2N.m torque, 12N.m abd/add) applied by sliding/rotating blocks attached to a frame	Mechanical /manual	Unspecified

Fitzpatrick et al, J Biomech 2016[89] (*AMTI VIVO* computer model)	Ankle, knee, TKR, hip, spine, shoulder, elbow, temporo-mandibular	3 translations, 3 rotations	Stress relaxation, creep, fatigue (force- or displacement-control)	Axial compression (4.5kN max), shear (1kN max), flexion (80N·m max)	Servo-hydraulics	Impractical
Maletsky et al, Knee Surg 2016[90] (*Kansas Knee Simulator*); Baldwin et al, J Biomech 2012[25] (*Kansas Knee Simulator* computer model)	Human knee (intact), TKR, human foot prosthesis	3 translations, 3 rotations	Stress relaxation[116], creep, dynamic (force-control)	Axial compression, shear, bending (10N·m abd/add), torsion (5N.m) &/or alignment via muscle actuation	Servo-hydraulics	Impractical
Forlani, PhD. Thesis (Università Degli Studi Di Bologna) 2015[91] (design only, not built nor tested)	Human knee (intact)	3 translations, 3 rotations	Creep	Axial compression, flexion, muscle actuation via multiple pulley-actuator systems	Pneumatics	Impractical
Chen et al, Med Eng Phys 2014[92]	Porcine stifle (intact)	3 translations, 3 rotations	Creep	Compression (1BW = 700N) aided via muscle actuation (350N each)	Electro-hydraulics	MR, CT
Freutel et al, J Magn Reson Imaging 2014[93]	Porcine knee (intact)	2 translations, 1 rotation	Creep	Axial compression (~2BW = 1.8kN max) via tensile actuator	Pneumatics	MR
Lawless et al, J Biomech 2014[94]; Ding et al, IECON 2011[95] (*Hexapod*, based on *Stewart platform*)	Human knee, spine (intact)	3 translations, 3 rotations	Creep, dynamic (force-control)	Axial compression (20kN max), shear (6kN max), bending (2kN·m max), torsion (1.5kN·m max)	Electro-mechanics	Impractical
McWalter et al, J Magn Reson Imaging 2014[96]	Human knee (intact)	1 rotation	Creep	Muscle actuation (60N) via hanging weight	Mechanical /manual	MR
Shalhoub at al, J Biomech 2014[97]	Human knee (intact)	1 rotation	Creep	Muscle actuation (175N max, quad) via hanging weight	Mechanical /manual or electro-mechanical	Impractical
Wünschel et al, Knee 2013[98]; Arthroscopy 2010[99]; Müller et al BMT 2009[100]; Lo et al, J Biomech 2008[101] (*Tuebingen Knee Simulator*)	Human knee (intact), TKR	3 translations, 3 rotations	Stress relaxation, creep, dynamic (force-control)	Axial compression (~250N), shear (~50N), bending, torsion, muscle actuation (>600N)	Electro-mechanics	Impractical
Shiomi et al, Osteoarthr. Cartil. 2012[102]; 2010[103]	Porcine knee (intact)	3 translations, 2 rotations	Stress relaxation	Axial compression (0.33BW = 300N), bending via screws & sliding parts	Mechanical /manual	MR
Siston et al, J. Biomech Eng. 2012[104]	Human ankle (intact), knee, TKR	1 translation, 3 rotations	Stress relaxation	Shear (150N), bending (25N.m)	Mechanical /manual	Unspecified

Butz J. Biomech 2011[105]; Chan et al, Magn Reson Med 2009[106]; Osteoarthr. Cartil. 2009[107]	Neonate porcine stifle (intact)	1 translation	Fatigue (force-control)	Axial compression (2BW = 156N max)	Electro-pneumatics	MR
Netravali et al., J. Biomech Eng. 2011[108]	Human knee (intact)	2 translations, 2 rotations	Stress relaxation, creep	Axial compression via rubber bands, while flexion, internal/external rotation & shear via prescribed displacements	Mechanical /manual	MR
Greaves et al, J Biomech 2010[13]; 2009[12]	Human hip (intact)	1 translation	Creep	Axial compression (2.3BW = 1.98kN max)	Electro-pneumatics	MR
Quenneville et al, J. Biomech Eng. 2010[109]	Human lower leg prosthesis	2 translations, 1 rotation	Impact (force-control)	Axial force (18kN max), flexion	Electro-pneumatics	Unspecified
Martin et al, J. Biomech Eng. 2009[110]; 2007[111]	Human knee (intact)	3 translations, 3 rotations	Stress relaxation, creep, fatigue (force-control)	Axial compression (2BW = 1.5kN max) via piston, while all other (5) load components via prescribed displacements	Electro-pneumatics	MR
Yildrim et al, J Orthop Res 2009[112]	Human knee (intact), TKR	3 translations, 3 rotations	Creep	Axial compression (73.4N), muscle actuation (267N max, quad; 172N max, hamstrings) via pulley-actuator system & springs respectively	Electro-mechanics	Impractical
Aubin et al, IEEE. Trans. Biomed. Eng. 2008[113] (*Rotopod R-2000*, based on *Stewart platform*)	Human knee, human foot prosthesis (intact)	3 translations, 3 rotations	Dynamic (force-control)	Axial compression (1BW max), shear, bending & torsion achieved via a plate mounted on a mobile platform, whose legs move around a fixed frame to change the plate's position & orientation	Electro-mechanics	Impractical
Papaioannou et al, J Biomech, 2008[114] (*Wayne State University knee loading system*)	Human knee (open)	2 translations, 1 rotation	Stress relaxation, creep, dynamic (force- or displacement-control)	Axial compression (2kN max), flexion	Servo-hydraulics	X-ray

Withrow et al, J Bone Joint Surg 2008[115]	Human knee (open)	3 translations, 3 rotations	Impact (force-control)	Axial compression (~2.09kN max) & flexion via dropping weight, muscle actuation (1.58kN max, quad; 394N max, single hamstring) via springs (adjustable preloading)	Mechanical /manual	Impractical
Clary, MSc. thesis (University of Kansas) 2006[116] (*QKR*)	Porcine knee (intact)	3 translations, 3 rotations	Stress relaxation, creep (allowing manual adjustments)	Axial compression, shear, bending (15.8N.m max), torsion via rotary potentiometers & disk brakes, muscle actuation (111N quad) via hanging weights	Electro-mechanics, mechanical /manual	X-ray
Si-hoe et al, J. Biomech. Eng. 2006[117]	Porcine, bovidae spine (dissected)	3 translations, 3 rotations	Stress relaxation, pseudo-creep (via equivalent stepwise compressive displacement)	Compression (5kN), shear (1kN) & bending (15N·m) via off-axis forces	Mechanical /manual	CT
Song et al, Osteoarthr. Cartil. 2006[16]	Ovine knee (cored)	1 translation	Creep	Axial compression (1.5BW = 650N max) via rig transverse loading	Electro-pneumatics	MR, CT
Fellows et al, J Biomech 2005[118]	Human knee (intact)	1 rotation	Creep	Muscle actuation via hanging weights	Mechanical /manual	MR, CT, X-ray
Maletsky et al, J Biomech Eng 2005[119] (*Purdue Knee Simulator: Mark II*)	Human knee (intact), TKR	3 translations, 3 rotations	Stress relaxation, creep, dynamic (force- or displacement-control)	Axial compression (~1.6kN max), shear, bending, torsion, muscle actuation (1.5kN max, quad)	Servo-hydraulics	Impractical
Fujie et al, J Biomech Eng 2004[120]	Human knee (intact)	3 translations, 3 rotations	Stress relaxation, creep, dynamic (force- or displacement-control)	Axial compression (100N), shear (100N), bending (2N.m), torsion	Electro-mechanics	Impractical
Li et al, J Orthop Res 2004[121]; Li et al, J Biomech 1999[122]	Human knee (intact)	3 translations, 3 rotations	Stress relaxation, creep, dynamic (force- or displacement-control)	Axial compression, shear, bending, torsion via robotic arm, muscle actuation (400N max) via hanging weights	Electro-mechanics (*Kawasaki UZ150* or *Unimate PUMA 762*)	X-ray
Herberhold et al, J Biomech 1999[123]; Magn Reson Med 1998[124]	Human knee (open)	2 translations, 1 rotation (patella)	Creep	P-F compression (1.5BW = 1.03kN avg.)	Electro-pneumatics	MR

Zavatsky, J Biomech 1997[125]; Petersilge et al, Clin. Orthop. Relat. Res. 1994[126]; Shoemaker et al, Clin. Orthop. Relat. Res. 1993[127] (*Oxford Knee-Testing Rig*)	Human knee (intact), TKR	3 translations, 3 rotations	Creep, dynamic (force-control)	Axial compression (44N), P-F compression (800N), shear (220N), bending, torsion, muscle tension (900N, quad) aided by hanging weights	Electro-mechanics	Impratical
Shelley et al, Proc Inst Mech Eng H 1996[128]; ASME Advances in Bioengineering 1991[129]	Human hip (anatomical model)	3 translations, 2 rotations	Creep	Axial compression (6BW max), muscle actuation (1.23 BW), flexion (60N·m)	Electro-mechanics (*Instron 1122*)	Impractical
Xerogeanes et al, Knee Surg, Sports Traumatol, Arthroscopy 1995[130]	Human knee (intact, open)	3 translations, 3 rotations	Stress relaxation, creep, dynamic (force- or displacement-control)	Axial compression, shear (100N), bending, torsion	Electro-mechanics (*Instron 4502*)	Impractical
Fujie et al, J Biomech Eng 1993[131]	Human knee (intact)	3 translations, 3 rotations	Stress relaxation, creep, dynamic (force- or displacement-control)	Axial compression (10N), shear (40N), bending(2N.m), torsion via robotic arm	Electro-mechanics	Impractical
Grood et al, J Bone Joint Surg 1988[132]	Human knee (intact)	3 rotations	Stress relaxation	Shear, bending, torsion	Mechanical /manual	Impractical

A2.4. Medical imaging & image processing

A2.4.1. Current medical imaging modalities

Radiography (X-radiation) is the most common modality for imaging bones. In this modality, X-rays are shined through objects and the remaining radiation collected, from which certain characteristics of the object's structure can be determined based on the absorbed radiation. There are different kinds of radiographic images (Figure 0-15), such as planar X-ray used for injury assessments, dual-energy X-ray absorptiometry (DXA) used to measure bone density or computed tomography to produce 3D images. X-ray can also extended to 3D via biplane imaging (e.g., RSA) and CT further extended to quantitative approaches, such as high-resolution peripheral quantitative CT (HR-pQCT), in order to map the bone mineral density in the images to the bone elastic modulus field. There are many other modalities, such as magnetic resonance (discussed separately), molecular and nuclear imaging, as well as hybrid modes, combining different techniques from individual modalities. On the other hand, there are techniques for increasing the contrast in medical images (e.g., contrast agents and/or image processing) in order to better distinguish the different issues in these images. In general, high resolution (HR), high SNR and short scanning times are sought-after conflicting objectives. Additionally, there are modality-specific issues, such as ring artifacts in reconstructed CT images, or varied MR artifacts such as those introduced by ferromagnetic metals, making them incompatible with this modality.

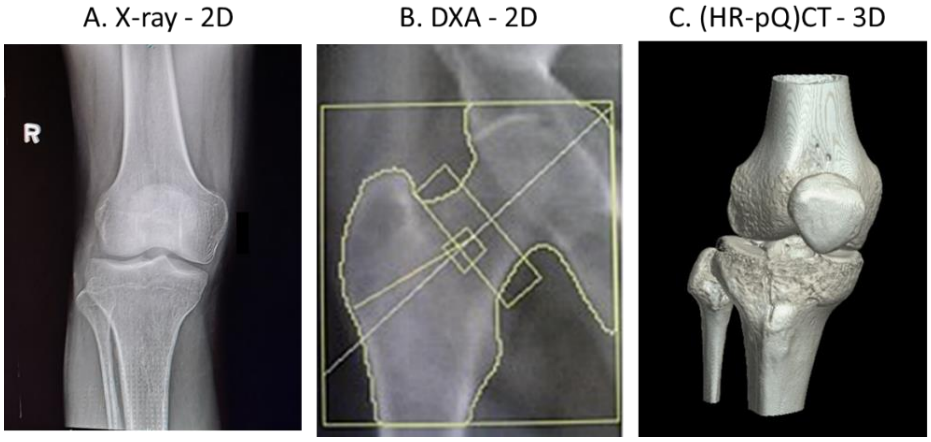

Figure 0-15: Radiographic medical images (note soft tissues absence). Taken from Wikimedia Commons[310,311].

A2.4.2. Image processing

To exploit the benefit of medical imaging, considerable resources and research efforts are also invested in the image processing field, especially when related to pre-processing (cleaning, repairing) images, distinguishing different objects in these images and manipulating them in order to get desired information. Image pre-processing is a key step, since any imperfections, artifacts or simply noise may propagate (or amplify) throughout the data processing pipeline, potentially affecting quantitative results. Hence, it is recommended that de-noising filters are applied to images prior to manipulating them (like some reconstruction algorithms may incorporate by default) and that such methods are evaluated so that quality is improved without losing useful information. To do this, it is common to simulate artifacts or noise on clean images, apply proposed de-noising algorithms to restore the purposely corrupted images to their original versions. This method also allows for objective evaluation of the de-noising methods suggested.

Different tissues in medical images often need to be identified, which is not an easy task, even when dealing with MRI images with enhanced contrast (with or without contrast agents). In fact, this task can be so challenging that not only computers struggle at automatically detecting different tissues, but humans also do, for which manual and semi-automatic segmentations depend on the data, tools used, as well as technician and/or researcher expertise. Once these tissues are distinguished, 3D volumes and/or binary masks (Figure 0-16) can be created and applied to the data in order to focus on those tissues of interest.

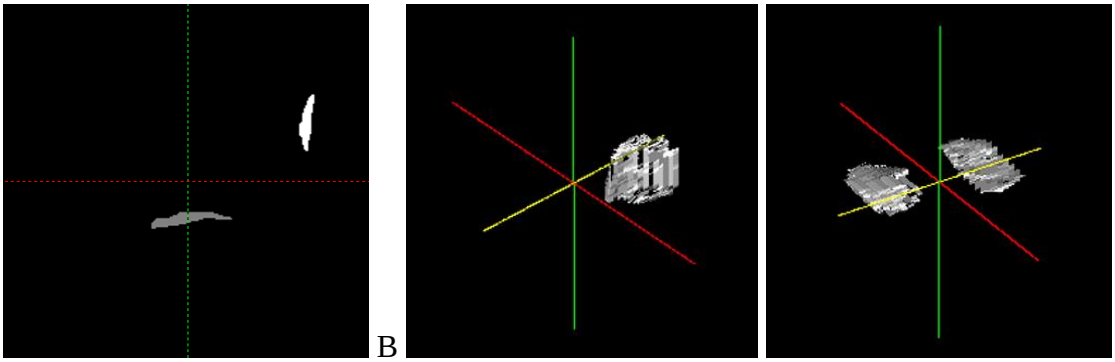

Figure 0-16: (A) 2D slice with segmented patellar and tibial cartilages and (B) corresponding volumes. Segmentation courtesy of Natasha Bzowey.

Another popular image processing algorithm is registration, in which one image is transformed to best fit the most salient features of another image. These transformations may involve scaling, translating and/or rotating an image to minimize the differences between this and other image, based on key geometric characteristics (Figure 0-17).

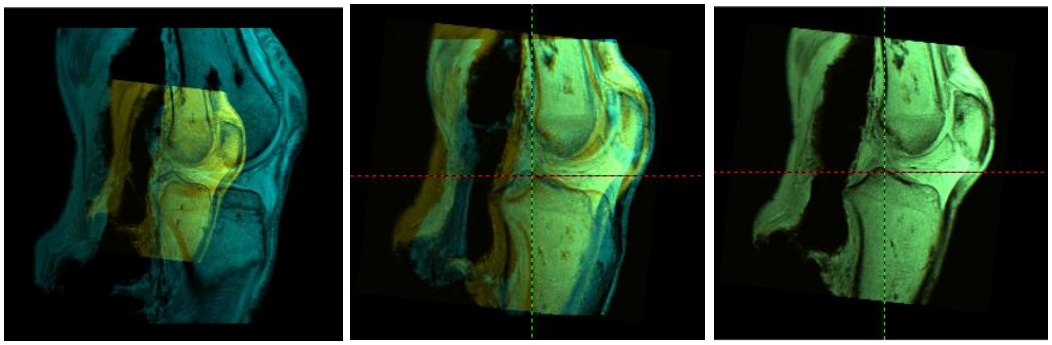

Before processing Scaling Aligning

Figure 0-17: Sample registration steps conducted on two different versions of the same image (green = base image, turquoise = object requiring registration)

In all these cases, automatic algorithms are generally faster; however, manual operations tend to be more accurate. Hence, semi-automatic processes are often used in practice. Artificial intelligence is gaining popularity for processing medical images; however, there are associated considerations (computer resources, running times and costs) related to neural network development, training and validation (which require fully processed datasets).

A3. Additional resources for MR creep rig system

A3.1. MSK biomechanics modelling protocols

Model information:

The dataset used to estimate the physiologic loading regime included a 3D model with 23 DOFs, 92 muscle-tendon actuators, containing legs, pelvis and torso[312], and associated joint kinematics and kinetics for walking:

- (Modified) *Gait2392_simbody.osim* model anthropometry based on inter-subject averages of five healthy males measurements, AVG ± SD: (688 ± 76)N BW, (1.77 ± 0.03)m tall, (26 ± 3)years
- *Subject01_walk1* kinetics (ground reaction forces) measured via force plates
- *Subject01_walk1* kinematics (joint coordinate angles) estimated from dynamic optimization for inverse kinematics and verified against motion tracking measurements

Link: https://simtk-confluence.stanford.edu:8443/display/OpenSim/Example+-+Estimating+Joint+Reaction+Loads

Modelling procedure for determining physiologic loading regime (for general purposes):

These are the general steps conducted using OpenSim 2.4.0 to obtain the estimated physiologic loading regime for this project; for more details regarding how to carry each of these steps, please refer to the SOP in Appendix A3.2.

1. Estimate muscle forces in order to select which muscle groups should be considered for experimental simulation
   a. Run the static optimization subroutine (using the model anthropometry, prescribed joint angles and GRFs as inputs) to estimate active muscle forces (Figure 0-18) and activations, which minimize the cost function,

$$J = \sum_{m} (a_m)^p, \tag{0-5}$$

involving individual muscle activations, a_m, whose arbitrary[i] powers, $(a_m)^p$, are added, subject to the Newton-Euler dynamic equilibrium equations as constraints.

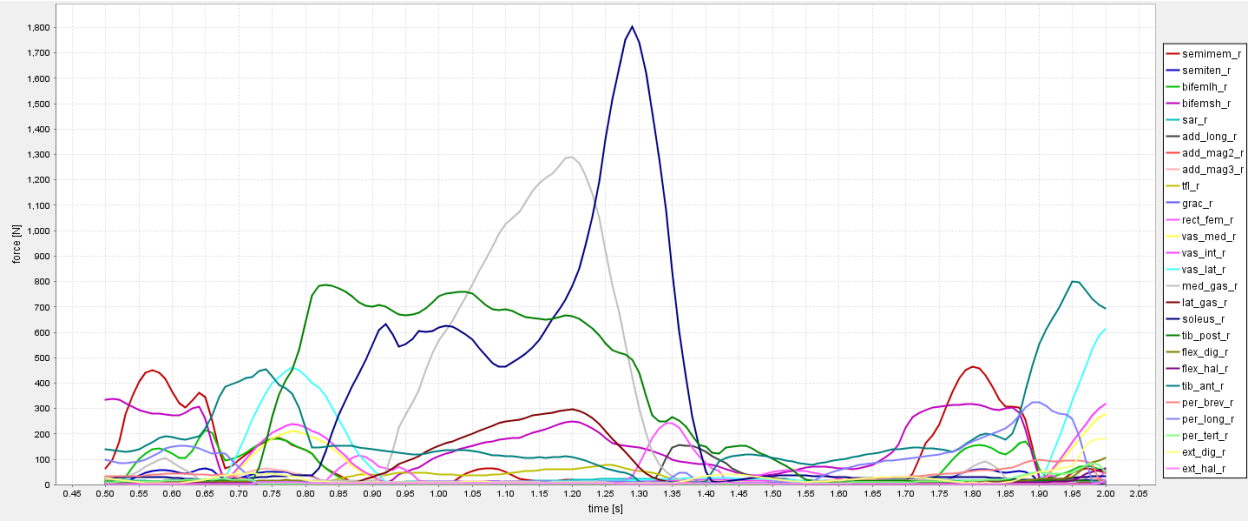

Figure 0-18: All lower limb muscle forces estimated throughout gait for Subject01_walk1

b. Run the external joint reactions subroutine (inverse dynamics using the exact same model anthropometry, prescribed joint angles and GRFs used for static optimization, and the statically optimized muscles as inputs) to check whether the static optimization yielded reasonable knee joint reactions. In general, this step allows users to select which joints and coordinate systems to export data for.

2. Select which muscle groups to use for experimental actuation and which ones to omit
   a. Determine which muscle forces are relevant based on their magnitude (Figure 0-19) relative to other muscles carrying much smaller loads.

[i] p is an arbitrary prescribed constant for all muscles m

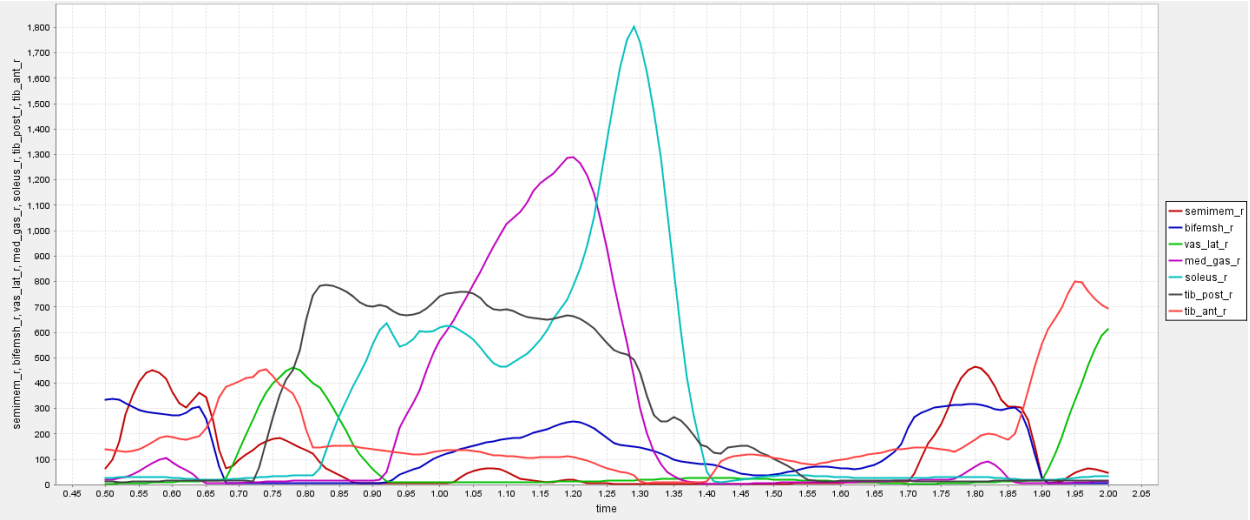

Figure 0-19: Lower limb muscle forces throughout gait for Subject01_walk1 after exclusion based on magnitude

b. Choose among relevant muscles based on practicality and availability ex vivo: Vastus lateralis, semimembranosus, biceps femoris short head and medial gastrocnemius[i], in this case (Figure 0-20)

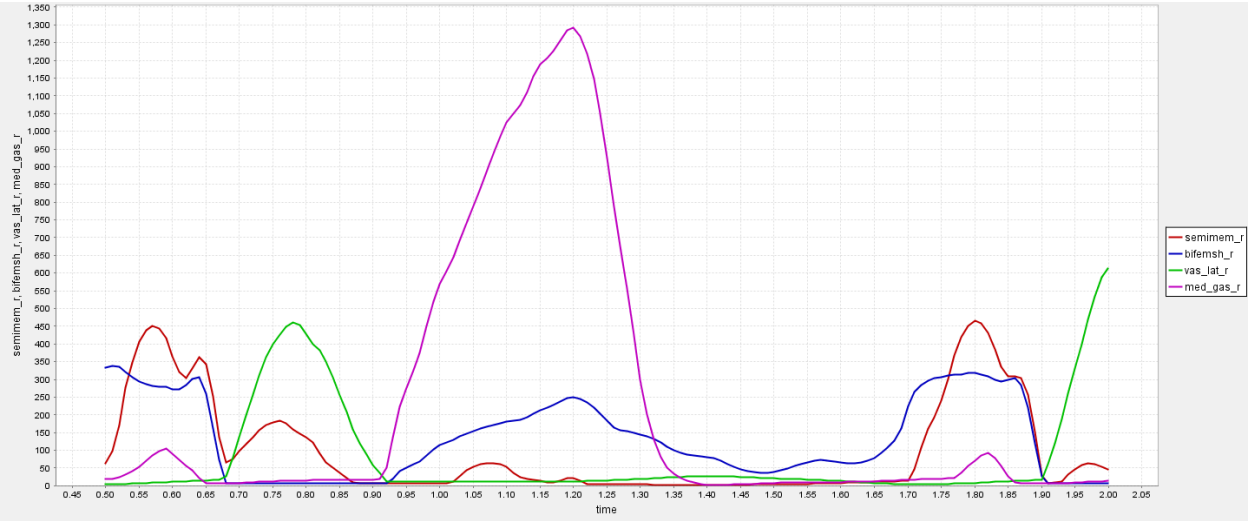

Figure 0-20: Relevant muscles for Subject01_walk1 after exclusion based on practical considerations

[i] Note that currently the rig design does not allow for actuating this muscle, so in the MSK biomechanics codes the machine loads are calculated in order to simulate the effect of this muscle in order to reach the external joint reactions only with the help of the vastus lateralis, semimembranosus and biceps femoris short head.

3. Estimate knee loading due to selected muscles only
    a. Turn off all muscles except the selected muscles (vastus lateralis, semimembranosus, biceps femoris short head and medial gastrocnemius)
    b. Run the static optimization subroutine to estimate these muscle forces
    c. Run the external joint reactions subroutine to estimate knee external loads (via inverse dynamics)
4. Export the following information for MSK processing (inputs to MSK biomechanics codes)
    a. Knee flexion as a function of time throughout gait
    b. Knee forces and moments as vector components
    c. Selected muscle forces as vector components
    d. Virtual marker trajectories attached[i] to the following sites:
        i. Knee center
        ii. Muscle insertion points (both ends) for all muscles selected
        iii. Tibia origin (marker placed at [0, 0, 0]m with respect to its local coordinate system), Ant-Pos marker at [1, 0, 0]m, Med-Lat marker at [0, 1, 0]m, Inf-Sup marker at [0, 0, 1]m
        iv. Marker placed along tibia axial direction where limb is to be cut (15cm from knee center)
        v. Femur origin (marker placed at [0, 0, 0]m with respect to its local coordinate system), Ant-Pos marker at [1, 0, 0]m, Med-Lat marker at [0, 1, 0]m, Inf-Sup marker at [0, 0, 1]m
        vi. Marker placed along femur axial direction where limb is to be cut (15cm from knee center)
        vii. Acetabulum
5. Normalize all loads with respect to body weight and height, in order to scale loading regime to match specimen anthropometrics

[i] Be careful they are not attached to the ground, as they will not follow the bodies of interest unless they are attached to them.

Modelling procedure specific to design purposes:

1. Estimate the maximum operating/loading conditions for the loading rig
    a. Scale the model to represent a 1.8m, 1kN person (largest, heaviest person the rig could simulate physical activities on)
    b. Turn off all muscles except the selected muscles
    c. Run the static optimization subroutine to estimate muscle forces
    d. Run the external joint reactions subroutine to estimate knee external loads
2. Export the same information required for determining the physiologic regime (i.e., step 4)

A3.2. SOP for MSK biomechanics modelling/processing for experimental simulation

Due to the vast scope (both in breadth and depth of many different aspects) of this project and thesis word limits, except for a few exceptions, only an index of the required materials for operating/repairing/modifying the this system (hardware/software) is provided here.

Please contact Dr. Emily McWalter to gain access to these materials:

A3.2.1. MSK biomechanics processing details

A3.2.2. MSK biomechanics code I: Continuous gait simulation

A3.2.3. MSK biomechanics code II: Discrete gait variability simulation

A3.2.4. Specimen misalignment calculator code

A3.2.5. MR creep rig configuration calculations (including muscle guide positions)

A3.3. SOP for MRI-compatible physiologic loading simulator for cadaveric joints

Due to the vast scope (both in breadth and depth of many different aspects) of this project and thesis word limits, except for a few exceptions, only an index of the required materials for operating/repairing/modifying the this system (hardware/software) is provided here.

Please contact Dr. Emily McWalter to gain access to these materials:

A3.3.1. Instructional video (tutorial/demo for MR creep rig)

A3.3.2. MRI-safe loading system (aka. “MR creep rig”) 3D CAD models and G-codes

A3.3.3. MRI-safe loading system (aka. “MR creep rig”) blueprints for main structural components

A3.3.3.1. Top assembly

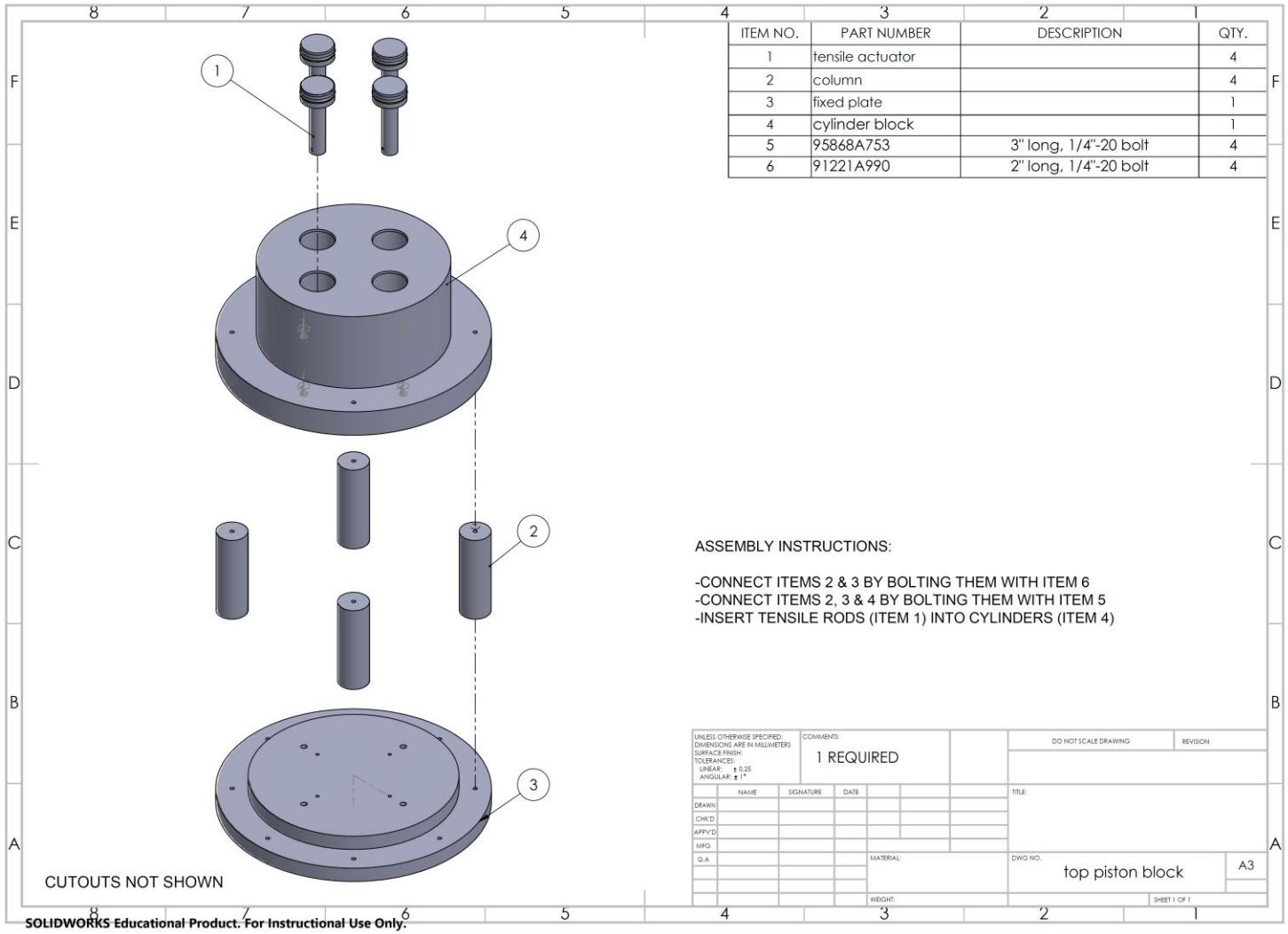

ITEM NO.	PART NUMBER	DESCRIPTION	QTY.
1	tensile rod		1
2	9557K305	O-ring (-327)	1

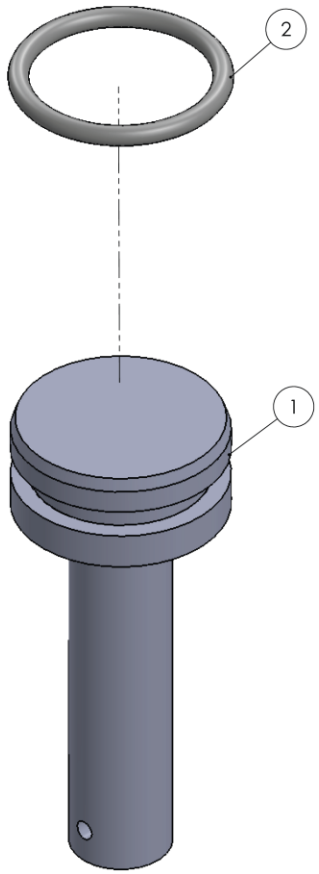

USE CHAMFER TO GUIDE O-RING

UNLESS OTHERWISE SPECIFIED:
DIMENSIONS ARE IN MILLIMETERS
SURFACE FINISH:
TOLERANCES:
LINEAR: ± 0.25
ANGULAR: ± 1°

COMMENTS:
4 REQUIRED

DO NOT SCALE DRAWING | REVISION

	NAME	SIGNATURE	DATE
DRAWN			
CHK'D			
APPV'D			
MFG			
Q.A			

MATERIAL:

WEIGHT:

TITLE:

DWG NO. tensile actuator

A3

SHEET 1 OF 1

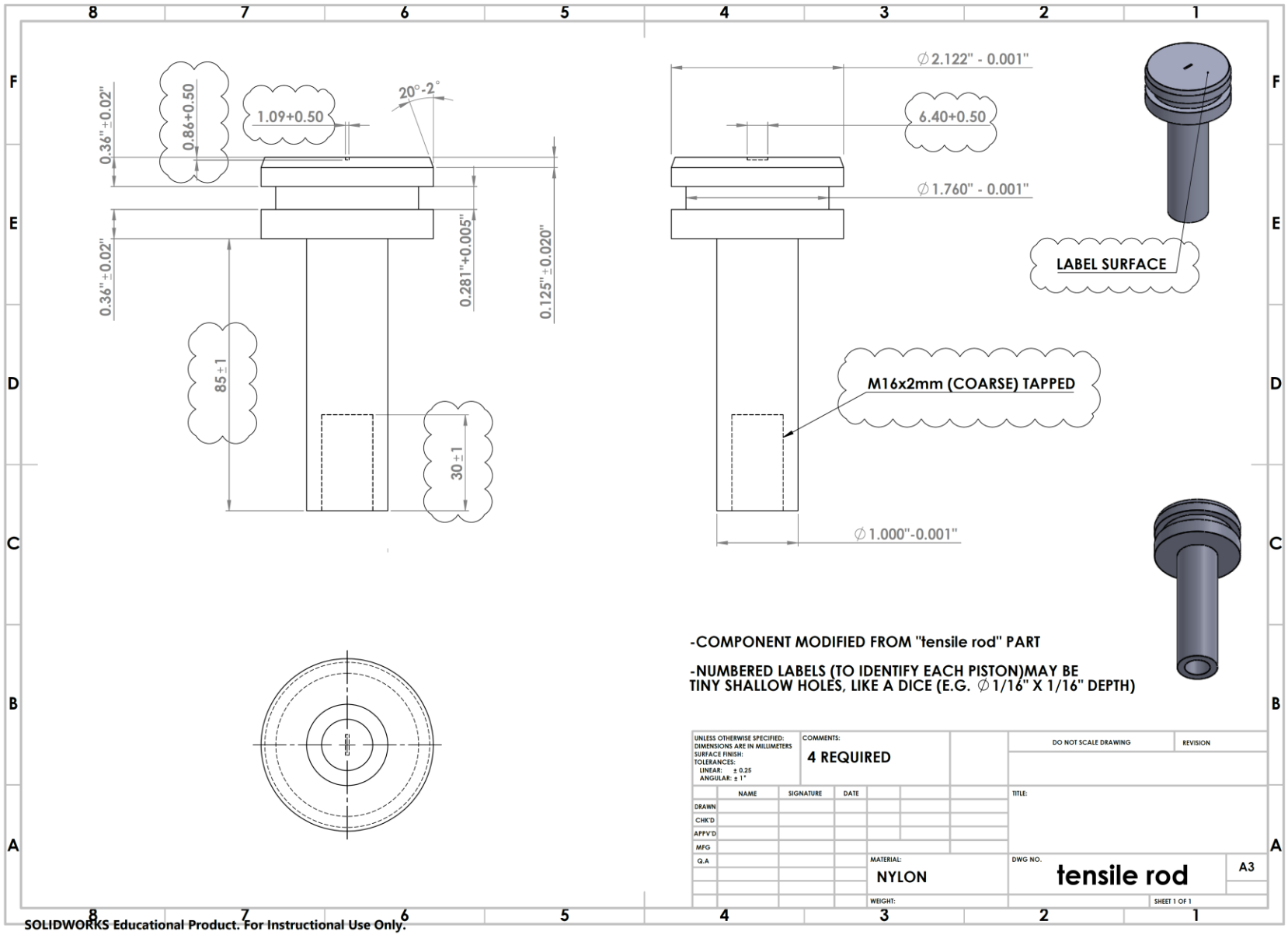

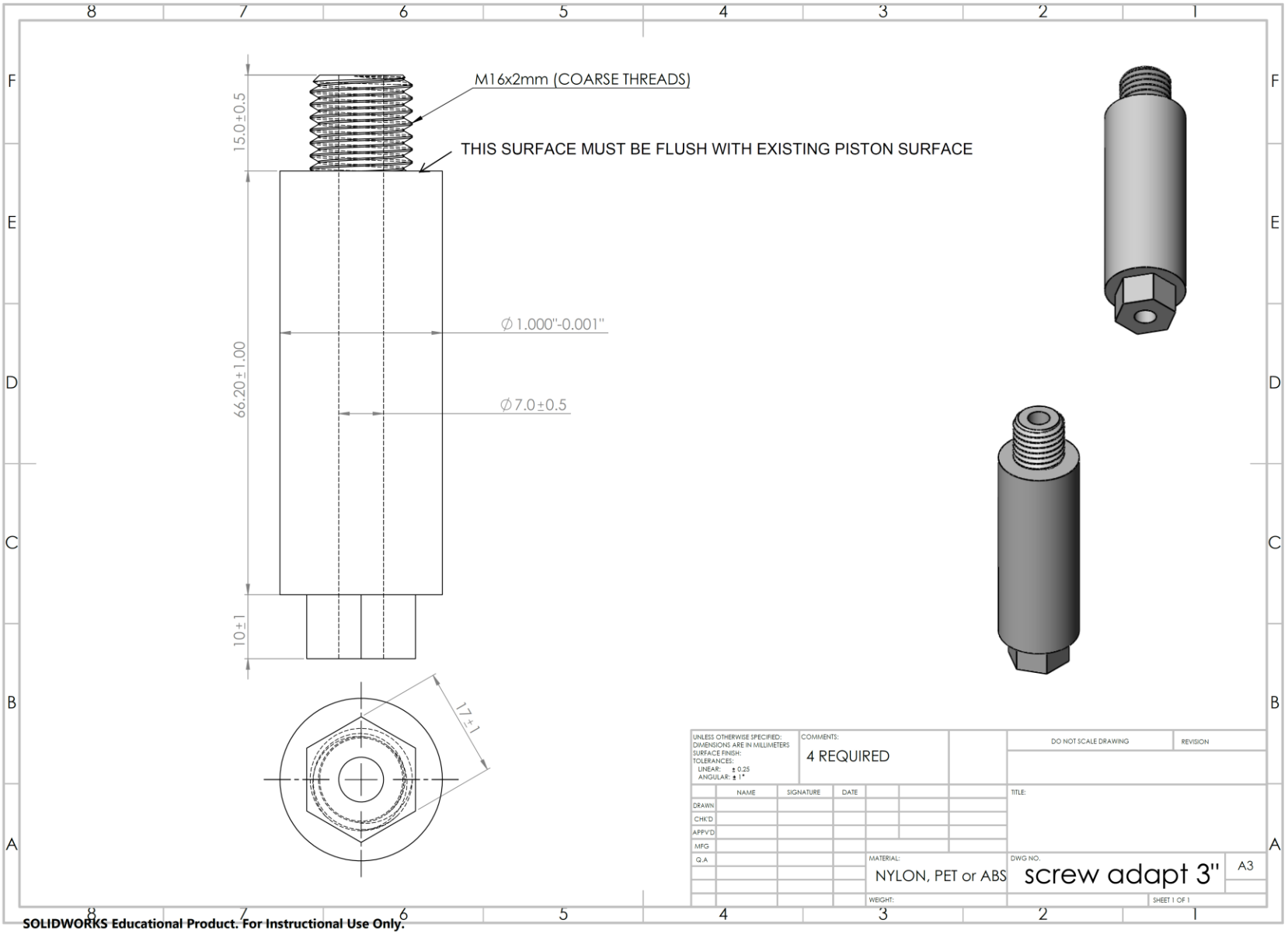

ITEM NO.	PART NUMBER	DESCRIPTION	QTY.
1	9557K295	O-ring (-318)	4
2	50775K329	Thread-hose adapter	4
3	top cylinder block		1
4	bottom cylinder block		1
5	9557K134	O-ring (-043)	4
6	95868A753	3" long, 1/4"-20 bolt	9

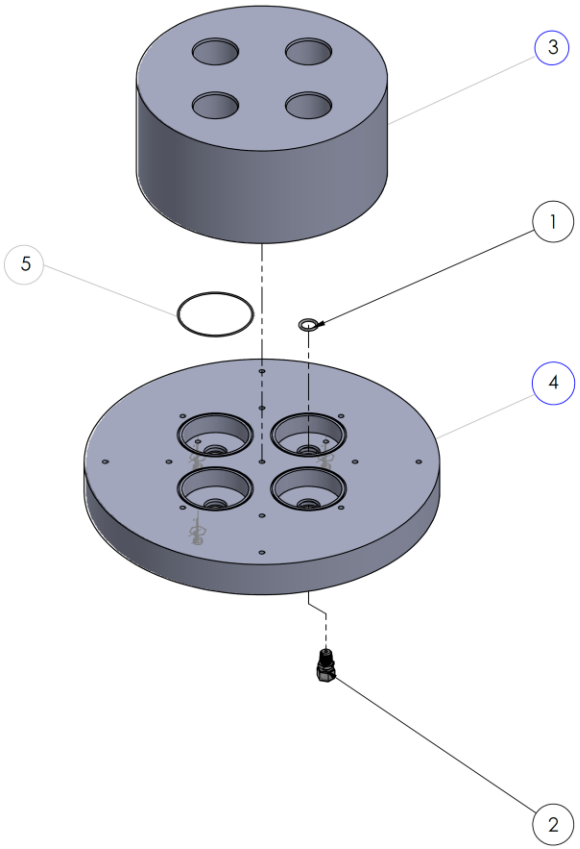

ASSEMBLY INSTRUCTIONS:

1. CONNECT ITEMS 1, 2, 4 & 5.

2. CONNECT ITEMS 3 & 4 BY BOLTING THEM WITH ITEM 6 IN A STAR PATTERN (TO DISTRIBUTE STRESS).

NB:
-USE CHAMFERS TO GUIDE O-RINGS

CUTOUTS NOT SHOWN

UNLESS OTHERWISE SPECIFIED:
DIMENSIONS ARE IN MILLIMETERS
SURFACE FINISH:
TOLERANCES:
LINEAR: ± 0.25
ANGULAR: ± 1°

COMMENTS: 1 REQUIRED

DO NOT SCALE DRAWING | REVISION

	NAME	SIGNATURE	DATE
DRAWN			
CHK'D			
APPV'D			
MFG			
Q.A			

MATERIAL:

WEIGHT:

TITLE:

DWG NO. cylinder block

A3

SHEET 1 OF 1

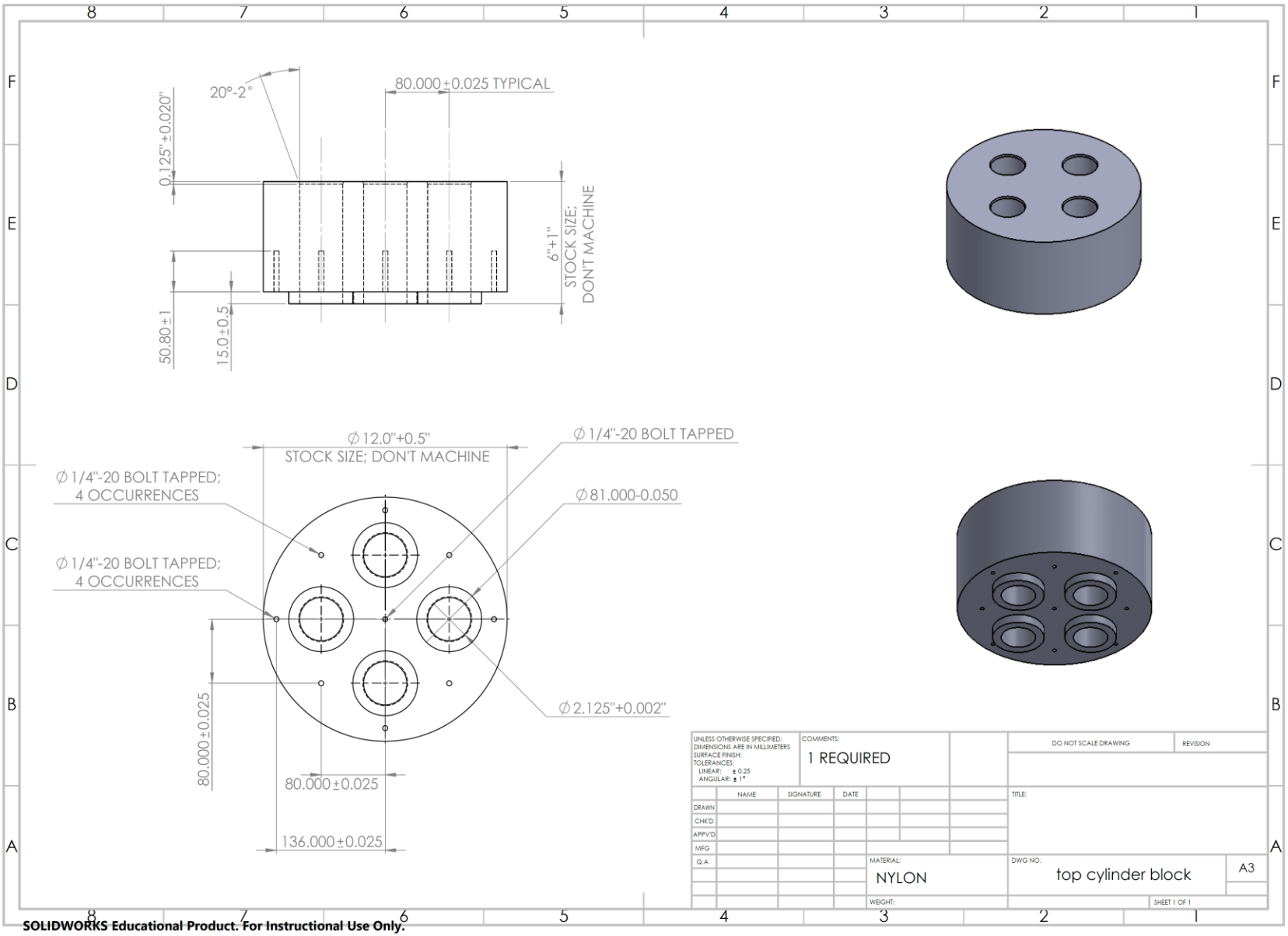

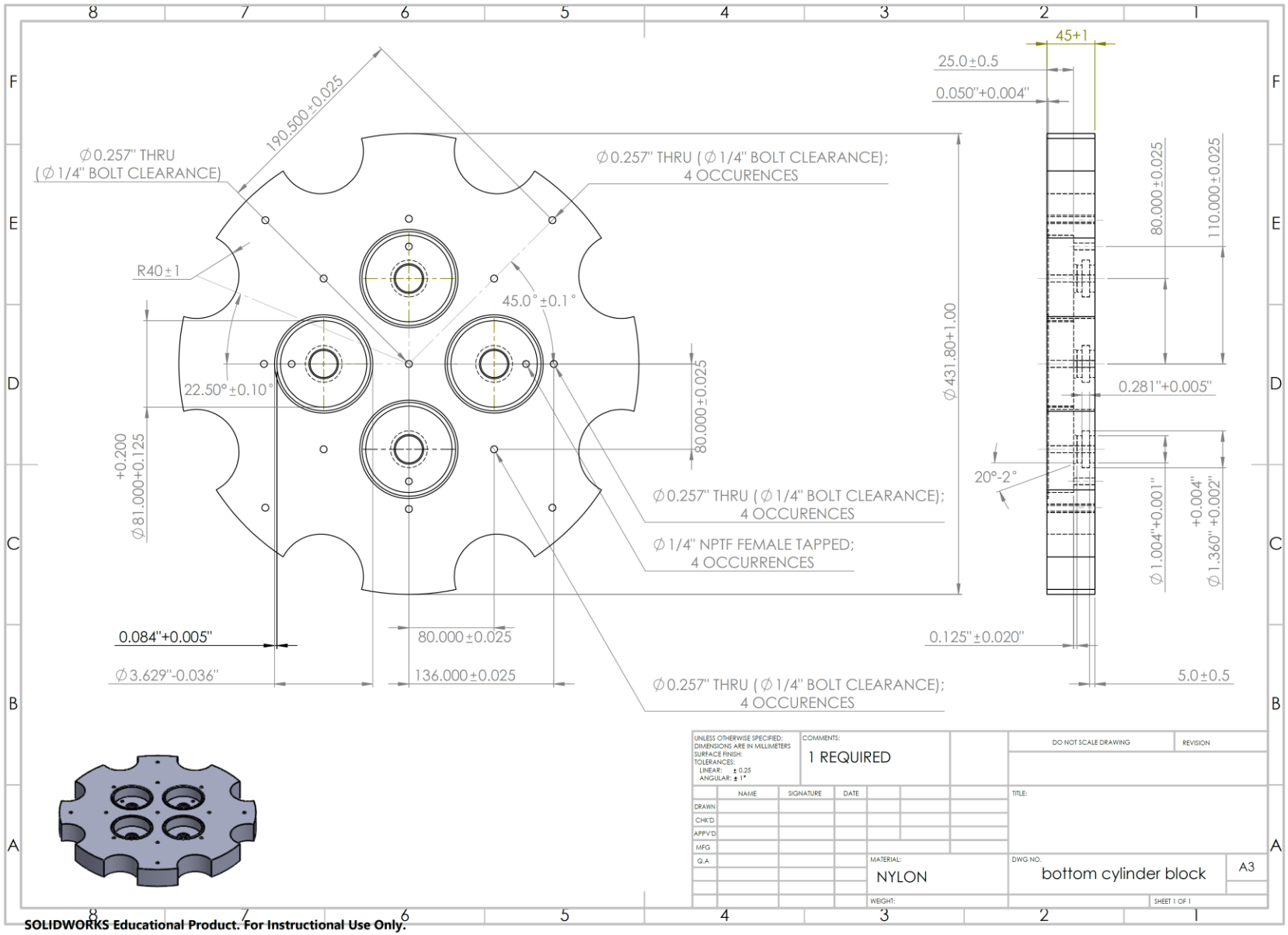

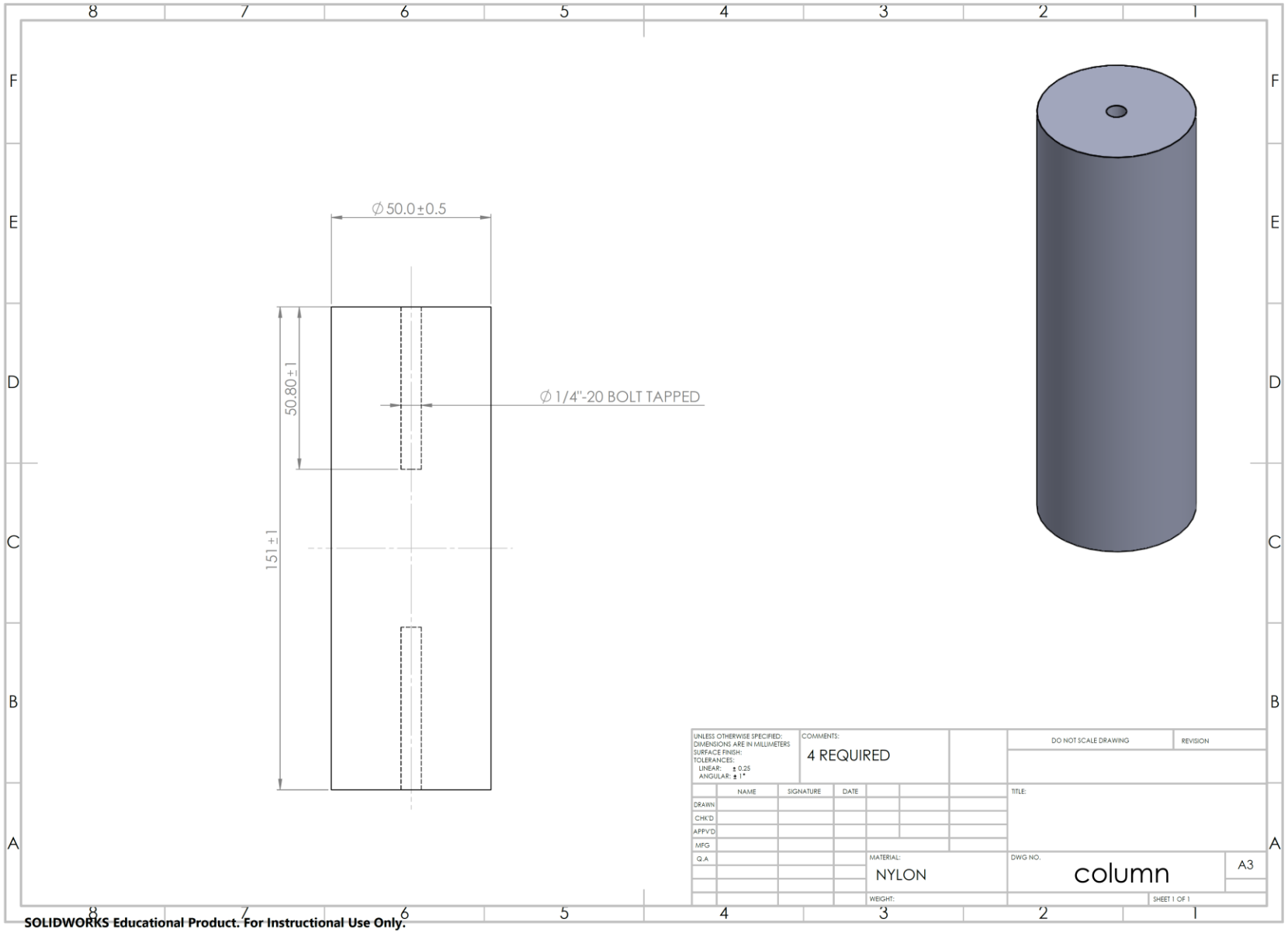

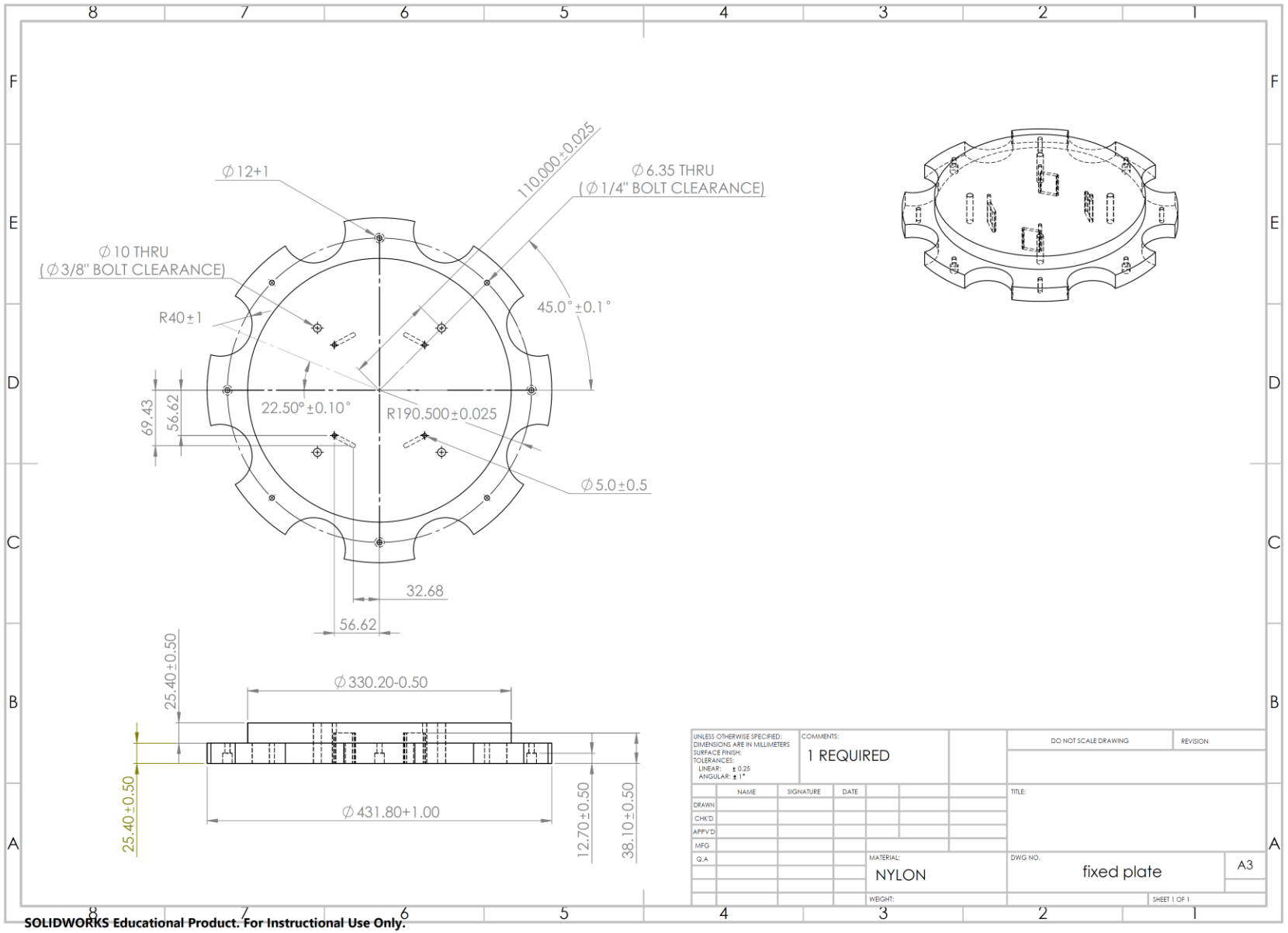

A3.3.3.2. Middle (specimen case) assembly

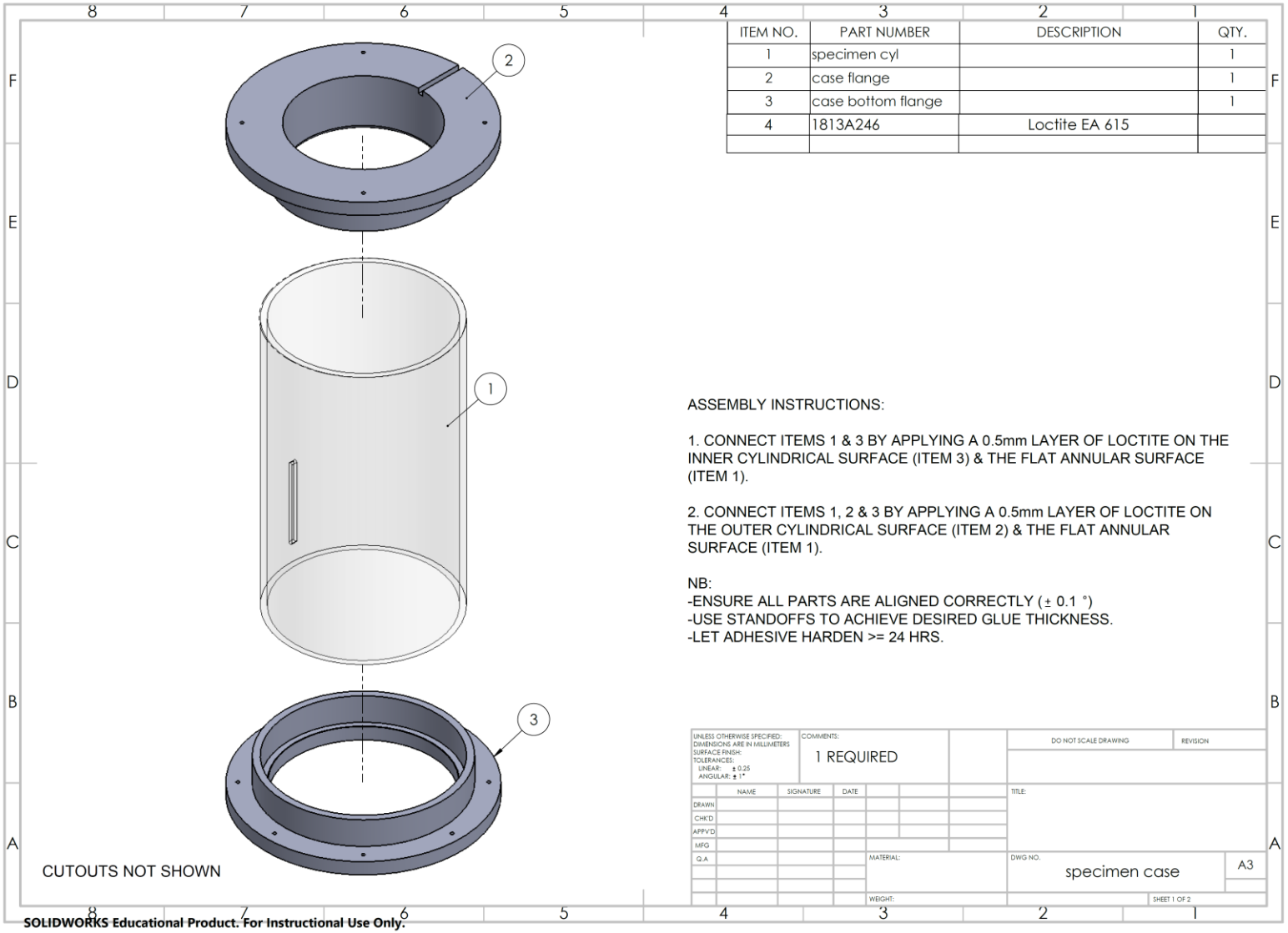

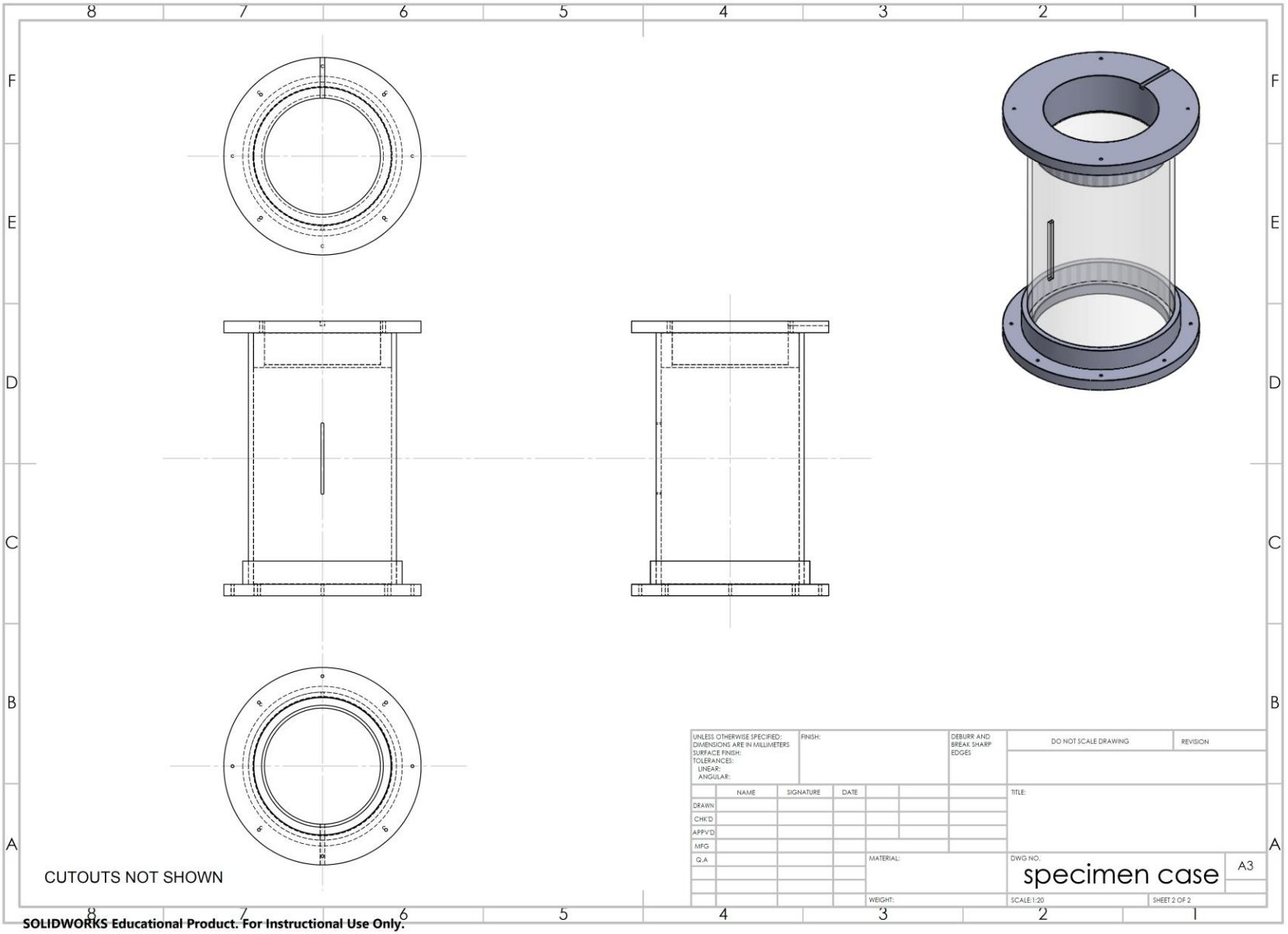

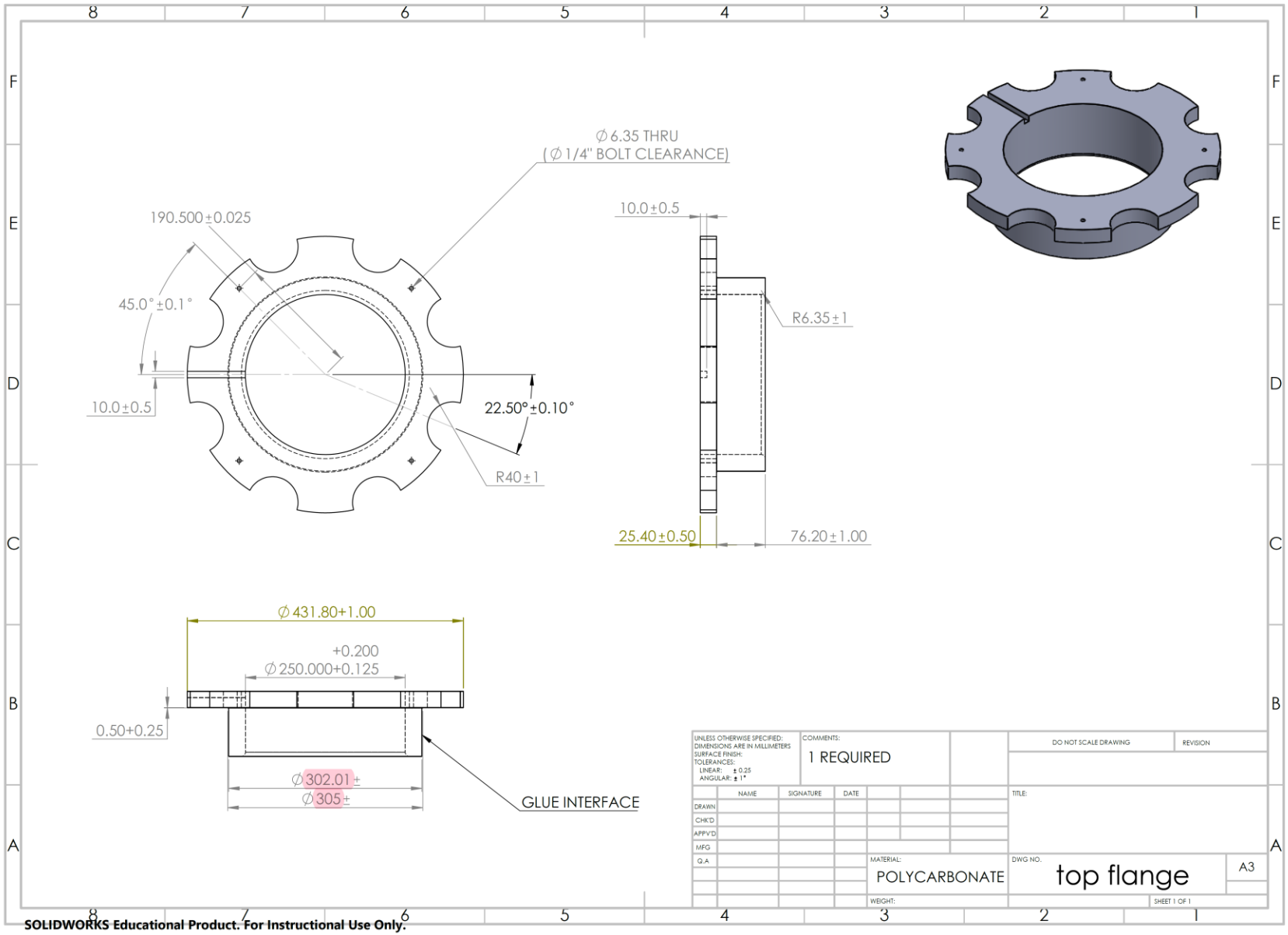

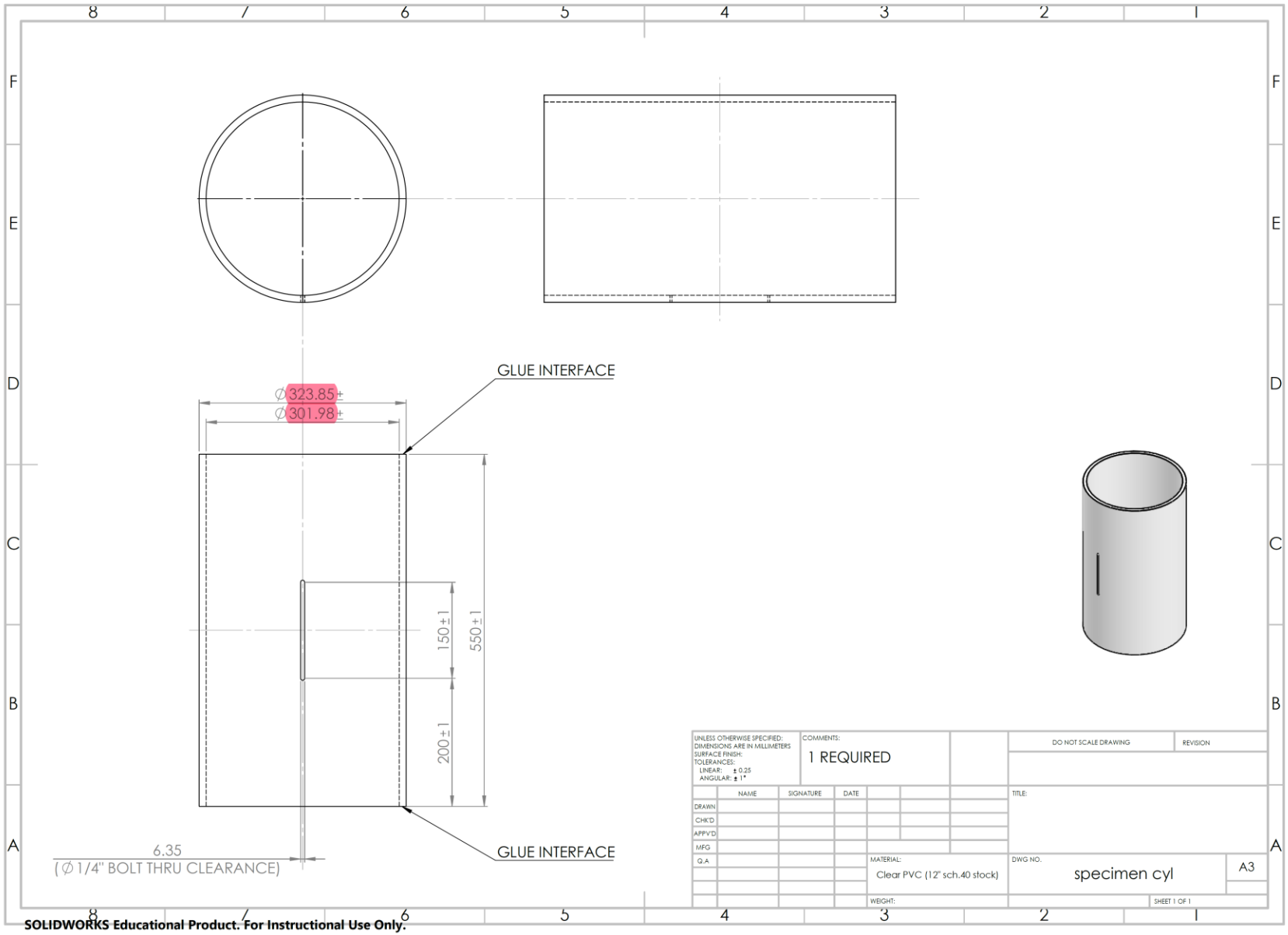

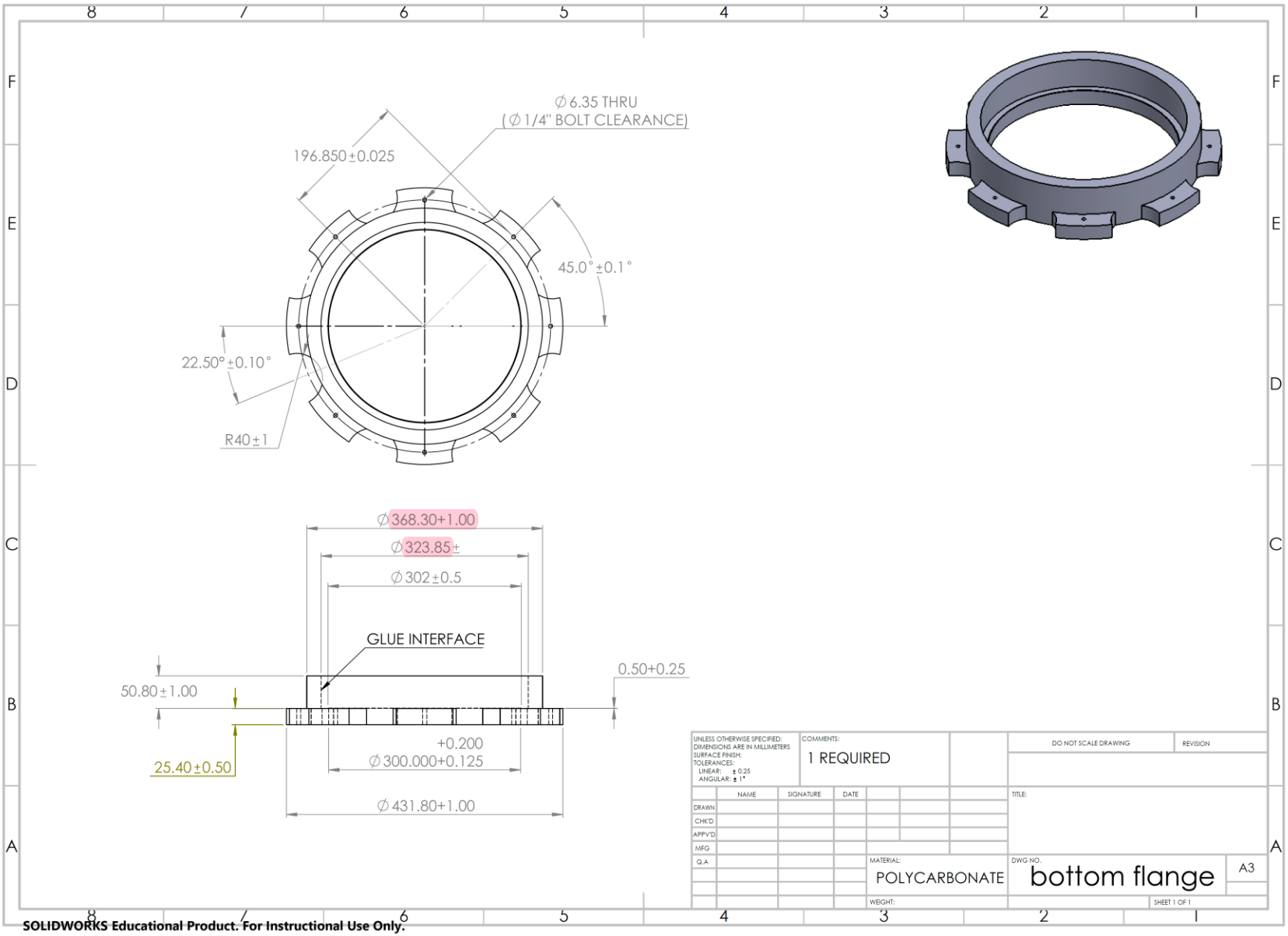

A3.3.3.3. Potted specimen assembly

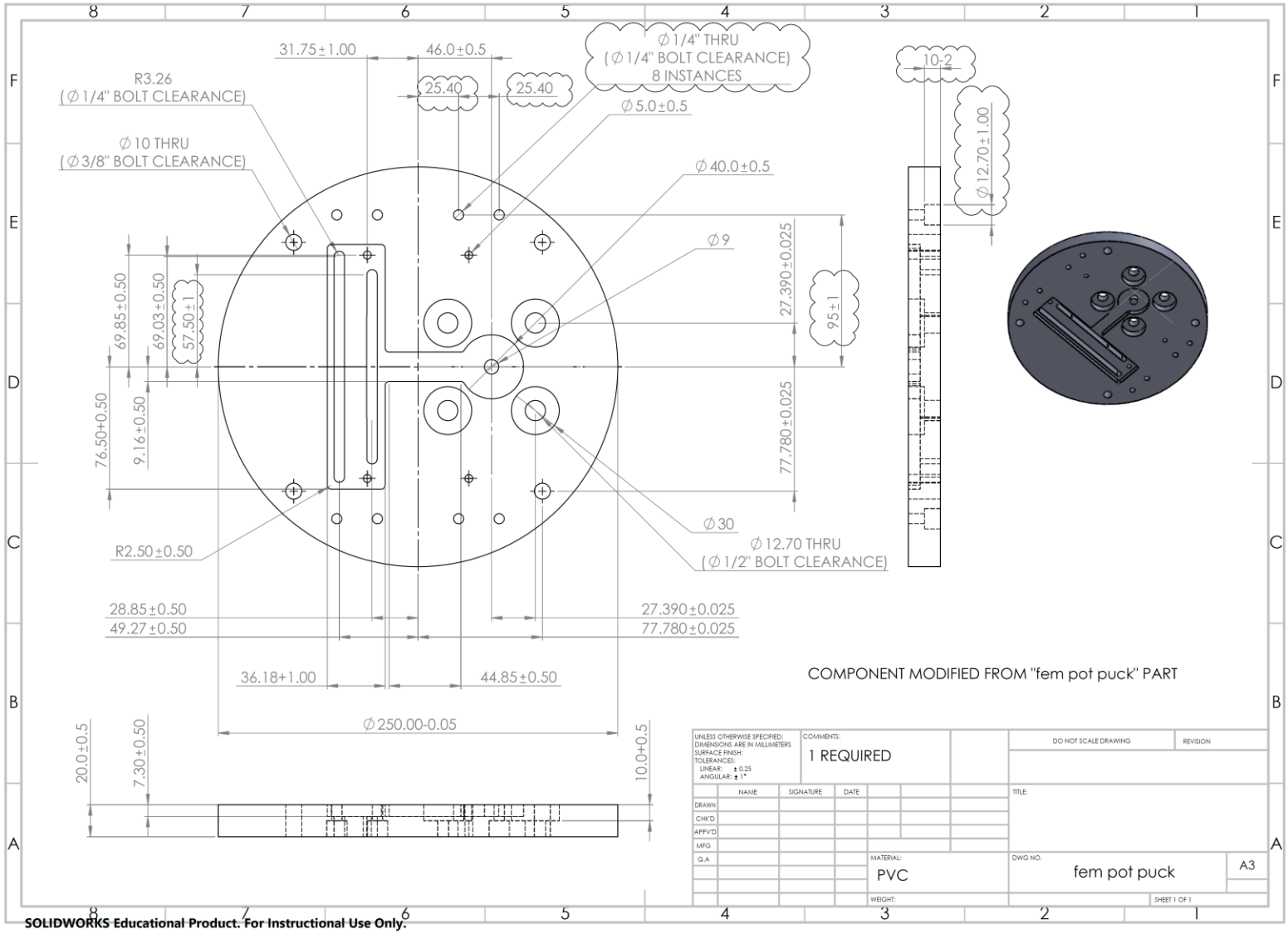

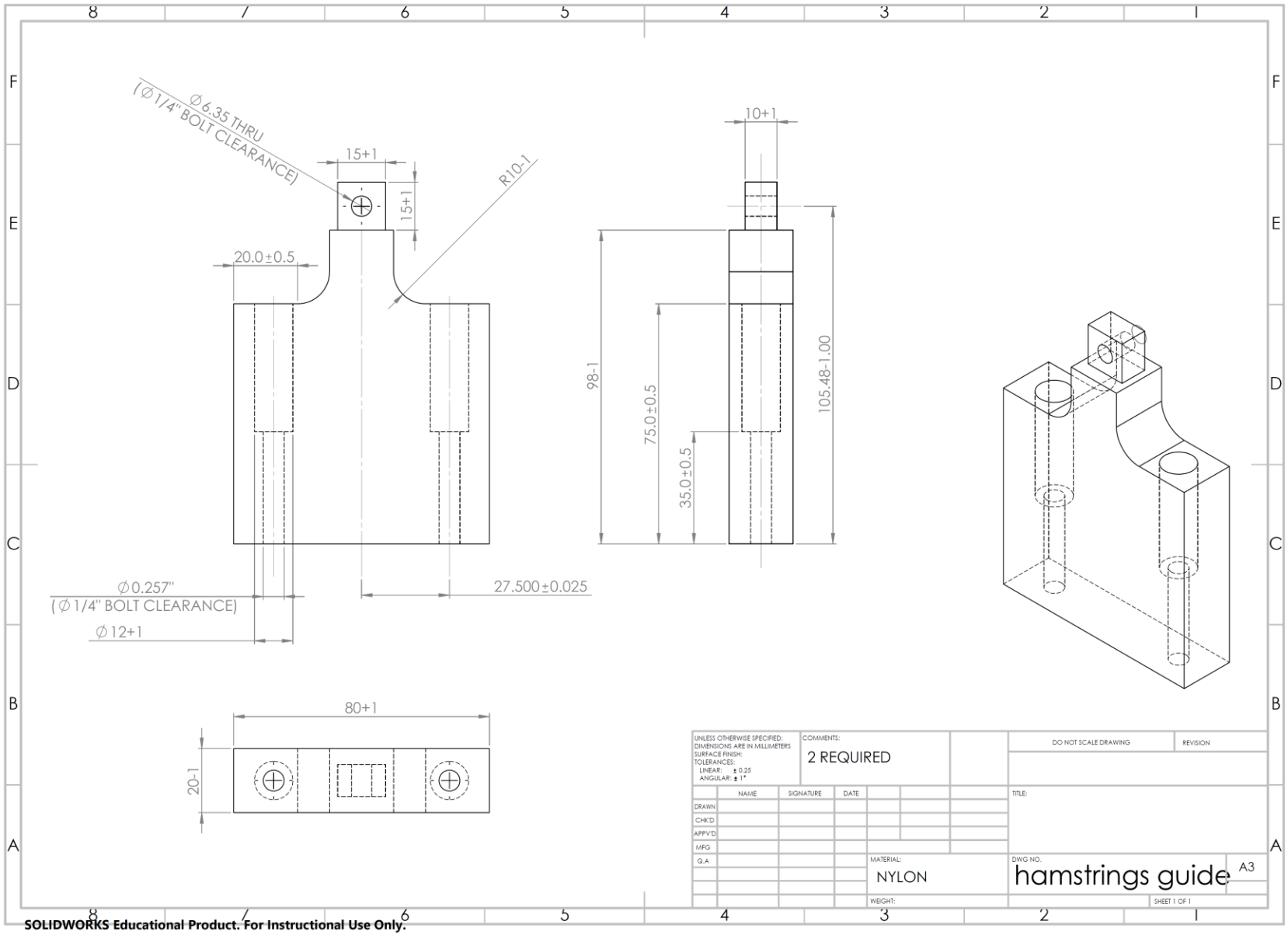

A3.3.3.4. Bottom assembly

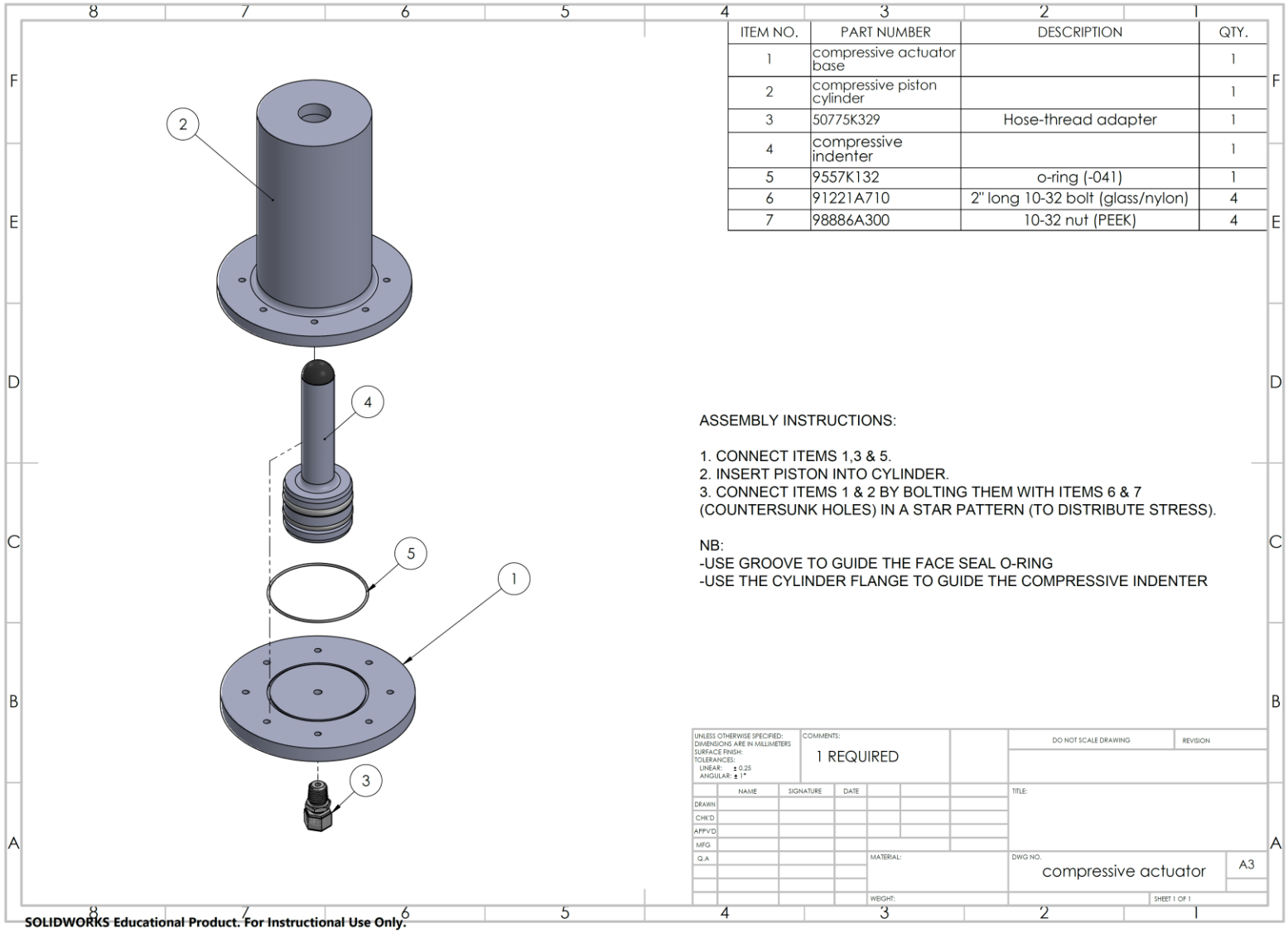

ITEM NO.	PART NUMBER	DESCRIPTION	QTY.
1	compressive actuator base		1
2	compressive piston cylinder		1
3	50775K329	Hose-thread adapter	1
4	compressive indenter		1
5	9557K132	o-ring (-041)	1
6	91221A710	2" long 10-32 bolt (glass/nylon)	4
7	98886A300	10-32 nut (PEEK)	4

ASSEMBLY INSTRUCTIONS:

1. CONNECT ITEMS 1,3 & 5.
2. INSERT PISTON INTO CYLINDER.
3. CONNECT ITEMS 1 & 2 BY BOLTING THEM WITH ITEMS 6 & 7 (COUNTERSUNK HOLES) IN A STAR PATTERN (TO DISTRIBUTE STRESS).

NB:
-USE GROOVE TO GUIDE THE FACE SEAL O-RING
-USE THE CYLINDER FLANGE TO GUIDE THE COMPRESSIVE INDENTER

UNLESS OTHERWISE SPECIFIED:
DIMENSIONS ARE IN MILLIMETERS
SURFACE FINISH:
TOLERANCES:
LINEAR: ± 0.25
ANGULAR: ± 1°

COMMENTS: 1 REQUIRED

DO NOT SCALE DRAWING | REVISION

	NAME	SIGNATURE	DATE
DRAWN			
CHK'D			
APP'V'D			
MFG			
Q.A			

TITLE:

MATERIAL:

DWG NO. compressive actuator

A3

WEIGHT:

SHEET 1 OF 1

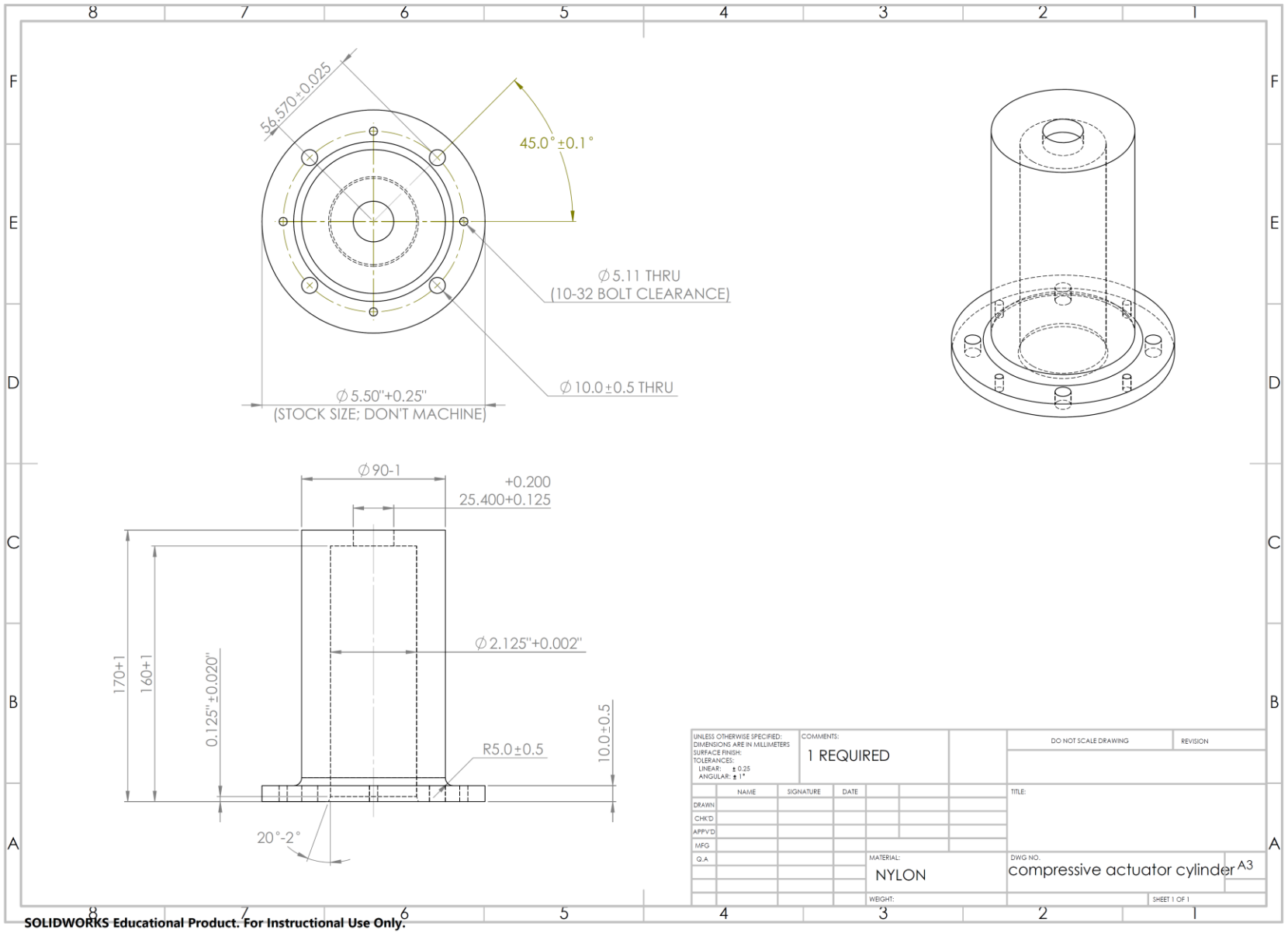

ITEM NO.	PART NUMBER	DESCRIPTION	QTY.
1	compressive piston		1
2	9557K305	o-ring (-327)	2
3	indenter tip		1
4	1813A246	Loctite EA 615	

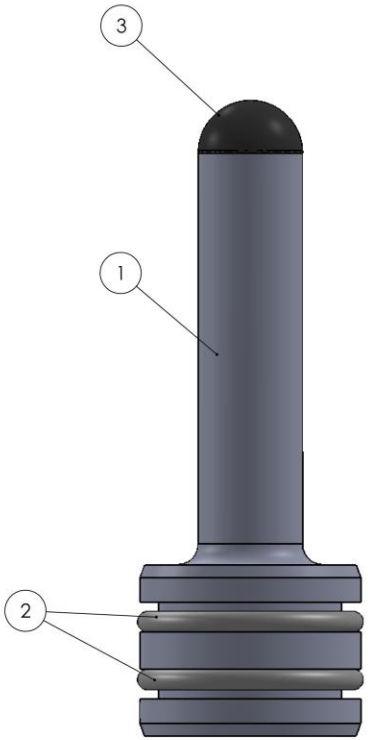

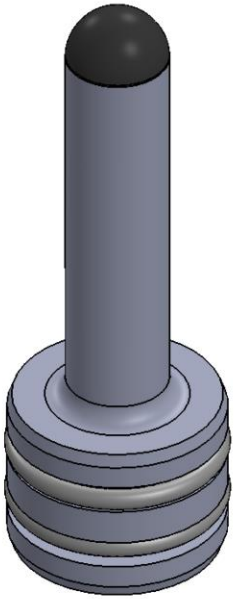

ASSEMBLY INSTRUCTIONS:

-GLUE ITEMS 1 & 3 WITH A 0.5mm LAYER OF LOCTITE

NB:
-USE CHAMFERS TO GUIDE O-RINGS
-USE STANDOFFS TO ACHIEVE DESIRED GLUE THICKNESS.
-LET ADHESIVE HARDEN >= 24 HRS.

UNLESS OTHERWISE SPECIFIED: DIMENSIONS ARE IN MILLIMETERS SURFACE FINISH: TOLERANCES: LINEAR: ± 0.25 ANGULAR: ± 1°	COMMENTS: 1 REQUIRED					DO NOT SCALE DRAWING	REVISION
	NAME	SIGNATURE	DATE			TITLE:	
DRAWN							
CHK'D							
APPV'D							
MFG							
Q.A				MATERIAL:		DWG NO. compressive indenter	A3
				WEIGHT:			SHEET 1 OF 1

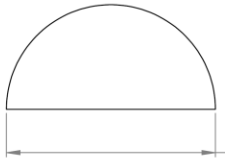

∅25.40 (STOCK SIZE; DON'T MACHINE DOWN)
JUST CUT BALL IN HALF

UNLESS OTHERWISE SPECIFIED: DIMENSIONS ARE IN MILLIMETERS SURFACE FINISH: TOLERANCES: LINEAR: ± 0.25 ANGULAR: ± 1°		COMMENTS: 1 REQUIRED				DO NOT SCALE DRAWING	REVISION
	NAME	SIGNATURE	DATE			TITLE:	
DRAWN							
CHK'D							
APPV'D							
MFG							
Q.A				MATERIAL: RUBBER		DWG NO. indenter tip	A3
				WEIGHT:			SHEET 1 OF 1

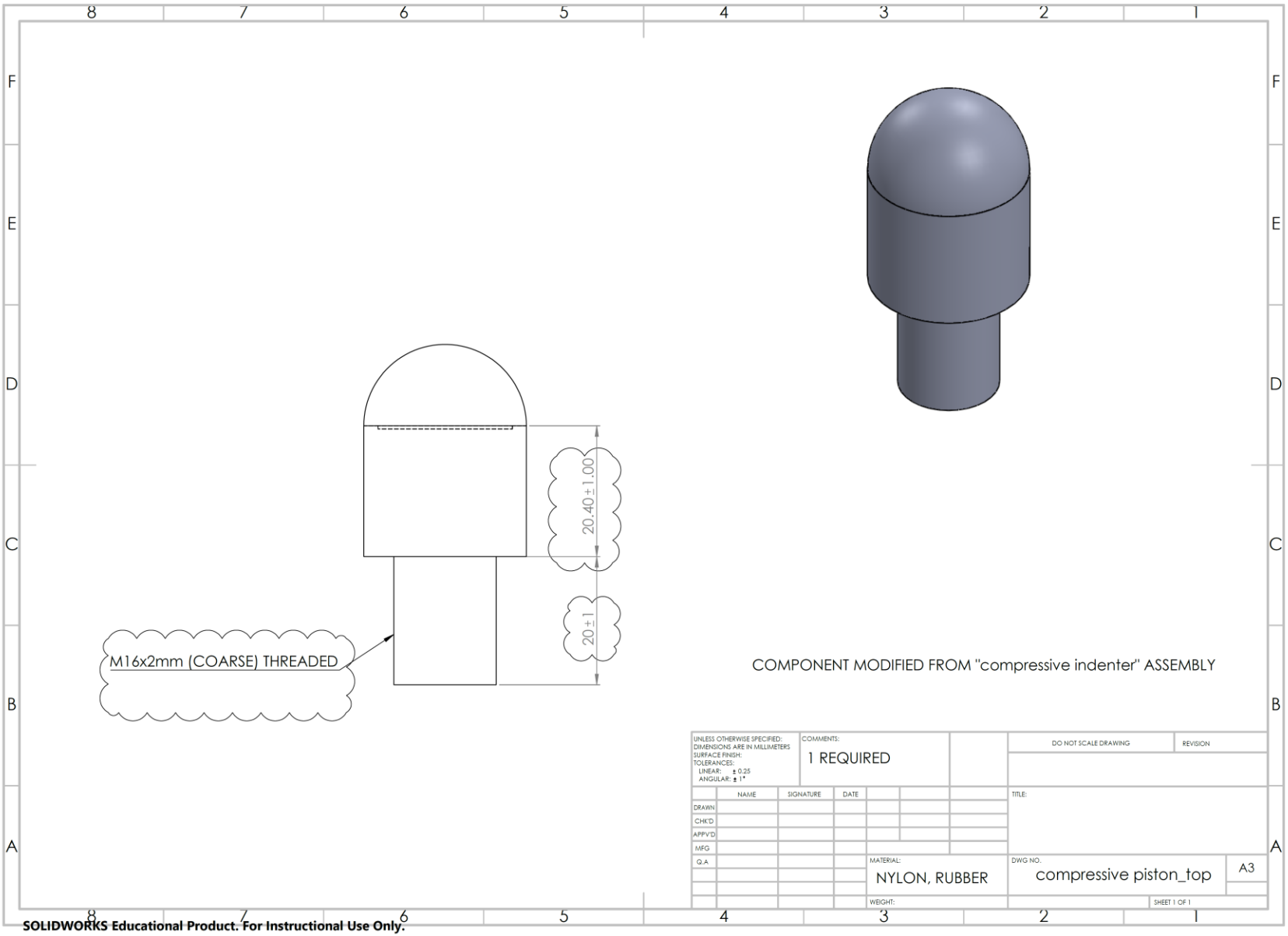

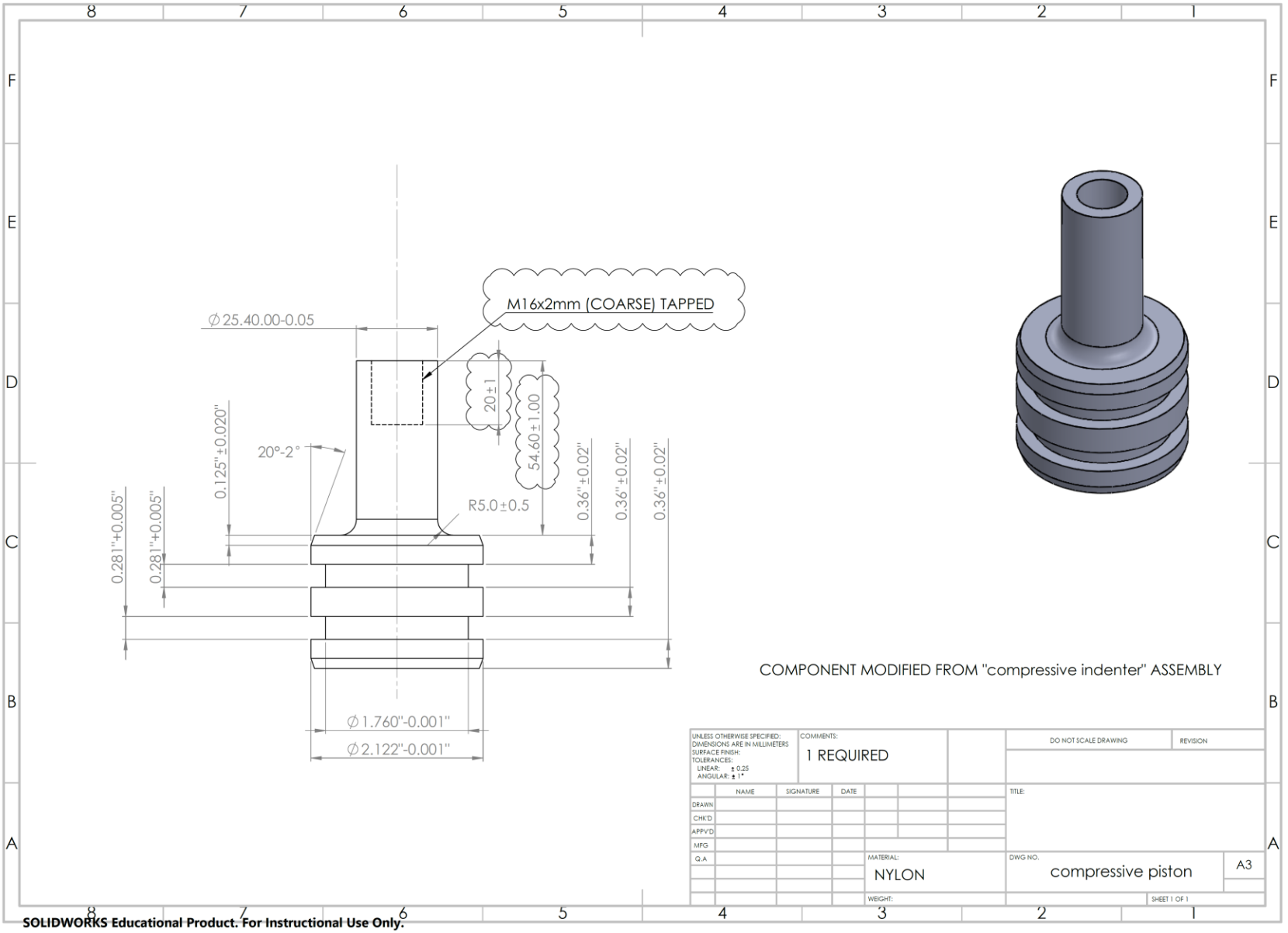

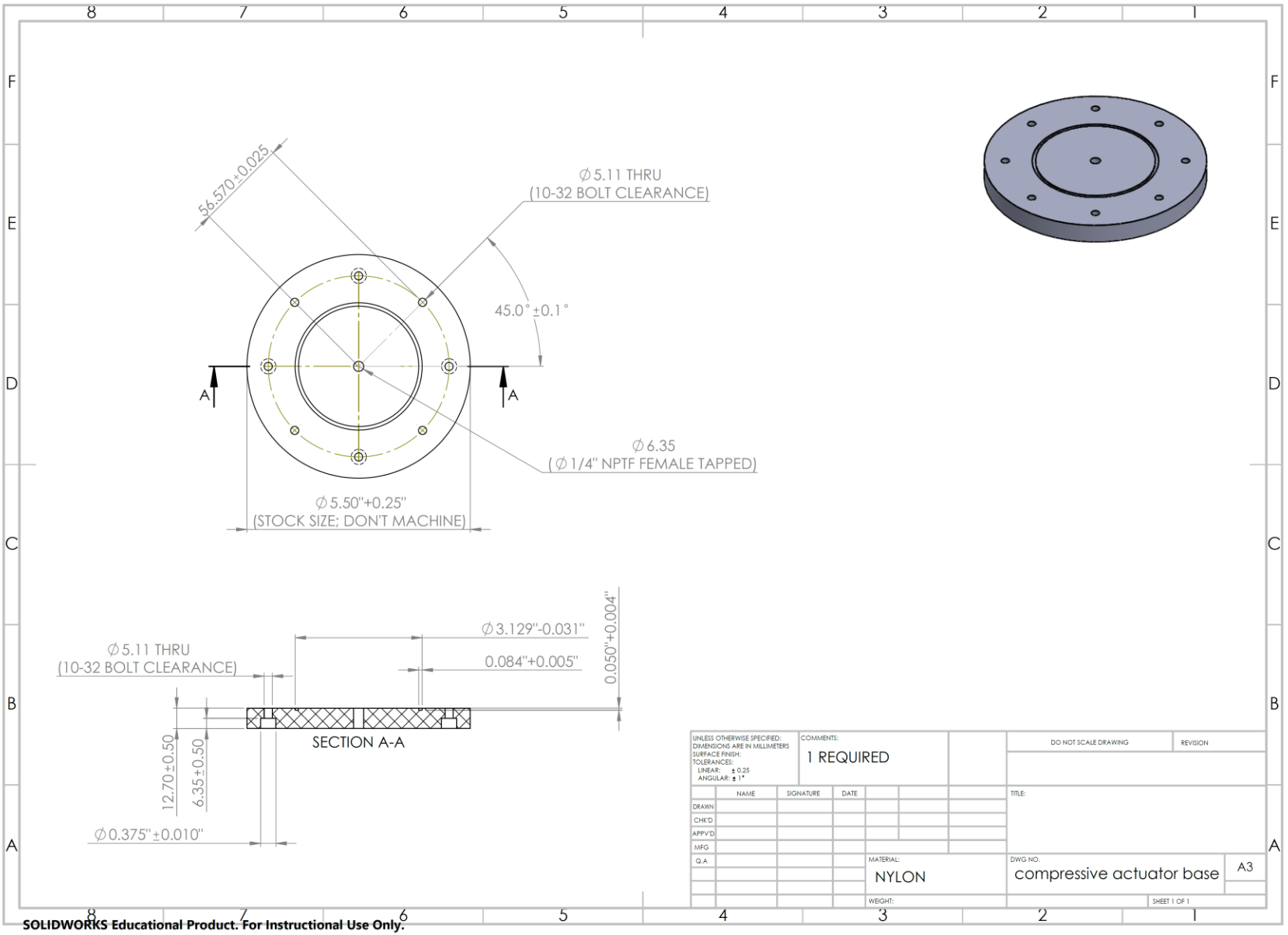

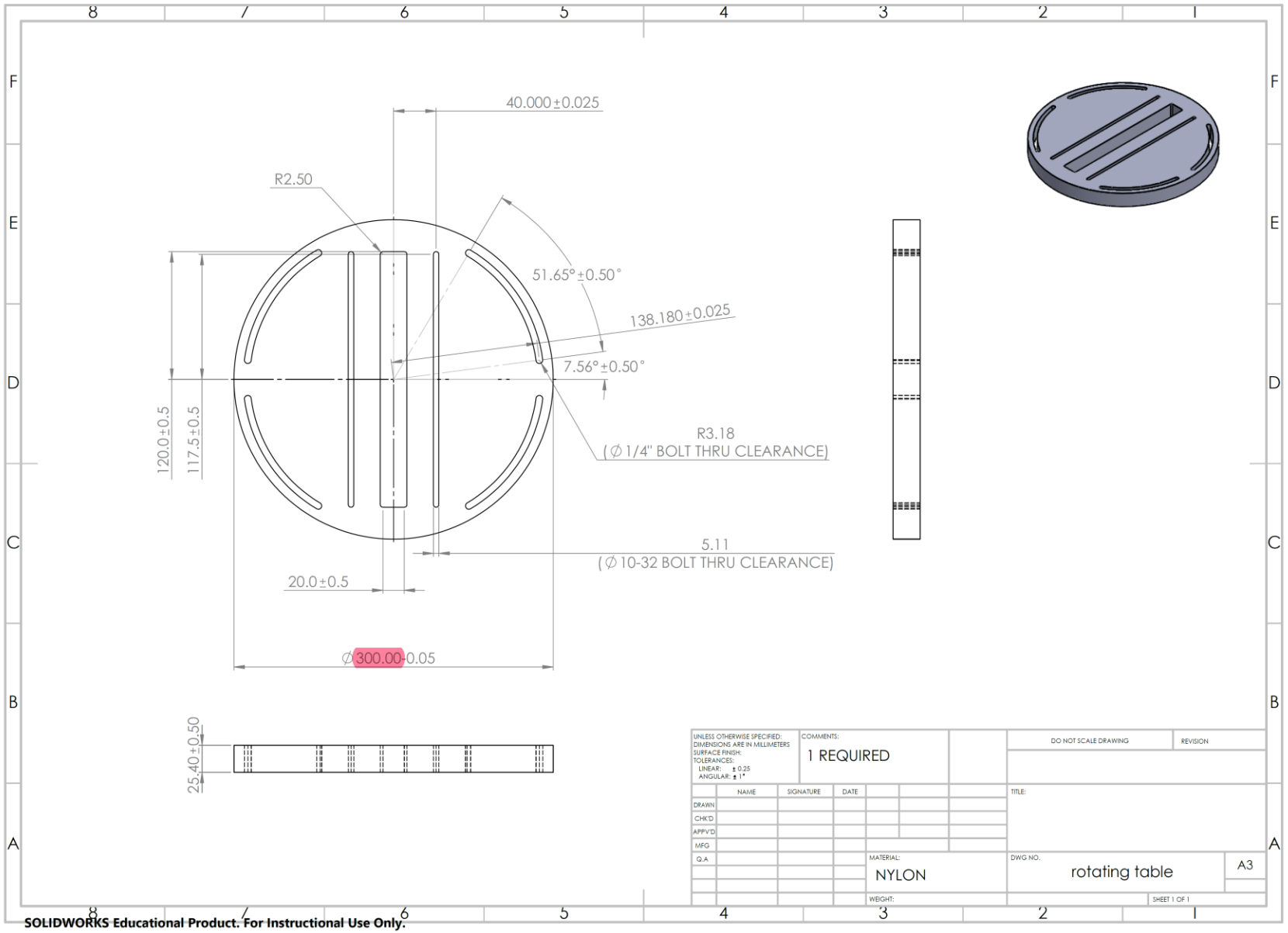

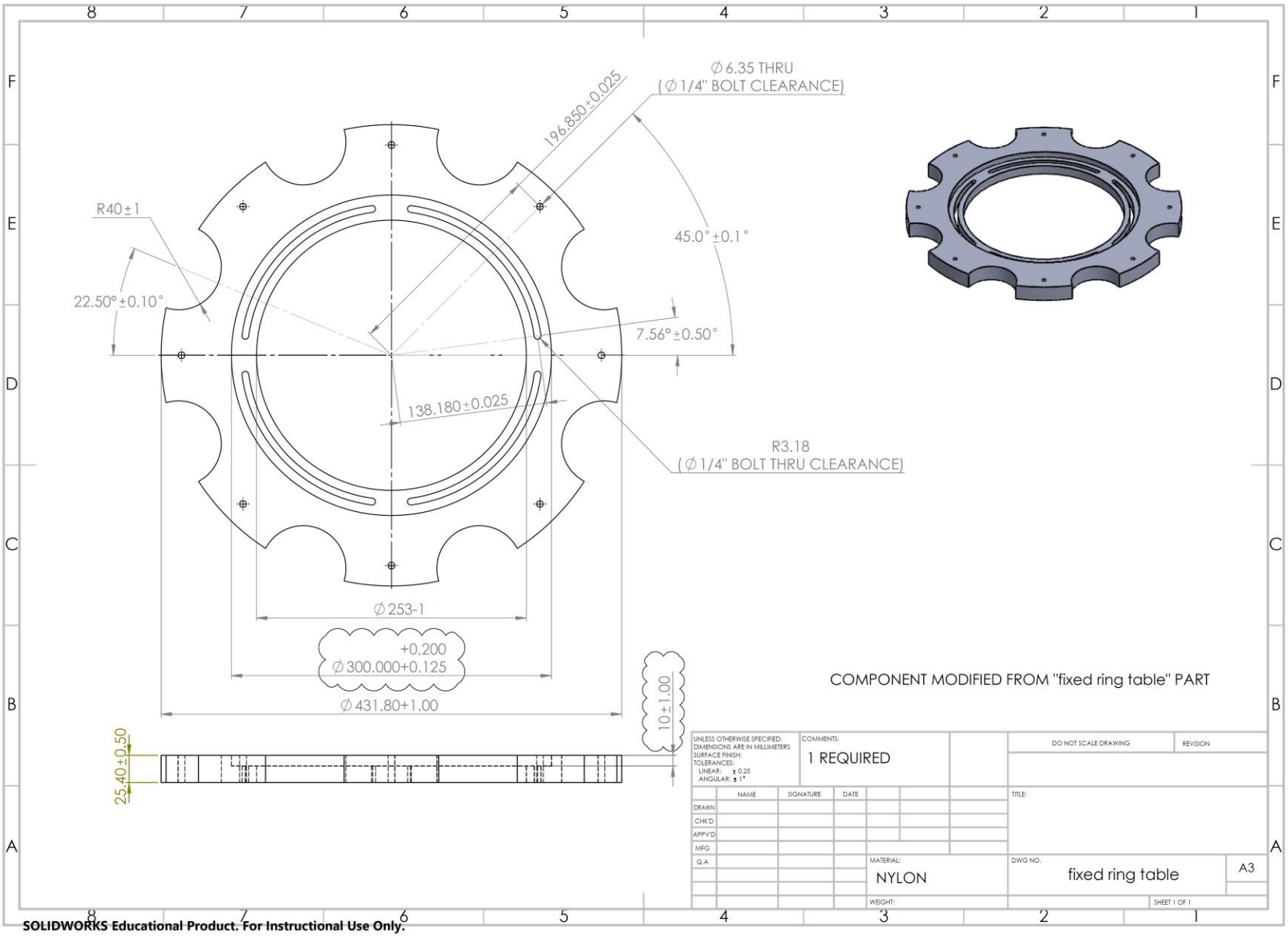

A3.4. Raw data

Due to the vast scope (both in breadth and depth of many different aspects) of this project and thesis word limits, only an index of the raw data acquired is provided here:

A3.4.1. Flex & rigid coil images

A3.4.2. MSK anonymous gait data (OpenSim subject)

A3.4.2.1. Anthropometrics (BW, dimensions)

A3.4.2.2. Kinematics (marker position, velocity, acceleration)

A3.4.2.3. Kinetics (GRFs)

A3.4.3. Friction measurements for compressive indenter / tibia pot interface

A3.4.4. MR creep rig calibration

A3.4.4.1. Load cell force data (tensile & compressive actuators)

A3.4.4.2. Pressure gauges data

A3.4.5. Loading variability for left/right knees (non-dimensionalized)

Please contact Dr. Emily McWalter to gain access to these materials.

A3.5. Processed data

Due to the vast scope (both in breadth and depth of many different aspects) of this project and thesis word limits, only an index of the processed data acquired is provided here.

Please contact Dr. Emily McWalter to gain access to these materials:

A3.5.1. Flex & rigid coils' SNR

A3.5.2. MSK anonymous gait data (1kN, 1.8m subject)

A3.5.2.1. Statically optimized muscle tension

A3.5.2.2. External knee joint reactions

A3.5.3. Loading regime & rig configuration (1kN, 1.8m subject)

A3.5.4. Friction coefficients for compressive indenter / tibia pot interface

A3.5.5. Rig calibration

To simulate a physiologic loading state, the correspondence between the pressures delivered by the compressor and the forces delivered to the specimen must be established. Ideally, the operator would have a direct readout of the applied forces sensed via load cells; however, MRI metal restrictions prevented this, as no MRI-compatible load cells could withstand the physiologic loading levels. The best alternative was calibrating the equipment and using calibration curves to set the knee loads at the MR scanner. Standard load cells, however, could be used inside a biomechanics lab (far from magnetic fields) to accomplish this. Thus, in order to measure applied loads and produce a calibration curve for the compressive actuator (axial force vs. cylinder pressure), a donut load cell was placed along the femur's mechanical axis (from acetabulum to knee centre) to measure compression (Figure 0-21). For the distinct tensile actuators' calibration curve (tensile force vs. cylinder pressure), a tensile load cell was connected to muscle cables to measure tension during calibration trials prior to imaging. Similar to other studies[16], an anatomic model (a life-size didactic 3D model of the knee, including plastic bones and rubber soft tissues) in extended configuration (rather than an actual specimen) was used for this purpose as well as for testing rig design modifications, as rig calibration is a characteristic of the loading device (irrespective of whichever specimen is used). Actuator pressures were recorded by webcams attached to the pneumatics control unit.

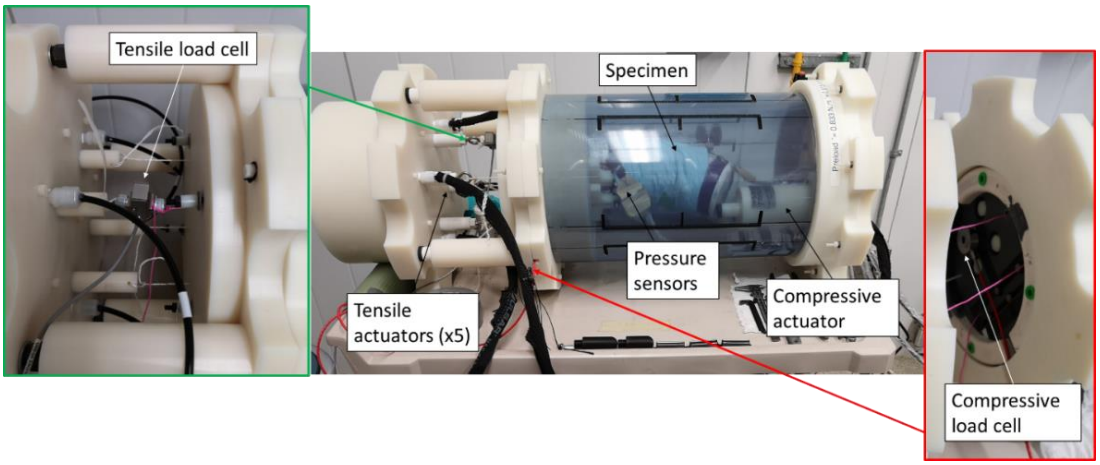

Figure 0-21: Calibration & input loading repeatability setup showing tensile (Omega LCM703-75) and compressive (FUTEKLTH350-FSH04307) load cells, and pressure sensors (novel pliance-x)

Both tensile and compressive actuators were calibrated, and they exhibit a piecewise behavior in the loading process, and substantial hysteresis during unloading (Figure 0-22).

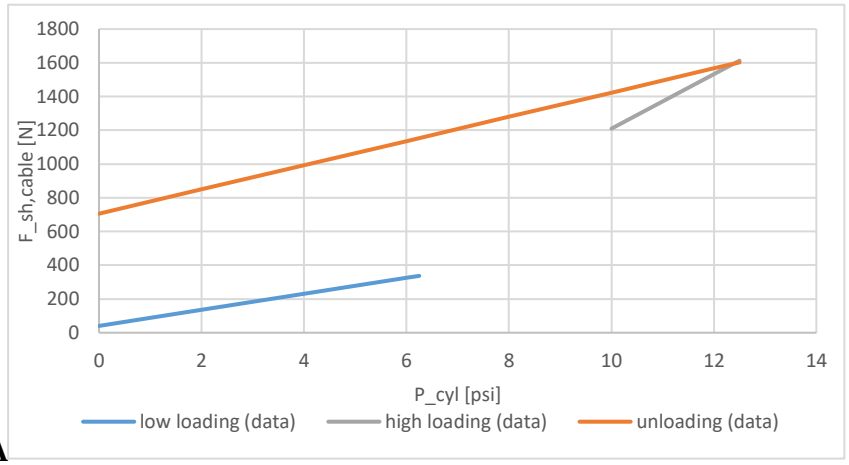

A

Configuration: Superlube oil, soft silicone o-rings, outsourced screw adapters
Comments: Anatomic model; truly isolated loading, always resetting piston position prior to loading; n=2 trials for low-level loading, n=3 for high-level loading, n=4 trials for hysteresis

F = 47.44*P + 40.5, 0 =< P =< 6.25 (low-level loading)
F = 161.333*P - 403.667, 10 =< P =< 12.5 (high-level loading)
F = 71.757*P + 705.655, 0 =< P =< 12.5 (unloading)

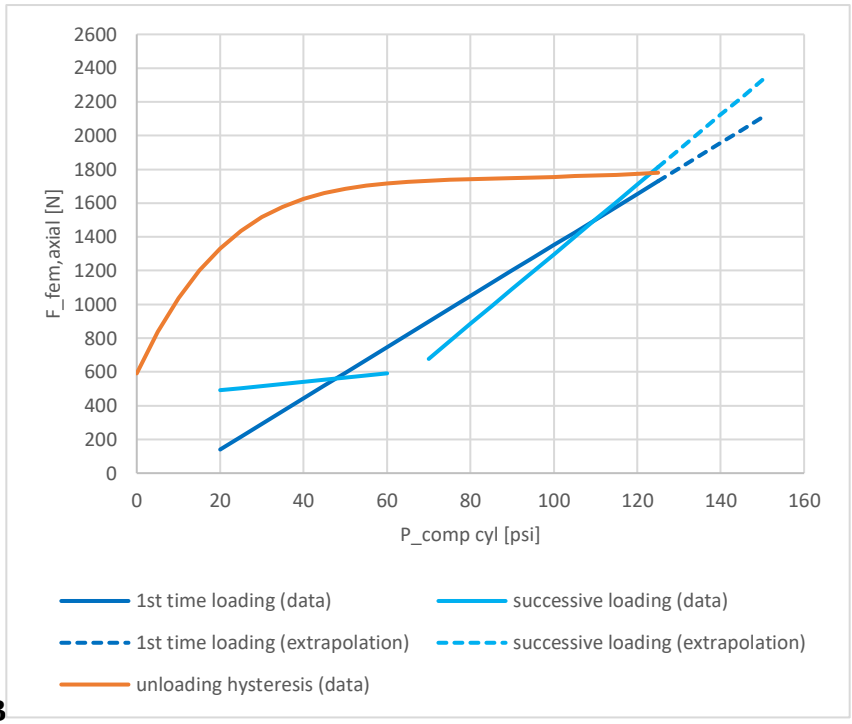

B

Configuration: WD-40 in compressive piston, medium silicone o-rings; WD-40 in natural rubber indenter tip
Comments: Anatomic model; partially coupled by muscle tension; rubber indenter glue shearing while collecting data; n=1 trials for loading for the 1st time, n=2 trials for low-level successive loading, n=2 trials for high-level successive loading, n=4 trials for successive hysteresis

F = 15.145*P - 162.88, 20 =< P =< 125 (1st-time loading)
F = 2.48*P + 442.17, 20 =< P =< 60 (low-level successive loading)
F = 20.654*P - 768.145, 60 < P =< 125 (high-level successive loading)
F = 9.651E-8*P^5 -4.892175E-5*P^4 + 0.01004475*P^3 - 1.0366575*P^2 +54.1355*P + 590.8975, 0 =< P =< 125 (unloading)

Figure 0-22: Average calibration curves & equations for tensile (A) & compressive (B) actuators

Substantial hysteresis is created by breakout friction after unloading tensile and compressive actuators. It is possible to eliminate this remaining breakout friction for the tensile case; however, it does not make practical sense to do this for the compressive piston, as doing so requires disassembling the rig. Hence, for this piston, there are different calibration curves for the first and subsequent loading periods. Due to the tensile calibration loads being too close to their breakout friction magnitude, a substantial range of force-pressure data during the loading process is missing. This is the case because to overcome the breakout friction, considerable pressure builds up before the applied force increases, but just when trespassing this threshold, the retracting piston applies a force so suddenly that the load cells DAQ system is not able to capture it even at its maximum sampling frequency.

A3.5.6. Agreement between processed MSK estimates & instrumented TKR measurements

Instrumented implants (e.g., OrthoLoad) and MSK models (e.g., OpenSim) are some of the best tools for approximating true healthy knee loading, from which experimental measurements are regarded as closer to reality[90]. Hence, to evaluate the differences in selected external knee joint loading (axial force and joint bending moments), data from eight OrthoLoad patients was used [AVG ± SD: (896 ± 133)N BW, (1.72 ± 0.04)m tall, (69 ± 5)years at TKR implantation, 25% females / 75% males, 75% left / 25% right knees]. These load-time profiles were normalized, throughout the entire gait cycle, for each individual with respect to BW, height and time. These curves were then averaged between participants to get a single set of load profiles (selected external knee joint loads as a function of gait) that would represent the OrthoLoad database (OrthoLoad, Charité, Berlin, DE: http://orthoload.com). The same knee joint loads processed from OpenSim data (Figure 3-2) were also normalized to BW and height and aligned in the time domain. At this point, the absolute errors (AE) and corresponding percent relative errors (%RE) were calculated for each instant throughout gait. To get a sense of how large absolute errors were with respect to the true value, they were compared the maximum value over time. This was done instead of comparing absolute to the instantaneous true signal, which oscillated closely about zero, which would have led to overshooting and a false sense of how large errors really are; thus

$$AE(t) = \left|L_{opensim}(t) - L_{orthoload}(t)\right|, \qquad \text{and} \tag{0-6}$$

$$\%RE(t) = \left|\frac{AE(t)}{max(L_{orthoload}(t))}\right| \times 100\%, \tag{0-7}$$

where *L* represents each of the selected external knee joint loads.

Despite TKR measurements being affected by altered contact due to the implant, for which differences are expected, these are still treated as the closest representation of true knee loading in the biomechanics field, so here they were considered as the ground truth in this assessment.

There is reasonable agreement (withing the context of biomechanics) between processed (OpenSim) MSK model-based estimates and (OrthoLoad) TKR measurements of knee loading,

including expected differences due to different population characteristics and health conditions (Figure 0-23). For the key gait time points considered, the largest differences were observed for the abduction/adduction moment at heel strike. Comparing OpenSim (young healthy males) to OrthoLoad (elderly with TKR-altered knee contacts and/or OA gait patterns) is not necessarily a fair assessment, but due to the limited options, it was deemed the best way (closest to true experimental validation) to evaluate whether MSK model-estimated loads are of similar magnitude and/or exhibit similar behaviour to gait.

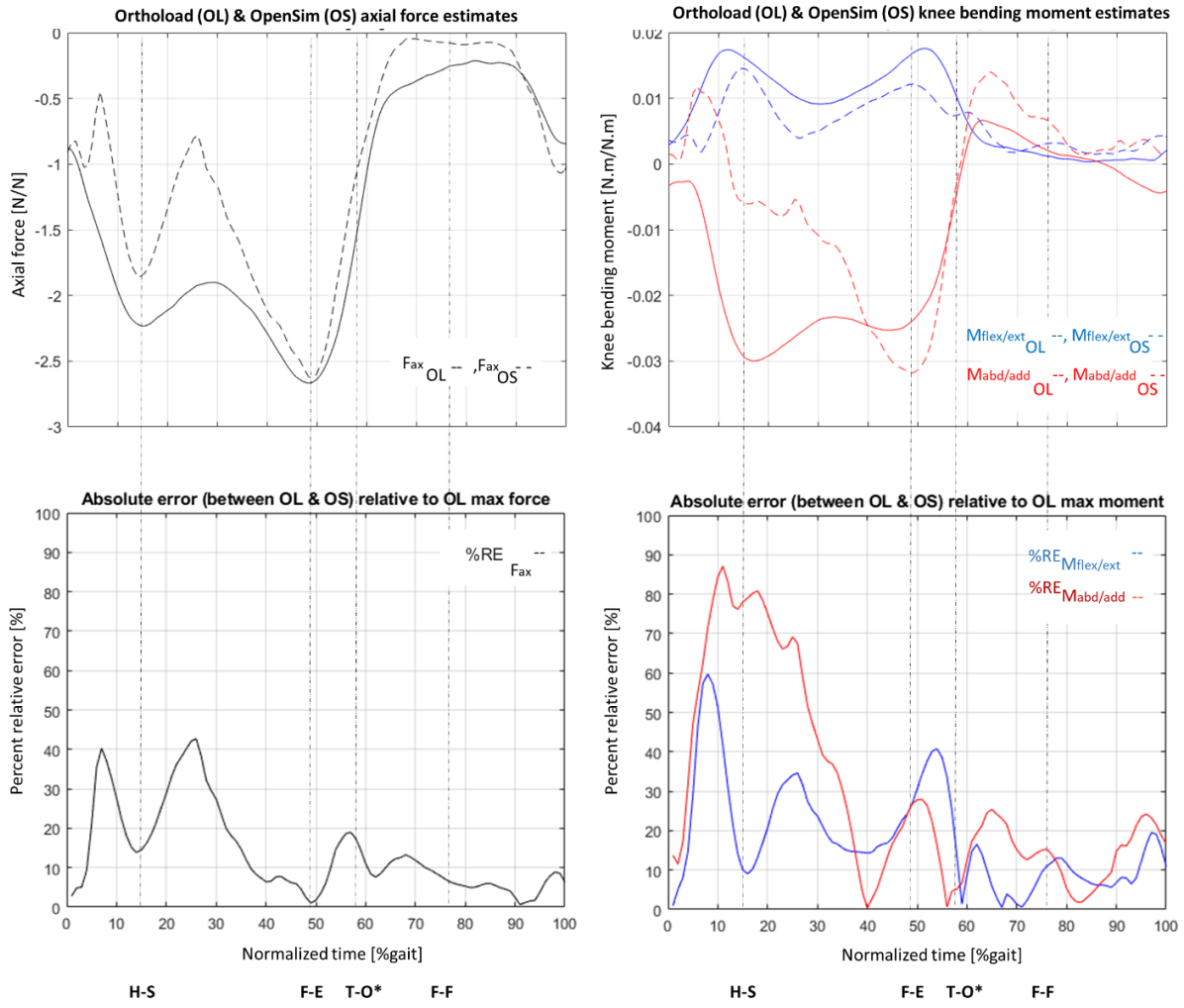

Figure 0-23: Expected similarities and differences between OpenSim MSK model-based estimates & OrthoLoad TKR measurements of knee loading; datasets agree for most highlighted gait time points (H-S, F-E, T-O*, F-F) with larger discrepancies for abduction/adduction bending moment

A4. Additional resources for study I

A4.1. Study design

This study involves nested data organized in the following statistical levels, each of which is further explained throughout the methods sections:

Level 1: Subject/species (e.g., anatomic model, bovine stifle joint, human knee)

Level 2: Joint compartment (P-F, T-F_med, T-F_lat)

Level 3: Gait time point (H-S, F-E, T-O*, F-F)

Level 4: Test # (long pre-conditioning, trial #1, trial #2, trial #3)

1. Load input variables: Knee flexion (θ_flex), vastus lateralis force (F_vasLat), short head biceps femoris force (F_bifemsh), semimembranosus force (F_semimem), shear force (F_sh,cable), axial compression (F_fem,axial), applied moment parallel to flexion/extension axis (M_x,applied), applied moment parallel to abduction/adduction axis (M_y,applied)
2. Load output variables: Contact area (A_contact), contact force (F_contact), geometric center (⟨C_x, C_y⟩), pressure center (⟨CP_x, CP_y⟩), regional minimum, maximum and average contact pressures (P_min, P_max, P_avg)

A4.2. SOP for ex-vivo contacts measurements using MR creep rig & novel system

Due to the vast scope (both in breadth and depth of many different aspects) of this project and thesis word limits, only an index of the raw data acquired is provided here.

Please contact Dr. Emily McWalter to gain access to these materials.

A4.2.1. Preliminary pressure sensors testing

Both calibration files were then checked by conducting simple tests (Figure 0-24) with gradually increasing loading complexity, in the laboratory, as data was collected using both calibration configurations during repeated testing:

1. Sensor orientation (probing sensor corners to determine coordinate directions)
2. Uniform loading (multiple known steady loads over flat surface larger than sensor)
3. Finite uniform loading (multiple known steady and transient loads over known flat surfaces smaller than sensor)
4. Non-uniform loading (transient load over curved surfaces smaller than sensor)
    - Rigid (metal) and compliant (rubber) indenters
5. Simulated knee contacts (transient load applied to 3DP disarticulated knee models in flexed and extended configurations)
    - P-F and T-F joints

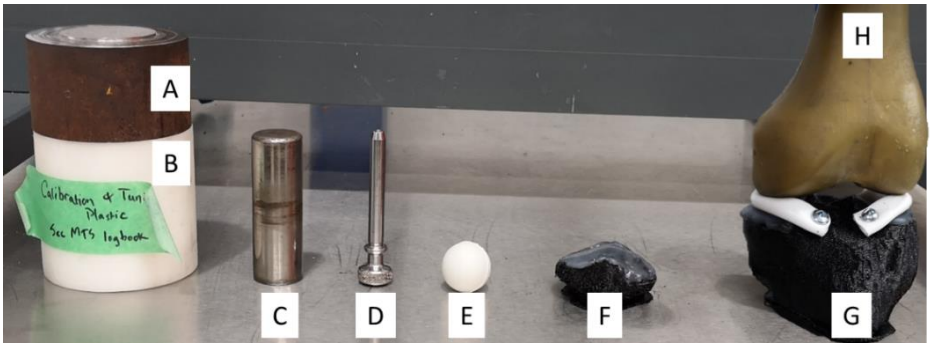

Figure 0-24: Sensor contact testing hardware: A. Steel puck, B. Nylon puck, C. Metal rod, D. Metal indenter, E. Rubber ball, F. 3DP patella with silicone cartilage, G. 3DP tibia with silicone cartilage and rubber menisci, H. Artificial femur

A4.2.2. Knee contacts processing code: Steady response

Due to the vast scope (both in breadth and depth of many different aspects) of this project and thesis word limits, only an index of the raw data acquired is provided here.

Please contact Dr. Emily McWalter to gain access to these materials.

A4.3. Testing protocols

A4.3.1. Mechanical testing protocols

A few modifications to the intended normal operating procedure were done to evaluate loading and response repeatability, mainly opening the knee capsule and inserting pressure sensors. The load cells used for calibration were also kept during the repeated trials, since they provided an accurate reading of loading conditions (additional to pressure gauge readings recorded with webcams) without interfering with physiologic simulation. In order to minimize setup time, the following protocol was adopted:

F-F:
1. Pre-conditioning phase (loading, 30min creep, unloading)
2. Trial 1 (loading, 10min creep, unloading)
3. Trial 2 (loading, 10min creep, unloading)
4. Trial 3 (loading, 10min creep, unloading)

F-E:
1. Pre-conditioning phase (loading, 30min creep, unloading)
2. Trial 1 (loading, 10min creep, unloading)
3. Trial 2 (loading, 10min creep, unloading)
4. Trial 3 (loading, 10min creep, unloading)

T-O*:
1. Pre-conditioning phase (loading, 30min creep, unloading)
2. Trial 1 (loading, 10min creep, unloading)
3. Trial 2 (loading, snapping, 10min creep, unloading)
4. Trial 3 (loading, 10min creep, unloading)
5. Trial 4 (loading, 10min creep, unloading)
6. Trial 5 (loading, 10min creep, unloading)

H-S:
1. Pre-conditioning phase (loading, 30min creep, unloading)
2. Trial 1 (loading, 10min creep, unloading)
3. Trial 2 (loading, 10min creep, unloading)
4. Trial 3 (loading, 10min creep, unloading)

A4.3.2. Loading rig configuration

Table 0-5 and Table 0-6 contain all the correct information required to set up the rig and simulate gait experimentally. As noted in study I, the author accidentally placed the compressive piston using right-knee values (r_piston, θ_piston), thereby approximating valgum in K07 (left knee); other than this, the rest of configuration and loading parameters corresponded to a left knee. This is not reflected in the following tables, which represent healthy walking conditions.

Table 0-5: Rig kinematic and kinetic parameters for walking experimental simulation (subject = K07, limb = right, sex = male, age = 68 years, height = 1.78m, BW = 743N)

Kinematic parameters	**Relative to**	H-S (%gait ~= 14.7%)	F-E (%gait ~= 49.0%)	T-O* (%gait ~= 57.2%)	F-F (%gait ~= 76.0%)
r_piston [mm]	r-θ table origin	60.2	2.1	25.2	~~167.7~~
θ_piston [mm]	r-θ table origin	-108.5	135	-107.7	~~85.7~~
x_vas [mm]	knee centre	~~10.7~~	~~2.6~~	~~10.2~~	~~11.5~~
l_vas [mm]	knee centre	~~34.9~~	~~27.3~~	~~30.8~~	~~39.5~~
x_bif [mm]	rig origin	~~15.6~~	~~14.9~~ ≈ 14.4 avg (Δx = 0.5)	~~13~~ ≈ 14.4 avg (Δx = 1.4)	~~15.4~~ ≈ 14.4 avg (Δx = 1)
l_bif [mm]	guide front face	~~20.3~~	25.5	16.5	19.1
x_sem [mm]	rig origin	-28.7	~~-20.3~~	~~-27.4~~	~~-37~~
l_sem [mm]	guide front face	14.8	~~15~~	~~14.1~~	~~19.9~~
h_tib pot guide [mm]	slot endpoint	27.3	6.2	21.2	~~181.3~~
~~x~~_sag,pulley [º]	eyebolt knot	~0	~45	~0	~45
θ_flex,ideal [º]	femur axis	21.7	5.1	17.2	69.3
Kinetic parameters					
F_fem,axial [N]		1312	1958	849	~~46~~
F_sh,cable [N]		212	394	178	~~6~~
F_bifemsh [N]		~~5~~	185	108	42
F_semimem [N]		118	~~16~~	~~3~~	~~4~~
F_vasLat [N]		343	~~9~~	~~14~~	~~14~~

Notes:

1) Data based on OpenSim simulation (processed by custom MSK biomechanics code) & K07 anthropometrics.
2) Kinematics depend on specimen insertion points' measurements (accurate within ± ~2.5mm, ± ~2.5º).
3) Theoretical values that are not achievable practically or that simply are not needed, are crossed off (pink values were ignored because corresponding forces are negligible for those instants; green values were ignored because repositioning would damage the guide attachment due to bone's finite life).
4) Guide location approximations (average of the relevant values throughout gait instead of their exact value) were used to reduce rig assembly/setup time whenever a parameter did not change much throughout gait, and so their absolute deviations from the average, Δx=abs(x_value – x_avg), were small.
5) See Appendix A3.2 for specific parameter's directions/sign conventions.

Table 0-6: Rig kinematic and kinetic parameters for walking experimental simulation (subject = K07, limb = left, sex = male, age = 68 years, height = 1.78m, BW = 743N)

Kinematic parameters	**Relative to**	H-S (%gait ~= 14.7%)	F-E (%gait ~= 49.0%)	T-O* (%gait ~= 57.2%)	F-F (%gait ~= 76.0%)
r_piston [mm]	r-θ table origin	60.2	2.1	25.2	~~167.7~~
θ_piston [mm]	r-θ table origin	-71.5	45	-72.3	~~94.3~~
x_vas [mm]	knee centre	~~-10.7~~	~~-2.6~~	~~-10.2~~	~~-11.5~~
l_vas [mm]	knee centre	~~34.9~~	~~27.3~~	~~30.8~~	~~39.5~~
x_bif [mm]	rig origin	~~-15.6~~	~~-14.9~~ ≈ -14.4 avg (Δx = 0.5)	~~-13~~ ≈ -14.4 avg (Δx = 1.4)	~~-15.4~~ ≈ -14.4 avg (Δx = 1)
l_bif [mm]	guide front face	~~20.3~~	25.5	16.5	19.1
x_sem [mm]	rig origin	28.7	~~20.3~~	~~27.4~~	~~37~~
l_sem [mm]	guide front face	14.8	~~15~~	~~14.1~~	~~19.9~~
h_tib pot guide [mm]	slot endpoint	27.3	6.2	21.2	~~181.3~~
~~x~~_sag,pulley [º]	eyebolt knot	~0	~45	~0	~45
θ_flex,ideal [º]	femur axis	21.7	5.1	17.2	69.3
Kinetic parameters					
F_fem,axial [N]		1312	1958	849	~~46~~
F_sh,cable [N]		212	394	178	~~6~~
F_bifemsh [N]		~~5~~	185	108	42
F_semimem [N]		118	~~16~~	~~3~~	~~4~~
F_vasLat [N]		343	~~9~~	~~14~~	~~14~~

Notes:

1) Data based on OpenSim simulation (processed by custom MSK biomechanics code) & K07 anthropometrics.
2) Kinematics depend on specimen insertion points' measurements (accurate within ± ~2.5mm, ± ~2.5º).
3) Theoretical values that are not achievable practically or that simply are not needed, are crossed off (pink values were ignored because corresponding forces are negligible for those instants; green values were ignored because repositioning would damage the guide attachment due to bone's finite life).
4) Guide location approximations (average of the relevant values throughout gait instead of their exact value) were used to reduce rig assembly/setup time whenever a parameter did not change much throughout gait, and so their absolute deviations from the average, Δx=abs(x_value – x_avg), were small.
5) See Appendix A3.2 for specific parameter's directions/sign conventions.

A4.3.3. Specimen log (K07)

This is a summary of the effective specimen preparation and testing procedures conducted on the specimen K07. Some time stamps are approximate, as the author was very busy preparing and conducting the full tests by himself, planning ahead to avoid any issues, and sorting out technical and logistic contingencies that came by. Rob Peace and Dr. Emily McWalter provided invaluable assistance during certain rig assembly steps and when storing the specimen after testing concluded. For more details, refer to the annotated specimen preparation SOP, and/or the video recordings of the rig assembly and the entire mechanical testing procedures.

Fresh frozen specimen kept in freezer prior to the following

<u>Sat 15.05.2021:</u>

~19:00 - Specimen taken out for thawing at room temperature

<u>Mon 17.05.2021:</u>

~10:30 - Specimen preparation:

I could go faster with bovine joint since I did not have to be that accurate (just a mock-up test)

- Dissection (lengthy, since trying to preserve knee integrity as much as possible, i.e. removing only what I need, checking I haven't ripped out the main ligaments by "playing" with knee)
    - found a little metallic clip in between the muscles (probably this specimen had a stent inside)
- Finding knee center
- Removing tissue from bones (really long)
- Drilling
- Potting (despite the use of zip ties, sagging prevented the specimen from fitting in the potting jig, which came apart in the process)
- Suturing muscles
- Bagging

12:30 - Specimen moved to fridge, while preparing the rest of the experiment

Tue 18.05.2021:

~13:00 – Specimen taken out for measuring insertion points

I had to connect it to fem puck (those nylon bolts gave me a hard time, since I cut them too long)

~18:00 - Specimen moved to fridge

Wed 19.05.2021:

~15:00 – Opening knee capsule & suturing novel pressure sensors (2 grommets broke)

~17:00

- Assembling rig (again attaching those forsaken nylon bolts to fem puck)
- Making new eyebolts

21:30

- Specimen moved inside rig & left surrounded by icepacks (while author ate dinner); from this point, specimen did not leave the rig until all tests were completed.
- Connecting rest of components (e.g., cables, load cells, guides, pulleys)

Thur 20.05.2021:

00:00 - Adding icepacks inside & outside rig

9:20

- Removing icepacks, thawing specimen
- Closing rig (preloading bottom flanges)

10:30 - F-F tests (specimen in rig without icepacks during lunch)

14:30

- Setting up rig for next flexion configuration
- F-E tests

18:45 – F-E tests conclude, setting up “igloo”

Fri 21.05.2021:

8:30

- Removing icepacks, thawing specimen
- Setting up rig for next flexion configuration

11:00

- T-O*tests (compressive indenter snaps => had to conduct five trials in total, after the preconditioning phase)
- Setting up rig for next flexion configuration

~17:30

- H-S tests: Had to make contact with compressive actuator 1st, then flex the knee & then finish reaching the target compression (else the specimen was away from the compressive piston reach)

~23:30 – Pressure sensors removed & specimen stored in freezer

A4.4. Raw data

Due to the vast scope (both in breadth and depth of many different aspects) of this project and thesis word limits, only an index of the raw data acquired is provided here:

1. Muscle insertion measurements (knee anatomic model, K07 subject)
2. MR creep rig loading input repeatability throughout gait (K07 subject)
    a. Load cell force data (tensile & compressive actuators)
    b. Pressure gauges data
3. MR creep rig loading output repeatability throughout gait (K07 subject)
    a. ASCI, MVA, FGT files acquired with 1MPa calibration
    b. ASCI, MVA, FGT files acquired with 2MPa calibration

Please contact Dr. Emily McWalter to gain access to these materials.

A4.5. Processed data

Due to the vast scope (both in breadth and depth of many different aspects) of this project and thesis word limits, only an index of the processed data acquired is provided here:

1. Loading variability for left/right knees (K07 subject)
2. MR creep rig loading input repeatability throughout gait (K07 subject)
    a. Tensile & compressive actuator forces
    b. Moments applied at tibia end
3. MR creep rig loading output repeatability throughout gait (K07 subject)
    a. ASCI, MVA, FGT files acquired with 1MPa calibration
    b. ASCI, MVA, FGT files acquired with 2MPa calibration

Please contact Dr. Emily McWalter to gain access to these materials.

A4.5.1. Muscle force repeatability

Muscle force repeatability (51.1 to 96.6 CV%), however, was lower compared to shear forces (6.46 to 37.0 CV%), even though both are actuated by the same type of tensile pistons (Table 0-7, Figure 0-25).

Table 0-7: Summary of applied muscle forces & their repeatability [intra-subject AVG ± SD (CV%)] of knee specimen (limb = left, sex = male, age = 68 years, height = 1.78m, BW = 743N); x-y-z coordinates relative to rig origin

Parameter	H-S (%gait ~= 14.7%, θ_flex,ideal = 21.7º)	F-E (%gait ~= 49.0%, θ_flex,ideal = 5.1º)	T-O* (%gait ~= 57.2%, θ_flex,ideal = 17.2º)	F-F (%gait ~= 76.0%, θ_flex,ideal = 69.3º)
F_vasLat [N]	579 ± 420 (72.46%)	0 ± 0 (0%)	0 ± 0 (0%)	0 ± 0 (0%)
F_semimem [N]	628 ± 504 (80.24%)	0 ± 0 (0%)	0 ± 0 (0%)	0 ± 0 (0%)
F_bifemsh [N]	0 ± 0 (0%)	822 ± 420 (51.09%)	822 ± 420 (51.09%)	762 ± 737 (96.64%)
F_sh,cable [N]	336 ± 124 (36.99%)	320 ± 21 (6.46%)	206 ± 32 (15.34%)	N/A

Key gait time points include heel-strike (H-S), full extension (F-E), approximate toe-off (T-O*) and full flexion (F-F).

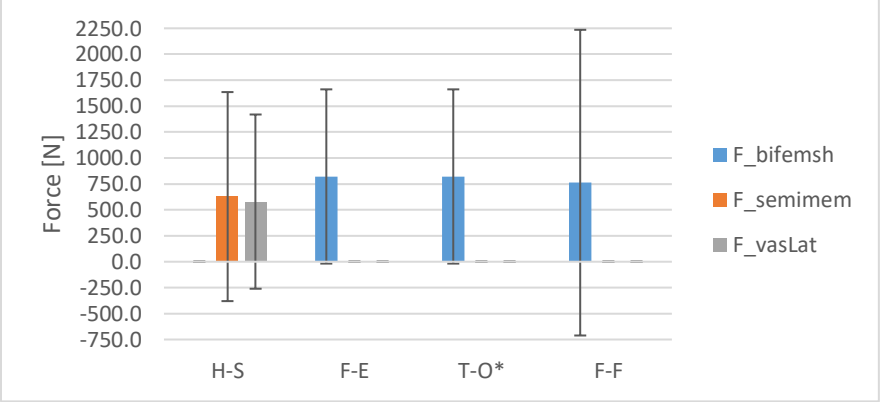

Figure 0-25: Muscle forces (F_bifemsh, F_semimem, F_vastLat) showed large variability for all gait time points

Poor repeatability in muscle loading may be simply an illusion. Is it not strange that while all four tensile actuators connected to the specimen are identical (same design, material, manufacturing), only one (supplying shear force) registers decent repeatability while the other three appear to be terrible? Despite all actuators being operated in the exact same manner by the same operator, muscle forces were measured in a different way. Shear and compressive forces had direct force readouts via load cells; however, muscle tensions were estimated by converting pressure gage readings (recorded via webcams) to forces via tensile calibration data. To complicate the situation further, statically optimized muscle loading was often negligible for the

specimen (normal BMI) and when considerable, it was around the same magnitude as breakout friction (i.e. when calibration curves were most unreliable due to missing data). It is true that the three cables were connected via sutures to tendons, but these pulley knots did not come apart or become loose during testing (they were still tight when taking the specimen apart to store it after all repeated tests) and there was no visible damage in these tissues. In general, these factors, in addition to a leak in the air compressor outlet (common issue for compressors at low pressures), made it more difficult to control muscle actuation. This leak, however, was present when setting the shear force delivery as well, whose repeatability was not impacted, and so, leaking was merely an inconvenience that did not impact muscle actuation repeatability. Hence, due to experimental limitations related to the challenges in tuning and measuring these loads, muscle tension measurements likely do not reflect their true (higher) repeatability and repeatability estimates of muscle forces should not be trusted too much, since it was not possible to measure their values very accurately. These precision errors are rather presented for completeness, and to describe the associated issues and how to overcome them in the future (section 6.4).

A4.6. Loading assessment via gait variability

A4.6.1. Determining loading conditions for gait variability simulation (methods)

It is important to know how accurately the intended knee loading conditions were actually applied experimentally. To determine whether the applied loads fell within healthy or pathologic ranges, one would need to compare experimental loading conditions and their variability over repeated tests against gait measurements and their variability. So, to get an approximate idea of these degrees of variability in normal and pathologic conditions for select external knee joint loading, a literature search was performed involving 34 different studies and three biomechanics textbooks. After screening for useful data for this project (axial force, flexion/extension moment and abduction/adduction moment data normalized to BW and height, at comparable speeds, on anatomic coordinates, available for H-S, F-E and T-O*), data from 15 different papers[40,46,51-63] remained available for characterizing gait variability (Table 0-8). This brief search may not include all relevant studies, but provides a reasonable estimate of gait variability.

Table 0-8: Gait variability literature search (some studies had data for >1 load or variability type)

Before screening

Variability	# studies
Healthy	26 papers[32,40,45,52-54,56-61,313-326] + 3 textbooks[28,327,328]
Pathologic	8 papers[39,46,55,57,59,60,62,63] + 1 textbook[327]

After screening

Variability	# studies	Pooling statistic (variability estimate)
Intra-subject, healthy	3 papers[40,53,56]	within-groups SD
Inter-subject, healthy	11 papers[40,51-54,56-61]	within-groups SD
Inter-subject, pathologic (general)	3 papers[46,62,63]	between-groups SD
Inter-subject, pathologic (varum)	1 paper[55]	sample SD
Inter-subject, pathologic (valgum)	1 paper[55]	sample SD

The inclusion (and complimentary exclusion) criteria of the scientific articles included:

- Containing measured or modelled kinetic data (axial force, flexion/extension moment and/or abduction/adduction moment), not just kinematic data,
- Providing data normalized to BW and height, and/or provide sufficient information to normalize it with respect to both anthropometrics (not just BW),
- Using Cartesian knee anatomic coordinates (not ground coordinates),

- Reporting SDs for key instances during the gait cycle (H-S, F-E and T-O*)[i], and
- Registering maximum speeds of 2m/s (or 125 steps/min),

Due to the somewhat different objectives, methods and limitations of each study, the data available and the corresponding pooling statistic were different for certain types of variability. For the case of the healthy studies, inter-subject SDs were reported for each gait time point; hence within-groups SD (with different sample sizes) allowed for combining such SDs from different studies. For the general pathologic case, not all papers reported inter-subject SDs but all reported the inter-subject AVGs for all gait time points; hence, between-groups SD enabled summarizing general pathologic variability[202]:

$$s_{wit} = \sqrt{\frac{SS_{wit}}{DF_{wit}}}, \tag{0-8}$$

$$SS_{wit} = \sum_{t=1}^{k} (n_t - 1){s_t}^2 \tag{0-9}$$

$$DF_{wit} = N - k \tag{0-10}$$

$$s_{bet} = \sqrt{\frac{SS_{bet}}{DF_{bet}}}, \tag{0-11}$$

$$SS_{bet} = \sum_{t=1}^{k} n_t {\overline{X_t}}^2 - \frac{1}{N}\left(\sum_{t=1}^{k} n_t \overline{X_t}\right)^2 \tag{0-12}$$

$$DF_{bet} = k - 1 \tag{0-13}$$

$$N = \sum_{t=1}^{k} n_{t,} \tag{0-14}$$

[i] F-F was not part of the selection criteria, since most data was collected only for the stance phase of gait.

where subscript *t* differentiates each of the *k* groups, n_t = group sample size, $\overline{X_t}$ = group sample mean, and s_t = group sample standard deviation. For the specific case of varum and valgum, variability was estimated from one study (as only this study had the required data for these disorders), for which the reported sample SD was used.

To get sense of the variability ranges for the entire population, 95% CIs were estimated based on the pooling statistic 2×SD, since selected knee loads can increase/decrease indefinitely (which would make their distributions symmetric), for each specific variability condition. Doubling the SD enabled capturing 27% more of a normal population than solely using 1 SD (68%); however, increasing the range by 3 SDs only produced a 2% increase with respect to 2 SDs. Whereas to simulate gait variability, an alternate version of the custom biomechanics algorithm, biomechanics code II (Appendix A3.2), was programmed to include inter- and intra-subject load variability for discrete gait time points. Here, selected components of the intended knee external loads determined via OpenSim (biomechanics code II inputs) were increased/decreased by the corresponding 2 SDs obtained from the literature search before running the code. This was done to calculate the necessary load BC ranges (code outputs) to produce the desired variability at the knee external reactions. This way, the variability in applied knee joint external loads could be evaluated by examining whether the load BCs (which are easier to measure) fell within their corresponding variability ranges. For healthy variability ranges, SDs were used to shift OpenSim loads instead of shifting the average values available in the literature because studies reported loads in different anatomic coordinates but did not provide enough information to transform all to a common coordinate system; hence, only the variance was extracted from the healthy studies. However, to estimate pathologic ranges, the averages provided in the literature had to be used as if they were expressed in the same anatomic coordinates, since they were significantly different from healthy loads. Normalized loading variability of different healthy and pathologic conditions was then simulated for the knee specimen to be used in the repeated trials (described in detail in section 4.2.3). The largest variability was found for general pathology, followed by a healthy condition, and varum and valgum malalignments (Figure 0-26); due to the data available in the literature, it was not possible to simulate variability for all loads applied experimentally, but rather only for certain load components.

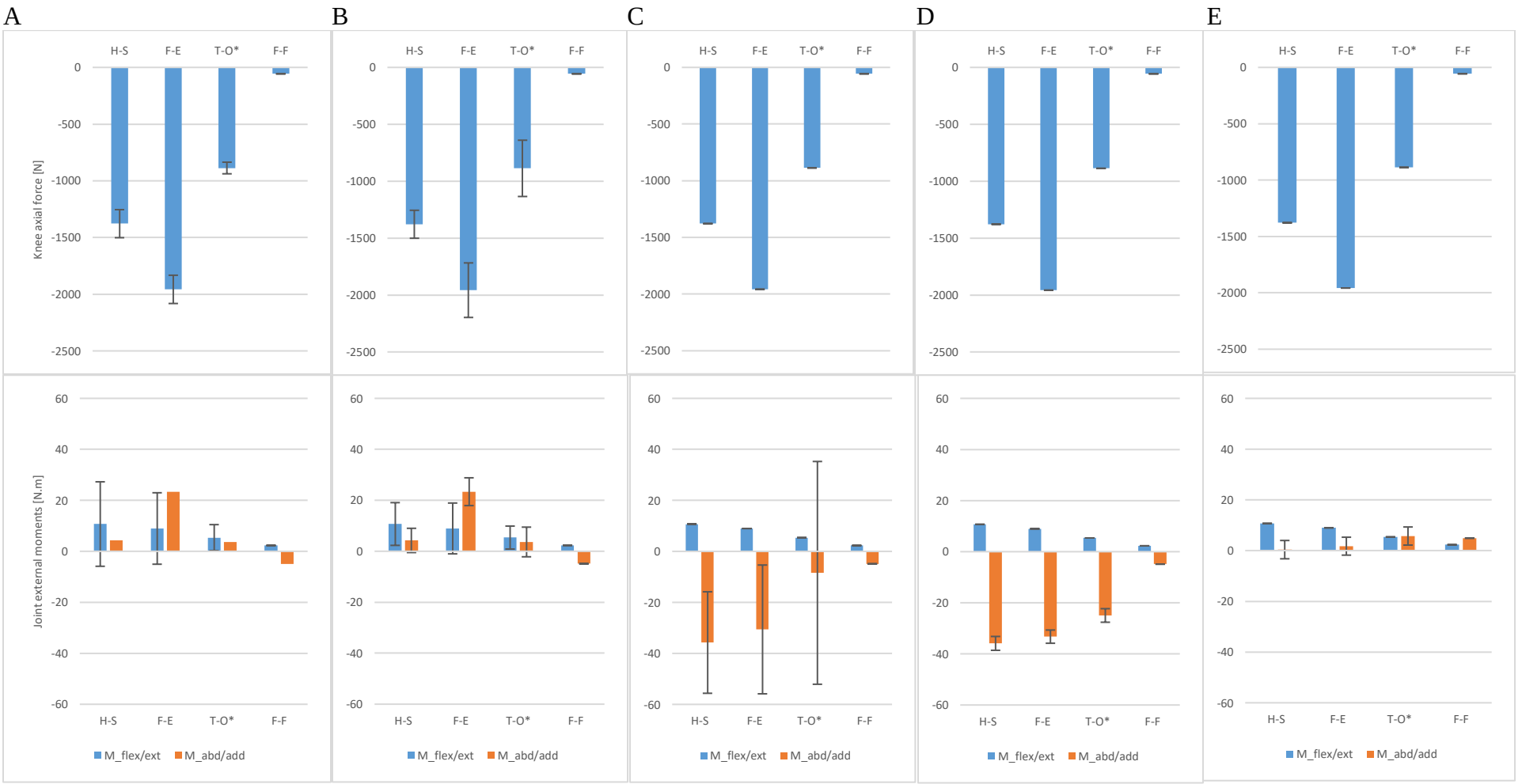

Figure 0-26: Intra-subject (A. Healthy) and inter-subject (B. Healthy, C. General pathologic, D. Varum and E. Valgum) loading condition variability bounds (AVG ± 2 SD) for left knee specimen used in study I (BW = 743N, height = 1.78m)

A4.6.2. Experimental repeatability comparison to gait variability (loading parameters)

For this study, the testing variability was compared to healthy and pathologic data measured via gait studies (by means of the MSK biomechanics code II, as described in section A4.6). This was done by comparing the loading conditions applied in the repeated tests (and their repeatability error) to the simulated variability bounds in these conditions scaled to match the specimen anthropometrics (Figure 0-26). Since the gait variability statistic had been scaled by 2 to approximate the variability bounds of 95% of each healthy and pathologic population, so was the intra-subject SD measured from the repeated tests.

A4.6.3. Agreement between experimental loading repeatability & gait loading variability (results)

The comparison of actual applied loads vs. MSK model target loads with simulated variability bounds (pooled from 15 papers, as explained in section A4.6.1) is a result in itself. Hence, this comparison is presented in this section, while its implications regarding pathology and possible physical explanations behind the observed behaviour are extended in the corresponding discussion section (section A4.6.4).

As demonstrated by this assessment, the rig is capable of simulating a realistic physiologic scenario that mostly resembles valgum malalignment. To begin with, within precision error, effective knee flexions ([29,31]°, [5,15]°, [13,23]° and [42,54]° 2SD ranges for H-S, F-E, T-O* and F-F) were close to desired MSK targets (21.7, 5.1, 17.2 and 69.3° for the same time points), presenting minor differences for H-S and larger differences for F-F (Figure 0-27).

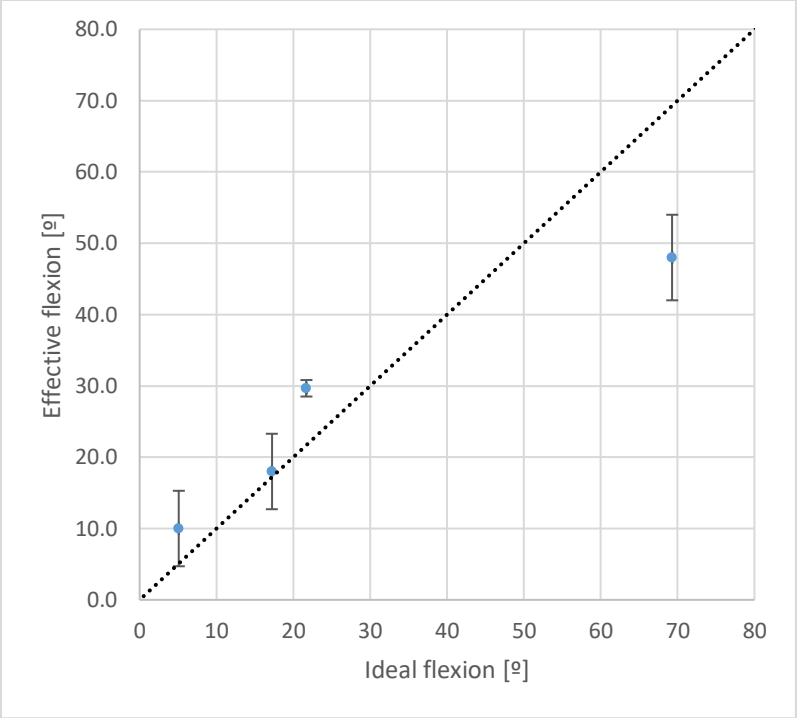

Figure 0-27: Ideal vs. actual knee flexion (effective values are AVG±2SD for n=3 repeated tests)

Effective knee compression ([-876, -779]N, [-1678, -1597]N and [-868, -779]N 2SD ranges for H-S, F-E and T-O*) is close to but not equal to the MSK target for most gait time points (-1312, -1958 and -849N for the same time points), except for T-O*, whose error bounds do encapsulate the desired analytical value (Figure 0-28). However, when compared to the healthy variability ranges, for all stance time points except H-S, effective axial compression falls within inter-subject variability ([-1624, -1132]N, [-2436, -1478]N and [-1381, -392]N 2SD ranges for the same time points) and is just outside intra-subject variability. Due to absence of variability data available for the three muscle groups considered (nor for the balancing shear force), the applied tensions are only compared to their corresponding intended values. For muscle loading, most average values are somewhat distant from theoretical values; however, their 2SD intervals all contain the ideal MSK targets. Note that, after adjusting for BW and height, static optimization (in OpenSim) generally yielded muscle loads of negligible magnitude (Table 4-3). On the other hand, all shear forces agree with theoretical values (within their repeatability ranges) except for F-E, whose value is still very close to the ideal curve.

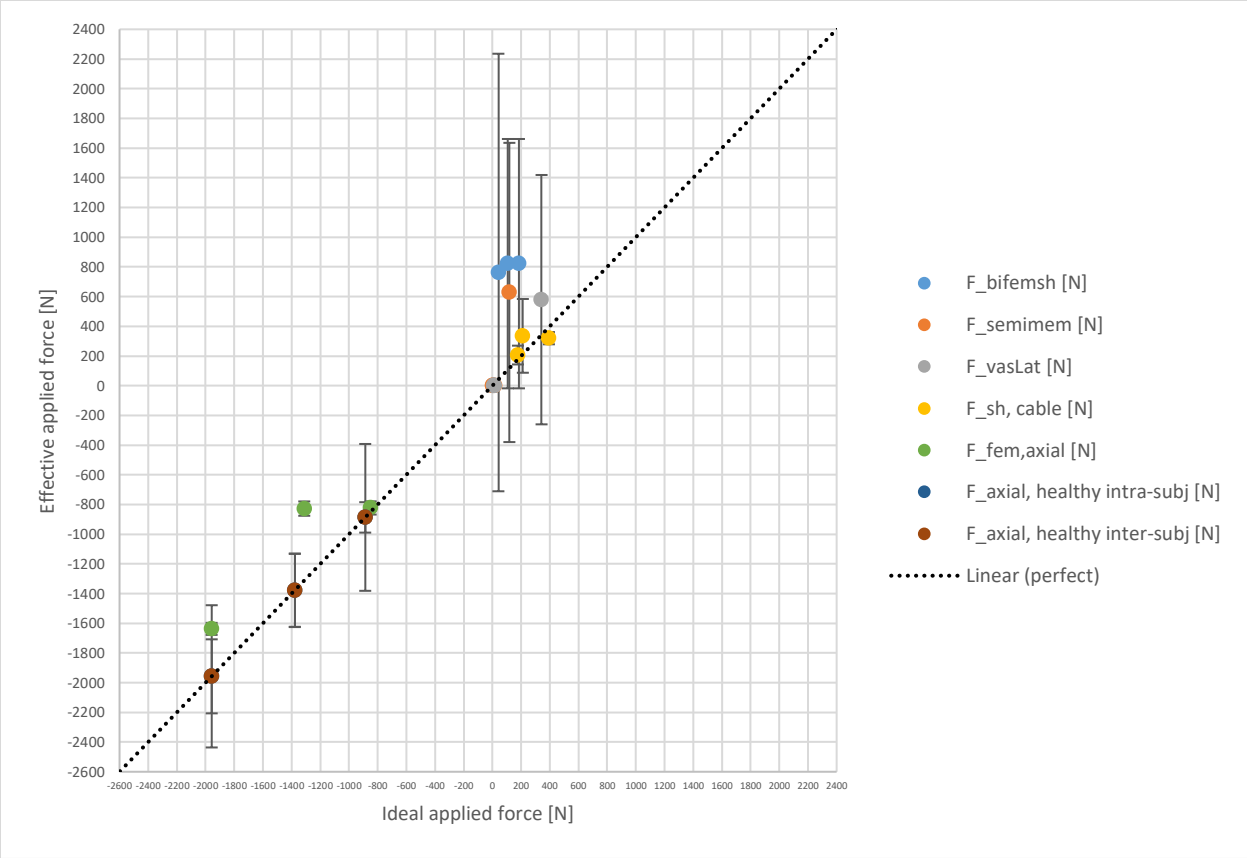

Figure 0-28: Ideal vs. effective applied forces (left knee), including healthy variability ranges (effective values are AVG±2SD for n=3 repeated tests). Applied forces include biceps femoris (F_bifemsh), semimembranosus (F_semimem) and vastus lateralis (F_vasLat) tensions, shearing force (F_sh,cable), and axial compression (F_fem,axial).

There are larger differences between applied moments and target values (Figure 0-29). The M_x moment parallel to the flexion/extension axis ([-21.6, -18.7]N.m, [-51.5, -4.0]N.m and [-28.0, -6.2]N.m 2SD ranges for H-S, F-E and T-O*) agrees very closely with the desired values (-39.8, -31.7 and -15.6N.m for the same time points), except for H-S, which shows a greater difference. As per gait variability, M_x is within normal variability (absence of abnormal variability data for the flexion/extension moment resulted in insignificant variation in the M_x BC, and thus M_x could not be compared to pathologic ranges). The M_y moment parallel to the abduction/adduction axis ([14.9, 16.7]N.m, [2.4, 2.5]N.m and [6.0, 6.6]N.m 2SD ranges for H-S, F-E and T-O*) exhibits substantial differences from intended values throughout gait stance (0.3, 31.6 and 8.6N.m for the same time points), especially for F-E. As such, M_y is outside the normal range, for which comparisons to pathologic ranges become especially important. As

clearly shown, the general pathologic variability ranges ([-0.1, 73.8]N.m, [-28.1, 72.5]N.m and [-80.5, 86.4]N.m 2SD ranges for the same time points) encompass the applied loading, as they are so broad. Furthermore, when compared to varum and valgum malalignments, experimental M_y almost shows agreement with valgum, while remaining very different from varum.

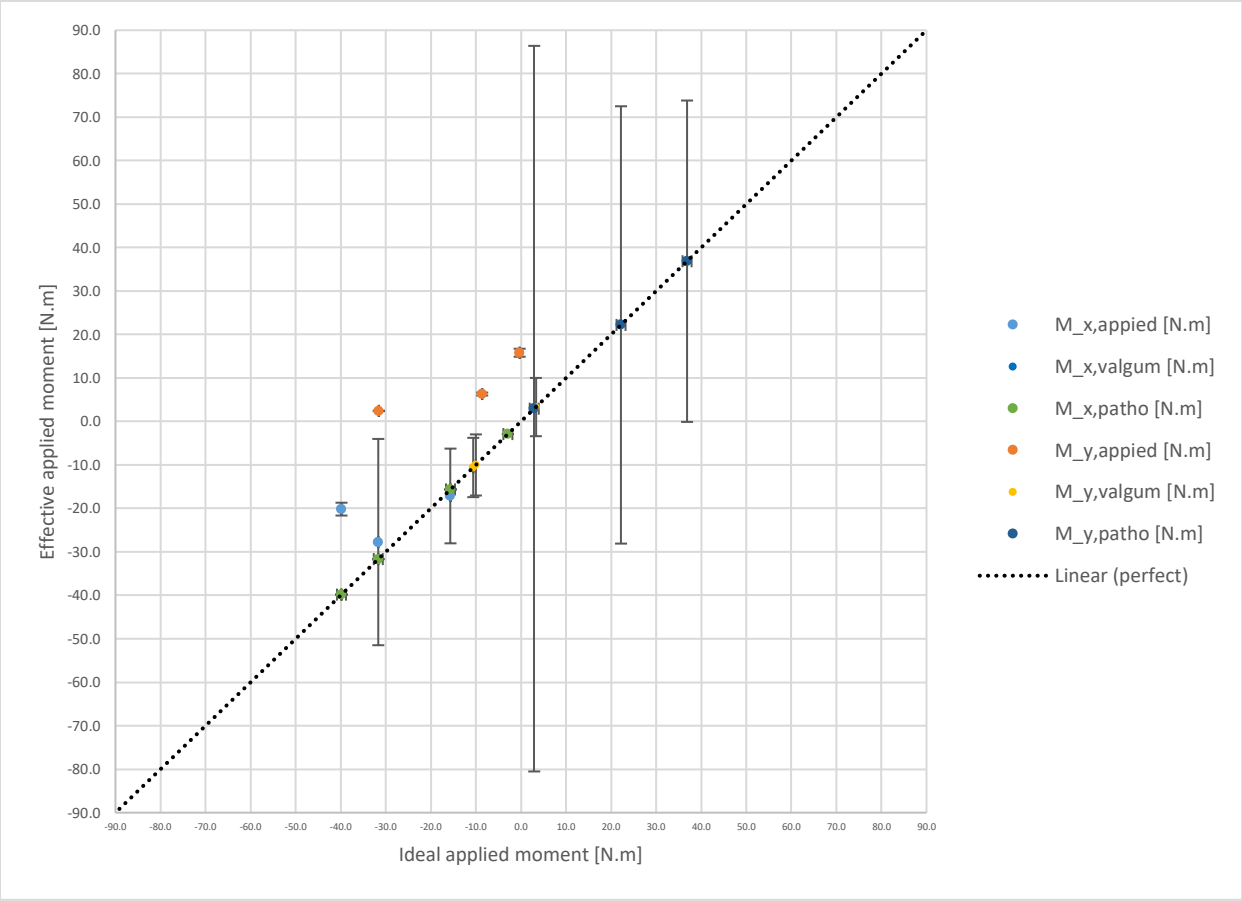

Figure 0-29: Ideal vs. effective applied moments (left knee) in rig coordinates, including general pathology & valgum ranges (effective values are AVG±2SD for n=3 repeated tests)

A4.6.4. Applied loading physiologic realism assessment against gait variability data (discussion)

After comparing the applied loading environment to healthy and pathologic gait variability, knee reactions partially agree with healthy and general pathologic conditions (close to valgum). Such a physiologically realistic pathologic simulation was (inadvertently[i]) achieved by shifting the compressive piston placement along the medial/lateral direction, thereby reversing moments parallel to the abduction/adduction axis. This also led to the lateral T-F plateau to bear more load than the medial counterpart for all stance configurations simulated, unlike in normal gait. Other than that, the loading regime is close to representing healthy behaviour. For instance, the only knee flexions that do not agree with intended values (within 95% confidence) take place for H-S (21.7º ideal vs. 30±1º effective) and F-F (69.3º ideal vs. 48±6º effective). These discrepancies are likely due to static-optimized loads (often low or negligible magnitudes for the specimen), which are merely one of the many possible muscle force configurations, and, in this case, not large enough (especially since omitting other muscles' activation) to reach the desired flexion.

In general, axial compression almost agrees with intended values; however, better agreement is seen with healthy inter-subject gait variability and partial agreement with healthy intra-subject variability. Aside from T-O* (-849N ideal vs. -823±45N effective), axial force does not agree with intended values (-1312N ideal vs. -828±48N effective for H-S, and -1958N ideal vs. -1638±40N effective for F-E). However, except for disagreement at H-S (-1378±246N), axial force does agree with the load BCs and their 2SD bounds (-1957±479N for F-E, and -887±494N for T-O*), which replicate inter-subject gait variability, and, except for full agreement at T-O* (-887±103N), it almost agrees with the load BCs and 2SD bounds (-1378±247N for H-S, and -1957±249N for F-E) representing intra-subject variability.

Lastly, applied bending moments (up to 2SDs) register some agreement as well as greater discrepancies with their intended values and gait variability. Aside for H-S (-39.8N.m ideal vs. -20.2±1.5N.m effective), M_x,applied agrees with ideal values (-31.7N.m ideal vs. -27.7±23.7N.m effective for F-E, and 15.6N.m ideal vs. 17.1±10.9N.m effective for T-O*). But

[i] I admit it… I accidentally introduced a valgum bias when applying these loads experimentally; the loading response was not originally intended to represent pathology.

for the case of M_y,applied, applied loads do not match intended values (-0.3N.m ideal vs. 15.8±0.9N.m effective for H-S, -31.6N.m ideal vs. 2.4±0.1N.m effective for F-E), almost showing agreement at T-O* (-8.6N.m ideal vs. 6.3±0.3N.m effective). When compared to general pathology variability bounds, no agreement is observed for M_x,applied BC (-39.8±0N.m for H-S, -31.7±0N.m for F-E, -15.6±0N.m for T-O*) but M_y,applied does agree (36.9±37.0N.m for H-S, 22.2±50.3N.m for F-E, 2.94±83.5N.m for T-O*). On the other hand, applied moments do not agree with valgum-related M_x,applied (-39.8±0N.m for H-S, -31.7±0N.m for F-E, -15.6±0N.m for T-O*), and they almost agree with valgum-related M_y,applied (3.31±6.71N.m for H-S, -10.0±7.03N.m for F-E), except at T-O* (-10.6±6.82N.m). Therefore, the applied loading ended up simulating a pathologic state that resembles valgum. Interestingly, what seemed as an unfortunate accident shed light on the non-straightforward medial/lateral knee load distribution and led to figure out how to alter experimental conditions to simulate healthy or pathologic behaviour.

A4.7. Preliminary findings on valgum-like human knee mechanical response during walking (exploratory)

This physiologic simulation revealed a complex loading response mechanism inside the knee joint throughout gait under valgum-like conditions involving pressure spikes at the T-F joints during stance (Figure 0-30). Knee loading seems to be mostly concentrated in the same location throughout walking. For the P-F joint, the CP is fairly centric and invariant to flexion. Similarly, CPs do not vary much over the T-F compartments. The largest CP excursions with flexion (still fairly small) occur for the lateral T-F joint. In general, P-F pressures are located on the lateral side (some medial portions are even unloaded) and their magnitude is significantly smaller than for their T-F counterparts for all gait time points (especially during stance). However, these distributions become highly non-uniform in the T-F compartments (both medial and lateral), developing pressure peaks.

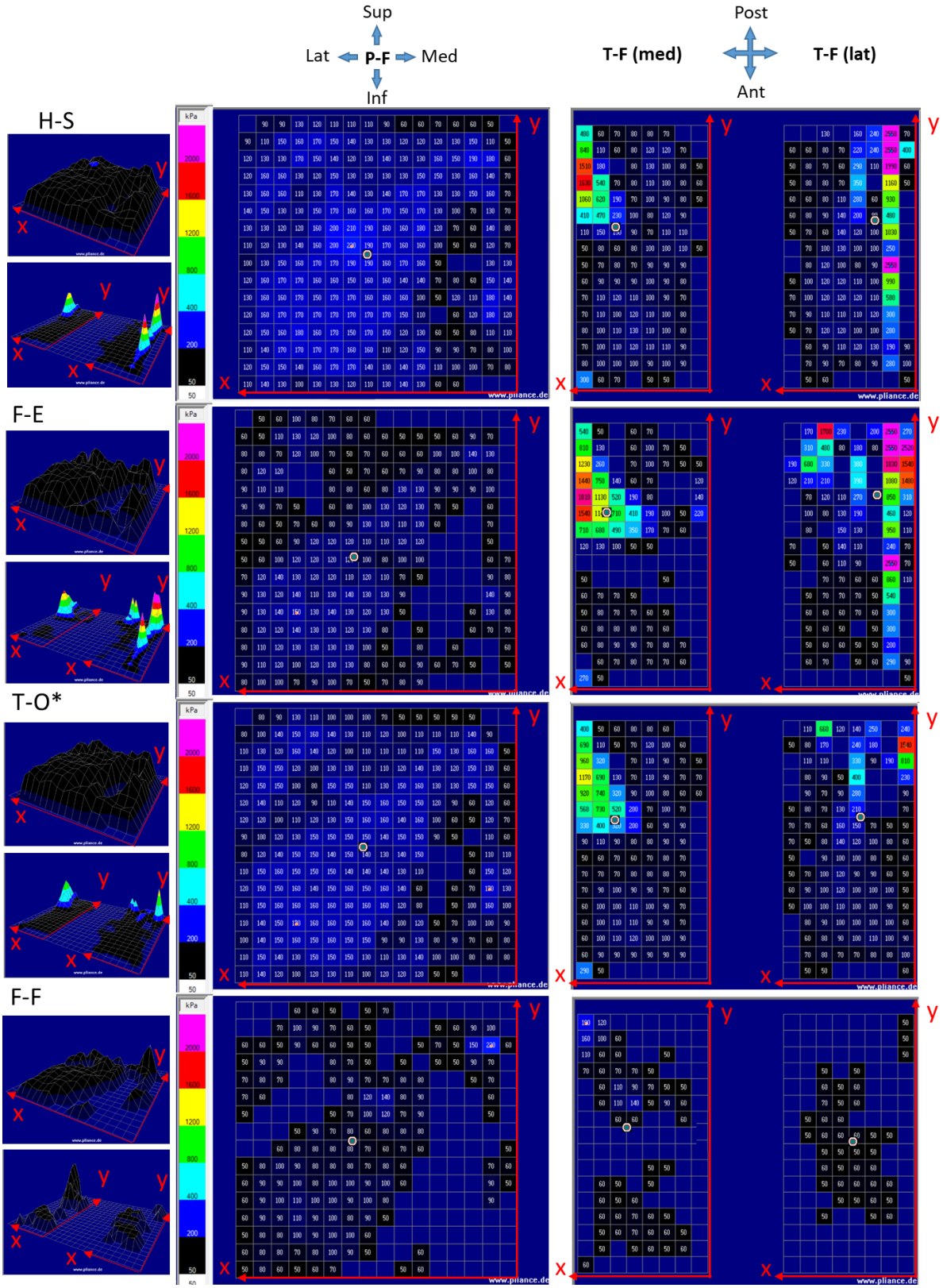

Figure 0-30: Steady contact pressure 2D distributions and pressure centers during gait & 3D thumbnails (last repeated trial)

A4.7.1.1. Preliminary associations between load input and contact response parameters

Contact forces seem to be directly related to (input) axial compression for the T-F joints and negatively related to axial compression for the P-F joint (Figure 0-31A). For all gait time points, contact area is always larger for the P-F compartment than for the T-F compartments (Figure 0-31B), and most of the entire cartilage surfaces (firmly attached to sensors adequately covering tibial and patellar articulating surfaces) seem to be touching except possibly at F-E and especially at F-F (Figure 0-30). Clearly during this time point, there is significant contact area reduction not only in the T-F compartments but also in the P-F compartment, accompanied by similar changes in force.

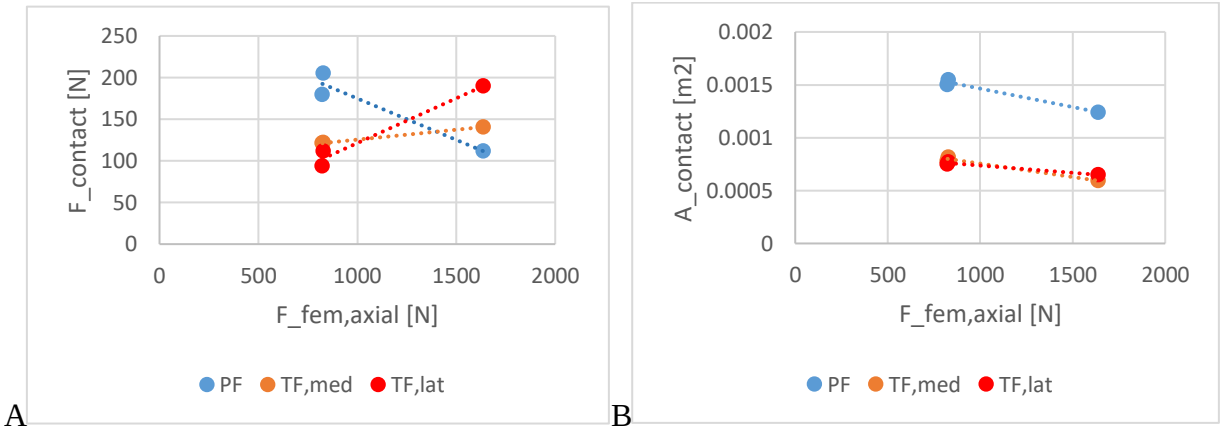

A B

Figure 0-31: Contact forces (A) and contact areas (B) vs. applied axial force magnitude trends during stance

Contact forces exhibit variation with knee flexion (Figure 0-32A). For medial and lateral T-F compartments, contact force decreases with flexion, whereas, for the P-F joint, it increases with flexion up to a point. As such, individual contact forces are much larger in T-F compartments than in the P-F compartment at low flexions (F-E), while these forces are individually smaller than the P-F force but collectively they add up to about the same magnitude at medium flexions (H-S, T-O*), and ultimately T-F forces are collectively smaller than the P-F force at high flexions (F-F). In general, for all compartments, contact forces are considerably smaller at F-F, when loading is only due to statically optimized muscle tension. Contact area exhibits a similar flexion variation as P-F contact force; however, this initial increase followed by a decrease in contact area is observed for all compartments, not just the P-F interface (Figure 0-32B), suggesting a potential relation.

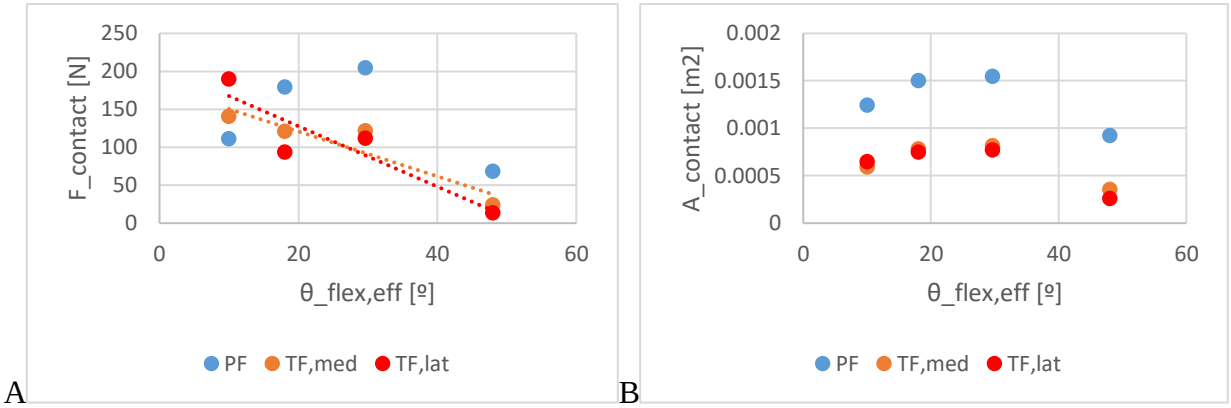

Figure 0-32: Contact force magnitudes (A) and contact areas (B) vs. knee flexion data show linear and non-linear trends

Indeed, contact forces are directly related to contact areas for all joints (Figure 0-33), almost following a linear trend for the P-F compartment and showing slight deviations from linear behaviour for the T-F compartments.

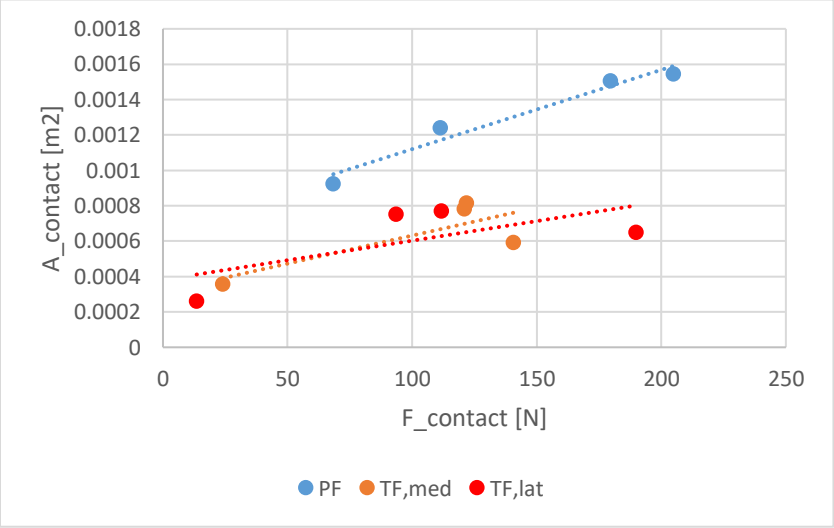

Figure 0-33: Linear trends between contact areas & contact force magnitudes

Contact pressures and axial compression seem to have the strongest association (Figure 0-34), as the regional maximum and average pressures exhibit an almost perfect linear behavior with this applied force in the T-F joints, despite the potential truncation due to sensor max calibration load cut-off (2.55MPa), while contact pressures seem detached from axial compression (especially maximum pressure).

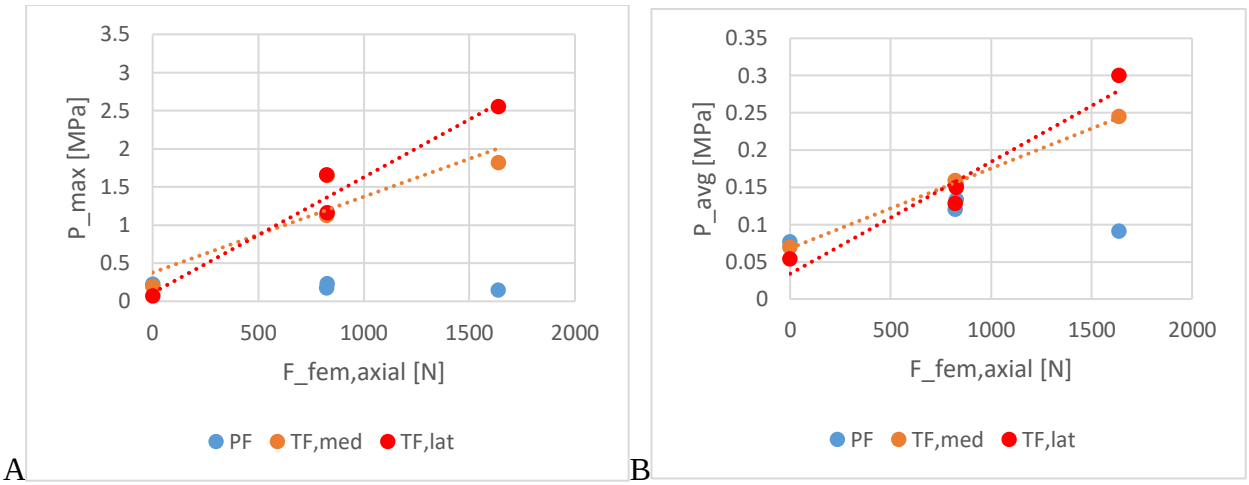

Figure 0-34: Regional maximum (A) and average (B) contact pressures vs. applied axial force magnitude register linear trends for the T-F joint only

Lastly, most centroids and centers of pressure practically do not seem to change during gait (Figure 0-35), as these locations remain fairly consistent (largest anterior-posterior variation registered is only ~2mm in the lateral T-F centroid) but axial force varies significantly throughout gait. Hence, geometry and pressure centers remain indifferent with respect to most applied moments (Figure 0-36A), except perhaps the lateral T-F pressure center anterior-posterior location and the applied moment parallel to the flexion/extension axis (Figure 0-36B), which varies ~10mm over this applied moment range. This further illustrates the differences (in location and excursion) between centers of geometry and pressure throughout walking; centroids and pressure centers are not necessarily coincident.

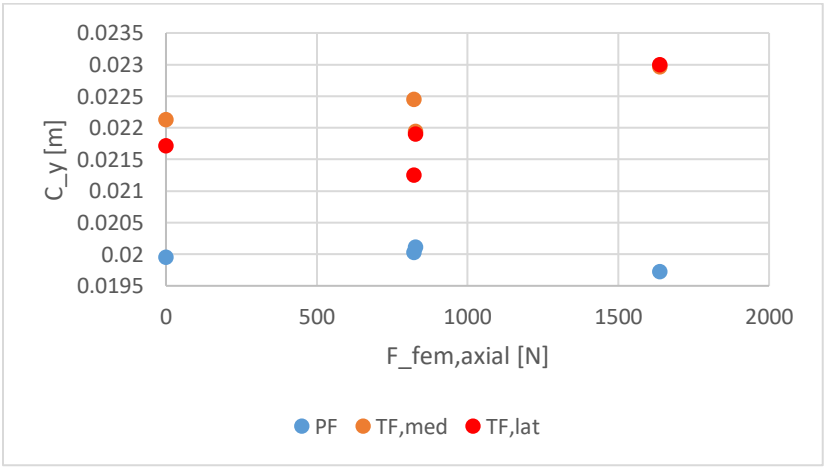

Figure 0-35: Largest anterior-posterior centroid (C_y) location variations seem independent from applied axial force magnitude changes during gait.

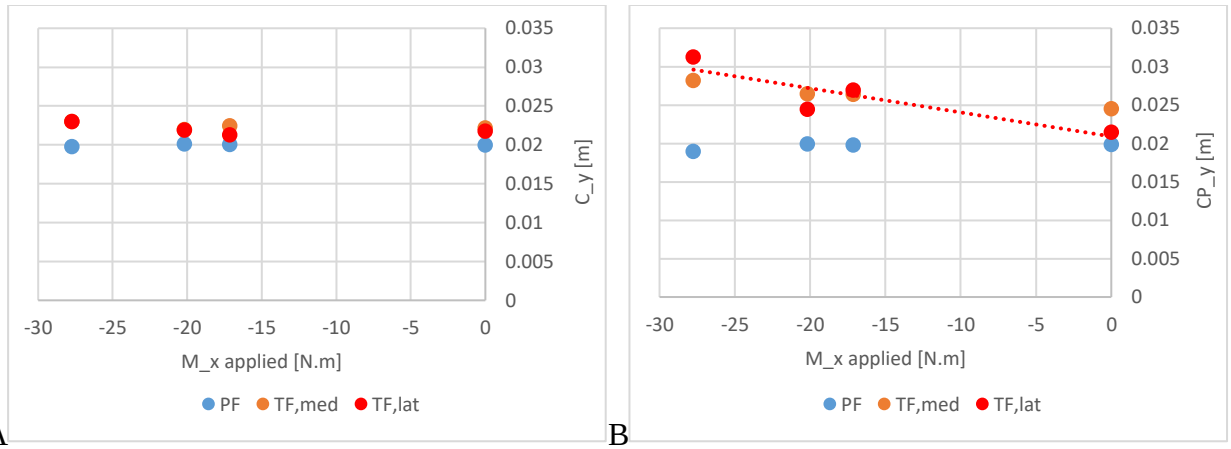

A B

Figure 0-36: Anterior-posterior location of centers of (A) geometry, C_y, & (B) pressure, CP_y, vs. applied moment parallel to flexion/extension axis, M_x,applied, only register a nontrivial trend for lateral T-F pressure center excursions

A4.7.1.2. Human knee mechanical response discussion

Preliminary findings show what gait may look like inside knees with valgum malalignment. Throughout this near-physiologic experimental simulation, however, the P-F joint remained mostly unloaded, especially at F-F (due to low statically optimized muscles). Nevertheless, loading transfer from T-F to P-F compartments is evident with increasing flexion, as shown by relationships between contact force, contact area and knee flexion (Figure 0-32A), while the contact pressure distributions opened a Pandora's box, as inquiries rise faster than answers. These load distributions exhibit a complex behavior, such as very high pressure peaks in the T-F joints. As expected, even when subjected to valgum (lateral bias), a large portion of knee loading still concentrates in the medial T-F compartment[329-331]. "Interestingly", however, the total contact forces in T-F (and P-F) compartments do not add up to account for the much larger applied compression. The scale of these differences is rather puzzling, e.g., for F-E (smallest knee flexion accompanied by almost exclusively axial loading), T-F contact forces add up to 331 N, while the axial compression (applied by the piston at one end and measured at the other with a load cell) is 1638 N. While it is possible the cartilage bear only a portion of the full axial force, highlighting the load-bearing role of other tissues (e.g., stress-shielding provided by bones and/or menisci), it is more likely this is mainly related to the pressure sensor limitations. This could be related to the sensor calibration (e.g., 2.55MPa maximum cut-off value) but, in that case, the large pressure peaks would be severely underestimated (which is even more peculiar), so maybe

it is related to sensor placement (e.g., small near menisci edge regions the sensors may not have covered), which could explain why the pressure patterns do not resemble characteristic meniscal wedges. Alternatively, the unusual pattern and pressure spikes could be due to sensors getting "pinched" near the bone peripheries because their placement was too far apart from knee center (medially and laterally).

Moreover, potential associations between contact and loading parameters may be lying underneath these mystic waters, noting of course that measurements pertain to a single specimen only. For instance, T-F contact forces exhibit a direct relationship with axial input force, while T-F contact areas are inversely related to this compressive force. Relationships between P-F contact forces and areas are occluded by low muscle loading; however, contact forces show a direct relationship with knee flexion for the P-F joint during stance, while these variables are inversely related for the T-F compartments during stance and swing. As such, for this specimen, contact forces and areas seem to exhibit a close direct relationship for the P-F and T-F joints, with more fluctuations for the T-F case. The strongest potential associations (resembling linear relationships for this specimen) exist between T-F contact pressures and axial force applied (Figure 0-34). Also, it seems that contact pressure remains somewhat invariant to applied loading, which could imply the patellar cartilage can transmit load more effectively than T-F cartilages or that simply the P-F joint was not loaded very much by statically optimized muscle forces. Lastly, despite similarities between centers of pressure and area, only centers of pressure (anterior/posterior location) are linked to applied bending moments (parallel to flexion/extension axis).

In this study, experimental contact measurements (novel pliance-x, placed between femoral cartilage and menisci) corresponded to loading equilibrium states, representing different points (H-S, F-E, T-O*, F-F) throughout gait subject to valgum malalignment. As stated earlier, throughout gait, the lateral T-F compartment was loaded more than the medial due to valgum. However, the medial compartment was still loaded significantly and peaks were found on the outer borders of both medial and lateral compartments (i.e. whereabouts the menisci sit); larger peaks were found on the lateral side, except a swing, where the only peak was found on the medial T-F compartment. Contact pressure peaks (potentially underestimated by sensor calibration) for the aformentioned simulated gait configurations were 1.65, 1.81, 1.12 and 0.19

MPa for the medial T-F joint, and 1.16, 2.55, 1.65 and 0.0667 MPa for the lateral T-F joint, which partially agree with some of the existing literature.

Differences and similarities have been found in T-F contact distributions via pressure sensing or FEM across different specimens. For instance, Naghibi Beidokhti et al.[86] found unique contact distributions for three specimens loaded at low levels (20N for rectus femoris, 20N in total for quadriceps, 106N for tibial compression) in stress relaxation via pressure sensors (Tekscan 4011) and FE models. However, in general, most of the compression was located in the medial condyle with peaks concentrated closer to the outer edges (knees 1 and 3) and on the condyle centre (knee 2). At 90º of knee flexion, resembling F-F, experimental peak contact pressures were 1.52MPa (knee 1 with excised MCL, LCL), ~0.6MPa (knee 2) and ~0.56Mpa (knee 3) and showed reasonable agreement with their corresponding optimized FE-predictions of 1.52MPa (knee 1), ~0.84 to ~1.08MPa (knee 2) and ~0.98MPa (knee 3). Papaioannou et al.[114] also measured contacts (Tekscan K-scan) and conducted FEM for three ex-vivo knees flexed at 10º and briefly compressed with 1.5kN, which is more comparable to the statically-approximate F-E simulations in study I. Short-term transient measurements showed pressures are concentrated on the medial compartment (with 2MPa and ~5.5MPa peaks near the condyle centre after 0.1 and 0.9s of loading). FE distributions for 0.1s (higher pressures on the medial exterior periphery with a posterior peak of 5.5MPa) differed from experimetnal measurements, but better agreed with them (5.5MPa peak at the condyle center, but also with high pressures on the periphery) after 0.9s of loading. Using one the most advanced, complete (and expensive) subject-specific full knee FE models available, Halonen et al.[144] examined the contact pressure distributions of a female test subject for 20 and 80% stance (1st and 2nd axial force peaks), corresponding to H-S and F-E configurations in study I. Once again, the medial T-F compartment was loaded more than the lateral throughout gait. At H-S, pressure peaks concentrated on the center of the medial tibial condyle and slightly on the border of the lateral tibial compartment; however the lateral peak shifted closer to the condyle center at F-E, during which peaks were more spread out. The medial and lateral cartilage respectively exhibited 13 and 11.7 MPa at H-S, and 13 and 7.95 MPa at F-E. Similarly, Yang et al.[332] only focused on FE modelling of three subjects under 3.5BW compression and 0.5BW shear at 25% stance (1st peak in abduction/adduction moment), corresponding to a time point between H-S and F-E, but examined normal, varum and valgum

malalignments. Compressive stress distributions showed that the knee is loaded more on the medial side for normal alignment, and more on the lateral side in valgum. For the normal case, there was a extremely fine peak in the medial femoral cartilage's interior edge; however, wider peaks were found in the lateral meniscus (close to the condyle center and by the posterior horn). For the case of valgum, the same peak was found for the femoral cartilage, while no peaks were present for the medial tibial cartilage nor meniscus. For the normal knee, maximum compressive stresses were 14.5 and ~3 MPa for medial and lateral femoral cartilages, and 13.3 and ~3 MPa for medial and lateral tibial cartilages; while in valgum, these were 12.7 and ~7 MPa for medial and lateral femoral cartilages, and 11.3 and ~6 MPa for the medial and lateral tibial cartilages.

Despite the expected subject-specific differences, a few trends are common to all measured and modeled pressure distributions. Among these, the medial T-F compartment carries more load than the lateral compartment for extended or slightly flexed knees, except for valgum malalignments (for which substantial loading remains in the medial compartment). Also, contact pressure spikes seem to always be present (either near the borders or close to the condyle centers) anteriorly according to Papaioannou et al., Halonen et al., Yang et al. and study I, and posteriorly according to Naghibi Beidokhti et al., Papaioannou et al. and Yang et al. In terms of magnitudes, T-F pressure peaks at F-F are much lower in study I (~1 order of magnitude below) compared to Naghibi Beidokhti et al.; however, the current specimen was likely unloaded at F-F by statically optimized muscle forces. Study I measurements do agree with published data, as evidenced by F-E pressure peaks after 0.1s of loading determined by Papaioannou et al. but not after 0.9s, which makes sense as load conditions in study I were supposed to be statically-equivalent representations of dynamic activity but are really just statically-approximate loads. Nevertheless, these F-E measurements in study I are drastically different from those predicted by Halonen et al. and so are H-S pressure peaks (both differing by another order of magnitude). There is better agreement between study I measures and F-E pressure peaks predicted by Yang et al. for healthy subject, with slightly larger differences for the valgum case; however, this agreement only takes place for the lateral condyle (medial pressure peaks being overestimated by FE by ~1 order of magnitude). As shown, in general, FE models seem to considerably over-predict contact pressure. These wide differences may be explained, however, by both numerical and experimental factors. As stated before, there are differences in applied loading, for instance,

study I corresponds to a static experimental simulation of valgum-like gait, while the aforementioned researchers simulated gait focused on short transient periods. Measured contact pressures also depend on the sensor used and its placement; the capacitive sensors used in study I are relatively stiffer and thicker compared to resistive Tekscan alternatives. Lastly, FE predictions strongly depend on the soft tissue material modeling, which needs to be conducted carefully due to the high sensitivity to Poisson's ratio, which easily leads to unreliable ill-conditioned situations, where minor tweaks in this parameter lead to all sorts of contact responses.

In conclusion, preliminary contact measurements showed complex intra-articular load distributions, which concentrated in the medial T-F compartment, even with the presence of valgum malalignment. However, as the knee flexed, this load transferred from the T-F to P-F joint. Moreover, soft tissue regions (often near anterior meniscal edges) experienced very high localized pressures throughout gait, agreeing with the literature overall. Whereas these pressure spikes may be underestimated in this study by pressure sensing limitations, findings suggest they might be overestimated by current FE models, highlighting the need for this type of experimental studies to corroborate this.

A5. Additional resources for study II

A5.1. Study design

This study involves nested data organized in the following statistical levels, each of which is further explained throughout the methods sections:

Level 1: Subject (human knees)

Level 2: Physiologic state (unloaded, loaded)

Level 3: Knee joint (P-F, T-F)

1. Mechanical variables (initial thickness, final thickness, displacement, engineering strain) at sites of interest
2. qMRI variables (initial T_2 time, final T_2 time, T_2 change, "T_2 strain"[i]) at sites of interest

[i] Previously defined informally to quantify percent changes or differences in T_2 time due to loading or pathology; however, its purpose in this study is to predict mechanical strain, inspired by how strain gauges' electrical resistance normalized change, $\Delta R/(R)_0$, is correlated with engineering strain.

A5.2. SOP for the qMRI-mechanics Correlations Assessment

Due to the vast scope (both in breadth and depth of many different aspects) of this project and thesis word limits, only an index of the raw data acquired is provided here.

Please contact Dr. Emily McWalter to gain access to these materials.

A5.2.1. qMRI-mechanics sampling code: T_2 time vs deformation

Due to the vast scope (both in breadth and depth of many different aspects) of this project and thesis word limits, only an index of the raw data acquired is provided here.

Please contact Dr. Emily McWalter to gain access to these materials.

A5.3. Testing protocols

Unfortunately, no specimen preparation, mechanical testing or specimen logs exist for study II specimens (K01-K06). In general, other than the stent removed from K01 (and the resulting void in those images), no abnormalities were found among the specimens, which depict a healthy state. A SOP was written, however, for preparing specimens for stress relaxation using the MRI-safe displacement-control rig.

Please contact Dr. Emily McWalter to gain access to these materials.

A5.3.1. Imaging protocols

In order to acquire morphologic and T_2 relaxation volumes suitable for qMRI-mechanics associations assessment, the following images must be taken in the following order for each specimen:

Load 0 (unloaded):

1. qDESS
2. T_2 relaxation time (5 morphologic scans)

Transient loading (after successive stress relaxation):

1. Steady-state detection (image subtraction every 15 min)

Load 1 (axially loaded):

1. qDESS
2. T_2 relaxation time (5 morphologic scans)

Please contact Dr. Emily McWalter to gain access to these materials.

A5.4. Raw data

Due to the vast scope (both in breadth and depth of many different aspects) of this project and thesis word limits, only an index of the raw data acquired is provided here:

1. MRI-safe load cell data for all 6 specimens
2. Steady state detection data via image subtraction
3. Load 0 (unloaded) images
    a. qDESS
    b. T_2 relaxation time
    c. Binary masks (patellar & tibial cartilages)
4. Load 1 (axially loaded) images
    a. qDESS
    b. T_2 relaxation time
    c. Binary masks (patellar & tibial cartilages)

Please contact Dr. Emily McWalter to gain access to these materials.

A5.5. Processed data

Due to the vast scope (both in breadth and depth of many different aspects) of this project and thesis word limits, only an index of the processed data acquired is provided here.

Please contact Dr. Emily McWalter to gain access to these materials:

1. Load 1 (axially loaded) images for all 6 specimens
    a. Deformation
        i. Change in position (displacement)
        ii. Nominal engineering strain
    b. T_2 relaxation response
        i. Change in T_2 time
        ii. T_2 time -strain
2. T_2 relaxation-deformation correlations
    a. Potential associations among initial metrics
        i. $(t)\_o$ vs. $(T_2)\_o$
        ii. $|(t)\_o|$ vs. $|(T_2)\_o|$
        iii. $\log|(t)\_o|$ vs. $|(T_2)\_o|$
        iv. $|(t)\_o|$ vs. $\log|(T_2)\_o|$
        v. $\log|(t)\_o|$ vs. $\log|(T_2)\_o|$

b. Potential associations among final metrics

   i. $(t)\_f$ vs. $(T_2)\_f$

   ii. $|(t)\_f|$ vs. $|(T_2)\_f|$

   iii. $\log|(t)\_f|$ vs. $|(T_2)\_f|$

   iv. $|(t)\_f|$ vs. $\log|(T_2)\_f|$

   v. $\log|(t)\_f|$ vs. $\log|(T_2)\_f|$

c. Potential associations among changes

   i. Δt vs. ΔT_2

   ii. $|\Delta t|$ vs. $|\Delta T_2|$

   iii. $\log|\Delta t|$ vs. $|\Delta T_2|$

   iv. $|\Delta t|$ vs. $\log|\Delta T_2|$

   v. $\log|\Delta t|$ vs. $\log|\Delta T_2|$

d. Potential associations among normalized changes

   i. ε_eng vs. ε_T_2

   ii. $|\varepsilon\_eng|$ vs. $|\varepsilon\_T_2|$

   iii. $\log|\varepsilon\_eng|$ vs. $|\varepsilon\_T_2|$

   iv. $|\varepsilon\_eng|$ vs. $\log|\varepsilon\_T_2|$

   v. $\log|\varepsilon\_eng|$ vs. $\log|\varepsilon\_T_2|$

3. Correlations assessment for potentially significant associations among normalized changes

    a. Abscissa normality (histogram, median, min, max, mean, variance, skewness, kurtosis)
    b. Ordinate normality (histogram, median, min, max, mean, variance, skewness, kurtosis)
    c. Residuals normality (Q-Q plot, histogram, median, min, max, mean, variance, skewness, kurtosis)
    d. Residuals homoscedasticity (residuals plot)
    e. Linear trend
    f. Significance (H_o: No correlation; H_1: Either positive or negative correlation)
    g. Correlation strength

A5.5.1. Thickness and T_2 changes further examination

Large inter-specimen SDs in measured morphology and T2 response (Figure 0-37) difficult detecting whether there were actual differences due to loading, especially thickness changes, while T_2 varies less across specimens (Figure 0-38).

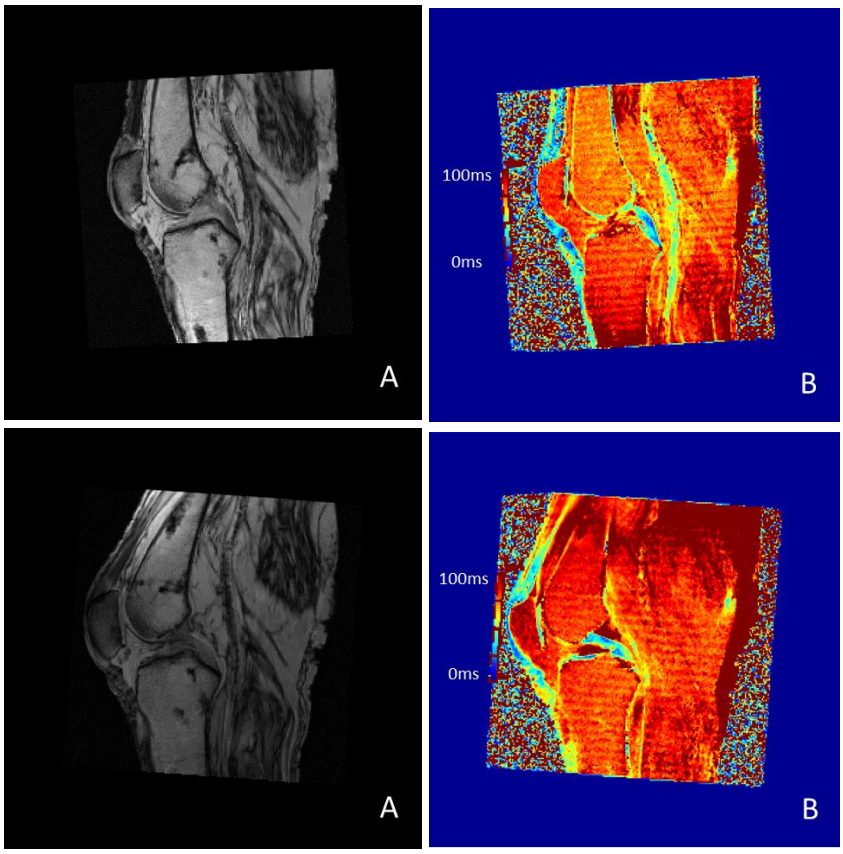

Figure 0-37: Sample qDESS image (A) & T_2 relaxation time map (B) sagittal slice containing trochlea (unloaded and loaded K06)

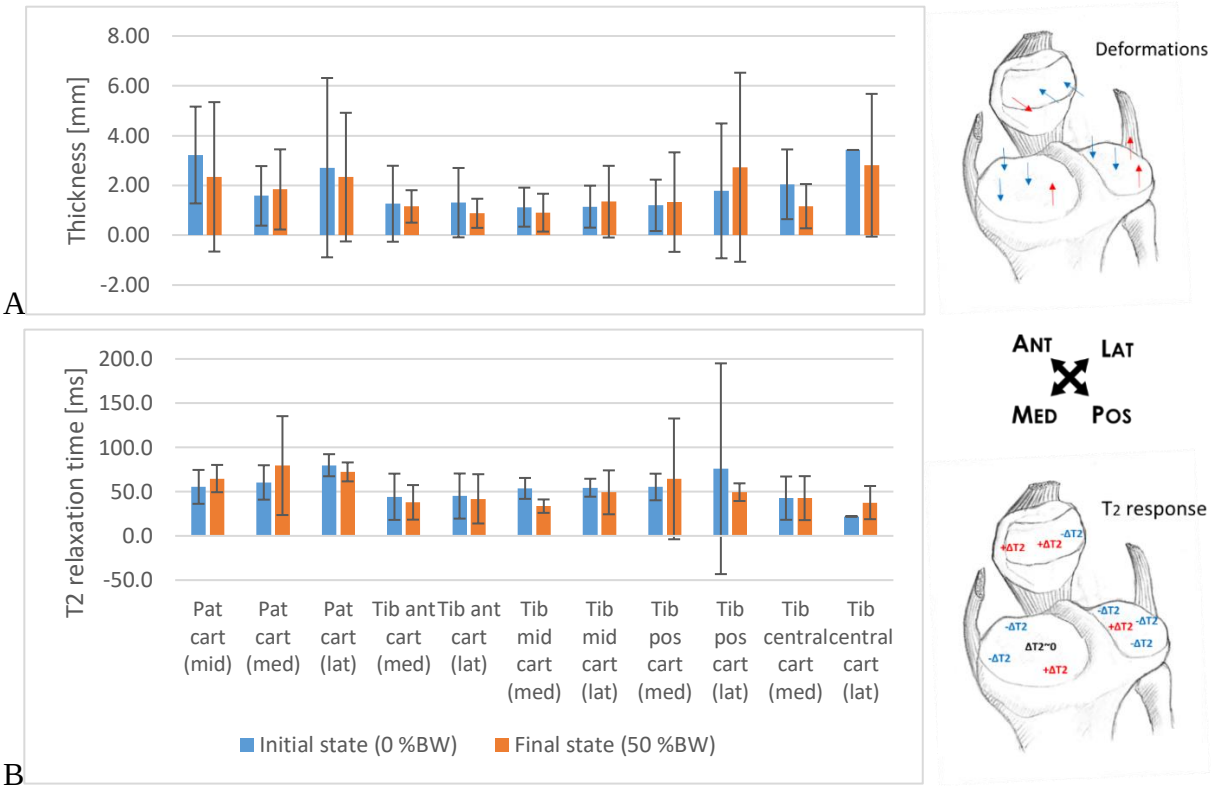

Figure 0-38: Thickness (A) and T_2 relaxation time (B) for unloaded and loaded states (AVG±2SD) and diagram showing change directions of average thickness and T2 relaxation time with load

Hence, paired box plots (Figure 0-39) were used to better visualize how individual thickness and T_2 time measures changed. Only based on direction of these changes, the majority of sites experienced reduction in thickness (except for medial patellar and lateral posterior tibial cartilages' which increased for most specimens, and middle patellar cartilage's which increased and decreased equally across specimens) and T_2 time (except for medial patellar, medial anterior tibial, lateral anterior tibial, medial central tibial and lateral central tibial cartilages' which increased for most specimens, and middle patellar cartilage's which increased and decreased equally across specimens).

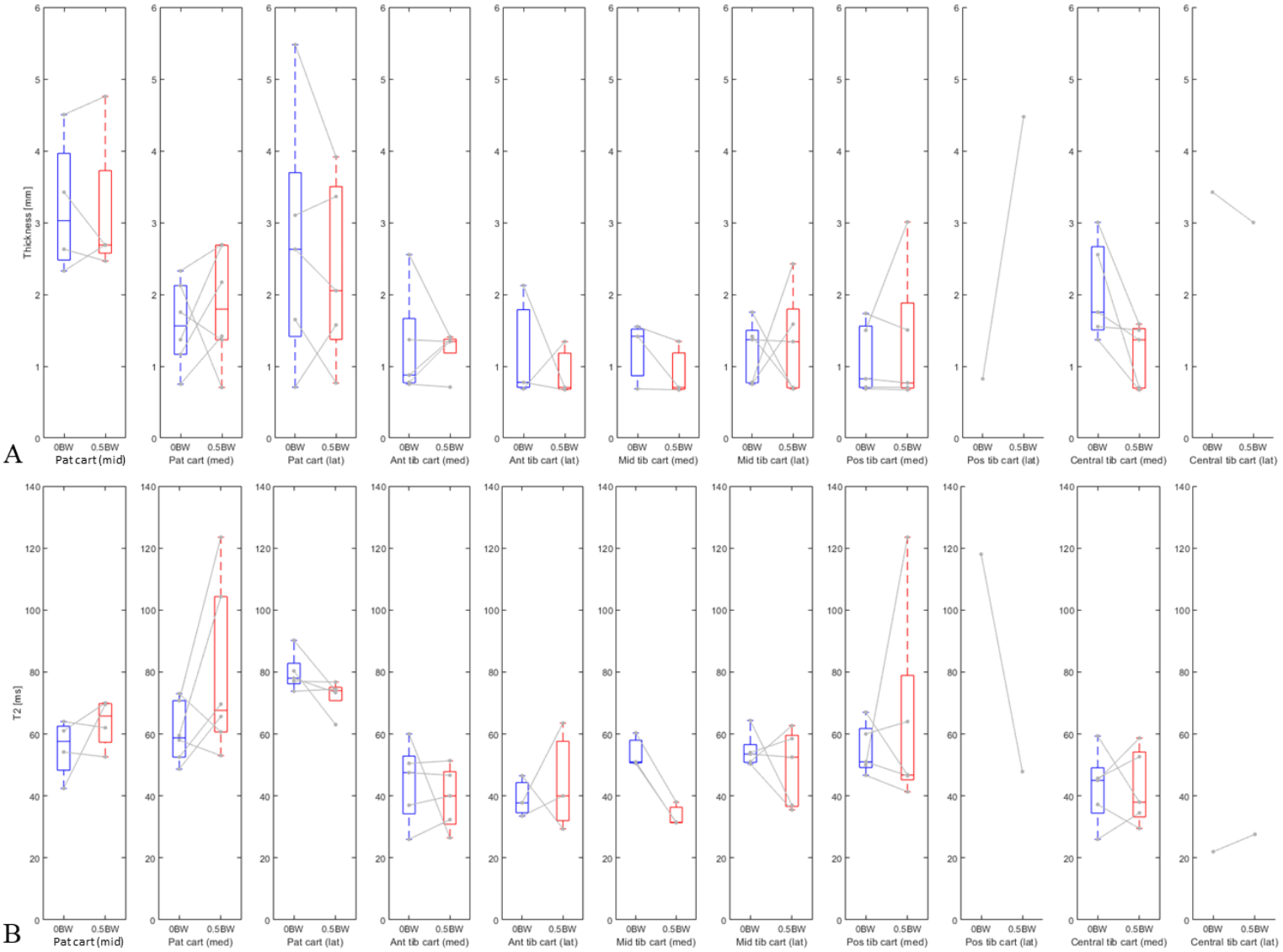

Figure 0-39: Individual and group changes in thickness (A) and T_2 relaxation time (B) measurements upon applied loading; note differences in sample size

As shown, the inter-subject SDs are usually larger than the magnitude of the associated changes (Figure 0-40, Figure 0-39), for which these should be interpreted with caution.

A

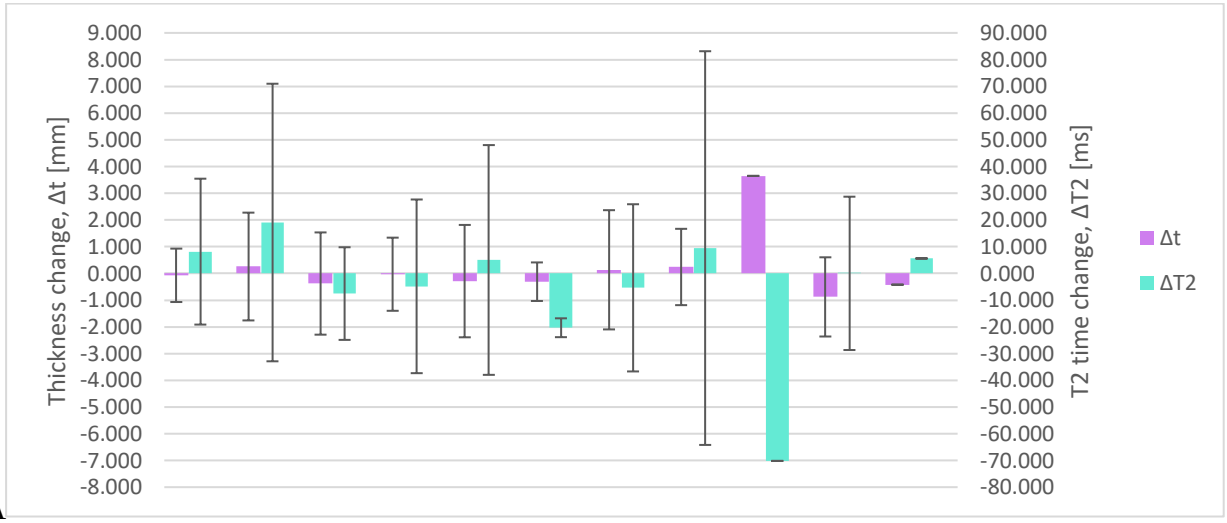

B

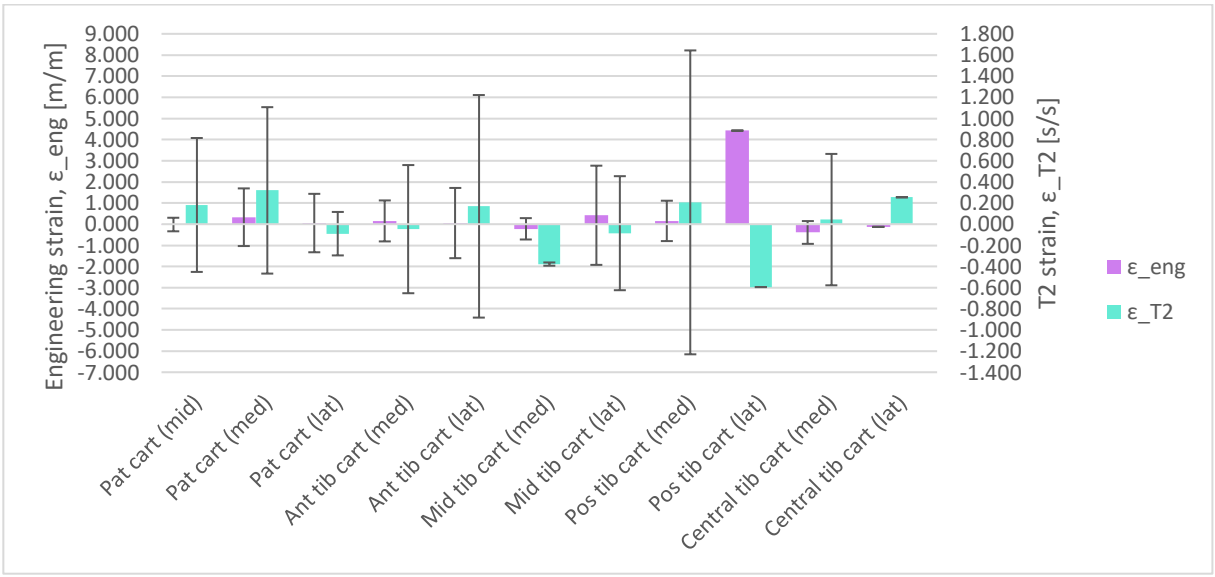

Figure 0-40: Absolute (A) and normalized (B) changes in thickness and T_2 relaxation time due to applied loading register copious inter-subject variability (AVG±2SD)

A5.5.2. T_2-deformation correlations assessment

The following data corresponds to the following checks conducted for the deformation (Figure 0-41) and T_2 relaxation (Figure 0-42) responses to simulated standing load measured in study II.

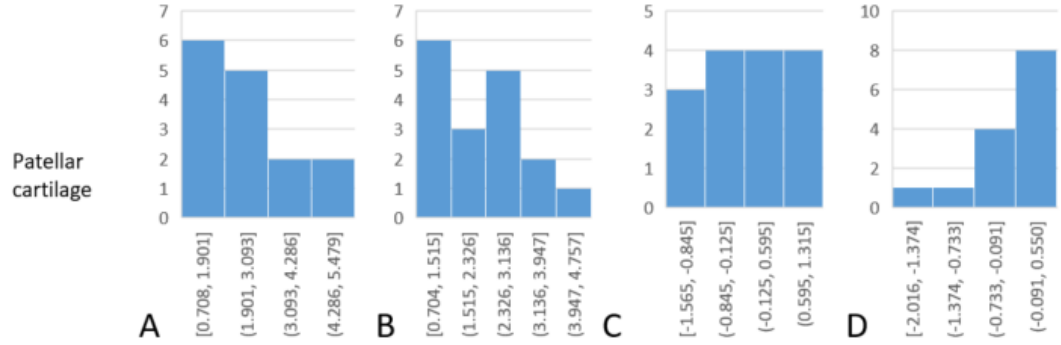

	A	B	C	D
Sample size	15	17	15	15
Median	2.327	2.170	0.254	0.053
Min	0.708	0.704	-1.565	-2.016
Max	5.479	4.757	1.315	0.550
Sample mean	2.396	2.163	-0.043	-0.140
Sample SD	1.331	1.176	0.870	0.682
AVG - 3SD	-1.595	-1.365	-2.653	-2.187
AVG + 3SD	6.388	5.691	2.568	1.907
Skewness	0.951	0.539	-0.290	-1.707
Kurtosis	0.813	-0.108	-0.819	3.388

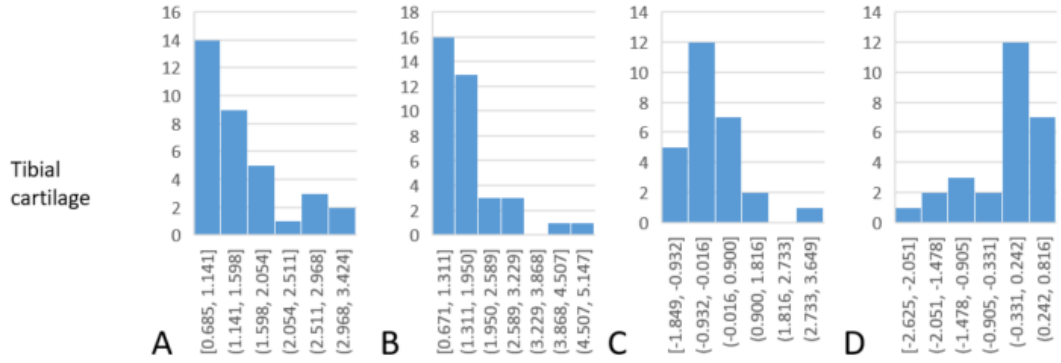

	A	B	C	D
Sample size	34	37	28	28
Median	1.370	1.342	-0.052	-0.067
Min	0.685	0.671	-1.849	-2.625
Max	3.424	5.147	3.649	0.816
Sample mean	1.427	1.501	-0.044	-0.297
Sample SD	0.738	1.068	1.085	0.814
AVG - 3SD	-0.787	-1.702	-3.299	-2.740
AVG + 3SD	3.640	4.705	3.211	2.146
Skewness	1.066	1.903	1.434	-1.222
Kurtosis	0.554	3.748	4.048	1.466

Figure 0-41: Histograms for mechanical measures: A. Initial thickness [mm], B. Final thickness [mm], C. Thickness change [mm], D. Engineering strain

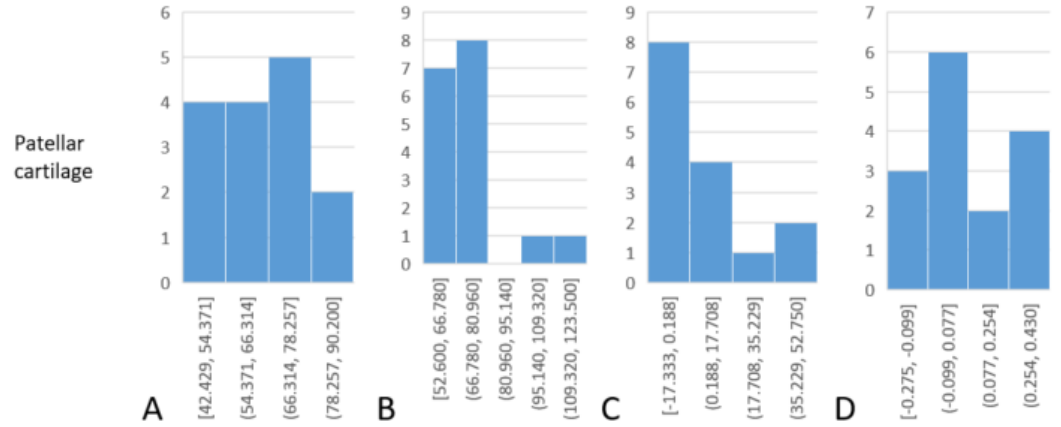

Sample size	15	17	15	15
Median	64.000	69.600	-0.250	-0.003
Min	42.429	52.600	-17.333	-0.275
Max	90.200	123.500	52.750	0.430
Sample mean	65.555	72.174	7.275	0.065
Sample SD	13.360	17.604	20.984	0.236
AVG - 3SD	25.476	19.362	-55.675	-0.644
AVG + 3SD	105.634	124.986	70.226	0.773
Skewness	0.038	1.934	1.031	0.343
Kurtosis	-0.718	4.256	0.380	-1.122

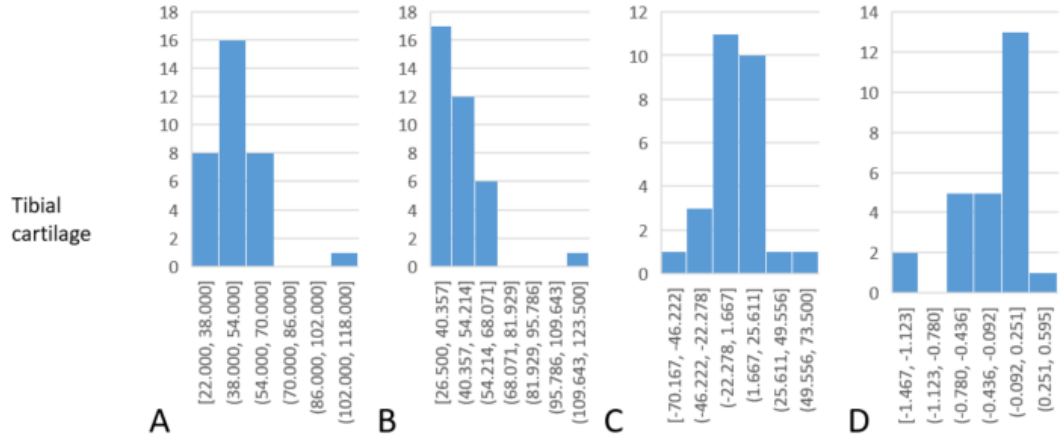

Sample size	34	37	28	28
Median	50.500	41.333	-0.917	-0.018
Min	22.000	26.500	-70.167	-1.467
Max	118.000	123.500	73.500	0.595
Sample mean	50.435	44.741	-4.077	-0.186
Sample SD	16.400	17.195	24.140	0.485
AVG - 3SD	1.234	-6.845	-76.495	-1.641
AVG + 3SD	99.636	96.327	68.342	1.268
Skewness	1.847	2.767	0.449	-0.957
Kurtosis	8.077	11.552	4.511	0.772

Figure 0-42: Histograms for T_2 relaxation measures: A. Initial T_2 time [ms], B. Final T_2 time [ms], C. T_2 change [ms], D. T_2 strain

However, what matters most for correlations is that their residuals are normally distributed, as well that their SD remains constant throughout the correlation domain, both of which seems to be the case among (intact and logarithmically transformed) initial metrics (Figure 0-43, Figure 0-44, Figure 0-45), especially for $\log|(t)_0|$ vs. $|(T_2)_0|$.

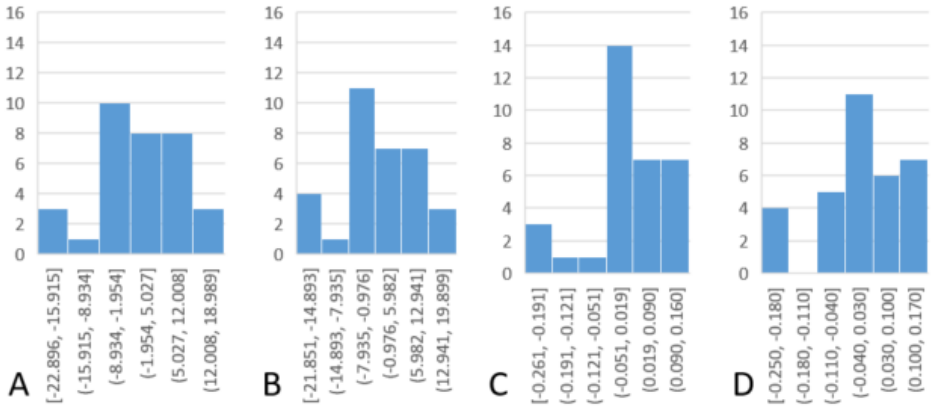

Sample size	33	33	33	33
Median	-0.648	-0.164	0.008	0.011
Min	-22.896	-21.851	-0.261	-0.250
Max	18.989	19.899	0.160	0.170
Sample mean	0.000	0.000	0.000	0.000
Sample SD	10.271	10.686	0.105	0.110
AVG - 3SD	-30.812	-32.058	-0.315	-0.329
AVG + 3SD	30.813	32.059	0.316	0.329
Skewness	-0.428	-0.310	-0.975	-0.859
Kurtosis	0.220	-0.125	0.969	0.585

Figure 0-43: Histograms for residuals of significant associations between initial thickness & corresponding T_2 time, after outlier/influence point removal: A. $(t)_0$ vs. $(T_2)_0$ or $|(t)_0|$ vs. $|(T_2)_0|$, B. $\log|(t)_0|$ vs. $|(T_2)_0|$, C. $|(t)_0|$ vs. $\log|(T_2)_0|$, D. $\log|(t)_0|$ vs. $\log|(T_2)_0|$

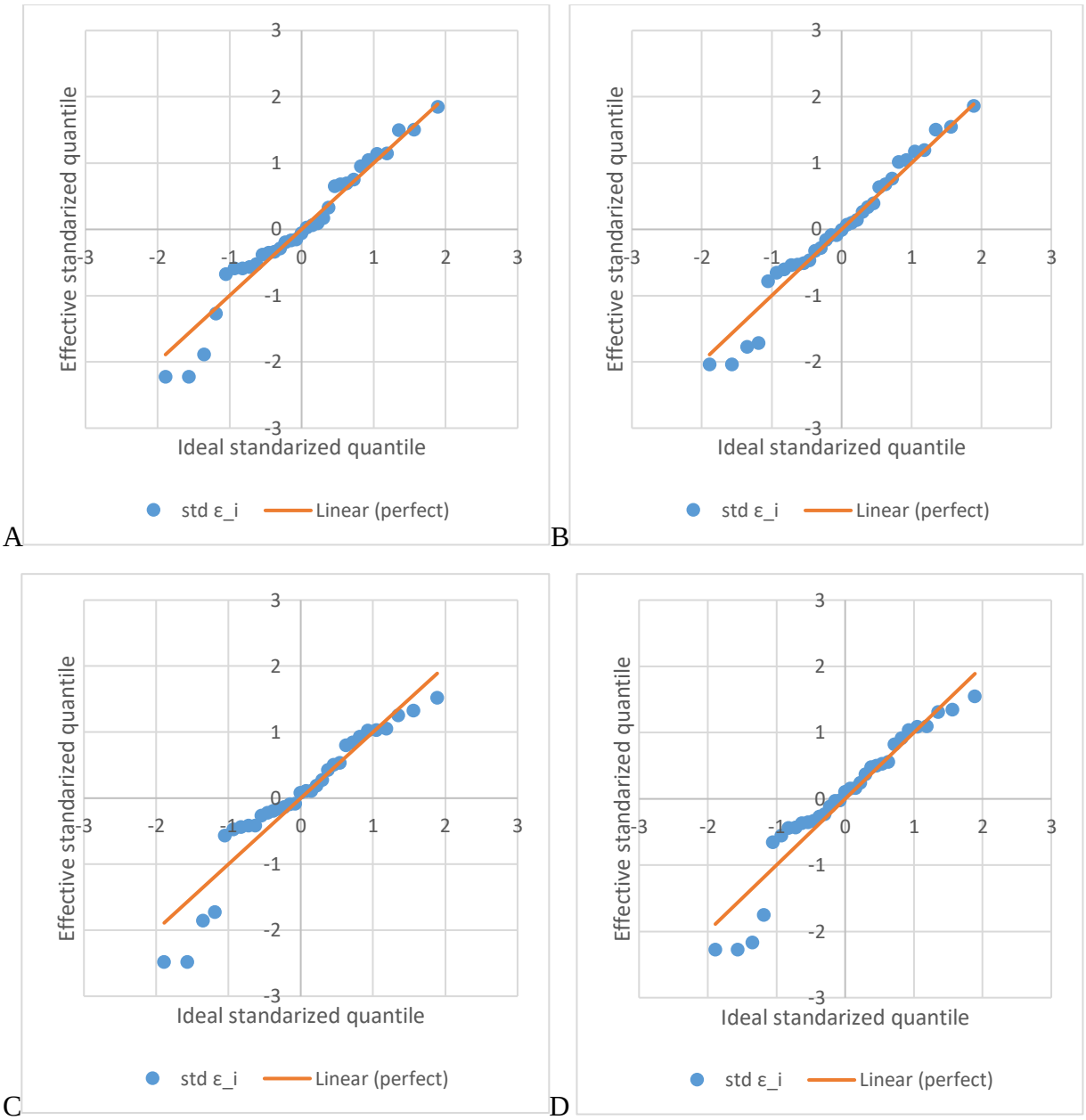

Figure 0-44: Q-Q plots for significant associations between initial thickness & corresponding T_2 time, after outlier/influence point removal: A. $(t)_0$ vs. $(T_2)_0$ or $|(t)_0|$ vs. $|(T_2)_0|$, B. $\log|(t)_0|$ vs. $|(T_2)_0|$, C. $|(t)_0|$ vs. $\log|(T_2)_0|$, D. $\log|(t)_0|$ vs. $\log|(T_2)_0|$

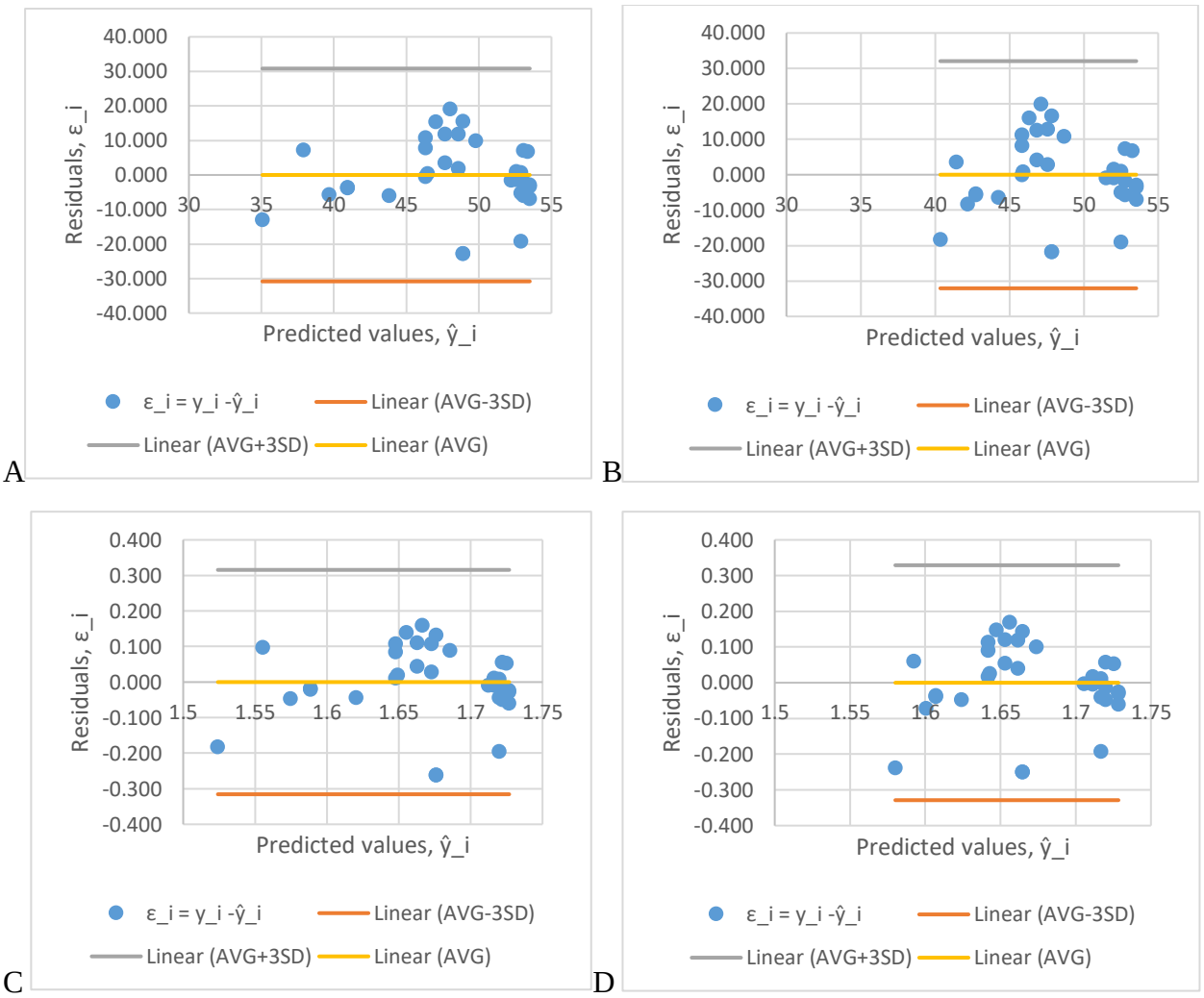

Figure 0-45: Residual plots for significant associations between initial thickness & corresponding T_2 time, after outlier/influence point removal: A. $(t)_0$ vs. $(T_2)_0$ or $|(t)_0|$ vs. $|(T_2)_0|$, B. $\log|(t)_0|$ vs. $|(T_2)_0|$, C. $|(t)_0|$ vs. $\log|(T_2)_0|$, D. $\log|(t)_0|$ vs. $\log|(T_2)_0|$

Based on the normality of initial thickness and T2 times and corresponding transformed expressions (as evidenced by their histograms, statistical moments and other descriptive statistical properties), and their best fit residuals' normality (evidenced by histograms, statistical moments, other descriptive statistics and close-to-ideal Q-Q plots), homoscedasticity (evidenced by residual plots bounded by 3SDs) and trend linearity, conducting correlations and linear best fits between these variables are justified.

A5.5.3. Outlier or influence point removal

Data prior to outlier removal:

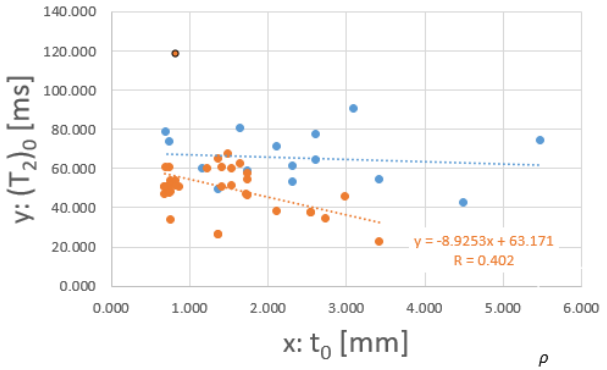

	Spearman Patellar (blue)	Pearson Tibial (orange)
ρ	-0.114	-0.402
p-value	0.685	**0.019**
n	15	34

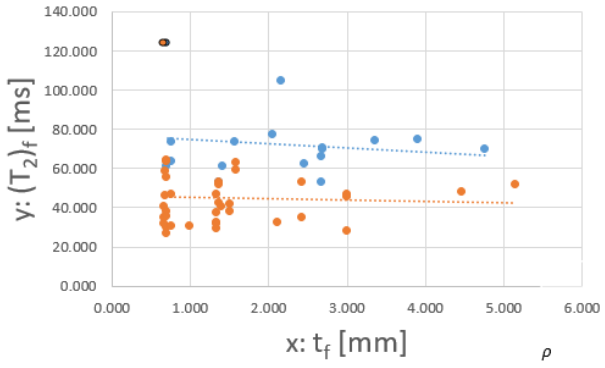

	Spearman Patellar (blue)	Pearson Tibial (orange)
ρ	0.098	-0.040
p (2-tailed)	0.707	0.816
n	17	37

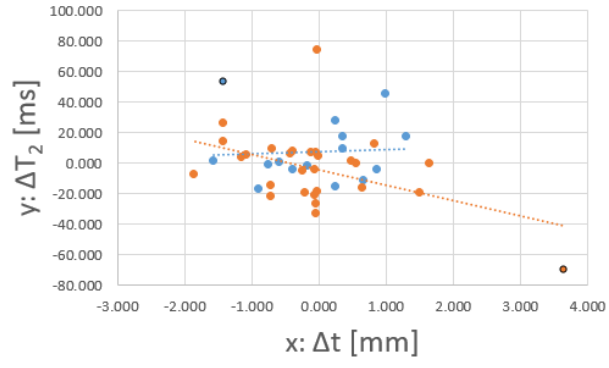

	Spearman Patellar (blue)	Tibial (orange)
r_s	0.111	-0.272
p-value	0.694	0.161
n	15	28

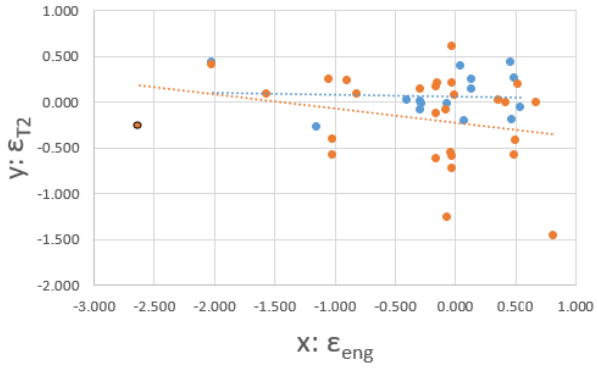

	Spearman Patellar (blue)	Tibial (orange)
r_s	0.091	-0.274
p-value	0.746	0.159
n	15	28

Figure 0-46: Deformation vs. T_2 relaxation metrics for patellar (blue) and tibial (orange) cartilages before outlier/influence point (delineated in black) removal; regression equation only for significant (bolded p-values) potential correlations

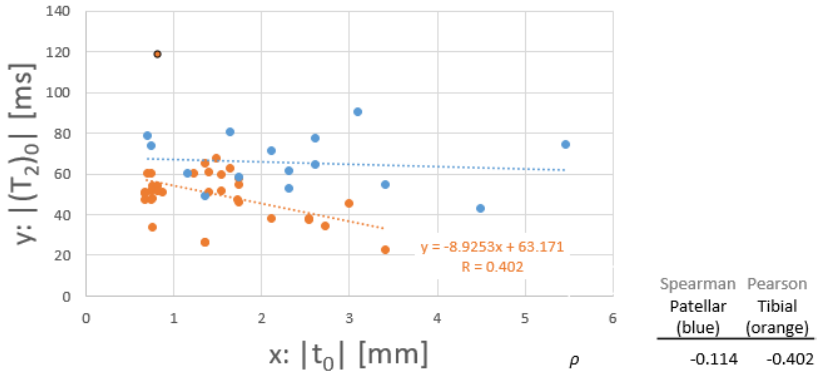

	Spearman Patellar (blue)	Pearson Tibial (orange)
ρ	-0.114	-0.402
p-value	0.685	**0.019**
n	15	34

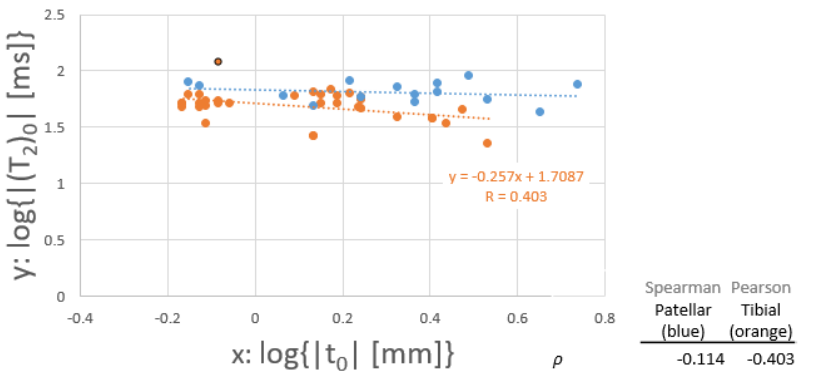

	Spearman Patellar (blue)	Pearson Tibial (orange)
ρ	-0.114	-0.403
p-value	0.685	**0.018**
n	15	34

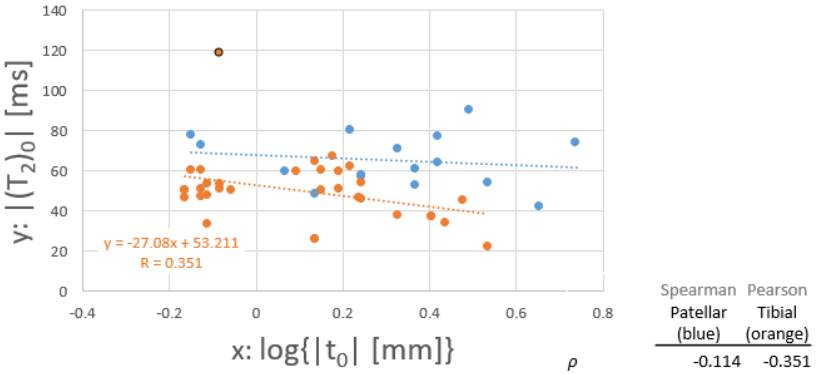

	Spearman Patellar (blue)	Pearson Tibial (orange)
ρ	-0.114	-0.351
p-value	0.685	**0.042**
n	15	34

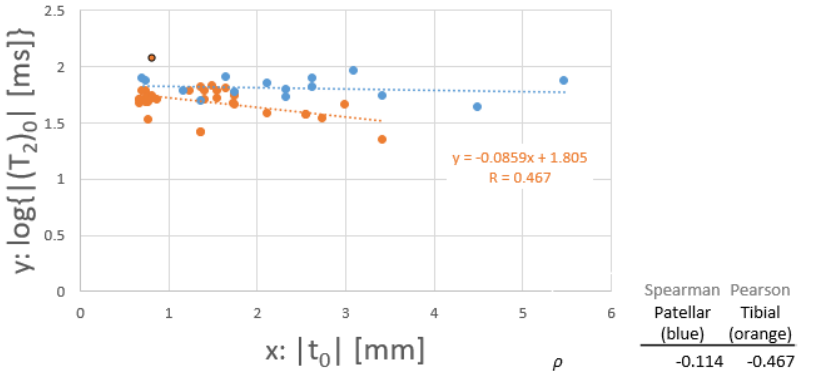

	Spearman Patellar (blue)	Pearson Tibial (orange)
ρ	-0.114	-0.467
p-value	0.685	**0.005**
n	15	34

Figure 0-47: Initial thickness vs. T_2 relaxation time, after logarithmic transformations, for patellar (blue) and tibial (orange) cartilages before outlier/influence point (delineated in black) removal; regression equation only for significant (bolded p-values) potential correlations

Notice that some data points (delineated in black) either have a very large magnitude or have considerable leverage on the correlation, which draws into question whether they can be trusted. For instance, the 150ms threshold filter might have missed some T_2 values, such as those close to 120ms (somewhat unrealistic). As such, these and other questionable data points (and their corresponding transformed expressions) were removed based on influence and leverage especially, and linear regressions recomputed for data without these outliers and/or influence points (Figure 5-7, Figure 5-8). Whereas correlation strength ($r = -0.437$, $p = 0.011$) and equations changed, they did not alter the overall results and conclusions, i.e. only initial cartilage thickness and corresponding T_2 relaxation signal were correlated moderately.

Data after outlier removal:

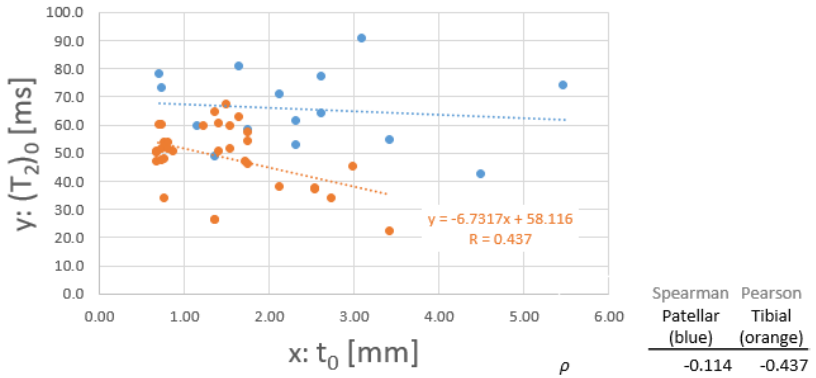

Spearman	Patellar (blue)	Tibial (orange)
ρ	-0.114	-0.437
p-value	0.685	**0.011**
n	15	33

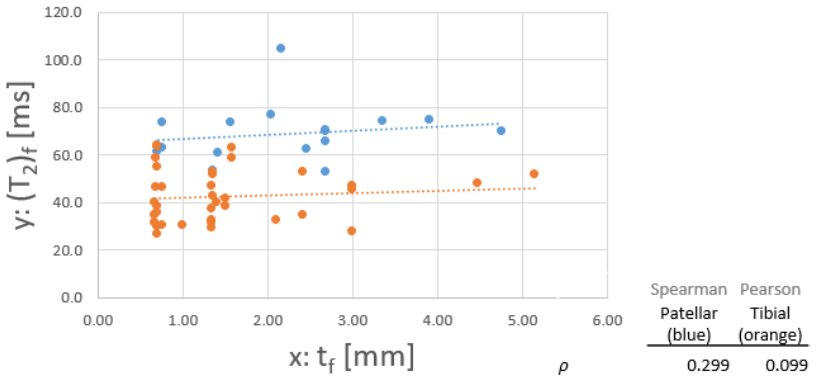

Spearman	Patellar (blue)	Tibial (orange)
ρ	0.299	0.099
p-value	0.260	0.567
n	16	36

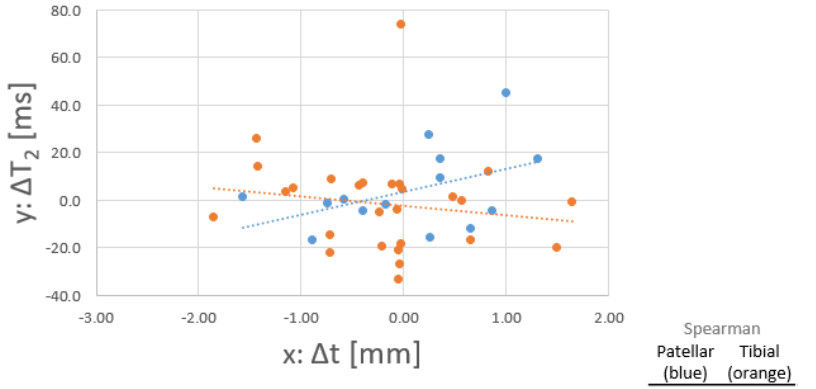

Spearman	Patellar (blue)	Tibial (orange)
r_s	0.341	-0.188
p-value	0.233	0.347
n	14	27

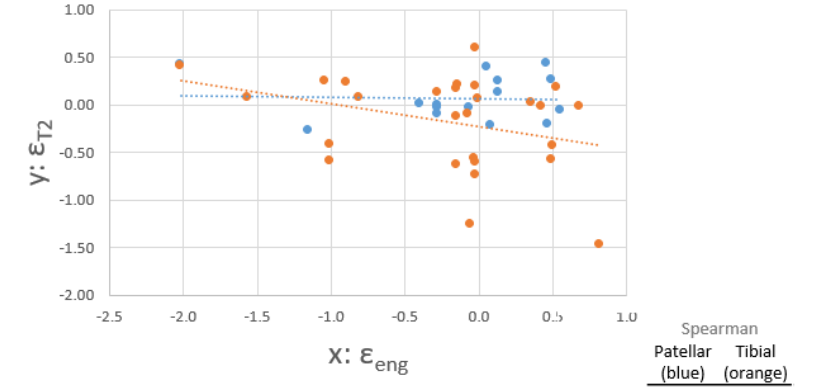

Spearman	Patellar (blue)	Tibial (orange)
r_s	0.091	-0.325
p-value	0.746	0.098
n	15	27

Figure 0-48: Deformation vs. T_2 relaxation metrics for patellar (blue) and tibial (orange) cartilages after outlier/influence point removal; regression equation only for significant (bolded p-values) potential correlations

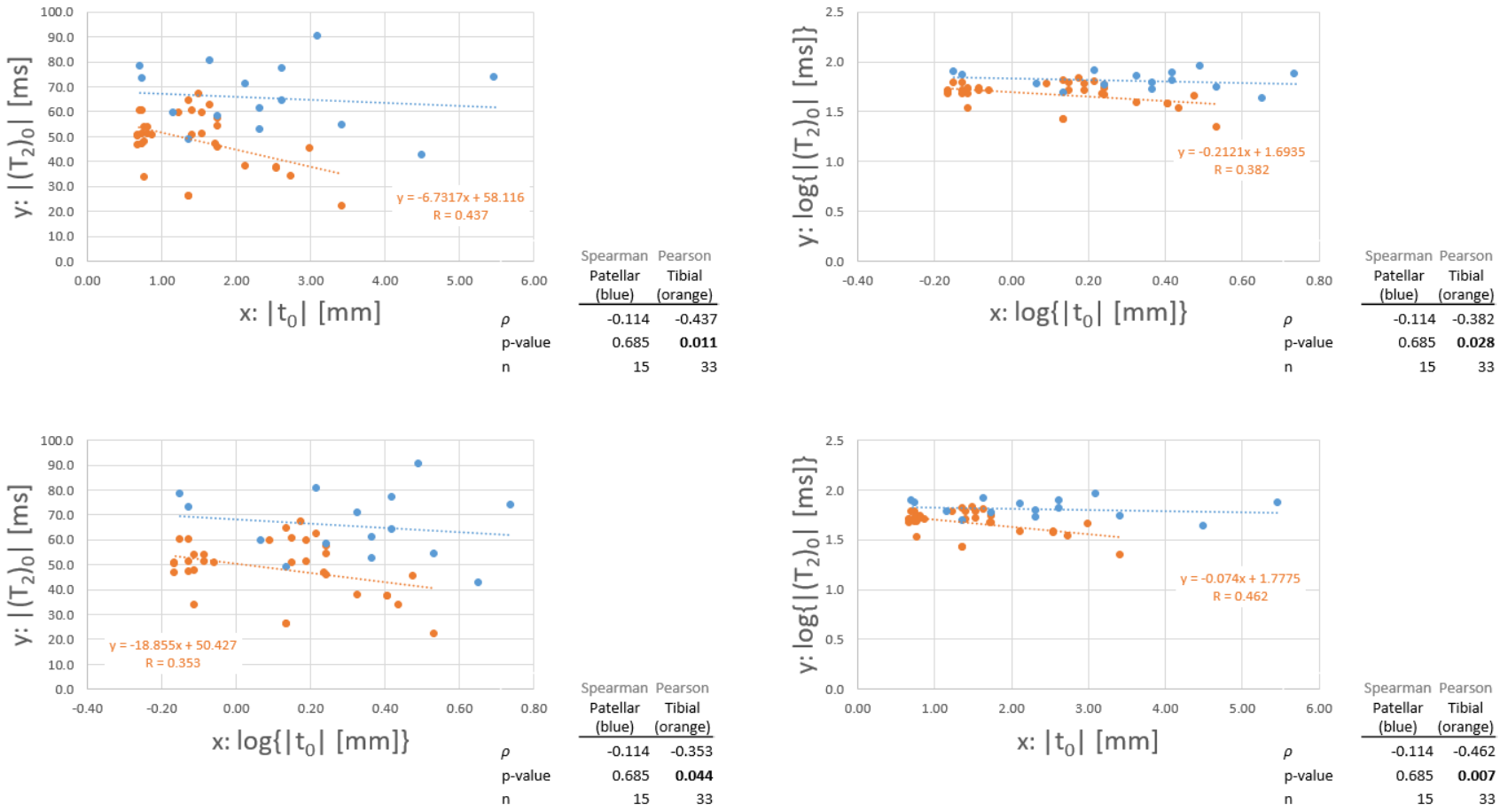

	Spearman Patellar (blue)	Pearson Tibial (orange)
ρ	-0.114	-0.437
p-value	0.685	**0.011**
n	15	33

	Spearman Patellar (blue)	Pearson Tibial (orange)
ρ	-0.114	-0.382
p-value	0.685	**0.028**
n	15	33

	Spearman Patellar (blue)	Pearson Tibial (orange)
ρ	-0.114	-0.353
p-value	0.685	**0.044**
n	15	33

	Spearman Patellar (blue)	Pearson Tibial (orange)
ρ	-0.114	-0.462
p-value	0.685	**0.007**
n	15	33

Figure 0-49: Initial thickness vs. T_2 relaxation time, after logarithmic transformations, for patellar (blue) and tibial (orange) cartilages after outlier/influence point removal; regression equation only for significant (bolded p-values) potential correlation

A5.5.4. T_2 relaxation time-thickness models for the unloaded tibial cartilage (exploratory)

As suggested by the data obtained, there are at least four possible resulting models for relating initial cartilage thickness [0.684813mm ≤ $(t)_0$ ≤ 3.42407mm] to its correspondent T_2 relaxation signal (Figure 0-50). Rewriting the previous linear fits (after outlier/influence point removal) leads to:

$$\text{Model 1: } (T_2)_0 = -6.7317(t)_0 + 58.116, \qquad R = 0.437 \tag{0-15}$$

$$\text{Model 2: } (T_2)_0 = -18.855 \cdot \log[(t)_0] + 50.427, \qquad R = 0.353 \tag{0-16}$$

$$\text{Model 3: } (T_2)_0 = 59.9101e^{-0.170391(t)_0}, \qquad R = 0.462 \tag{0-17}$$

$$\text{Model 4: } (T_2)_0 = 49.3742(t)_0{}^{-0.2121}, \qquad R = 0.382 \tag{0-18}$$

After checking the normality of the statistical distributions of the variables involved (especially their residuals) and the correlation themselves for normality, homoscedasticity and linearity (Appendix A5.5.2), it was found that the best-fit models, showing an inverse relation between initial thickness and initial T_2 relaxation time in tibial cartilages, are all similar.

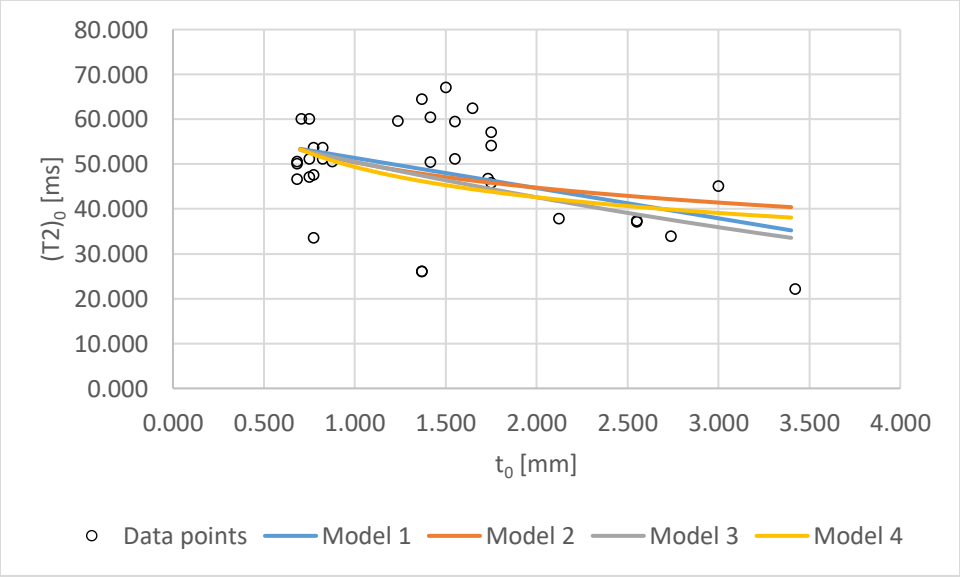

Figure 0-50: Significant best-fit models (after outlier/influence point removal) for initial T_2 relaxation time as a function of initial cartilage thickness do not exhibit major differences but rather all point towards an inverse relation between these parameters in tibial cartilages.

An assessment of the correlated variables (initial thickness and T_2 relaxation time, in their original and log-transformed expressions) was performed to verify that assumptions were met by linear regressions. This analysis showed that all best-fit models obtained (Figure 0-50) were appropriate, as there was a clear linear trend between variables, and their residuals were homoscedastic and normally distributed; however, it also showed that the majority of related measured variables followed expected statistical distributions (Appendix A5.5.2). Thickness and T_2 times exhibit positively skewed distributions, which makes sense, as they are always positive quantities. For the same reason, thickness change, engineering strain, T_2 change and T_2 strain would be expected to have negatively skewed distributions, since, in general, they represent compressions or reductions (negative quantities). However, only strains are negatively skewed, while thickness and T_2 changes follow nearly normal distributions. This, however, can be a consequence of the central limit theorem, since random variable averages [or (scaled) linear combinations of random variables] are normally distributed, regardless of the individual random variables' distributions. Clearly, thickness and T_2 changes are linear combinations of initial and final random variables, while strains may deceivingly seem scaled linear combinations. It might be easiest to see that engineering strain is not a normally distributed random variable, according to its finite elasticity definition involving the stretch ratio (a ratio of random variables or another skewed random variable), for which strain must always be skewed (positively for tension and negatively for compression). The same reasoning applies to T_2 strain and its "stretch ratio".

The different best-fit models themselves (obtained by applying different combinations of logarithm transformations) were very close to each other, for which the overall conclusions remained the same. Similarly, outlier/influence point removal did not change the fact that there appears to be an inverse trend between T_2 relaxation time and tibial cartilage thickness in unloaded tibial plateaus. Among these, best-fit models 1 and 2 are perhaps the most reliable, as their residuals follow a normal distribution the closest, while those for models 3 and 4 deviate slightly (although may fit the data better). Whereas other nonlinear transformations could have been tested to enhance model fit, it becomes more difficult to justify that those more complicated models describe real life processes, instead of simply artificially fitting random noise. Hence, we only dare to suggest there may be an inverse relation between unloaded tibial cartilage thickness and T_2 relaxation time.

A6. Additional resources for future studies

A6.1. Mechanical testing & imaging protocols

Once the system is verified (e.g., repeatability) and/or validated as best as possible, the following intended mode of operation (normal operation), which due to Covid19 could not happen, can be implemented at an MR scanner.

Before conducting the physiologic simulation (H-S, F-E, T-O*, F-F), one must acquire all desired images (e.g., qDESS, T_2 relaxation) for the unloaded state. Then, one must measure the specimen misalignment (using the fiducials and misalignment calculator), so that it can account for during the gait simulation. Hence, localizer images of the knee must be acquired for an extended and flexed configuration. Since these images are used to estimate the center of the knee from bony landmarks, it is not necessary to load the knee when extended to the high gait levels or that this loading is held for several hours to reach viscoelastic equilibrium. Instead, the knee can be in a fully axial (F-A) configuration but only loaded to 1 BW, while for the flexed configuration the unavoidable loading that comes with F-F simulation is acceptable.

Then (probably during another day/imaging session), the specimen can be loaded physiologically to the desired gait time point for > ~2.5 hours. Once steady state has been reached, all valves must be closed and pressure released from the pneumatic lines prior to disconnecting the compressor. The rig (carrying the loaded specimen) can be then transported on a cart to the MRI centre (RUH, UofS, Saskatoon, SK). For placing the rig into the MR scanner (Figure 0-51), it may help to roll the rig from the cart to a stretcher (both at the same height), and then from the stretcher to the MR bed (adjusting the height until they are both the same). The rest of the equipment in the control room can be connected to the rig via hoses through a duct in the control room wall. Finally, imaging can proceed, starting with steady state detection via imaging (see recommended protocol below). Once all sequences have been acquired for this simulated gait instant, the specimen must be unloaded and reoriented in a configuration corresponding to the next desired gait time point.

A

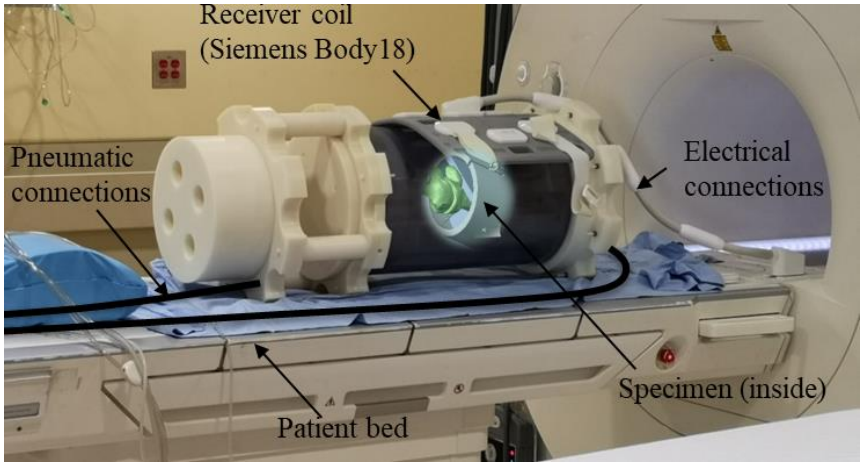

B

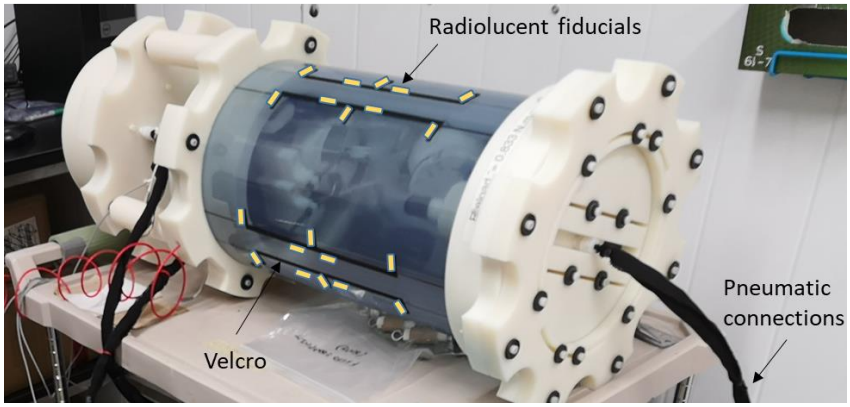

Figure 0-51: Normal operation (N1) mechanical testing setup: A) MR creep rig + Body 18 coil at MR scanner (Siemens Magnetom Skyra) – flange cutouts allow pneumatic/electric cables to pass through; B) MR creep rig without flex coil to show fiducials

It is recommended that each specimen is tested/imaged in an MR scanner in the following order to minimize rig assembly/setup time, and high costs associated with MR scanning times:

1. Load 0 (e.g., qDESS, T_2 relaxation)
2. Load F-A (localizer for alignment assessment)
3. Load F-F (localizer for alignment assessment)
4. Load F-F (e.g., steady-state detection, qDESS, T_2 relaxation)
5. Load H-S (e.g., steady-state detection, qDESS, T_2 relaxation)
6. Load T-O* (e.g., steady-state detection, qDESS, T_2 relaxation)
7. Load F-E (e.g., steady-state detection, qDESS, T2 relaxation)

A6.2. Further improvements/extensions

Future work involves addressing the limitations found in the individual studies, so that, when their individual methodologies are integrated, they allow achieving the overall objective of bridging the gap between tissue- and joint-level mechanical and qMRI load responses.

Whereas the OpenSim loading regime does include torque effects (i.e. internal/external rotation), the current MR creep rig design does not allow substantially applying this loading mode (other than that resulting from negligible medial/lateral specimen positioning error relative to the rig center and the shear force guide). However, the specimen's femoral pot and/or contacting puck could be redesigned to allow medial lateral shift control. This can help correct or take advantage of potting "misalignments" in the form of moment arms, which could be used to supply torque (and its physiologic variability) in load control by means of the anterior (balancing) shear force. Incorporating the gastrocnemius tension is perhaps more challenging. Due to how ex-vivo knees are cut (mid shank), this muscle must be pulled distally in order to load it, which probably requires a whole new tensile actuator mounted on the r-θ table, in such a way that it does not interfere with the compressive actuator placement.

Further aspects of system repeatability are yet to be assessed, such as the intra- and inter-observer precision of specimen misalignment, via the specimen misalignment calculator algorithm, which requires user input. Similarly, intra- and inter-observer precision of qMRI-mechanics program should be evaluated, since user judgement when selecting bony and soft tissue landmarks, despite being guided by predefined guidelines, may affect measurements and ultimately impact correlations. Also, when integrated with a MR scanner, imaging repeatability should be evaluated by repositioning the rig in the scanner. While tempting, it is not recommend to evaluate the testing reproducibility via specimen repositioning (i.e. remounting the specimen between imaging sequences), since that procedure is very long and expensive for this rig and should be minimized whenever possible.

On the longer term, some of the steps in the research pipeline could be accelerated via automation. Given the high accuracy and precision requirements of specimen preparation, rig assembly/disassembly and mechanical testing (all lengthy processes), robotics could be used to assist researchers or conduct some of these activities for them. A heavily involved route for

improving image acquisition by drastically increasing SNR and resolution may involve 7T systems and yet another MRI-safe, small-scale (pseudo) load-control device (much more compact and maybe limited in some aspects due to spatial constraints). Lastly, artificial inntelligence algorithms could also be used to process the imaging data (resampling, registration and segmentation) with greater speeds and consistency.

A6.3. Main future research direction for this project

Some of the next steps for this project were inspired by wanting to resolve whether contact pressure and T_2 spikes were related (although they seem different independent phenomena), which requires comparing and/or correlating those datasets. In fact, by doing this, one can build up and significantly improve upon the latest research and relate true mechanical properties to qMRI metrics and microstructure in a full-joint physiologic state describing physical activity. To execute this strategy (Appendix A6.1), one must adopt the previous plan (Figure 1-1), which could not be conducted due to Covid19. Here, HR morphologic and T_2 images must be first obtained for the knee unloaded at full extension, for determining strains later on. This must be followed by low-resolution morphologic images at full extension (loaded at 1BW) and full flexion (loaded by the corresponding muscle tension) for determining the knee center's average location throughout flexion from bones relative orientation and estimating the specimen misalignment with respect to the loading rig. Next, unlike previously, the specimen must be loaded to steady state for any loading configurations of interest (e.g., H-S, F-E, T-O*, F-F), as described in study I but accounting for specimen misalignment this time, and each loaded state imaged similarly to study II. Unless MRI-compatible pressure sensors are developed, to obtain the same deformation response as in the subsequent contact testing, ex-vivo knees must be then open in order to insert "dummy" sensors (same material and geometry as in actual pressure sensors, but without the MRI-incompatible metallic components). In order to align imaging data to the contact pressure distributions, the actual pressure sensors (whose placement should coincide with their fake versions, e.g., via registration marks) should be probed to delineate the tissues of interest. Measuring both of these mechanical responses (contact stress and tissue deformation) unlocks estimating in-situ local material properties (without explant or indentation testing, but from imaging and contact data under true physiologic loading conditions representative of joint habitual usage), which can be correlated to tissue-level qMRI and microstructural properties. And the key to all this is registering the surface contact stress fields (T-F, P-F) to the strain fields, thereby generalizing the qMRI-mechanics algorithm to include both axial strain and contact stress distributions. At this point, the choice of constitutive model is also critical for the overall goal and many strategies could be adopted; due to resolution limitations, bulk approaches (e.g., TIPE or nonlinear models) are suggested in lieu of modelling

individual composite elements. At this stage of research, larger sample sizes can be involved, which should be easier now, as no additional repeated measures should be required beyond this thesis, which should free up some time in the finite life of specimens for chasing this type or other research questions. Lastly, to reduce the costs of testing these or future ideas, we recommend taking advantage of the loading device versatility and using anatomic models or ex-vivo joints from animals (e.g., bovine, porcine, ovine), like researchers often do. If necessary, similar assessments could be done by computer using the loading rig's CAD or FE models, like some researchers do after developing such a complex loading system[25,89]. Also, in order to make the best use out of the specimens after contacts testing, the remaining tissues could be used in indentation and/or tissue-level mechanical testing (e.g., unconfined or confined compression).

A6.4. Additional future projects

Additional aspects of the current research questions or other (new) research questions can be investigated using the tools, techniques and data produced in this project. Some of the ideas that had been collected throughout this project (which were tempting to integrate in the present research, but limited by reality) include:

1. Evaluating the effect of healthy or pathologic conditions in gait loading.
2. Exploring the role other physical activities (e.g., running, jumping, incorporating, sitting down) play in tissue- and joint-level function.
3. Applying the tools and methodologies to study other joints (e.g., hip, elbow, shoulder, spine, neck) and/or species (e.g., bovine, porcine, ovine).
4. Developing and/or evaluating physical treatments (e.g., unloading the medial T-F plateau via valgum-like loading, which could be practically achieved using inclined soles).
5. Developing and/or evaluate repair techniques or implant designs.
6. Evaluating the performance of different contrast agents before using them in vivo.
7. Exploring qMRI-mechanics links with other sequences (e.g., $T_{1\rho}$, dGEMRIC, qMT) in order to have a more complete qMRI description of tissues.
8. Evaluating the effect of normal and/or abnormal variability on contact deformation and qMRI responses.